Field observations and numerical simulations on the role of local structures and seismic source characteristics in the influence of external earthquakes in volcanic and hydrothermal activity

Dissertation

zur

Erlangung des Doktorgrades (Dr. rer. nat.)

der

Mathematisch-Naturwissenschaftlichen Fakultät

der

Rheinischen Friedrich-Wilhelms-Universität Bonn

vorgelegt von

Cristian Farías

aus

Temuco, Chile

Bonn 2015

Angefertigt mit Genehmigung der Mathematisch-Naturwissenschaftlichen Fakultät
der Rheinischen Friedrich-Wilhelms-Universität Bonn
am Steinmann-Institut für Geologie, Mineralogie und Paläontologie

1. Referent: Prof. Dr. Stephen A. Miller
2. Referent: Prof. Dr. Andreas Kemna

Tag der Promotion:
Erscheinungsjahr: 2015

Diese Dissertation ist auf dem Hochschulschriftenserver der ULB Bonn
http://hss.ulb.uni-bonn.de/diss_online elektronisch publiziert.

Abstract

Earthquakes can trigger volcanic and hydrothermal activity at a large distance range and a wide time window. While advances in observations in the last two decades have helped to establish that there exist a causal connection between earthquakes and volcanism, the underlying physical mechanisms that control such interaction are not completely understood.

In this thesis I study the influence of earthquakes in volcanic and hydrothermal zones using field observations and numerical simulations. The observations come from the data retrieved in a field campaign at Nevados de Chillán volcano, located in central-south Chile. This composite volcanic/hydrothermal system recorded an interesting response to two large aftershocks of the Maule earthquake, of magnitudes $M_W = 6.1$ and $M_W = 7.1$, with both of them located about 200 km from the system. The complex recorded an increase in local seismicity for the first, smaller event, and a slight decrease in seismicity for the larger earthquake.

To have a better understanding of the underlying physical mechanisms that control the earthquake influence in a volcanic/hydrothermal system I used numerical simulations to quantify the dynamic and static changes induced by the earthquake in simple systems composed by fluid reservoirs connected to geological faults. Results show that, while the earthquake characteristics dominate its influence in a volcanic region, the local structures play a very important role, altering both the static and dynamic changes induced by the earthquake. The results unveil a far more complex earthquake impact in a volcanic/hydrothermal system that it has been considered so far, with local structures, such as fluid reservoirs and geological faults, being important players in the modulation of the earthquake influence on the system. Finally, I present the results of a simulation of the Nevados de Chillán response to the two large aftershocks of the 2010 Maule earthquake. Results show that the sum of the earthquake characteristics with the geometry of the local structures are key to understand the different effects that the two events have in the volcanic/hydrothermal system, with the $M_W = 6.1$ being more important at a fluid level, which is congruent with the field observations.

The results presented in this thesis support the idea of a complex relationship between earthquakes and volcanic/hydrothermal activity, in which both the earthquake characteristics and the local structures of the volcanic/hydrothermal system must be taken into account.

Zusammenfassung

Erdbeben können vulkanische und hydrothermale Aktivität über eine große Distanz und über ein großes Zeitfenster hinweg verursachen. Während Fortschritte in den letzten zwei Jahrzehnten in der Beobachtung geholfen haben einen kausalen Zusammenhang zwischen Erdbeben und Vulkanismus zu bestätigen, sind die zugrunde liegenden physikalischen Mechanismen, die einen solchen Zusammenhang kontrollieren noch nicht vollständig verstanden.

In dieser Arbeit untersuche ich den Einfluss von Erdbeben in vulkanischen und hydrothermalen Gebieten mit Hilfe von Feldbeobachtungen und numerischen Simulationen. The Felddaten wurden durch eine Messkampagne am Vulkan Nevados de Chillán in zentral-süd Chile gewonnen. Dieses gemischte vulkanische/hydrothermale system zeigte eine interessante Antwort auf zwei starke Nachbeben des Maule Erdbebens mit den Magnituden $M_W = 6.1$ und $M_W = 7.1$, beide Nachbeben jeweils knapp 200 km entfernt. Für das erste, kleinere Beben wurde ein Anstieg in lokaler Seismizität beobachtet, aber eine leichte Abnahme für das stärkere Beben.

Für ein besseres Verständnis der zugrunde liegenden physikalischen Mechanismen des Einflusses von Erdbeben auf vulkanische / hydrothermale systeme, verwende ich numerische Simulationen, um die durch das Erdbeben verursachten dynamischen und statischen Veränderungen in einem simplen System bestehend aus einem Fluidreservoir und einer geologischen Verwerfung zu quantifizieren. Die Ergebnise zeigen, dass die lokalen Strukturen sehr wichtig sind, da sie die statischen und dynamischen Veränderungen des Erdbebens beieinflussen. Zudem dominieren die Charakteristiken der Erdbeben die Wirkung auf die vulkanische Region. Die Ergebnisse offenbaren einen weit komplexeren Einfluss der Erdbeben auf das vulkanische und hydrothermale System als bisher angenommen. Lokale Strukturen, wie Fluidreservoire und geologische Verwerfungen sind wichtige Faktoren bezüglich der Wirkung des Erdbebens auf das System. Abschließend präsentiere ich Ergebnisse einer Simulation der Antwort des Nevados de Chillán auf die zwei erwähnten Nachbeben des 2010 Maule Erdebebens. Die Ergebnisse zeigen, dass die Summe der Erdbebencharakteristika zusammen mit der Geometrie der lokalen Strukturen der Schlüßel zum Verständnis der untschiedlichen Reaktionen des Systems auf die beiden Beben sind, da das Nachbeben der Stärke $M_W = 6.1$ für die Fluidbewegung wichtiger ist, was sich auch mit den Feldbeobachtungen deckt.

Die Ergbenisse, die ich in dieser Arbeit vorstelle, unterstützen die Idee einer kom-

plexen Beziehung zwischen Erdbeben und vulkanischer/hydtothermaler Aktivität, in welche sowohl die Erdbebencharakteristika als auch die lokalen Strukturen des Systems berücksichtigt werden müssen.

Contents

Chapter 1

Introduction

Today, global society is more susceptible to distant perturbations than it was in previous decades. Even a moderate volcanic eruption can prove largely troublesome to people living thousands of kilometers away, as is it reflected by the disruption of more than 95000 flights in Europe in 2008, due to the eruption of Eyjafjallajökull(BBC, 2010). In addition, damages to the economy due to the earthquake-induced destruction are larger than ever before, due to the high level of connection between countries, and the growing concentrations of population in regions potentially affected by large seismic motions. For instance, combined economical losses due to the $M_W = 9.1$ Tohoku and $M_W = 8.8$ Maule earthquakes were estimated to be around USD$260 billion(UNEP, 2011)(Times, 2011), with the Japan earthquake being the most costliest natural disaster in the history of mankind. People's life is also directly affected, due mainly to direct destruction and infrastructure damage generated by earthquakes and volcanic eruptions, and also by posterior effects such as tsunamis and floods. During the history of mankind, millions have perished due to natural disasters, and a much larger amount have lost their houses and other properties. Such impact makes critical to advance in the research of these phenomena.

The vast majority earthquakes and volcanic eruptions are generated in regions close to the boundaries between tectonic plates. Earthquakes occur due to the unlocking of two sections of these plates, and generate a rupture on the crust. Earthquake magnitude scale exponentially with the size of the rupture. On the other hand, volcanic eruptions are generated by the rise of overpressurized fluids that are trapped in the Earth crust. The size of a volcanic eruption depends largely on the type of magma that is risen from the crust up to the atmosphere. In general, more viscous magmas tend to contain a larger gas content, thus confining a higher gas pressure, which generate a more explosive, and destructive, volcanic eruption. Generally, the most destructive earthquakes occur in subduction zones, where a tectonic plate moves towards another, in a convergent motion, and it slides beneath the other plate. The region of the world where the largest earthquakes are generated is the called "Ring of Fire", which is composed by the different subduction zones on the Pacific Ocean, affecting four different continents directly. Normally, volcanic arcs are generated in

subduction zones by the relative motions between plates, which favor the rise of fluids, making this "Ring of Fire" the region in which most active volcanoes are located. Nevertheless, other regions like Italy, Iceland, and Turkey, do present a high rate of earthquakes and volcanism, reflecting that the occurrence of these phenomena is global and not only constrained to some regions in the world.

1.1 Volcanic and hydrothermal systems

Volcanoes are regions of the Earth where magma arises into the surface. Magma is a very viscous fluids that forms from the partial melting of the rocks that live deep in the litosphere-astenosphere boundary. It migrates up the crust, and can be stored in several magma chambers located at depths that go from several hundred meters to some kilometers. By the time it is stored in a superficial chamber, it contains various volatiles, with water being the most important of them. Other important gases are CO_2 and SO_2(Gonnermann and Manga, 2007), with this last one giving that particular smell to active volcanic regions. Due to the high temperature of the magma, heat is transferred from the fluid to the surrounding host rock. Most of the time, water is confined at the vicinity of the magma chambers, and it is thus heated up by the magma. This high-pressurized fluid, that contains several different minerals dissolved on it, can also ascend to the surface, producing mainly hot springs, fumaroles, and sometimes geysers.

A volcanic eruption can occur in many ways. Magma can reach the surface due to a large overpressure at the magma chamber level, or a sudden pressure gradient can be formed when the surface load is suddenly removed(Gonnermann and Manga, 2007). Due to the high content of volatiles, magma can get to the surface in a very explosive manner. The explosivity depends strongly on magma viscosity, which in turn depends on its composition. Less viscous magmas produce less explosive eruptions, like in the volcanoes in Hawaii, whilst more viscous magmas are most likely to produce explosive eruptions. One particular example of a volcanic eruption that involved a highly viscous magma was the plinian eruption of Chaitén volcano in Chile, which started on May, 2008. It is not unusual that the water that is present in the vicinity of the magma chamber can enter in contact with the magma, thus producing *phreatomagmatic eruptions*. It is often assumed that most eruptions have a phreatomagmatic component in them. Another way to induce an increase in overpressure at magma chamber include the crystallization of volatiles inside the fluid, or magma-mixing, which can drastically increase the internal magma pressure, even leading it to a breaking point, like what is believed to have happened in the 1883 eruption of the Krakatoa volcano, in Indonesia(Mandeville et al., 1996).

While the particular dynamics of each eruption are very complex, a categorization exist in terms of their volcanic explosivity index (VEI). Fig. 1.1 show pictures of the most known ones. The less explosive eruptions are called *hawaiian*, which are

Figure 1.1: Different types of volcanic eruptions: a) Mauna Loa volcano showing a hawaiian eruption, typical of loe viscosity magmas. b) Strombolian eruption recorded at Llaima volcano, in south Chile. c) Vulcanian phase of the Eyjafjallajökull, in Iceland. d) Plinian eruption of Chaitén volcano, which involved a rhyolitic magma, of very high viscosity. Pictures are taken from the internet.

very effusive, and involve magmas with a small content of gas trapped inside them. They arrive into the surface forming lava flows, and their VEI of these eruptions is usually between 0 and 1. Magmas with a larger viscosity, typically basaltic to andesitic, usually have a more important gas content, thus generating explosions when the magma arises into the surface. When the explosions are not very energetic and are produced rhythmically, the eruption is called *strombolian*. While large pieces of solidified magma are thrown into the atmosphere during these explosions at distances that can reach several hundreds of meters, lava flows are also observed, particularly after the magma has lost some of its volatile content. The VEI of these eruptions often range between 2 and 3. *Vulcanian* eruptions are often observed at volcanic centers that have more viscous magmas, usually andesitic. Here, important columns of tephra are generated after the difference between the inner volatile and atmospheric pressure is so large that magma breaks in very small pieces. These eruptions are more explosive and have a VEI between 3 and 4. When the VEI is greater or equal to 5, we talk about *plinian* eruptions, paroxysmal events that can affect the Earth at a global level. Tephra columns reach height of tens of kilometers, and can generate massive *pyroclastic flows* that destroy everything in its path. Important eruption of this type were recorded in 1980 in Mt. St. Helens (VEI=5), and in 1815 at Tambora volcano (VEI=7), with this last one producing the famous *year without summer* in Europe . These type of eruptions get their name in honor of Pliny the Younger, who first described the AD 79 eruption of mount Vesubius, in Italy, that destroyed and buried the cities of Pompeii and Herculaneum.

During an eruption, and depending on the regional geographical characteristics, lahars can also be produced. Although their reach is local, they can be very dangerous, being capable to bury entire towns. One very known example is the disappearance of the town of Armero, in Colombia, after the eruption of the Nevado del Ruiz volcano, in 1985, where 25000 people lost their lives.

1.1.1 Volcanic seismicity

The dynamics of an active volcanic region are controlled by the regional tectonics and the fluid movement beneath the surface. These motions generate earthquakes that have a particular signature, and are related to several volcanic and/or tectonic processes.

Volcanic systems have local tectonic faults, that play an important role on their dynamics. Earthquakes can be generated inside these structures, and have the characteristics of tectonic earthquakes. The faulting dynamics of these earthquakes define their *focal mechanism*, that can be used to infer the local stress state of the system. Fluid mobilization can also trigger fracturing and mobilizitation of preexistent faults in the crust, generating earthquakes. These seismic events are often localized near, or in, the regional tectonic structures, suggesting that they are connected to the fluids. They are called *Volcano Tectonic earthquakes* (VT). They

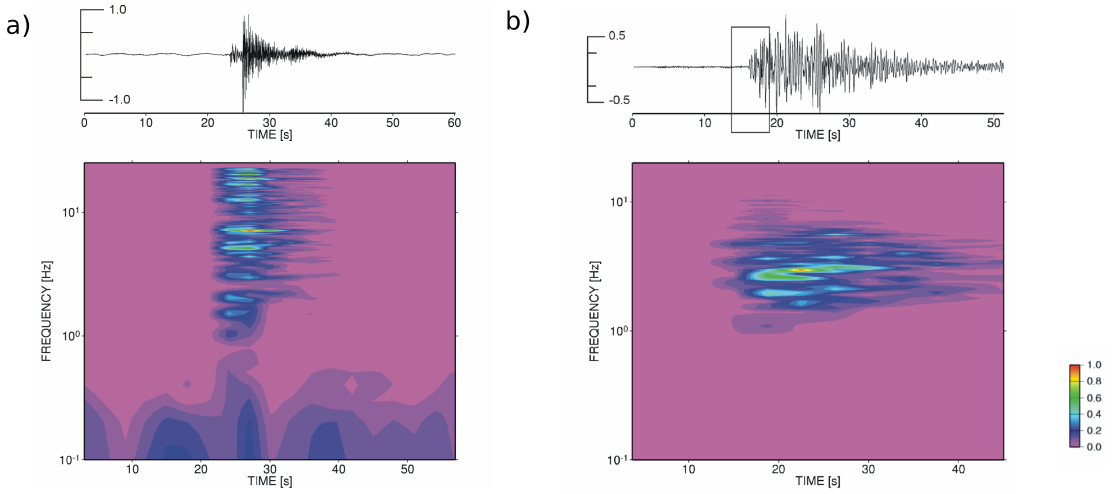

Figure 1.2: Waveforms and spectrogram of VT events recorded by a seismometer located nearby a volcanic zone. a) Deep VT event, showing a clear P- and S-wave onset, and a frequency content higher than 5 Hz. b) Shallow VT event, where no clear distintion between P- and S-wave arrivals can be made. Frequency content is lower than in the case of a), with most oscillation frequencies in the $1 - 5$ Hz range. Pictures taken from (Wassermann, 2012)

indicate both tectonic and fluid driven activity, and are very helpful to identify the main sources of volcanic and hydrothermal activity. Magnitudes for these events vary from microseismic to moderate values, depending on the strength of the fluid activity.

Fig. 1.2 presents the typical waveform recorded for VT events at a seismometer located in a volcanic system. The characteristics of these waveforms vary depending on the location of the source. For deep earthquakes, generated at a depth greater than 2 km, clear P- and S- wave onsets can be observed in a seismograph, with oscillation frequencies that are normally higher than 5 Hz. P- and S-waves arrivals are not easy to detect for shallow VT earthquakes, and the frequency content of the recorded waveforms is in the lower $1 - 5$ Hz range.

Fluid mobilization can also occur without generating clear fractures, but still recording a clear signal in a seismograph. One type of these signals is characterized by low frequency oscillations, without the presence of an S-wave, and is called an *Long Period earthquake*, or LP. An increase in the occurrence of LP events is often correlated with an increase on fluid activity, particularly magma. Another type of event related to fluid motion is the *volcanic tremor*. In a seismogram this is seen as a long-lasting signal, with a peculiar frequency content composed by a main frequency of oscillation plus several overtones. In the case of hydrothermal tremor, the frequency content tends to be higher. While the occurrence of this type of signal is often related to periods of high volcanic and/or hydrothermal activity, and are indicators of a possible eruption, their nature is not completely understood. It has

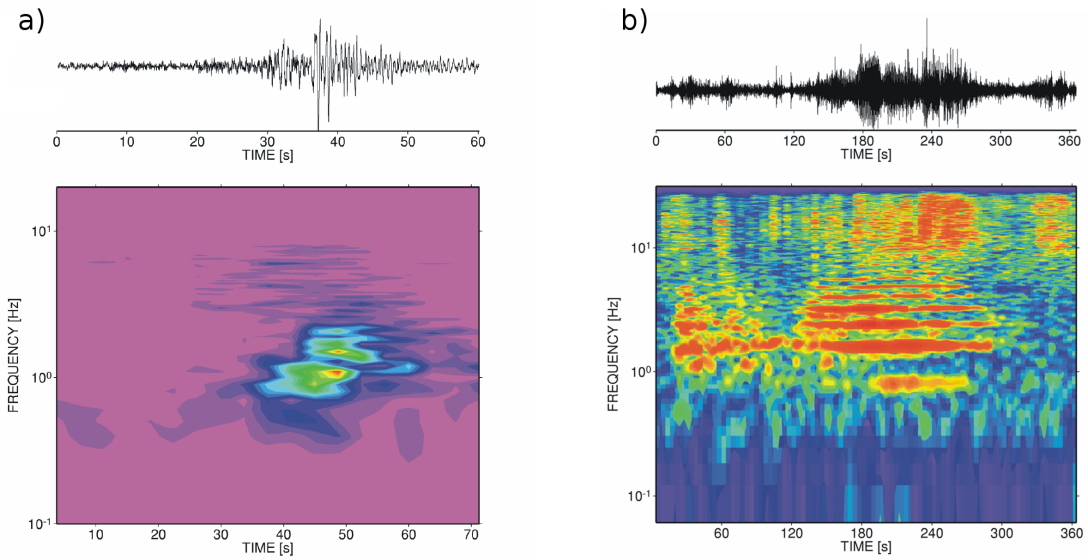

Figure 1.3: Waveforms and spectrogram of an LP event (a), and a tremor event (b). LP event highlights a low frequeny band, and does not have a S-wave. The volcanic tremor signal shows a harmonic behavior, with a dominant band around 2 Hz and several overtones. The waveform is long and without impulsive onsets. Pictures are taken from (Wassermann, 2012).

been suggested that these type of events are generated by resonances at the conduit level of the volcano, and a superposition of other volcanic earthquakes(Wassermann, 2012). Fig. 1.3 shows common traces of LP and tremor events.

Sometimes, after a fluid-driven crack is generated, fluid can mobilize into this new crack. This mechanism is believed to be captured in a *hybrid event*, that represent a mixture between a VT and a LP event. It is composed by an impulsive phase that is similar to the one of a VT event, even with a comparable frequency content, but it does have a larger coda, with a predominance of lower frequencies, resembling an LP event.

Volcanic and hydrothermal seismic signatures vary from one volcano to another, but the most common events are the ones described here. In chapter 2 I present more details on the use of volcanic seismology in the study of the dynamics of a volcanic/hydrothermal system, with a complete description of the seismic activity of the Nevados de Chillán volcanic complex, in central-south Chile.

1.2 General theory of earthquakes and elastic spaces

1.2.1 Elastic and poroelastic spaces

To describe the dynamics of the Earth's crust, we have to consider stresses and strains. Stress is a physical quantity related to the total force F applied into a

body with surface A, it is defined by $\sigma = F/A$. It can be decomposed in a normal component σ_n and a tangential, or shear, component, τ. Strain is the measure of the deformation of the body, and it is denoted by e. In three dimensions, both quantities are represented by a rank-2 tensor. In a cartesian coordinate system, the stress tensor is given by

$$\sigma = \begin{pmatrix} \sigma_{xx} & \sigma_{xy} & \sigma_{xz} \\ \sigma_{yx} & \sigma_{yy} & \sigma_{yz} \\ \sigma_{zx} & \sigma_{zy} & \sigma_{zz} \end{pmatrix} . \tag{1.1}$$

The stress tensor is symmetric, meaning that $\sigma_{xy} = \sigma_{yx},\ \sigma_{xz} = \sigma_{zx}$ and $\sigma_{yz} = \sigma_{zy}$. The elements of the diagonal of the stress tensor are called normal stresses, whilst the remaining ones are the shear stresses. It is always possible to find a coordinate system in which the stress tensor is diagonal. There, it has the following form:

$$\sigma = \begin{pmatrix} \sigma_1 & 0 & 0 \\ 0 & \sigma_2 & 0 \\ 0 & 0 & \sigma_3 \end{pmatrix} \tag{1.2}$$

with $\sigma_1,\ \sigma_2$, and σ_3 being the *principal stresses*. This tensor has three invariants, given, in a three-dimensional cartesian coordinate system, by

$$I_1 = \frac{1}{3}\left(\sigma_{xx} + \sigma_{yy} + \sigma_{zz}\right) , \tag{1.3}$$

$$I_2 = \sigma_{xx}\sigma_{zz} + \sigma_{yy}\sigma_{zz} + \sigma_{xx}\sigma_{zz} - \sigma_{xy}^2 - \sigma_{yz}^2 - \sigma_{xz}^3 , \tag{1.4}$$

$$I_3 = \sigma_{xx}\sigma_{yy}\sigma_{zz} + 2\sigma_{xy}\sigma_{xz}\sigma_{yz} - \sigma_{xy}^2\sigma_{zz} - \sigma_{xz}^2\sigma_{xx} - \sigma_{xz}^2\sigma_{yy} . \tag{1.5}$$

Here, the first invariant is called the *mean stress*, which is related to the total volumetric change induced in a body due to the action of stress on it.

The strain tensor is related to the deformation of a body $\mathbf{u}$, which in a cartesian coordinate system is $\mathbf{u} = u_x\hat{x} + u_y\hat{y} + u_z\hat{z}$. In the same coordinate system, the strain tensor is given by

$$e = \frac{1}{2}\begin{pmatrix} 2\dfrac{\partial u_x}{\partial x} & \dfrac{\partial u_x}{\partial y} + \dfrac{\partial u_y}{\partial x} & \dfrac{\partial u_x}{\partial z} + \dfrac{\partial u_z}{\partial x} \\ \dfrac{\partial u_y}{\partial x} + \dfrac{\partial u_x}{\partial y} & 2\dfrac{\partial u_y}{\partial y} & \dfrac{\partial u_y}{\partial z} + \dfrac{\partial u_z}{\partial y} \\ \dfrac{\partial u_z}{\partial x} + \dfrac{\partial u_x}{\partial z} & \dfrac{\partial u_z}{\partial y} + \dfrac{\partial u_y}{\partial z} & 2\dfrac{\partial u_z}{\partial z} \end{pmatrix} . \tag{1.6}$$

There is a linear relation between the stress and strain tensors. This fact allow us to write the equations of motion of the space, in the following way:

$$\rho\frac{\partial^2 u_i(\mathbf{x},t)}{\partial t^2} = \frac{\partial \sigma_{ij}(\mathbf{x},t)}{\partial x_i} + f_i(\mathbf{x},t) , \tag{1.7}$$

$$\frac{\partial \sigma_{ij}}{\partial t} = \lambda\delta_{ij}\theta + 2\mu e_{ij} , \tag{1.8}$$

where λ and μ are the *Lamé coefficients* and ρ the density of the solid. Here, $i = 1, 2, 3$ and $j = 1, 2, 3$ are indexes and $e_{kk} = e_{11} + e_{22} + e_{33}$ is the trace of the strain tensor. In a cartesian coordinate system, $e_{kk} = e_{xx} + e_{yy} + e_{zz}$. External body forces are denoted by $f_i(\mathbf{x}, t)$, and δ_{ij} is the Kronecker delta.

In a 2-D space composed by the $x - z$ plane, where gravity is present, the equations of motion are

$$\frac{d\sigma_{xx}}{dt} = (\lambda + 2\mu)\frac{\partial v_x}{\partial x} + \lambda\frac{\partial v_z}{\partial z}\,, \tag{1.9}$$

$$\frac{d\sigma_{zz}}{dt} = (\lambda + 2\mu)\frac{\partial v_z}{\partial z} + \lambda\frac{\partial v_x}{\partial x}\,, \tag{1.10}$$

$$\frac{d\sigma_{xz}}{dt} = \mu\left[\frac{\partial v_z}{\partial x} + \frac{\partial v_x}{\partial z}\right]\,, \tag{1.11}$$

$$\frac{dv_x}{dt} = \frac{1}{\rho}\left[\frac{\partial \sigma_{xx}}{\partial x} + \frac{\partial \sigma_{xz}}{\partial z}\right]\,, \tag{1.12}$$

$$\frac{dv_z}{dt} = \frac{1}{\rho}\left[\frac{\partial \sigma_{xz}}{\partial x} + \frac{\partial \sigma_{zz}}{\partial z}\right] + g\,, \tag{1.13}$$

where v_x and v_z are the displacement velocities, defined by $v_i = \partial u_i/\partial t$. Here we are using the sign convention in which the z-coordinate is defined to go downwards. When no external body forces are applied, two solutions of the system of equations composed by Eqs. (1.7) and (1.8) are the scalar potentials Φ and Ξ, which satisfy the wave equations

$$\nabla^2\Phi(\mathbf{x}, t) = \frac{1}{\alpha^2}\frac{\partial^2\Phi(\mathbf{x}, t)}{\partial t^2}\,, \tag{1.14}$$

$$\nabla^2\Xi(\mathbf{x}, t) = \frac{1}{\beta^2}\frac{\partial^2\Xi(\mathbf{x}, t)}{\partial t^2}\,, \tag{1.15}$$

where α and β are wave velocities, given by

$$\alpha = \sqrt{\frac{\lambda + 2\mu}{\rho}}\,, \qquad \beta = \sqrt{\frac{\mu}{\rho}}\,.$$

The potentials Φ and Ξ are solutions of the equations of motion of the space, and are called P and S waves, respectively. The ground motion due to P-waves is parallel to the wave direction, whilst the ground motion due to S-waves is perpendicular to the wave direction. Fig. 1.4 shows how ground moves due to plane P and S waves.

The inner dynamics of the Earth move the tectonic plates on which we stand. This motion generates deformations at several surfaces of the crust, which are called *faults*. There, a relative motion between the two faces of the surface is generated. Due to the friction between them, which can be enhanced by some asperities, sometimes

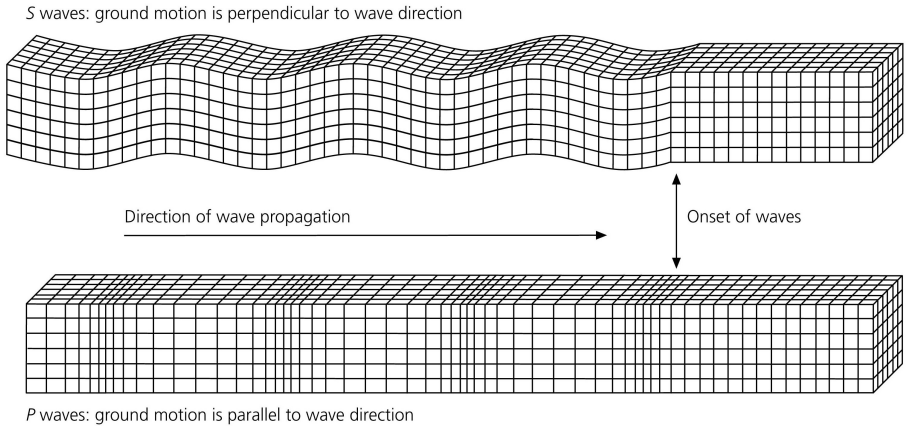

Figure 1.4: Displacement produces by plane P and S waves. P waves induce ground motion that is parallel to the wave direction, whilst the ground motion is perpendicular to the wave direction for S waves. Taken from (Stein and Wysession, 2003)

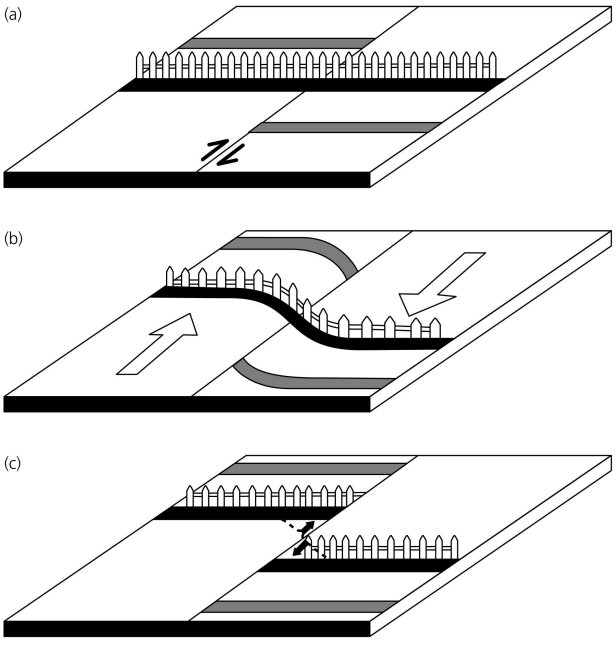

Figure 1.5: Basic sketch of how an earthquake is generated: a) a fault zone moves in a natural way, because of the Earth's inner dynamics. b) At some point, the fault gets locked, and no movement is recorded, thus building up strain and, consequently, stress. c) When the strain is too large, both faces of the fault suddenly move respect to each other, generating an earthquake, and releasing seismic waves. Picture taken from (Stein and Wysession, 2003).

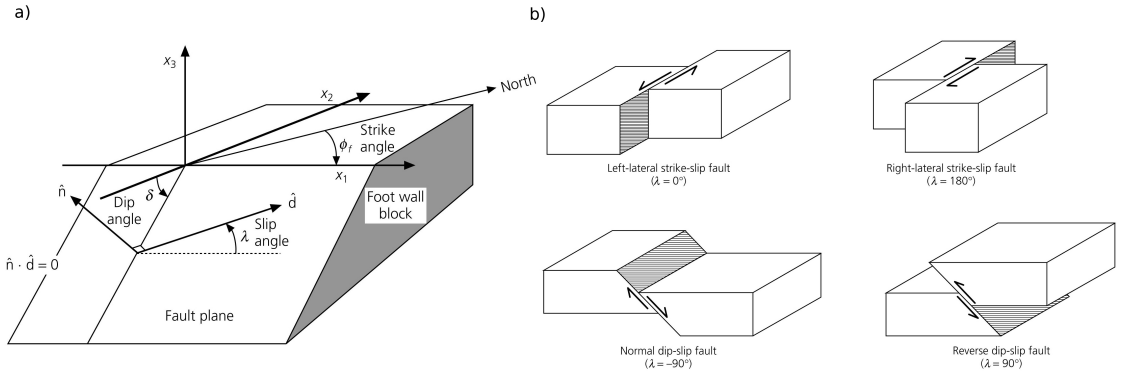

Figure 1.6: a) Geometry of a fault, with indications of each one of the three angles that define the relative motion between two blocks in a fault. More details on how these angles are measured can be found in the text. b) The most basic types of faulting, each one defined by a particular value of the slip angle. Picture was taken from (Stein and Wysession, 2003).

the fault gets locked, and no motion is perceived. This generates deformation in the whole space, but particularly at the fault, building up stress. When the strain is too large, the two faces suddenly move respective to each other, releasing the stress and generating seismic waves that move through the whole planet, shaking the ground. When these waves arrive at our position, we say that we *feel* an earthquake. After the earthquake occurs, the normal motion at the fault continues, and at some point in time it will be locked again, and the same situation will be repeated. Fig. 1.5 shows this process in a graphic way.

The relative displacement between the two faces of the fault can be defined by three angles: dip, strike, and slip. In a cartesian coordinate system, the dip angle is measured respective to the $x_1 - x_2$ plane, and marks the inclination of the fault plane. The strike angle is measured between a vector that follows the direction of the fault and the direction of the north. The slip angle is related to the displacement vector $\hat{d}$, is perpendicular to the vector normal to the fault plane $\hat{n}$, and is measured respect to the $\hat{x}_1$ direction. Different values of the slip angle define the *focal mechanism* of the earthquake. Fig.1.6 shows the most basic ones: strike-slip and dip-slip. The focal mechanism of each earthquake is important in both the characteristics of the waves released, as well as the long-term impact such a dislocation has in the space around it.

When an earthquake occurs, a rupture zone is created at the fault. The size of its area and the absolute value of the displacement vector are critical to define the size of the earthquake. In fact, the *seismic moment* is given by

$$M_0 = \mu S|\mathbf{d}|\,,$$

and it is used to define the earthquake magnitude M_W by using the relation

$$M_W = \frac{2}{3}\log_{10}(M_0) - 6\,, \tag{1.16}$$

where M_0 is measured in $\mathrm{N}\cdot\mathrm{m}$. Thus, there is a logarithmic relation between the size of the rupture zone with the magnitude of the earthquake.

The equations of motion of the elastic space have three main parameters: the density of the solid, ρ, the first Lamé coefficient, λ, and the second Lamé coefficient, μ, also known as the *shear modulus*. These last two parameters are elastic constants of the medium, and are very useful to describe the motion of seismic waves. Nevertheless, for engineering purposes, where it is important to study the structural properties of a system, the Young modulus E, the bulk modulus K, and the Poisson ratio ν are more useful. Any parameter of these five can be calculating starting from only two of them. In particular, if we start with known values for the Young modulus and the Poisson ratio, we can calculate μ, λ, and K as follows:

$$\mu = \frac{E}{1(1+\nu)}\,, \tag{1.17}$$

$$\lambda = \frac{E\nu}{(1+\nu)(1-2\nu)}\,, \tag{1.18}$$

$$K = \frac{E}{3(1-2\nu)}\,. \tag{1.19}$$

The stresses and velocities in an elastic space change during and after a perturbation such as an earthquake. To assess its influence on a particular region of the space, is it relevant to analyze the values of several physical quantities.

The volumetric change is related to the trace of the stress tensor, or mean stress. In a cartesian coordinate system, it is given by

$$\Theta(\mathbf{x},t) = \frac{1}{3}(\sigma_{xx}(\mathbf{x},t) + \sigma_{yy}(\mathbf{x},t) + \sigma_{zz}(\mathbf{x},t))\,. \tag{1.20}$$

This quantity gives us information about the current volumetric regime of one section of the elastic space, with the sign of this value giving us information of whether it is being expanded or compressed. In our sign convention, more used in the study of rock mechanics, a positive value for Θ denotes compression, and a negative value for Θ corresponds to extension.

When in a presence of a structure, such a geological fault, one of the important questions is how it will move during and after an earthquake. In particular, we are more interested in how the seismic motion can affect the long term motion of such an structure. The normal stress σ_n is an useful quantity, as its value tells

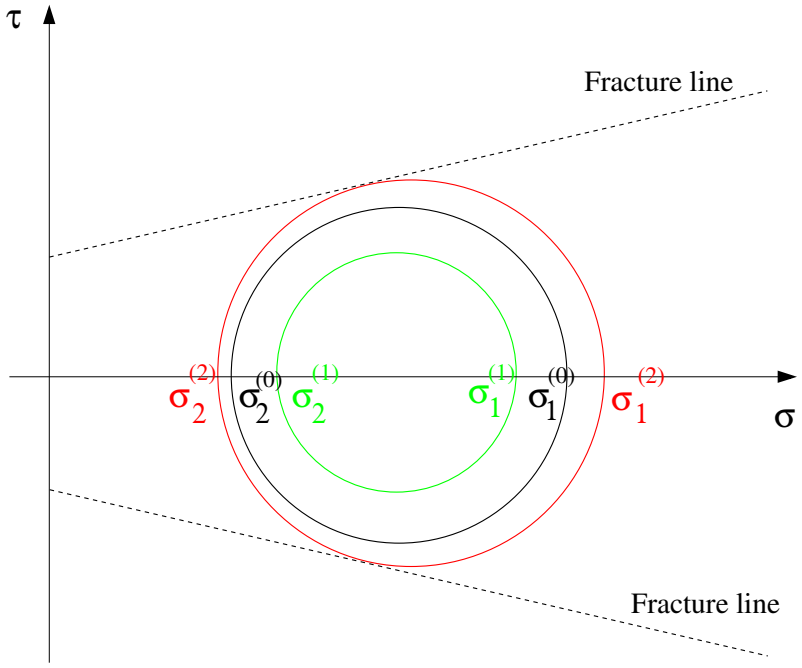

Figure 1.7: Mohr circle representation of the dynamic effect of an earthquake that produces a fracture at a distant body. Before the earthquake, the stress state is such that the Mohr circle is the one represented in black. With the first motions produced by the seismic event, σ_1 is reduced and σ_2 is increased, thus reducing the radius of the Mohr circle sketched in green. At some point, the earthquake-induced changes in the principal stresses are such that the Mohr circle, in red, touches the failure lines, and a the body breaks.

us whether faulting is promoted or discouraged at the structure under study. In our sign convention, a negative value for σ_n indicates unclamping, where faulting is promoted, while a positive value for σ_n indicates clamping, where faulting is discouraged. In a two dimensional cartesian coordinate system, the normal stress is given by

$$\sigma_n(\mathbf{x},t) = \frac{\sigma_{xx}(\mathbf{x},t)+\sigma_{yy}(\mathbf{x},t)}{2} + \frac{\sigma_{xx}(\mathbf{x},t)-\sigma_{yy}(\mathbf{x},t)}{2}\cos 2\theta + \sigma_{xy}(\mathbf{x},t)\sin 2\theta\,, \quad (1.21)$$

where θ is the angle of inclination of the fault, measured respect to a line parallel to the $\hat{x}$ direction.

An earthquake produces changes in the local stress tensor of a body. When these changes are too large to bear, the body can break. The *Coulomb-Mohr failure criterion* gives a relation between normal and shear stresses that is fulfilled when a fracture occurs. This relation can be stated as

$$|\tau| = \tau_0 + \tan\phi\sigma\,,$$

where ϕ is the *angle of internal friction* of the solid, and τ_0 is the *cohesive strength* of the material. In a $\tau - \sigma$ plot, a circle is defined by the values of two principal

stresses σ_1 and σ_2. If the values of the principal stresses are such that this circle, called *Mohr circle*, touches the failure lines, the solid breaks. A simple way in which we can show how an earthquake can produce fracture in a remote place is by looking at the situation presented in Fig. 1.7. At the beginning, the stress state of the region is defined by a particular value of σ_1 and σ_2, in black. During the passage of the seismic waves through the region, the values of the principal stresses change, affecting also the Mohr circle. First they take values such as the circle is the one colored in green, reducing the faulting potential, and afterwards σ_1 is increased and σ_2 is reduced in a way that the Mohr circle touches the fracture line. At this point, a fracture is produced.

An extension of this failure criterion that is very useful is the analysis of the Coulomb yield function, which depends on the stress state of the particular body at one point in time. If the yield function is larger than zero, the body fractures. In a two-dimensional coordinate system, the yield function is given by

$$f(\mathbf{x},t) = \sqrt{\frac{1}{4}(\sigma_{xx}(\mathbf{x},t) - \sigma_{zz}(\mathbf{x},t))^2 + \sigma_{xz}^2(\mathbf{x},t)} - \frac{1}{2}(\sigma_{xx}(\mathbf{x},t) + \sigma_{zz}(\mathbf{x},t)) \sin\phi - \tau_0 \cos\phi \,. \tag{1.22}$$

The main scope of this thesis is the study of the interaction between seismic waves and fluids trapped in the crust. It is therefore needed to account for the role of fluids in the equations of motion that model the Earth's crust. In the linear poroelastic theory this is achieved by defining the *effective stresses*. They are the responsible for the deformation of the system, and are given by

$$\sigma_{ij}^{\text{eff}} = \sigma_{ij} - \delta_{ij} P \,,$$

with δ_{ij} the Kronecker delta, and P the fluid pressure, also known as *pore pressure*.

With this definition, the equations of motion are changed, replacing σ_{ij} with σ_{ij}^{eff} in Eq. (1.8). Normal stress and Coulomb yield function definitions also change, with σ_{ij}^{eff} replacing σ_{ij}.

1.3 Earthquake-volcano interactions

Fluid dynamics are crucial for the behavior of volcanic and hydrothermal systems. One interesting question is how these dynamics change when affected by an external perturbation, such as an earthquake. Until 15-20 years ago, volcanic and hydrothermal activity were considered to be completely independent from the occurrence of tectonic earthquakes. Nevertheless, some historical observations have suggested that there is a connection between the phenomena. One of the first observations on this type of connection was made by Darwin in Chile after the 1935 megathrust Concepción earthquake, where he reported four chilean volcanoes entering in a an eruptive phase at the same time(Darwin, 1840). In this last two decades, advances in observation techniques and more in-depth historical studies have shown that there is

a connection between earthquakes and volcanic/hydrothermal activity, both in the short and in the long term, and in a wide spatial window. From the statistical point of view, Eggert and Walter(Eggert and Walter, 2009) found that volcanic eruptions following a $M_s \geq 7.0$ event are most likely to happen in a time window of just few days after the main shock, and at distances lower than 250 km. This point out to an almost immediate effect of the earthquake, possibly working at fluid level. Manga and Brodsky (Manga and Brodsky, 2006) estimated that about 0.4% of the total number of explosive eruptions occur within in a small time window of few days after a large earthquake. According to (Watt et al., 2009), this number is one order of magnitude larger than the one that could be expected with no causal relation between earthquakes and volcanic eruptions.

Historical records and field observations suggest that the influence of an earthquake in a volcanic/hydrothermal system is not bounded to a small range of distances and time delays, but that is very complex. Immediate responses to earthquakes are often found in hydrothermal fields in the form of increases in seismicity, at distances that can go from the earthquake near field to several thousands of kilometers from it. Not all the immediate responses end in an eruption. Examples of distant and short-term connections include the increase in seismicity recorded at Uturuncu volcano, in Chile-Bolivia, to the $M_W = 8.8$ 2010 Maule earthquake, located more than 2000 km away from the volcanic center(Jay et al., 2011). Another response of this type is the sudden increase of local seismicity at the Long Valley Caldera after the $M_W = 7.3$ 1992 Landers earthquake(Johnston et al., 1995), and another increase in local seismicity at Yellowstone caldera to the $M_W = 7.9$ 2002 Denali earthquake, located several thousands of kilometers away from the volcanic system. A well known response from a volcano to an earthquake in the short term was recorded in south Chile, where 38 hours after the $M_W = 9.5$ 1960 Chile earthquake, the Cordón Caulle volcano entered in a very explosive eruptive phase. The volcanic system was located right on top of the rupture region, so it is believed that the amount of stress transferred from the earthquake into the system was very large(Barrientos, 1994). Interestingly, this was the only volcano of the region that recorded an eruption in the year that followed the earthquake, even when most of the region experienced similar stress changes. This suggests that the earthquake acts like a trigger of volcanic activity, and needs a pre-existing activity level that is high enough for triggering.

The long-term influence of an earthquake into the volcanic/hydrothermal system depends on how the original perturbation affects the regional stress tensor. These changes can last for several decades, but they only affect a small area around the rupture zone of one particular earthquake. The eruption of Calbuco volcano in 1961, one year after the $M_W = 9.5$ 1960 Chile earthquake, is believed to be connected with the long-term influence of the main shock. Redoubt volcano in Alaska also entered in a period of high activity almost one year after the $M_W = 9.2$ 1964 Alaska earthquake. This was followed by eruptions in January and October, 1966(Walter and Amelung, 2007). It has also been suggested that, due to post-seismic stress transfer, earthquakes might still affect volcanoes several decades after their occurrence, with

one example being the 1991 eruption of Hudson volcano, almost 30 years after the 1960 megathrust Chile earthquake(Marzocchi et al., 2002)(Bebbington and Marzocchi, 2011a). This idea is also supported by recent GPS studies that have shown how the regional stress field continues to present anomalies due to the occurrence of a large earthquake several decades after its occurrence. One example of this was observed for the 1960 Chile earthquake, the largest ever recorded. More than 50 years after the earthquake, the regional displacement field at the volcanic chain shows an anomalous direction of motion(Khazaradze et al., 2002).

Permanent changes in the stress field produced by an earthquake are called *static stress changes*. They decay rapidly from the rupture region of the earthquake, as r^{-3}, with r the distance from the earthquake hypocenter to the volcanic/hydrothermal system(Manga and Brodsky, 2006), thus being significant in a region that of only a couple of rupture lengths long. Large values for volumetric static stress changes are in the range of $0.01 - 1$ MPa. This is a small value when compared with estimations of the volumetric stress values of a magma chamber at a certain depth. For instance, Terakawa *et al*(Terakawa et al., 2013) found that magma at Ontake volcano, in Japan, was confined at depths between 5 and 12 km, with overpressures up to 100-150 MPa. Considering the lithostatic pressure at 12 km deep is around 353 MPa, the total pressure inside the magma body is about 503 MPa. Thus, a static stress increase of 1 MPa accounts for only 0.002% of the total pressure at that depth, which is very low. This suggests that an earthquake can trigger eruptions at systems that are already very close to a critical state(Fujita et al., 2014). The role of static stress transfer can be more important when the magma body is located at more superficial places. For example, considering a 5 km deep magma chamber with a 100 MPa overpressure, the sum of the lithostatic pressure plus the overpressure is about 160 MPa. Then, an increase of 1 MPa accounts for 0.006% of the total pressure. While this value is three times larger than the one obtained at a depth of 12 km, it is still very low. Another possible static stress triggering mechanism considers that the earthquake can create openings at the volcanic system that can in turn be occupied by the highly-pressurized fluids. This has often been used to explain responses of volcanoes that are located close to the rupture zones of very large earthquakes(Walter and Amelung, 2007)(Bonali, 2013).

Theoretical estimations of the change in the static stress tensor due to an earthquake are often based on the work of Okada(Okada, 1985), with several variations(Walter and Amelung, 2007)(Walter and Amelung, 2006). The value of these changes does not only depend on the magnitude of the earthquake and the distance from the rupture to the observation point, but also on the focal mechanism of the earthquake. Estimations of static stress transfer are also used to calculate the change in Coulomb stress, which can gives information about how local volcanic structures might move after the earthquake, and also on which places are the most affected by the original seismic event. The goal is to look for the influence of the earthquake as an input that unchain a series of other physical mechanisms, that might led a volcanic zone to an eruptive phase. Nevertheless, the value of this input is so small at large distances

that changes in the static stress are not likely to explain responses of volcanoes located more than 1000 km away from the rupture zone.

Dynamic effects of an earthquake are transient, but cover a wider region(Hill, 2008). Changes on the dynamic stress tensor, induced by the passage of the seismic waves on a particular zone, decay more slowly than static stress changes, as $r^{-1.66}$, with r the distance from the volcanic/hydrothermal system to the earthquake hypocenter(Manga and Brodsky, 2006). Dynamic stress changes are the dominant influence of an earthquake at large distances from the rupture zone. According to Hill(Hill, 2008), dynamic stress triggering models are often characterize in two main types: the ones that consider the effect that the waves have in promoting the creation of new ruptures on critically stressed faults, and the ones that consider the role of the wave motion in the fluids that are trapped in the crust, identifying them as the main promoters of volcanic and hydrothermal activity. The first type of models do account for the immediate reactivation of fault zones, and can help explain the apparition of swarms right after the passage of the seismic waves. The second type of models do admit the possibility of a delay on the response, due to the typical time scales of the fluid dynamics. The role of the waves in the gases trapped in the fluids are considered to play an important role, with advective overpressure(Sahagian and Proussevitch, 1992), earthquake-induced volatile exsolution(Sparks et al., 1977) and rectified diffusion(Brodsky et al., 1998) being three of the proposed models. Fluid characteristics dominate the influence of the seismic waves, with lower viscosity fluids being more likely to be affected by the dynamic changes on the stress tensor during the earthquake. This explains why most of the distant responses to earthquakes are recorded at the hydrothermal system. This can be very important, as new openings can be created during the earthquake, which in turn can allow the water to be mixed with magma, generating an important increase in volcanic activity, that can be measured some days after the main shock.

The effect of an earthquake in a volcanic/hydrothermal system also depends on the earthquake directivity, although this factor has not been widely studied. Observations show how not all the systems that are located at the same distance form an earthquake react in the same way to the seismic event(Convertito et al., 2013). A well known case is the response of several fault systems and hydrothermal fields to the 2002 $M_W = 7.9$ Denali earthquake. The zones that showed an increase on the seismicity were located along a line that followed the direction of the earthquake rupture(Gomberg et al., 2004). Another interesting case is the volcanic response of the chilean volcanic arc to the $M_W = 9.5$ 1960 south Chile earthquake. Out of the 25 active volcanoes that suffered post-seismic volumetric expansion, four erupted in the year following the earthquake. Only two of those four volcanoes were located in regions where small volumetric changes were recorded, in contrast with the lack of a response from the 15 active centers that suffered important volumetric extensions(Walter and Amelung, 2007). While this might be related to the critical state of the volcanic/hydrothermal system, the role of the directivity can be also important.

Local structures, such as fault systems, have an important influence on the dynamics of the volcanic region. They are important players in controlling the volcanism at a particular center(Cembrano and Lara, 2009), and the dynamics of new eruptions(Wicks et al., 2011). They also play a key role in destabilization of overlying volcanic systems(Merle et al., 2001)(Lagmay et al., 2000). Nevertheless, their role in both the static and dynamic influence of an earthquake in a volcanic/hydrothermal system has not been extensively studied.

Due to the lack of direct measurements on the key physical quantities that control the volcanic and hydrothermal processes, it is critical to advance in the development of better indirect observations. Satellite-based techniques, such as InSAR, have been very useful to determine the stress state of a particular volcanic zone(Ruch and Walter, 2010). Very interesting observations of the influence of earthquakes in volcanic zones are the subsidence of the volcanic edifices recorded in the volcanic arcs of Chile and Japan, after the 2010 Maule earthquake(Pritchard et al., 2013) and the 2011 Tohoku megathrust(Takada and Fukushima, 2013). These observations are also correlated with seismic observations of periods of high activity(Brenguier et al., 2014), and provide us with more information on the underlying physical processes that control the interaction between an earthquake and a volcanic/hydrothermal zone.

Apart from advances in observation techniques, new developments on theoretical tools of analysis are critical. Numerical simulations on the movement of high-pressurized fluids beneath the crust provide us with an important tool to study the underlying physical mechanism that control volcanic and hydrothermal processes. They have been applied to the study of the ascension of magma along volcanic conduits(Longo et al., 2006)(Papale, 1999), dyke intrusion(Annen et al., 2001), magma chamber and eruption dynamics(Proussevitch and Sahagian, 1998)(Neri et al., 2002)(Kereszturi et al., 2014). Numerical simulations have also been used to explain the origin of certain types of volcano earthquakes(Bean et al., 2014). Numerical simulations of fluid injection in poroelastic spaces have also been used to understand how fractures can be generated by fluid dynamics(Heinze et al., 2015)(Miller et al., 2004). And while they are also useful in the description of earthquake dynamics(Chouet and Julian, 1985)(Bizzarri, 2011)(Bizzarri, 2012), they have not been extensively used to understand the influence of earthquakes in volcanic and hydrothermal systems.

In this thesis I present the results of the study of the effect of medium to moderate sized earthquakes in the volcanic and hydrothermal activity. I begin in chapter 2 with a description of the seismicity of the Nevados de Chillán complex, a basaltic-andesitic volcanic and hydrothermal system located in central-south Chile. From December, 2011, to April, 2012, four broadband stations were deployed atop and in the surroundings of the main cone of the system, finding that the majority of the activity has a hydrothermal origin. During the time of the experiment, two major aftershocks of the 2010 $M_W = 8.8$ Maule earthquake were recorded on January 24$^{\text{rd}}$

and March 25th, 2012. Both events, of magnitudes $M_W = 6.1$ and $M_W = 7.1$, respectively, were located around 200 km away from the volcanic complex. The system showed a reaction to the first, smaller event, with a sudden increase on the number of tremor events, followed by an important increase on VT event rate when tremor activity subsided. This period of high activity lasted for many days. The reaction of the system to the second event was completely different, with a slight reduction on VT event rate. These observations point to a complex earthquake-volcano interaction at a hydrothermal level, and a triggering mechanism based on dynamic stress transfer is proposed.

In chapter 3, I present results from several numerical simulations on the influence of earthquakes in volcanic/hydrothermal systems. I analyze the role of several small $M_W = 4.0$ earthquakes located in the vicinity of a fluid reservoir connected to a main fault, and also the effect of many $M_W = 6.1$ earthquakes located 100 km away from the hydrothermal system, this time composed by two fluid reservoirs, each one connected to a fault. The intention behind the first experiment is to understand the role of local volcano tectonic seismicity on the system dynamics, where both static and dynamic changes are important. The scope of the second experiment is to analyze a system where the relevant influence of an earthquake is purely dynamic. The main goals of this chapter are to understand the role of several earthquake characteristics, such as the dip and strike angles, and the local role of the structures such as the fault system and the fluid reservoirs in the influence of an earthquake in the volcanic/hydrothermal region, with an emphasis on the hydrothermal field, which is more likely to be affected by medium sized earthquakes. To perform this study a new set of poroelastic codes was developed. Earthquakes were synthetically generated, and both the short and long term effects of the earthquake in the hydrothermal region were captured.

In chapter 4 I present the results of a numerical simulation of the situation described in chapter 2. The role of the focal mechanisms of the earthquakes and their relative position respect to the main system fault of the Nevados de Chillán complex play an important part in the analysis. The influence of the local structures is also very relevant, as they can modulate the effect that distant earthquakes have on the system. At the end of the chapter I present a new explanation of the data presented in chapter 2.

Chapter 2

Seismic activity of the Nevados de Chillán volcanic complex after the 2010 $M_W = 8.8$ Maule, Chile, earthquake

Abstract

Couplings between large magnitude subduction zone earthquakes and the subsequent response of their respective volcanic arcs are generally accepted, but the mechanisms driving this coupling are not known. The 2010 Maule earthquake ($M_W = 8.8$) ruptured approximately 500 km along strike in the South-Central part of Chile, and provides an opportunity to investigate earthquake-volcano interactions. In an exploratory campaign, we deployed four broadband seismometers atop and surrounding the Nevados de Chillán volcanic complex because it is located directly behind one of the two primary slip patches of the Maule Earthquake. The data recorded (from December 2011 to April 2012) shows significant seismic activity, characterized by numerous volcano tectonic events and tremor episodes occurring within the volcanic complex. We recorded two strong aftershocks of the Maule earthquake ($M_W = 6.1$ in January 2012, and $M_W = 7.1$ in April 2012) and investigated the response of the volcano to the incoming seismic energy. We find that volcanic tremor increased significantly upon arrival of the seismic waves from the $M_W = 6.1$ event, which was then followed a few hours later by a significant increase in volcano-tectonic events when tremors subsided. This delay between tremor and volcano-tectonic events suggests that fluid and/or magma migration (manifested as tremor) readjusted the local stress state that then induced the volcano-tectonic events. The increased activity

This chapter is published as: C. Farías, M. Lupi, F. Fuchs, SA. Miller. Seismic activity of the Nevados de Chillán volcanic complex after the 2010 Mw8.8 Maule, Chile, earthquake, *Journal of Volcanology and Geothermal Research*, 2014, 283:116-126.

persisted during the subsequent two weeks. In contrast, the $M_W = 7.1$ event, which occurred at a similar epicentral distance from the volcano, did not produce any significant seismic response of the volcanic complex. Analysis of the particle velocity records of the two events show that the volcanic system was perturbed in different ways because of the incidence angle of the incoming energy, inducing a back-elliptical vertical and fault parallel motion for the $M_W = 6.1$ and no clear directional dependence for the $M_W = 7.1$. This suggests dilatation-induced fluid migration within the complex, and a kinematic mechanism of the perturbation rather than the perturbation amplitude. Our results demonstrate the importance for continued monitoring of the arc behind Maule, with an increased seismometer and GPS array density to determine the style of deformation currently occurring in the arc.

2.1 Introduction

The influence of large magnitude earthquakes on volcanic activity has been a long-standing topic in Earth sciences. Recent improvements of monitoring networks combined with accurate analyses of historical records may allow a better understanding of the mechanisms underlying earthquake-volcano interactions. Static and dynamic stress triggering have been proposed to explain why volcanic systems may react to remote earthquakes. However, the debate on the physical processes controlling such interaction is still on-going and large data sets are necessary to distinguish between existing ideas (Marzocchi et al., 2002)(Eggert and Walter, 2009)(Bebbington and Marzocchi, 2011a).

Static and dynamic stress triggering operate at different time-scales and distances. Dynamic triggering is induced by immediate effects caused by the passage of seismic waves through a geological system at or near a critical state (Hill et al., 2002)(Ichihara and Brodsky, 2006). Numerical studies suggest that the convex structure of folded and faulted geological layers in volcanic and hydrothermal systems can focus seismic energy enhancing local stress variations (Davis et al., 2000)(Lupi et al., 2013). This affects the physical equilibrium of the system and promoting fluid pressure variations by suggested mechanisms of rectified diffusion (Brodsky et al., 1998), volatile exsolution (Sparks et al., 1977)(Manga and Brodsky, 2006), and other manifestations of rising fluids (Hill et al., 2002). Dynamic stress triggering operates over short time-scales (i.e. the immediate response to passing seismic waves), however, volcanic responses can occur up to several days after the earthquake because of the time required by the perturbed system to evolve. (Brodsky and Prejean, 2005) and (Hill, 2008) show that dynamic stresses can travel great distances as stress decays according to $1/\mathrm{R}^{1.66}$, with R being the distance from the hypocentre. Heat flux variations (Harris and McNutt, 2007)(Delle Donne et al., 2010), seismic swarms (Hill et al., 1995) and transient deformation (Johnston et al., 1995) are among the most common effects induced by transient seismic waves in volcanic centres. Examples of volcanic activity triggered by dynamic stress fronts are the eruption of Cordón Caulle volcano, Chile, 38 hours after the $M_W = 9.5$ Valdivia (1960) earthquake (Lara et al., 2004), swarming in the Long Valley caldera, USA, few minutes after

the $M_W = 7.3$ Landers (1992) earthquake (Hill et al., 1993), the increase of seismicity of the Uturuncu volcano, Bolivia, immediately after the arrival of the surface waves induced by the $M_W = 8.8$ Maule earthquake (Jay et al., 2011), and the sudden increase in Volcano-Tectonic (VT) seismic activity at Llaima volcano, Chile, after the Maule earthquake (Mora-Stock et al., 2012).

Static stress triggering mechanisms are proposed to explain marked increases of volcanic activity over longer time-scales (from months to decades). Static stress variations promoted by large magnitude earthquakes decay according to $1/\mathrm{R}^3$ and are proposed to be caused by the post-seismic viscoelastic relaxation of the upper lithosphere (Walter and Amelung, 2007), or intermediate timescale changes in local kinematics (Lupi and Miller, 2014). Additionally, upwelling of deep fluids following mega-thrust earthquakes may be favored due to reduced normal stresses exerted on the volcanic plumbing system and that may modify the physical state of magmatic reservoirs. A new mechanism (Lupi and Miller, 2014) to explain the post-seismic increase of eruptive rates proposes that reductions of the horizontal principle stress ($\sigma_1 = \sigma_H$) induced by mega-thrust earthquake transforms the stress regime from a compressional environment to a strike slip faulting regime in the arc, which in turn favors the mobilization of magmas. This is in agreement with recent findings that show the coexistence of compressional and transpressional tectonic regimes over long time-scales in the Suban basin, Sumatra (Hennings et al., 2012), and with seismic activity occurring in volcanic arcs residing atop subduction zones recently affected by mega-thrust earthquakes (i.e. Sumatra, Chile, and Japan). The $M_W = 9.5$ Valdivia (1960) earthquake and its fore- and after-shocks (four foreshocks greater than $M_W = 7.0$, including a $M_W = 7.9$) induced large static stress variations in the volcanic arc. The geomechanical perturbation of this megathrust event may have induced the eruptions of Cordon Caulle (1960), Copahue (1960), Nevados de Chillán (1965), and possibly Quizapu (1967) and Planchón-Peteroa (1967) volcanoes. Static stress variations may last for decades as shown by cGPS measurements that indicate that the back-arc facing the 1960 Valdivia rupture zone is currently dominated by westwards displacements (Khazaradze et al., 2002)(Brooks et al., 2011).

Central Chile is an ideal natural laboratory for investigating subduction zone earthquakes and the subsequent response of volcanic arc because of the 2010 $M_W = 8.8$ Maule earthquake and its rich aftershock sequence (including events as large as $M_W = 7.1$). The area is extremely remote and rugged, and thus complicates the logistics of instrumentation, but this also offers a low-noise environment for seismic studies. It was observed in September 2010 that a Ml 5.2 earthquake at Planchón-Peteroa volcano was followed few hours later by a volcanic eruption, and our goal was to search for similar behavior around the Nevados de Chillán volcano. We chose the Nevados de Chillán complex because it resides directly behind the high slip patch of the Maule earthquake, and has a geometrically intriguing feature of striking NW-SE that may be in part controlled by post-megathrust kinematics. In an exploratory campaign, we deployed four broadband stations from December 2011 to April 2012 around the Nevados de Chillán volcano, and recorded numerous volcano tectonic (VT) events, volcanic tremor, and background activity. We also recorded the response of the complex to two distant Maule aftershocks ($M_W = 6.1$ at 192

km distance and $M_W = 7.1$ at 200 km distance), and found different reactions of the volcano complex. The observed behavior provides insights into the mechanisms driving the triggered response of the volcano plumbing system.

2.2 Geodynamic and geological setting of Central Chile

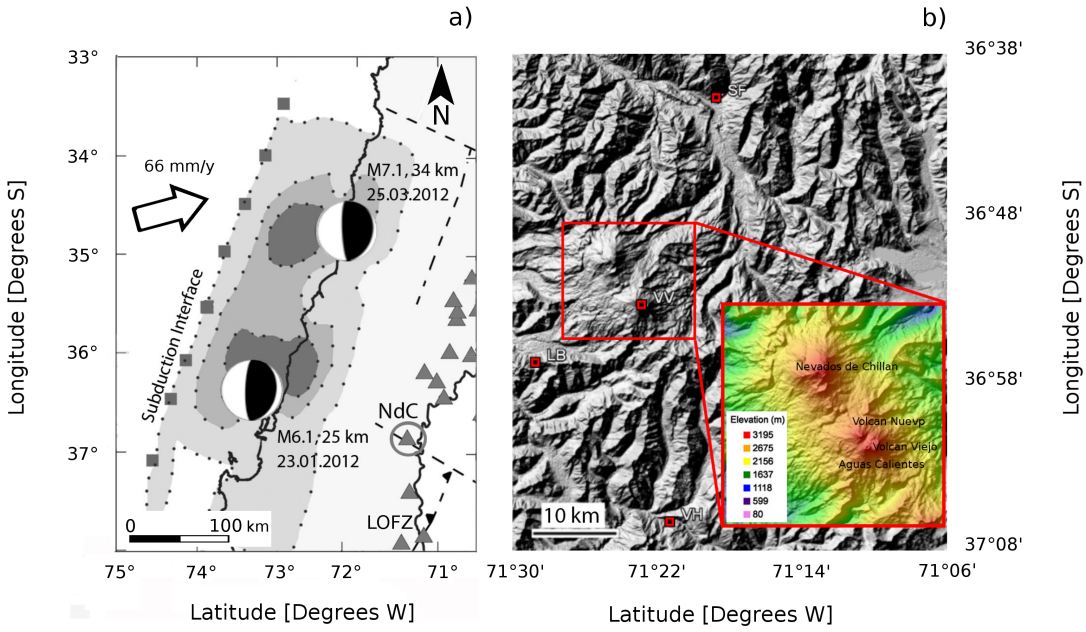

Figure 2.1: a) Geodynamic setting of Chile between 33° and 38° and array distribution. The slip of the Maule earthquake is taken from USGS and dark grey indicates the maximum slip of 14 m occurred at 35 km deep (Moreno et al., 2010). The southern and northern beach-balls mark the locations and focal mechanisms of the January 23^{rd}, 2012, M6.1 and March 25^{th}, 2012, M7.1 aftershocks, respectively. The northern portion of the Liquiñe-Ofqui Fault Zone (LOFZ) is also marked in the map. b) Topographic image of Nevados de Chillán volcanic complex. The red dotted square indicate the location of the temporary stations and the inset shows the three main cones of the system.

The tectonic setting of Chile from 33°S to 47°S is characterized by the oblique subduction of the Nazca plate underneath the South American plate (Fig. 2.1a). Plate convergence of approximately 66 mm yr^{-1}, is accommodated by large-magnitude earthquakes along the length of the collision zone, and arc volcanism is ubiquitous. The most prominent geological feature of this part of Chile is the NNE-SSW striking Liquiñe-Ofqui Fault, a right-lateral transpressional fault zone running from 38°S to 47°S. Monogenetic cones and basaltic to andesitic volcanoes (i.e Villarrica, Llaima, Osorno) reside upon the Liquiñe-Ofqui Fault, while more evolved volcanic systems (i.e Nevados de Chillán, Copahue) reside along NW-SE striking lineaments, antithetic to the direction of the arc (Cembrano, 1992)(Cembrano et al., 1996)(Lavenu

and Cembrano, 1999)(Cembrano et al., 2000)(Lange et al., 2008)(Cembrano and Lara, 2009). Morphological evidence shows that the Liquiñe-Ofqui Fault terminates approximately near the Copahue volcano (38°S) (Cembrano and Lara, 2009), but strike-slip moment tensor solutions of shallow seismic activity following the Maule earthquake document that strain partitioning extends in the arc also between 33°S and 38°S (Lupi and Miller, 2014). (Nakamura, 1977) suggests that the large scale distribution of volcanoes and their elongation can provide insights into the stress orientation at the regional scale. (Lupi and Miller, 2014) propose a 'bookshelf' mechanism to explain the occurrence of NW-SE trending lineaments across the Chilean and Argentinean border.
Nevados de Chillán experienced significant static stress changes induced by the Maule earthquake (Lupi and Miller, 2014), which was one reason for choosing this site for investigation. Additionally, (Dzierma and Wehrmann, 2010) studied the (pre-Maule) probability of a VEI≥2 eruption within the next ten years for ten Chilean volcanoes located between 33°S and 42°S. Their analyses showed that Llaima, Villarrica, and Nevados de Chillán volcanoes are the most likely candidates to erupt, followed by Puyehue and Calbuco volcanoes. From hereafter the we will refer to the Nevados de Chillán volcanic complex as NdC.

The NdC volcanic complex (Fig. 2.1b) consists of 24 cones distributed along a 12 km long lineament striking approximately N290 (Fig. 2.1b) (Gonzalez-Ferrán, 1995). Volcán Nuevo, Volcán Viejo and Volcán Nevados are the three main volcanic centres. Volcán Nuevo resulted from the 1906 eruption that occurred immediately after the 1906 Valparaíso earthquake. Table 2.1 provides detailed information about the location of mega-thrust epicenters and the occurrence of volcanic activity at NdC. Due to the recent explosive activity of the Volcán Nuevo and to the rapid development of tourism in the area, the NdC is considered a high-risk volcano.
Figure 2.2 shows the cumulative number of eruptions of the NdC during the past century and the occurrence of mega-thrust earthquakes nearby the NdC. Since the recorded VEI of many eruptions is similar, as showed in Table 2.1 the comparison of both time series can show interesting insights. It emerges that from 1900 to 1940 the volcano appeared more sensitive to external perturbations than in present time, and only in three cases (1906, 1914, and 1928) the volcano entered in an eruptive phase almost immediately after the occurrence of a mega-thrust earthquake.

2.3 Seismic network and methods

We deployed four Trillium 240 broadband seismometers equipped with Reftek130 data loggers around and atop the NdC complex from December 2011 to April 2012. Data were continuously recorded at a sampling rate of 100 Hz. We used a STA/LTA triggering algorithm (Withers et al., 1998) to mark the events, which we inspected manually to determine P- and S-wave arrivals. We used SEISAN (Ottemöller et al., 2011) and the 1D velocity model reported in Table 2.2. Our temporary network consisted of one station (VV) atop the NdC volcano surrounded by three stations

Date	Magnitude	Epicentre	Eruptive characteristics	Eruption VEI	Distance [km]
16.08.1906	8.2	Valparaíso	FV, E, LF, MF	2	420
–.–.1907	–	–	FV, E	1	–
29.01.1914	8.2	Constitución	E	2	250
–.–.1923	–	–	FV	2?	–
10.04.1927	–	–	E	2?	–
30.11.1928	8.2	Talca	FV, E	2?	210
17.01.1934	–	–	E	2?	–
02.07.1935	–	–	FV, LF, MF	2?	–
24.01.1939	8.2	Chillán	–	–	100
–.–.1945	–	–	–	–	–
–.–.1946	–	–	FV, E	2?	–
22.05.1960	9.5	Valdivia	–	–	350
–.–.1965	–	–	FV	–	–
–.–.1972	–	–	FV	–	–
–.07.1973	–	–	FV, E, PF, LF, D	2	–
03.03.1985	8.0	San Antonio	–	–	400
29.08.2003	–	–	C, RF, E, PH	1	–
21.01.2009	–	–	–	–	–
27.02.2010	8.8	Maule region	–	–	140

Table 2.1: Historic eruptions of NdC volcano and historic mega-thrust earthquakes that occurred within 500 km from the complex, since 1900 AD. Distance stands for the distance between the epicentre location and the NdC. the eruptive events always occurred at the Volcán Nuevo, except once (2^{nd} of July 1935, Volcán Viejo). For several historical records both the exact date and the VEI of the eruption is not specified. Mega-thrust events are shaded in grey and under "eruptive characteristics" we list historic information about the eruptions: C stands for central emission, FV for Flank Vent emission, RF for Radial Fissure emission, E for explosive eruption, PF for Pyroclastic Flows, PH for Phreatic eruption, LF for Lava Flow, D for Dome creation, and MF for Mud Flow. Historic eruptions and mega-thrust events are taken from (Siebert et al., 2012) and (SSN, 2013), respectively.

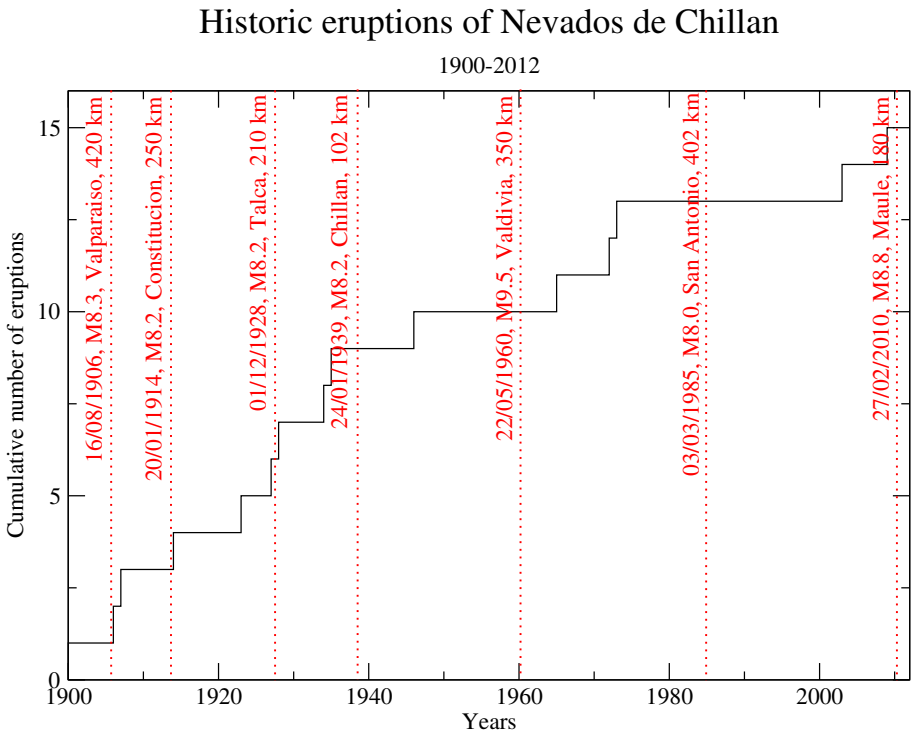

Figure 2.2: Cumulative number of eruptions of Nevados de Chillán volcanic complex and mega-thrust events since 1900. Dotted vertical lines indicate mega-thrust earthquakes whose hypocentre was located less than 500 km from the volcano. Details on date, magnitude, and epicentre-volcano distance are shown in the vertical sentences. More information about eruptive behaviors can be found in Table 2.1. Note that the historic earthquake records may be affected by non systematic reporting.

(LB, VH, and SF) (Fig. 2.1) approximately 20 km from VV station (Table 2.3). Sporadic technical problems resulted in some discontinuity in our dataset. The time window presented here (from December 26th, 2011, to February 5th, 2012) is continuous. Our array is the first ever used to study the NdC complex, but accessibility in this remote region resulted in a non-optimal geometry. Nevertheless, epicenter locations are well constrained North-South, but accuracy is limited in the East-West direction.

2.4 Results

We registered many different events during our experiment, with the vast majority recorded by station VV only and identified as Volcano-Tectonic (VT) earthquakes (Wassermann, 2012)(McNutt, 2005), (Fig. 2.3), and tremor events (Fig. 2.4). In the first case, waveforms were 10 to 40 s long, with frequency content higher than 5 Hz. Among this type of event we defined three sub-categories: i) Events characterized by clear P- and S-wave onsets, with a dominant band around 8 Hz. Our network allowed us to manually locate approximately 50 earthquakes, with magnitudes ranging from Ml 0.1 to Ml 1.8 and depths from 0.1 km to 30 km; ii) events lacking of a clear S-wave

Depth [km]	v_p [km/s]	v_p/v_s
0	5.51	1.75
5	6.28	1.75
20	6.89	1.75
35	7.40	1.75
45	7.76	1.75
55	7.94	1.75
90	8.34	1.75

Table 2.2: 1-D velocity model used for NdC, with v_p and v_s being P-wave and S-wave velocities, respectively. This model is based the work of (Bohm et al., 2002) and it is currently in use by the Volcanologic Observatory of the Southern Andes (OVDAS, in Spanish) in Chile.

Location	Station	Latitude	Longitude	Elevation [m]
Las Bravas	LB	36.926 S	71.501 W	1799
Valle Hermoso	VH	37.078 S	71.340 W	1217
San Fabián	SF	36.670 S	71.287 W	824
Volcán Viejo	VV	36.872 S	71.370 W	3118

Table 2.3: Location of the four seismic stations deployed around Nevados de Chillán volcanic complex.

onset, with a lower frequency band, typically around 6 Hz, which are shallow VT events according to the literature (Wassermann, 2012); iii) swarm events dominated by frequencies from 13 to 15 Hz (Fig. 2.3), which occurred between 16:00 UTC and 19:00 UTC of January 5$^{\text{th}}$, 2012.

Tremor events last approximately 60 s and can also be separated into two sub-categories according to the shapes of the waveform and their occurrence patterns. The most common tremor was characterized by an excitement of the 8 Hz band, and was recorded by station VV only. Similar events were recognized by (Leet, 1991) who described them as composite hydrothermal-magmatic tremor. Another possible source for this type of event is the superposition of several very shallow VT events. The second type of tremor occurred only between January 6$^{\text{th}}$ and January 8$^{\text{th}}$, twenty hours after the high frequency VT swarm (spike of Fig. 2.6). These signals were recorded by VV, LB, SF, and VH stations and were marked by clusters of high-amplitude signal dominated by 2 and 8 Hz frequencies (Fig. 2.4b).

2.4.1 Seismic activity

Figure 2.5 shows the distribution of seismic events around the NdC. The NW-SE cross-section across the volcanic edifice shows that seismic activity clusters beneath the South-Eastern flank of the cone Volcán Viejo, and more specifically below the Aguas Calientes valley, which is an area characterized by fumarolic activity and hot springs. We could not locate several VT events because they did not appear in all

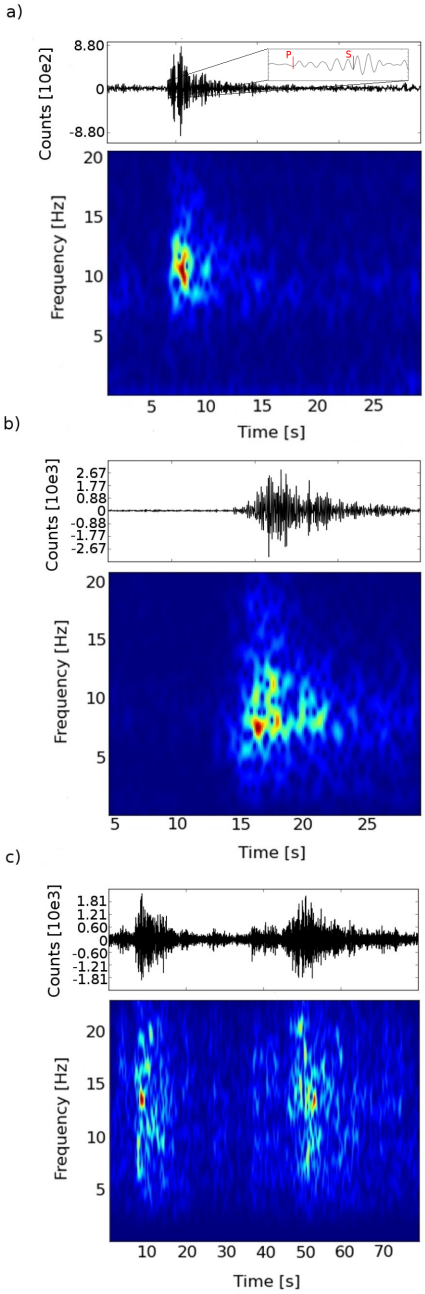

Figure 2.3: Volcano tectonic events at the Nevados de Chillán. a) deep VT, with an inlet with P- and S- wave arrivals marked in red, b) shallow VT, and c) high frequency swarm events found in the dataset for Nevados de Chillán from December 26th, 2011, to February 5th, 2012.

the stations of our array, and most of them were only registered by VV station. However, due to the lack of a clear S-wave onset in most of them, and the short time between the arrival of P and S-waves (generally separated by less than a second), it is likely that these events were originated at shallow depths, in the surrounding of Volcán Viejo cone (see shaded areas of Fig. 2.5). Deeper events are more dispersed

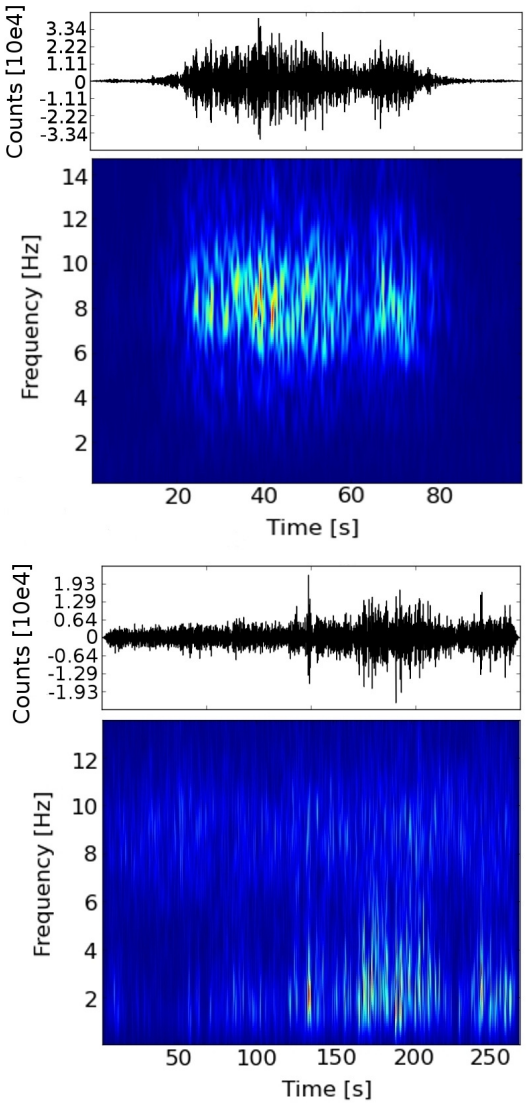

Figure 2.4: Trace and spectrogram of tremor events. a) High frequency tremor event found throughout the normal activity of the volcano. b) Spasmodic volcanic tremor found in NdC complex after the swarm occurring on the 5^{th} of January 2012.

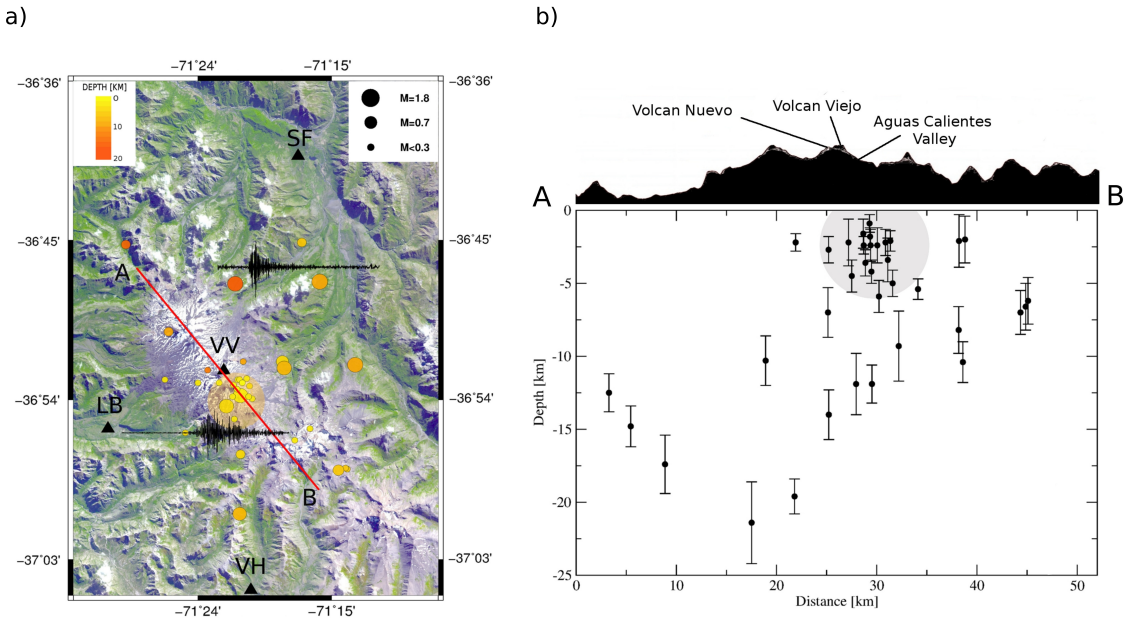

Figure 2.5: a) Epicenter map of the seismic events within the Nevados de Chillán volcanic complex. Stations are marked as black triangles. Typical signals for shallow and deep VT events are drawn next to the location of the respective type of event. Note the difference of the waveform for both deep and shallow events. The orange circle marks the region where the non-locatable shallow events may be located. b) Locations of the events, from the perspective of the transverse cut marked by the red line in a), with A and B being the same points marked there. The error bars indicate the uncertainty of the locations in the vertical direction. Due to the geometry of the array, some extra uncertainty should be added in the left-right component of the locations in the cross section. The grey area is the projection along the line and the vertical direction of the yellow circle in a). Notice how most of the shallower events are located beneath the Aguas Calientes valley.

and range from 10 to 25 km deep and fall outside the volcanic complex. Magnitudes of the shallow events range between Ml 0.1 to Ml 0.8 while the deeper events have somewhat larger magnitudes (the largest being a Ml 1.8 earthquake).
Figure 2.6 shows the number of VT events per hour recorded at station VV from December 26$^{\text{th}}$, 2011, through February 5$^{\text{th}}$, 2012. The peak on the left-hand side of the chart highlights a seismic swarm that occurred on January 5$^{\text{th}}$, 2012 at 17:00 UTC, and lasted for 2.5 hours. During this interval VT events are marked by a higher frequency content (see Fig. 2.3c), with a dominant band around 13-15 Hz, and with a remarkably shorter coda compared to other VT earthquakes recorded during our seismic campaign. Twenty hours after this swarm, the VT event rate decreased down to approximately one event per hour and continuous tremor marked by clusters of high-amplitudes emerged.

2.4.2 Response to large regional earthquakes

On January 23$^{\text{rd}}$, 2012, a $M_W = 6.1$ aftershock occurred at the subduction interface (25 km deep, USGS), approximately 192 km from the NdC volcanic complex (Fig.

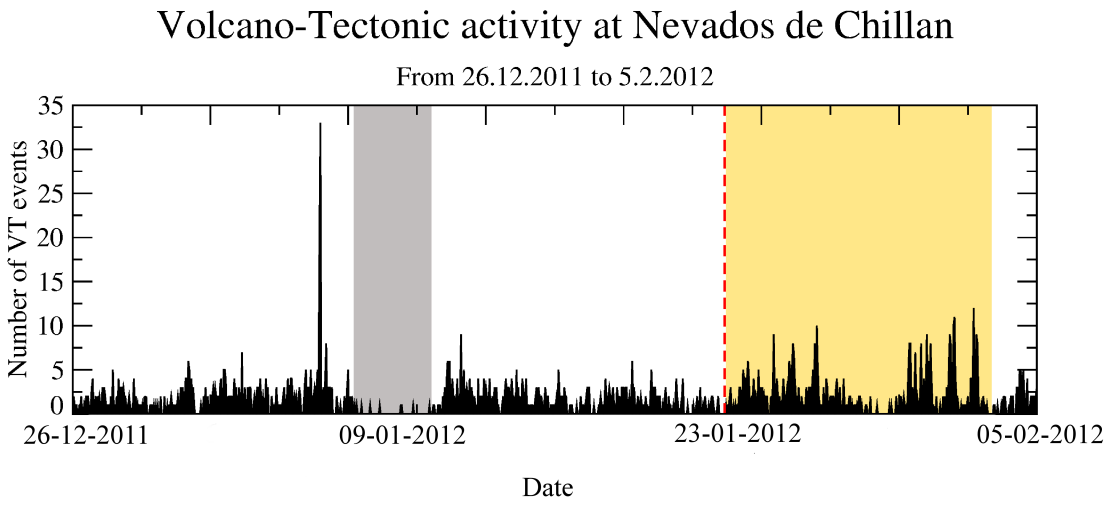

Figure 2.6: Seismicity at Nevados de Chillán from December 26th, 2011, to February 5th, 2012. Grey and orange bands show periods of strong background tremor and triggered seismicity after a M6.1 regional earthquake, respectively.

2.1). The volcanic activity at NdC before the event was low, with less than one event per hour. The $M_W = 6.1$ earthquake occurred at 16:04 UTC, afterwards (17:04 UTC) tremor activity increased noticeably and lasted for approximately nine hours. When tremor stopped at 02:00 UTC, the VT event rate increased to an average of 3.5 events/hour. Figure 2.7 shows the total number of tremor and VT events before and after the occurrence of the $M_W = 6.1$ earthquake, highlighting the onset of double-couple events after tremor subsided. A second large aftershock of the Maule mega-thrust earthquake occurred on March 25$^{\text{th}}$, 2012, 200 km away (34 km deep, USGS) from the NdC complex (Fig. 2.1). At the time, station VV was suffering 12 hours of daily data loss due to energy-storage issues. Nevertheless, we captured the signal of the $M_W = 7.1$ earthquake and analyzed the VT rate of the available data. Comparing the $M_W = 7.1$ post-seismic records with the ones that followed the Mw 6.1 we found that before the $M_W = 7.1$ earthquake the seismic activity was particularly intense with an average of three events per hour (Figure 2.8). However, the available data show that the VT rate decreased to one event per hour after the earthquake. Although our analysis is biased by the lack of data, the reduction of the number of events per hour following the $M_W = 7.1$ aftershock is clearly shown. This type of response is similar to that recorded for Mt. Wrangell and Mt. Veniaminof volcanoes after the 2002, $M_W = 7.9$ Denali earthquake (Sánchez and SR., 2004).

2.5 Discussion

We investigated the seismic activity of the NdC complex after the Maule earthquake and found that seismic activity mainly occurs from 2 to 5 km deep beneath the region called Aguas Calientes, a valley known for its natural hotsprings and fumaroles.

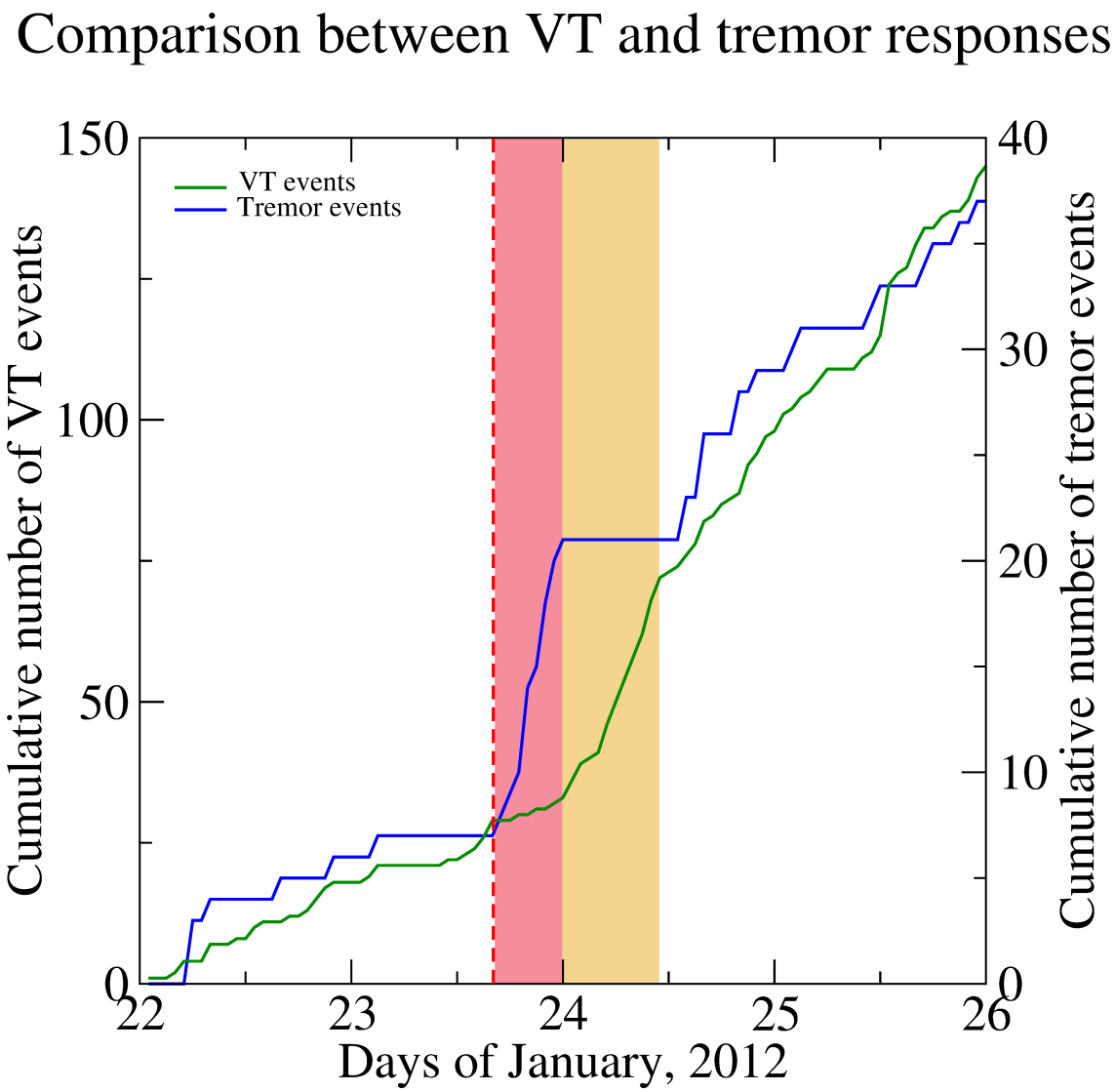

Figure 2.7: Number of VT events per hour on Nevados de Chillán volcano before and after the M6.1 aftershock. The vertical dashed line marks the occurrence of the M6.1 and the red-shaded region highlights a strong increase of tremor events after the M6.1 earthquake. Next, tremor subsides and the number of VT events strongly increase (yellow-shaded area).

Deeper events also occur below the volcanic complex down to approximately 20 km deep. We did not locate several low-magnitude seismic events because they did not appear on a sufficient number of stations. However, their waveforms are characteristic of shallow VT events. This points to a local origin that may be within the volcanic system, possibly beneath the Aguas Calientes valley. The location of this shallow seismicity plus the type of tremor events we recorded in our campaign suggest that the activity at the NdC has a strong hydrothermal component, thus making the volcano an active hydrothermal-magmatic system.

We observed different responses of the NdC to two large Maule aftershocks (M_W = 6.1, Fig. 2.7 and M_W = 7.1, (Fig. 2.8) originating at similar hypocentral distances

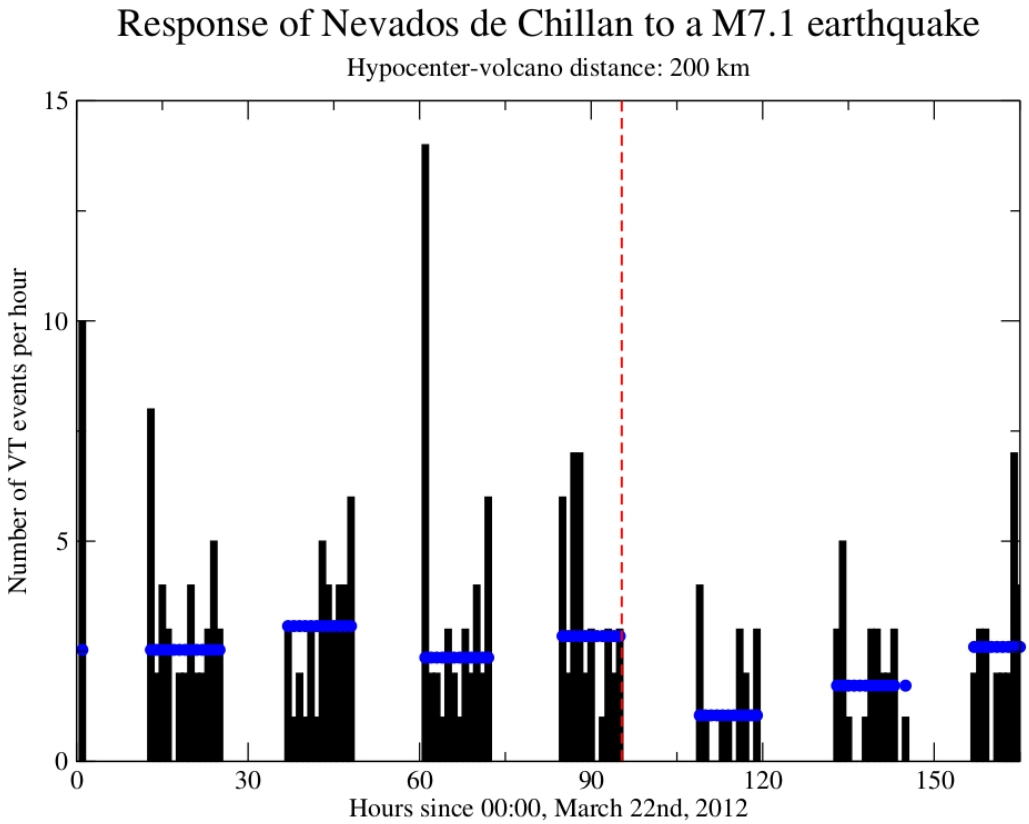

Figure 2.8: Number of VT events per hour occurring at the Nevados de Chillán volcano before and after the M7.1 aftershock. The vertical dashed line marks the occurrence of the M6.1 and blue lines mark the average number of VT events per hour.

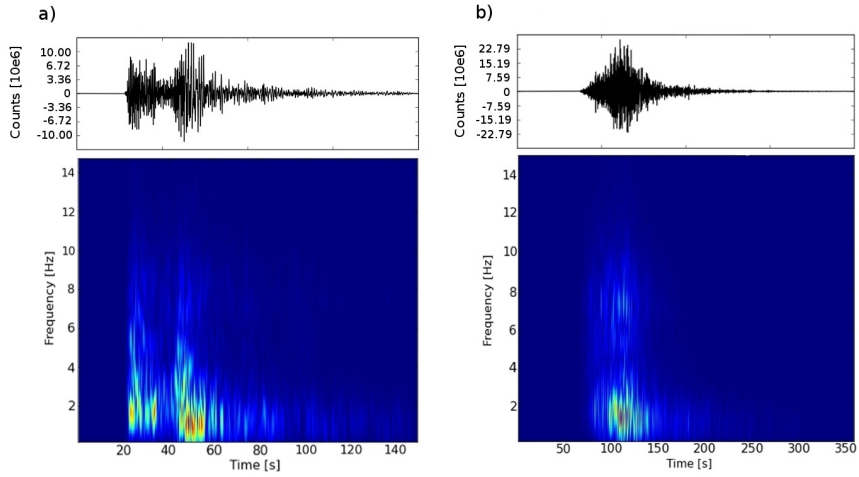

Figure 2.9: Waveform and spectra for the M6.1 and M7.1 earthquakes.

from the NdC. We identified a triggered response of the NdC after the $M_W = 6.1$ event but not after the $M_W = 7.1$ event. Note that although data loss during the $M_W = 7.1$ event introduces a bias, we registered a decrease in VT when compared to the behavior prior to the $M_W = 7.1$ event (blue lines in Fig. 2.8 indicate the average

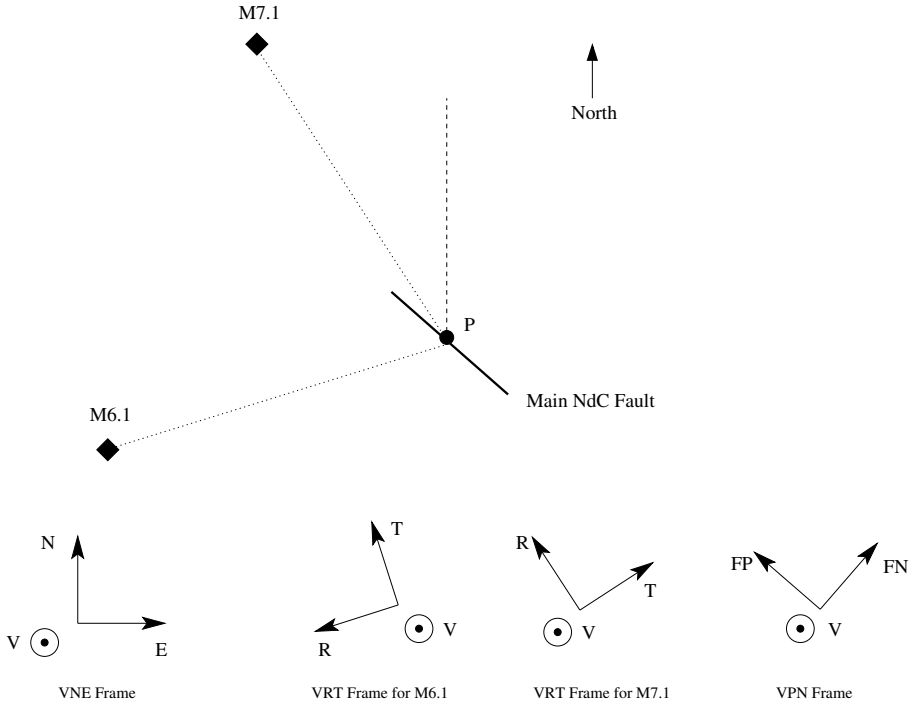

Figure 2.10: Schematic representation of the relative location of the $M_W = 6.1$ and $M_W = 7.1$ events to the main lineament of the Nevados de Chillán volcanic complex, and the different coordinate frames used in our analysis. More detail on each one of the frames is given on the text.

rate). Figure 2.9 shows the waveforms and spectra of the two aftershocks of the Maule earthquake. The maximum amplitudes in a ground motion seismograph of the two events are comparable and are on the order of 1 to 2 mm for the vertical component at station VV. Using particle motion plots, we investigated the effect of the incidence angle of the incoming seismic waves and found that the difference between the effect produced by the two events may lie there. Figure 2.10 shows a scheme of the different coordinate frames used in the observation point given by the location of VV station. Figures 2.11, 2.12, and 2.13 show particle velocity motion plots for both earthquakes in station VV, filtered between 0.01 Hz and 0.1 Hz, in different coordinate systems: Vertical/North/East (VNE), Vertical/Radial/Transversal (VRT) for both events, and Vertical/NdC Fault Normal/NdC Fault parallel (VNP). In the VNE frame the most noticeable feature is how the particle motion induced by the $M_W = 6.1$ event presents a dominant motion along the East and Vertical directions, with amplitudes around 10 mm s^{-1}, while the $M_W = 7.1$ event induced velocities with maximum amplitudes on the order of 20 mm s^{-1}, but without any preferential orientation. The induced particle motion in the VRT frame shows how, for the $M_W = 6.1$ event, the transverse movement is significantly smaller than the radial one, suggesting that the wave train is mostly dominated by Rayleigh waves rather than Love waves. In the case of the $M_W = 7.1$ event, there is no clear dominance of either transverse or radial motion modes. Finally, on the VPP frame it can be appreciated how the $M_W = 6.1$ event induced a motion oblique to the main fault of

the NdC complex, which may help to create a fault-parallel motion, thus enhancing a stress change along the main lineament of the system. On the other hand, the $M_W = 7.1$ does not show a preferred direction of motion.

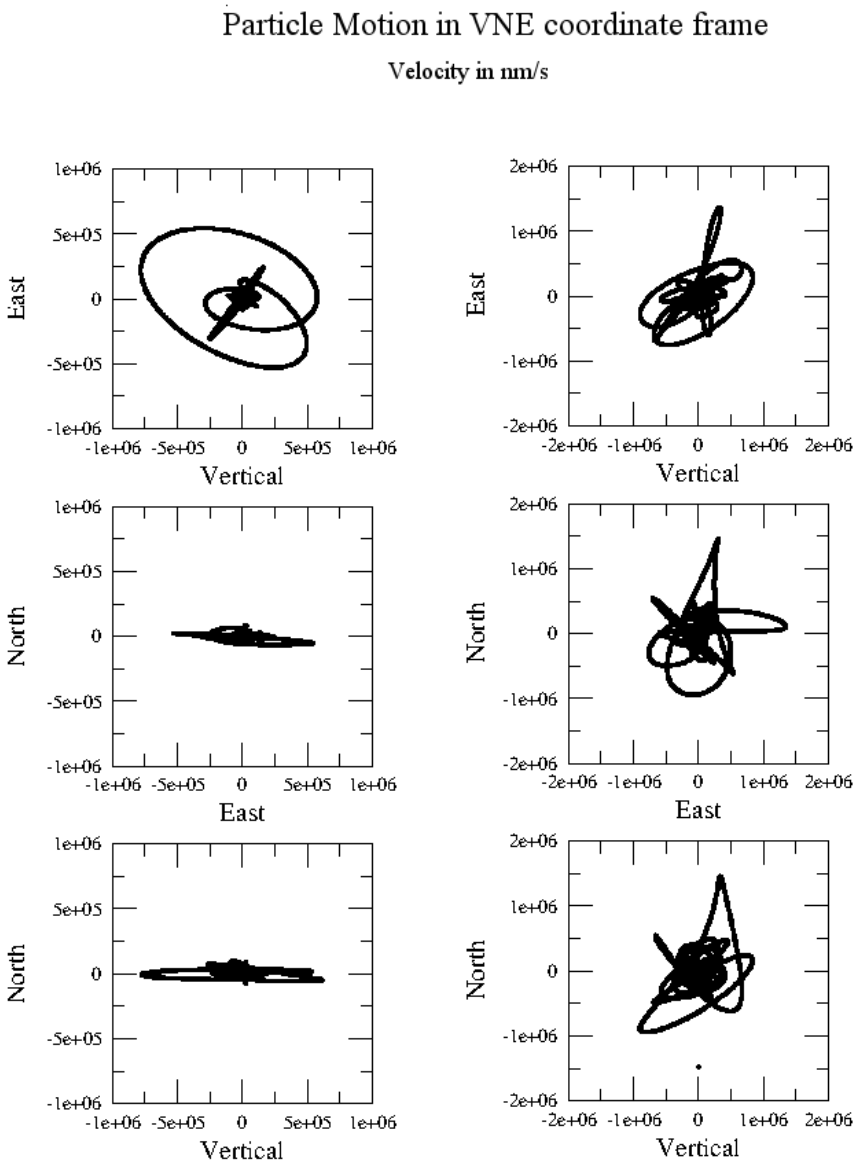

Figure 2.11: Velocity particle motion plots in Volcan Viejo station for the $M_W = 6.1$ and $M_W = 7.1$ event in the VNE frame. The signal was filtered between 0.01 Hz and 0.1 Hz and the velocity is measured in nm/s. The N-V axes identify the North-Vertical plane, E-V the East-Vertical plane and the N-E axes identify the North-East plane. Note the dominant oscillatory behavior induced by the M6.1 earthquake on the N-Z and N-E planes in contrast to the motion induced by the M7.1.

The analysis of particle motion in the three different coordinate frames suggests that the $M_W = 6.1$ event may have induced a elliptical motion in the main fault of the NdC, with dominant fault-parallel and vertical components, thus promoting the

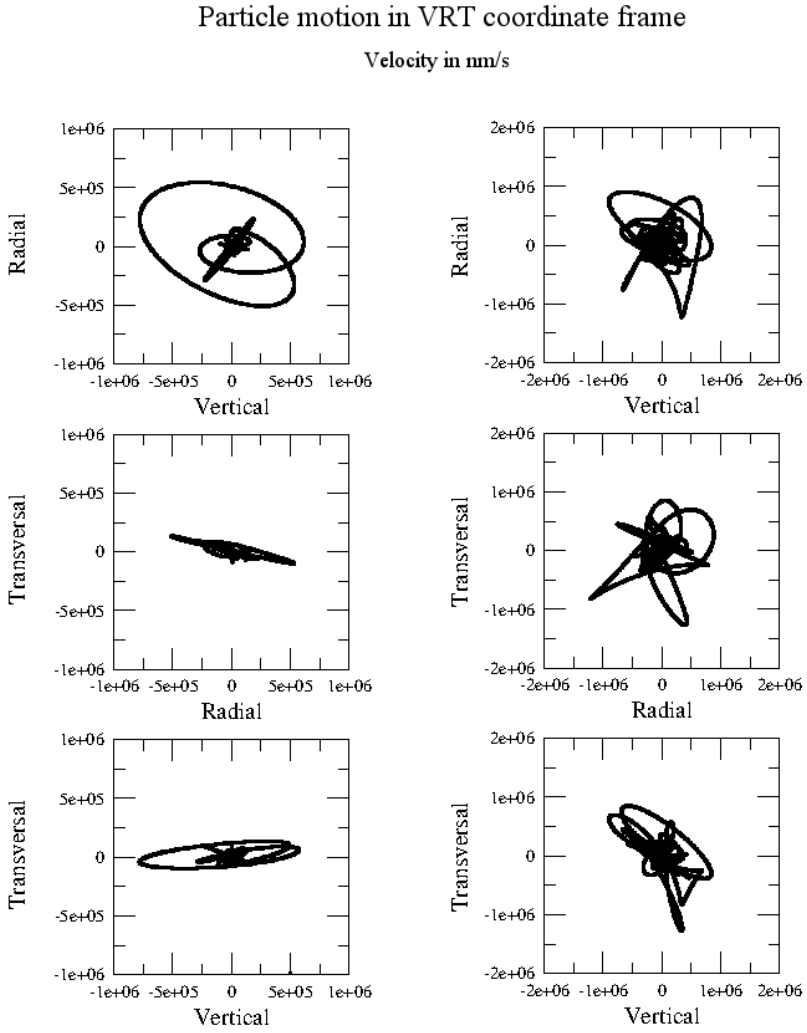

Figure 2.12: Velocity particle motion plots in Volcan Viejo station for the $M_W = 6.1$ and $M_W = 7.1$ event, each one in a frame rotated to its backazimuth (VRT frame). The signal was filtered between 0.01 Hz and 0.1 Hz and the velocity is measured in nm/s. For each earthquake, the R-V axes identify the Radial-vertical plane, T-Z the Transverse-Vertical plane and the T-R axes identify the Transverse-Radial plane.

creation of spaces for the fluids to arise and move along the lineament, as reflected by the important increase on seismicity right after the passage of the wave train. This indicates that the observed behavior of triggered tremor followed by VT events was controlled by a dilatational processes due to the Rayleigh waves. This is consistent with other studies that report triggered tremor due to the passage of the Rayleigh waves in regions like Japan after the 2004 Sumatra-Andean Earthquake (Miyazawa and Mori, 2005)(Miyazawa and Mori, 2006). In a more general workframe, our observations are also consistent with other studies showing permeability increases correlating with passing seismic waves (Kitagawa et al., 2002)(Elkhoury et al., 2006).

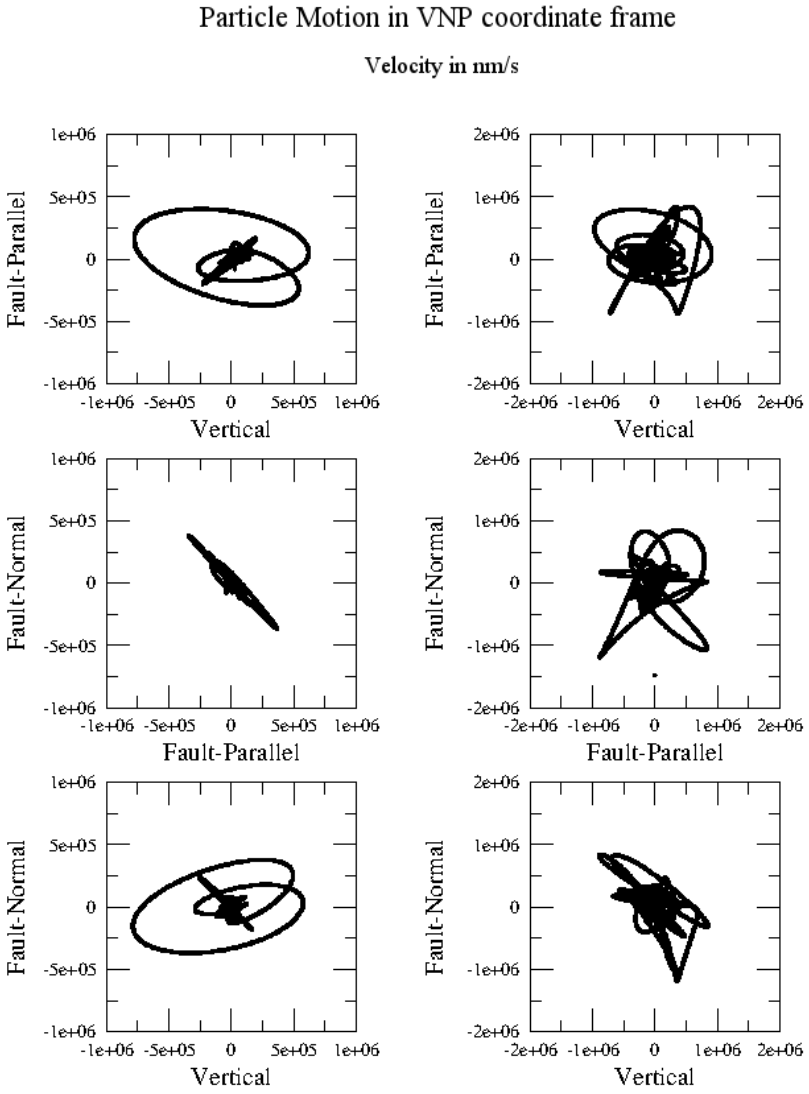

Figure 2.13: Velocity particle motion plots in Volcan Viejo station for the $M_W = 6.1$ and $M_W = 7.1$ event, in the VNP coordinate frame. The signal was filtered between 0.01 Hz and 0.1 Hz and the velocity is measured in nm/s. The FP-Z axes identify the Fault-Parallel/Vertical plane, FN-Z the Fault-Normal/Vertical plane and the FP-FN axes identify the Fault-Parallel/Fault-Normal plane.

2.6 Conclusions

We presented data from a seismic campaign that took place from December 2011 to April 2012 around the Nevados de Chillán (NdC) volcanic complex, in Central-Southern Chile. We recorded numerous Volcano-Tectonic (VT) and tremor events within the volcanic complex. The majority of the events were shallower than 5 km deep and occurred beneath the South-East flank of the volcano. Two major

aftershocks ($M_W = 6.1$ and $M_W = 7.1$) of the 2010 Maule earthquake, at similar distances for the NdC elicited different responses. The response to the $M_W = 6.1$ event was characterized by an increase of tremor activity one hour after the earthquake, followed by a marked increase of VT events when the tremor subsided. This strongly suggests a fluid driven mechanism induced by the passage of the seismic waves. In contrast, the $M_W = 7.1$ event did not trigger a response of NdC. We propose that this difference in behavior is a result of the incidence angle of incoming energy, where the $M_W = 6.1$ showed predominantly EW (arc-oblique) particle motion and the $M_W = 7.1$ showed no particular oscillatory path. An alternative explanation could be that the response to the $M_W = 6.1$ event relaxed the system and therefore was not perturbed sufficiently to induce a response from the $M_W = 7.1$. Future seismic campaigns with a higher density array will allow triggered responses to be constrained with better accuracy.
The volcanic arc behind the Maule earthquake is an excellent natural laboratories for investigating earthquake-volcano interactions, and should be instrumented in the future to better understand earthquake-volcano interactions and the internal dynamics of perturbed arc systems.

Acknowledgments

Cristian Farias thanks the Becas Chile scholarship program for supporting his work. Humanitus Sidoarjo fund is thanked sor supporting Matteo Lupi. Daniel Basualto from Observatorio Volcanológico de los Andes del Sur (OVDAS) is acknowledged for providing us the 1-D velocity model. Cristian Sepulveda and Gustavo Aldea are acknowledged for their help in the field and logistical support.

Chapter 3

Numerical study on the influence of pre-existing local structures and seismic source characteristics in earthquake-volcano interactions.

Abstract

Using numerical simulations, we studied the influence of several earthquakes in the dynamics of trapped, high-pressurized fluids, connected to a geological fault system. We studied both dynamic and static changes induced by a seismic event, finding that, while they are dominated by the earthquake characteristics, the role of the local structures has a major importance on the system dynamics. The fluid reservoir affects the wave motion, distorts the static overpressure pattern induced by the external earthquake, and concentrates the kinetic energy of the incoming wave on its boundaries. The static volumetric pattern inside the fault system gets also altered by the local structures. The role of the faults is particularly important for the system dynamics, as they concentrate kinetic energy inside themselves, and also have breakwater-like characteristics, preventing some regions to receive the full impact of the earthquake. Local structures also have an important impact on the change of the regional Coulomb yield function. With applications to earthquake triggering of hydrothermal and volcanic activity, our results unveil a complex connection between external perturbations and the dynamics of volcanic and hydrothermal system, in which the local structures play an important role.

The results from this chapter will be submitted to *Journal of Geophysical Research* as an article with the title "Numerical study on the influence of pre-existing local structures and seismic source characteristics in earthquake-volcano interactions", by C. Farías, B. Galván, and S. Miller.

3.1 Introduction

The study of the fluid movement beneath the Earth surface is one of the most interesting topics in geosciences, with applications in seismology(Miller et al., 2004), volcanology(d'Acremont E. et al., 2003)(Todesco et al., 2004), oil and gas extraction(Yu et al., 2015), among many others. In volcanic processes, where fluid dynamics dominate the activity in one particular region, an interesting question is how this motion can be affected by different geological settings, and by external dynamic perturbations such as earthquakes. Advances in observation techniques during the last three decades have allowed to establish the notion that earthquakes can affect the activity of a volcanic/hydrothermal system, both in the long and short term. Studying a global catalog, Eggert and Walter(Eggert and Walter, 2009), found that volcanic eruptions following a $M_s \geq 7.0$ earthquake are most likely to occur within few days after the main shock, and at a hypocenter-volcano distance lower than 250 km. Manga and Brodsky (Manga and Brodsky, 2006) estimated that about 0.4% of the total number of explosive eruptions occur within in a small time window of few days after a large earthquake, with this number being at least one order of magnitude larger than if there were no causal relationship between the number of eruptions and the number of earthquakes at a global scale(Watt et al., 2009). At a more local scale, Watt analyzed the historic volcanic eruption rate in Chile after $M_W \geq 8.0$ in Chile, and found an important increment in the number of volcanic eruptions following the $M_W = 8.2$ and $M_W = 9.5$ earthquakes. He also concluded that the distance of influence of an earthquake in volcanic eruption rate was large, ranging from its near-field to more than 500 km away from the rupture zone, suggesting that both static and dynamic stresses transferred by the earthquakes might have played a role in enhancing these eruptions(Watt et al., 2009). It has also been suggested that earthquakes might still affect volcanoes several decades after the main shock, due to post-seismic stress transfer(Marzocchi et al., 2002)(Bebbington and Marzocchi, 2011a). This idea is also supported by recent GPS studies that have shown how the regional south Chile stress field, which involves the local volcanoes, is still affected decades after the 1960 $M_W = 9.5$ megathrust Valdivia earthquake(Khazaradze et al., 2002).

Both historical records and field observations have identified different time and space scales for earthquake-volcano interactions. While the dynamic effects of the passage of the seismic waves are transient, and cover a wider region(Hill, 2008), post-seismic effects, mainly due to the total change on the stress field after the earthquake, can last for several years, but the region affected by them is usually smaller(Manga and Brodsky, 2006). Immediate reactions from hydrothermal and volcanic centers are mostly related to an increase on local seismicity, which may lead to an eruption afterwards, but heat flux variations(Harris and McNutt, 2007)(Delle Donne et al., 2010) and transient deformations(Johnston et al., 1995) have also been observed during an earthquake. Examples of dynamic responses involve the Uturuncu volcano response to the 2010 Maule Earthquake(Jay et al., 2011), located more than 2000 km away from the volcano, and the sudden increase in seismicity at the Long Valley

Volcanic Caldera, after the 1992 $M_W = 7.3$ Landers earthquake(Johnston et al., 1995). Post-seismic responses include the overall increase of volcanic eruptions in Chile in the two years following the 1960 $M_W = 9.5$ earthquake(Watt et al., 2009), and the simultaneous eruption of 4 volcanoes in Chile after the 1835 Concepción Earthquake(Darwin, 1840), among many others examples in different places of the world, such as Cascadia and Japan(Hill et al., 2002).

The estimation of the static stress changes due to an earthquake on a volcanic region has been the most preferred theoretical tool to study the connection between a volcanic eruption and an earthquake. They are permanent and have allowed to estimate the post-seismic volumetric regime at a magmatic zone(Walter and Amelung, 2006)(Walter and Amelung, 2007), and also they are used to calculate the normal and Coulomb stresses at a particular structure in order to infer the structural impact of the main shock in the volcanic/hydrothermal region(Bonali, 2013). The value of these changes, nonetheless, decays very rapidly from the rupture zone, and thus they are negligible after a couple of fault lengths. It is very unlikely that distant responses to large earthquakes might be caused by static stress changes(Manga and Brodsky, 2006).

Fluid dynamics play a major role on a volcanic and hydrothermal activity. Unfortunately, to this day it is not possible to obtain direct measurements of important parameters such as fluid overpressure. It has been only in the last years, with advances in noise and focal mechanism tomography, that the location and internal pressure of fluid reservoirs for some volcanoes has been estimated. In the case of the Ontake volcano, Terakawa *et al*(Terakawa et al., 2013) found that fluid was confined at depths between 5 and 12 km, with overpressures up to 100-150 MPa. When considering that the total internal fluid pressure is the sum of hydrostatic-plus over-pressure, and given that at 15 km depth the lithostatic pressure is 367.5 MPa, then large static stress changes, of the order of 1 MPa account for less than 0.2% of the total pressure of the fluid, which supports the idea of the earthquake as the trigger of a system that is very close to its critical state(Fujita et al., 2014).

The role of the earthquake directivity in its influence on the dynamics of a volcanic/hydrothermal system has not been widely studied, but it also has an importance. Field observations have shown how not all the fault zones and volcanic/hydrothermal systems react in the same way to a particular earthquake, and in some cases clear response areas have been found(Convertito et al., 2013). A well known case is the seismic response of this is the dynamic reaction of several systems to the 2002 $M_W = 7.9$ Denali earthquake. There, most responses where found to be places along a line that followed the direction of the earthquake rupture(Gomberg et al., 2004).

The role of local structures, such as fault systems in the volcanic region, have been identified as important players in controlling the volcanism at a particular center(Cembrano and Lara, 2009), and the dynamics of new eruptions(Wicks et al., 2011). The role of faults in the destabilization of overlying volcanic edifices has also been established(Merle et al., 2001)(Lagmay et al., 2000). Nevertheless, the static and dynamic role of these structures in the influence of an earthquake in a volcanic/hydrothermal region has not been extensively studied.

Given the lack of direct measurements on fluid motion, developments on indirect observation techniques and numerical simulations are key to understand the influence of external perturbations in a volcanic/hydrothermal system. InSAR observations have helped to understand the structure of the regional stress state at volcanoes(Ruch and Walter, 2010), and they have also been useful to see the changes produced by earthquakes in volcanic regions. An example of this are the episodes of subsidence of volcanic edifices after the 2010 Maule(Pritchard et al., 2013) and 2011 Tohoku(Takada and Fukushima, 2013) earthquakes, which might be related to fluid motion induced by earthquake. These episodes are also correlated with periods of unusually high activity, like the occurrence of a $M_W = 6.4$ earthquake near Mount Fuji, after the Tohoku earthquake(Brenguier et al., 2014).

Numerical simulations have been widely used in geosciences. In volcanic processes, they have been applied to study the ascent of magma along volcanic conduits(Papale, 1999), magma convection, mixing, and ascent dynamics(Longo et al., 2006)(Longo et al., 2008), dyke intrusion(Annen et al., 2001), magma chamber dynamics(Proussevitch and Sahagian, 1998), lava flows(Kereszturi et al., 2014), eruption dynamics(Neri et al., 2002), and in volcano seismicity(Bean et al., 2014). These tools have also been very useful in rock mechanics(Heinze et al., 2015), and simulations of fluid motion in the crust. The last ones, in particular, have been used to understand the behavior of several swarms and aftershocks sequences around the world, such as the cases of the aftershock sequence of the L'Aquila earthquake(Miller et al., 2004), the 2005 volcano-tectonic earthquake swarm in the Andaman Sea(Kundu et al., 2012), and the aftershock sequence of the 2001 Bhuj earthquake, in India(Gahalaut et al., 2008). Numerical simulations also been used in the study of the dynamics of earthquakes and their corresponding seismic waves(Chouet and Julian, 1985)(Bizzarri, 2011)(Bizzarri, 2012). Nevertheless, in the interaction between earthquakes and volcanic activity, numerical methods have not been widely used. For instance, they have been used to assess the permanent, static, influence of a seismic event in one region, but without taking into account the coupling between the earthquake seismic waves and the fluid dynamics at the volcanic/hydrothermal region(Gahalaut et al., 2008)(Kundu et al., 2012).

In this article, we present results from several numerical experiments on the dynamic and static influence of an earthquake in a volcanic/hydrothermal region. We do this by studying the characteristics of two 2-D settings, composed by a system of fluid reservoirs connected to simple fault systems. This is achieved by using a new set of numerical codes that solve a system of coupled differential equations composed by the equations of motion of a fluid saturated poroelastic space with a non-linear diffusion equation which considers the dynamic role of the earthquake. To add to the understanding of the earthquake-volcano interactions, we studied the effect of several $M_W = 4.0$ events located nearby the volcanic/hydrothermal system, and the influence of many $M_W = 6.1$ earthquakes, located a bit more than 100 km away from the studied setting. Due to the magnitude/distance ratio of these experiments, both static and dynamic stresses are relevant for the first type of experiment, while only the dynamic stresses are important for the second one. This variety allow us to have a better understanding on the role of local structures and earthquake directionality

in the effect of earthquakes in volcanic activity.

3.2 Theory and Methodology

In this article, we study two main types of 2-D experiments, which operate in different spatial planes. The first type, called "vertical experiment", is performed in the $x-z$ plane, while the second type, known as "NS experiment" is defined in the $x-y$ plane. All vertical experiments do account for the dynamic role of gravity but, which is not the case for all the NS experiments, as they are defined at a plane with a fixed depth.
To simulate the interaction between waves and fluid motion, we start from the motion equations for a poroelastic space in 2-D. For the case of the vertical experiment, they are

$$\frac{dv_x}{dt} = \frac{1}{\rho}\left[\frac{\partial \sigma_{xx}^{\text{eff}}}{\partial x} + \frac{\partial \sigma_{xz}^{\text{eff}}}{\partial z}\right], \tag{3.1}$$

$$\frac{dv_z}{dt} = \frac{1}{\rho}\left[\frac{\partial \sigma_{xz}^{\text{eff}}}{\partial x} + \frac{\partial \sigma_{zz}^{\text{eff}}}{\partial z}\right] + g\,, \tag{3.2}$$

$$\frac{d\sigma_{xx}}{dt} = (\lambda+2\mu)\frac{\partial v_x}{\partial x} + \lambda\frac{\partial v_z}{\partial z}\,, \tag{3.3}$$

$$\frac{d\sigma_{zz}}{dt} = (\lambda+2\mu)\frac{\partial v_z}{\partial z} + \lambda\frac{\partial v_x}{\partial x}\,, \tag{3.4}$$

$$\frac{d\sigma_{xz}}{dt} = \mu\left[\frac{\partial v_z}{\partial x} + \frac{\partial v_x}{\partial z}\right], \tag{3.5}$$

while in the NS experiment, they are given by

$$\frac{\partial v_x}{\partial t} = \frac{1}{\rho}\left[\frac{\partial \sigma_{xx}^{\text{eff}}}{\partial x} + \frac{\partial \sigma_{xy}}{dy}\right], \tag{3.6}$$

$$\frac{\partial v_y}{\partial t} = \frac{1}{\rho}\left[\frac{\partial \sigma_{xy}}{\partial x} + \frac{\partial \sigma_{yy}^{\text{eff}}}{dy}\right]. \tag{3.7}$$

$$\frac{\partial \sigma_{xx}}{\partial t} = (\lambda+2\mu)\frac{\partial v_x}{\partial x} + \lambda\frac{\partial v_y}{\partial y}\,, \tag{3.8}$$

$$\frac{\partial \sigma_{yy}}{\partial t} = (\lambda+2\mu)\frac{\partial v_y}{\partial y} + \lambda\frac{\partial v_x}{\partial x}\,, \tag{3.9}$$

$$\frac{\partial \sigma_{xy}}{\partial t} = \mu\left[\frac{\partial v_x}{\partial y} + \frac{\partial v_y}{\partial x}\right], \tag{3.10}$$

Here, we are using the convention that compression is positive, and a coordinate system where gravity goes in the positive direction of $\hat{z}$. Also, we are using effective stresses, defined by

$$\sigma_{ik}^{\text{eff}} = \sigma_{ik} - \delta_{ik}P\,, \tag{3.11}$$

where δ_{ik} is the Kronecker delta, and P is the total pressure, given by the addition of the hydrostatic pressure P_{static} plus the overpressure P_{over}.
The fluid diffusion is modeled following the treatment of Miller (Miller et al., 2004), and Kundu (Kundu et al., 2012), by using the non-linear diffusion equation:

$$\frac{dP_{\text{over}}}{dt} = \frac{1}{\phi(\beta_{\text{f}} + \beta_{\phi})} \left[\nabla \frac{\kappa}{\eta} \nabla P_{\text{over}} \right] + \dot{\xi} \,, \tag{3.12}$$

where β_{f} and β_{ϕ} are fluid and pore compressibility, κ is the permeability, η is fluid viscosity, and $\dot{\xi}$ is a source term, which might depend on the volumetric stress change. Permeability κ is a function of normal stress, and is given by

$$\kappa = \kappa_0 \exp\left(-\frac{\sigma_n}{\bar{\sigma}}\right) \,, \tag{3.13}$$

where κ_0 is the permeability at zero effective stress, $\bar{\sigma}$ is a constant, and σ_n is the normal stress, defined by

$$\sigma_n = \frac{\sigma_{xx}^{\text{eff}} + \sigma_{zz}^{\text{eff}}}{2} + \frac{\sigma_{xx}^{\text{eff}} - \sigma_{zz}^{\text{eff}}}{2} \cos 2\theta + \sigma_{xz}^{\text{eff}} \sin 2\theta \,, \tag{3.14}$$

for the vertical experiment, and by

$$\sigma_n = \frac{\sigma_{xx}^{\text{eff}} + \sigma_{yy}^{\text{eff}}}{2} + \frac{\sigma_{xx}^{\text{eff}} - \sigma_{yy}^{\text{eff}}}{2} \cos 2\theta + \sigma_{xy}^{\text{eff}} \sin 2\theta \,, \tag{3.15}$$

for the NS experiment. In these equations, θ is the dip angle of the particular plane in which normal stress is measured.

Fluid viscosity η is usually a function which depends on pressure and temperature, and it has a different form for different fluids(Kushiro et al., 1976)(Giordano et al., 2008)(Karki and Stixrude, 2010). In the case of water, it is modeled as temperature-dependent function, given by

$$\eta_{\text{water}} = a_1 \times 10^{a_2/T - a_3} \,, \tag{3.16}$$

where a_1, a_2, and a_3 are constants, and T is the temperature, in Kelvin, which depends on depth according to:

$$T = T_0 + a_4 h \,, \tag{3.17}$$

with h the depth and T_0 the temperature at surface, in dry conditions. In the NS experiment, this value is fixed.
The source term in Eq. (3.12) depends on the change in volumetric stress. According to Gahalaut *et al.*(Gahalaut et al., 2008), it is given by

$$\dot{\xi} = B \frac{d\sigma_{\text{V}}}{dt} \,, \tag{3.18}$$

with σ_{V} the volumetric stress and B the Skempton coefficient. Previous studies(Kundu et al., 2012) have used this term as the starting point of a fluid diffusion

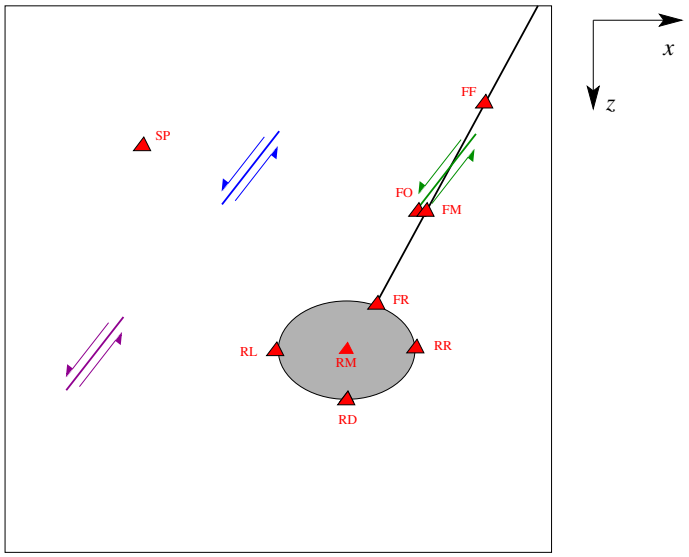

Figure 3.1: Physical system, with the locations of the stations and the three considered families of earthquakes. The epicenter of type 1 earthquakes, in blue, is located in a point in the space, at a similar distance from the reservoir and the main system fault. Type 2 earthquakes, in green, are generated with their epicenter at the main fault. Finally, type 3 events are located at the left hand side of the reservoir, and they are the more distant earthquakes to the system main fault. They are sketched in purple.

simulation, with σ_V being equal to the static volumetric stress change due to an earthquake. This procedure, however, does not account for the dynamic, more impulsive, stress changes due to the passage of a wave in the system. In our procedure for the vertical experiments, we solve the system of differential equations given by Eqs. (3.1), (3.2), (3.3), (3.5), and (3.4), coupled with Eq. (3.12), and the equations therein, thus taking full account of both the co- and post-seismic effects of an earthquake in fluid motion. In the case of NS experiments, we change the equations of motion for the poroelastic space with Eqs. (4.4), (4.5), (4.1), (4.2), and (4.3).

3.2.1 Experiment settings

3.2.1.1 Vertical Experiment

Fig. 3.1 presents a sketch of the physical system under treatment. It is composed by a overpressurized hydrothermal reservoir at depth d, connected to a geological fault, which is represented as an inclined line with different elastic properties and a larger permeability than the rest of the space. The fluid reservoir is characterized by larger Young's modulus and Poisson ratio than the used in the rest of the space. The value of the overpressure inside the reservoir is P_{over}. Later, an earthquake is generated at a particular space point, and the objective is to follow the temporal and spatial evolution of stresses, velocities, and fluid pressure.
To follow the temporal behavior more easily, nine stations were located in several points in the space. The details of the quantities they record, as well as some of their location details, are given in Table 3.1. They are located so we can take a closer

look at the behavior of the fluid dynamics, and then contrast these measurements with others obtained in stations which reproduce the background activity. All the relevant physical quantities are recorded in each one of them, at a rate of 200 data points per second.

Name	Code	Relative Location
Space	SP	Space
Fault Far	FF	Fault
Fault Out	FO	Space, next to Fault
Fault Mid	FM	Fault
Fault Res	FR	Fault, next to Reservoir
Res Left	RL	Space, next to Reservoir
Res Mid	RM	Reservoir
Res Right	RR	Space, next to Reservoir
Res Down	RD	Space, next to Reservoir

Table 3.1: Detail of the used stations, including name, abbreviations, and relative location in the system. Here, space stands for any point which is not in the system fault or in the fluid reservoir.

The system fault is inclined in an angle φ_{fault} respective to the horizontal axis. It is defined as a region in the space with different elastic properties, which are the following:

$$E_{\text{fault}} = 0.7E\,, \qquad \nu_{\text{fault}} = \nu\,, \tag{3.19}$$

with E the Young's modulus and nu the Poisson ratio. Also, permeability 100 times larger at the fault than at the rest of the system.
Using this setting, we performed two main types of experiments. The first one consisted in study of the influence of several $M_W = 4.0$ earthquakes, located at three different locations, characterized by the value of their dip angle. For each location, we generated 26 events, with dip angles between the 50° and 75°. Type 1 earthquakes are located near the middle of the domain, with a similar epicentral distance to both the fluid reservoir and the mid point of the system main fault. Type 2 earthquakes have their epicenter at the main fault, and type 3 earthquakes are generated to the left of the reservoir, being the most distant ones to the local structures. To isolate the role of the system main fault, we performed the same simulations, but without the presence of this structure. Following the conclusions of experiments on elastic parameters of fluid saturated rocks(Heap et al., 2014), we changed the value of Young's modulus and Poisson ratio to $E_{\text{res}} = 1.5E_0$ and $\nu_{\text{res}} = 1.1\nu_0$, where E_0 and ν_0 are the corresponding values in the space, outside the local structures.
The second type of experiment consisted in the study of the role of different elastic parameters for the fluid reservoir in the system dynamics. For this, we chose a type 3 earthquake, with a 75° dip angle, and a type 1 earthquake, with a 60° dip angle, as main perturbations. We then proceed to perform several experiments, each one

with a different set of values for both the Young's modulus and Poisson ratio at the fluid reservoir.

3.2.1.2 NS experiment

Long distance connections of hydrothermal fields are usually considered to occur due to the wave receiver being close to a critical state(Manga and Brodsky, 2006). Nevertheless, the role of local structures has not been widely taken into account. To study the earthquake influence in a volcanic/hydrothermal system when static stress changes are small at the reservoir level, we set up a two dimensional experiment, where we generate several $M_W = 6.1$ earthquakes, located 100 km away from a two mirroring faults, to study the effect of dynamic stress transfer in the system, subjected to changes in both epicenter location and strike angle value.
Our system of interest consist on a two dimensional poroelastic space, with a fault system composed of two mirroring structures, and fluid reservoirs at the middle of each fault. We then generate earthquakes far from the fault region, and follow both the dynamic and static changes induced by them. The setting is then affected by several $M_W = 6.1$ earthquakes, located at three main points in space, but at the same 100 km distance to the reservoir of the easternmost fault. Strike angle is changed in all the three locations, in the $[-15^o : 15^o]$ range.

Fig. 3.2 shows the setting of the experiment. We have a 2-D poroelastic space in the North-East plane, at a depth h, with two faults, which are regions in the space with a lower Young's modulus, and a larger permeability, just as in the case of the vertical experiment. The strike angle of the faults is $\pm\theta$. Two fluid reservoirs are also present, both with the same initial overpressure $\mathbb{P}_{\text{over}}$. Young's modulus and Poisson's ratio at the reservoirs are the same as the ones used in the vertical experiment.

To follow the dynamic behavior of the relevant physical quantities, we placed nine stations in important regions of the system. They allow us to get a better impression of the differences between nearby structures. Right hand side subfigure of Fig. 3.2 and Table 3.2 show more details on their precise location.

3.2.2 Initial stress state

Before starting any experiment, initial profiles for stresses and velocities must be found. The stress profile depends largely on the location of both the fault system and the reservoirs. To obtain it, we begin by setting initial conditions, and then let the system evolve up to its point of equilibrium. The resulting stresses and velocities profiles are the initial conditions for the experiments.
For the vertical experiment, the initial conditions we impose are the following:

$$\sigma_{zz} = \rho g h\,, \qquad \sigma_{xx} = 1.5\sigma_{zz}\,, \tag{3.20}$$

where ρ is the rock density, g is the gravity acceleration, and h is the depth. In our

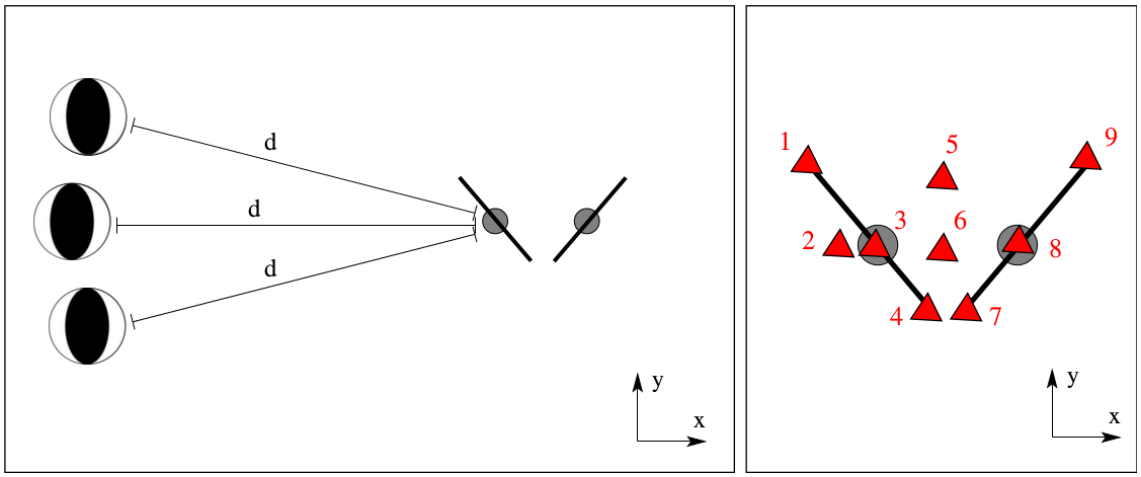

Figure 3.2: Left: Basic setting of our experiment. $M_W = 6.1$ earthquakes are generated at three different locations, all located at a distance $d = 100$ km from the first fluid reservoir. The fault system is composed by two main structures, each one with a fluid reservoir near its mid point. Right: Close up to the fault system, showing the location of the nine stations used for timeseries recording. Names for each stations are: 1 - Fault West Up (FWU), 2 - Reservoir West (RSW), 3 - Reservoir (RS), 4 - Fault West Down (FWD), 5 - Space Up (SPU), 6 - Space Mid (SPM), 7 - Fault East Down (FED), 8 - Reservoir Fault East (RFE), 9 - Fault East Up (FEU). More details in station placement are in Table 3.2

St. Number	St. Name	Acronym	Location	Young's modulus
1	Fault West Up	FWU	Upper west fault corner	Low
2	Reservoir West	RSW	West to the westernmost fault	Normal
3	Reservoir	RS	Western reservoir	High
4	Fault West Down	FWD	Lower west fault corner	Low
5	Space Up	SPU	Space between faults, up	Normal
6	Space Mid	SPM	Space between faults, mid	Normal
7	Fault East Down	FED	Lower east fault corner	Low
8	Reservoir Fault East	RFE	Eastern reservoir	High
9	Fault East Up	FEU	Upper east fault corner	Low

Table 3.2: Details on station placement, including station number, name, acronym, relative position respective to the fault system, and detail on Young's modulus at its position, where "normal" stands for the value for the normal elastic space, "low" represents a lower value, proper of the fault zone, and "high" represents a higher value, which is related to the reservoir region.

sign convention, compression is positive.

The hydrothermal reservoir is considered as an elliptic region defined by a overpressure Δp_0, and it is connected to the system fault. The whole space is considered to be fluid saturated, so the quantity responsible for deformations is the effective stress. Total pressure is given by the sum of the hydrostatic pressure plus the overpressure.

$$P = \rho_{\mathrm{f}} g h + P_{\mathrm{over}} \,. \tag{3.21}$$

Here, ρ_{f} is the fluid density, and P_{over} is the overpressure in any point in space.

To obtain the initial stress state before the earthquake arrival, we have to solve our system of differential equations in a long time, without earthquake generation, until we reach a stable solution. To avoid wave propagation due to the system structures, such as the fluid reservoir, and also to reduce calculation time, we used a Mass Scaling method, introduced by Rozhko (Rozhko, 2007), with a density $\rho_{\mathrm{comp}} = 10^8$ kg/m^3 and a viscous damping damping equal to 0.2.

Fig. 3.3 shows the equilibrium stress profiles, right before the arrival of an earthquake. Notice how the system main fault is clearly visible.

The procedure is similar for NS experiments, only that the system of differential equations to solve changes. Fig. 3.4 shows the relevant stress profiles before any earthquake generation.

3.2.3 Grid and absorbing layers

In all the experiments, we solved the partial differential system of equations by using a explicit a finite difference method, with a staggered grid, following the procedure of Saenger(Saenger et al., 2000). Fig. 3.5 presents a sketch of the used grid. The total size of the grid is 400×400 points for the vertical experiments, and 800×800 points for the NS experiments. Pressure, overpressure, total and effective stresses, are measured in the same points, while velocities are calculated in the intermediate points. The implementation of the method was done in a series of new poroelastic codes in C++, using OpenMP(Board, 2013) as a parallelization routine.

3.2.4 CPML

The outcome of numerical simulations which involve wave propagation depends strongly on the boundary conditions, as they help to define the physical system under treatment, and dominate how the system behaves in the long term. One major issue when solving wave equations under any numerical method is composed by the the spurious wave reflections at the boundaries. This is a numerical, non-physical phenomenon, and significantly affects the simulation, generating artificial results.

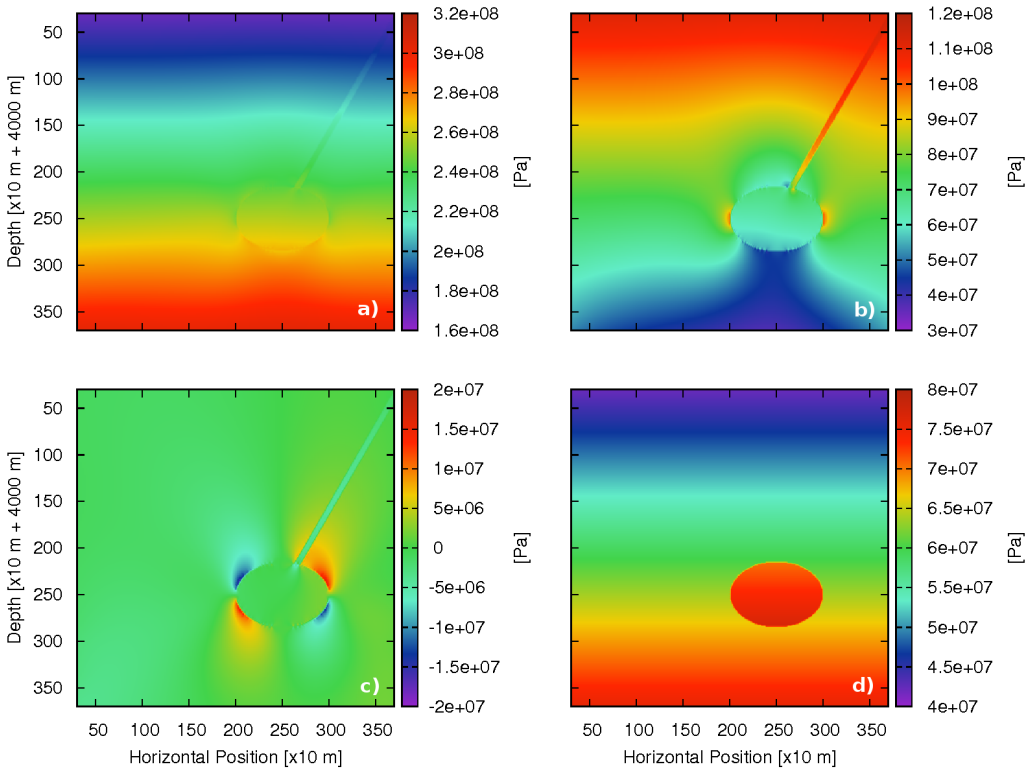

Figure 3.3: Stress and pressure profiles before the arrival of an earthquake in the vertical experiment. We present: a) σ_{xx}, b) σ_{zz}, c) σ_{xz}, and e) P. The structures are clearly visible here.

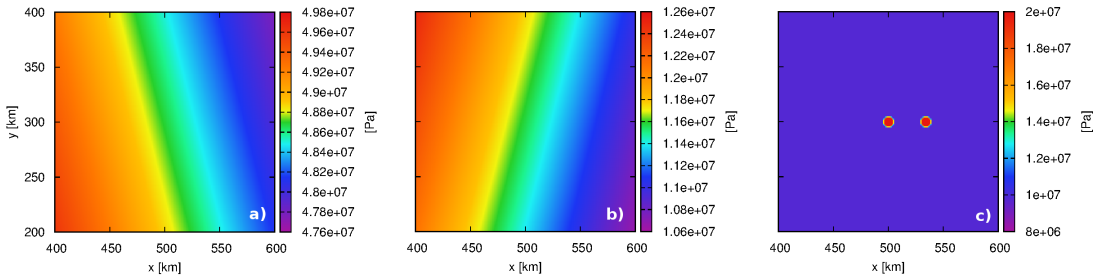

Figure 3.4: Initial stress and pressure profiles for the NS experiments. Here, we present: a) σ_{xx}, b) σ_{zz}, and c) P, showing the two fluid reservoirs, and a stress gradient from left to right.

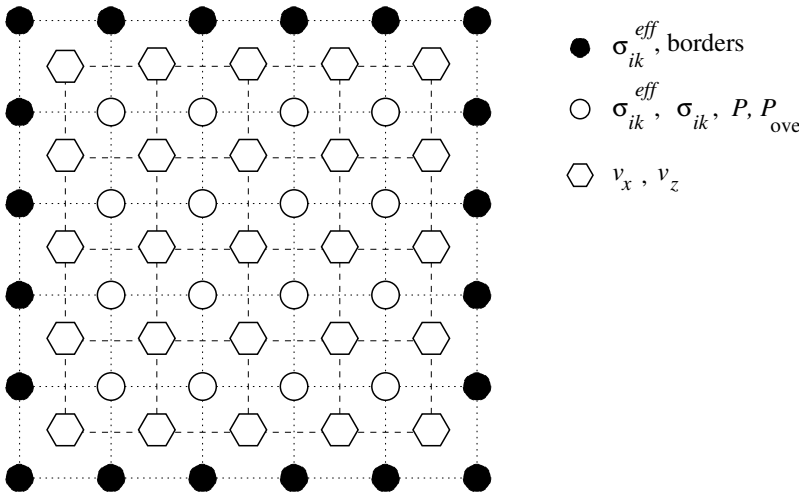

Figure 3.5: Sketch of the grid used in our computational codes. Stresses and pressures are defined in the same grid points, but the velocities are calculated in the grid nodes between them. Boundary conditions are imposed in the total stresses at the black points.

One method to avoid this situation is to use Convolutive Perfect Matched Layers (CPML) in the borders of the domain, which will prevent most of the non-physical reflections. The application of this method to elastic space was introduced by Drossaert and Giannopoulos (Drossaert and Giannopoulos, 2007), while the application to poroelastic media was developed by Martin *et al*(Martin et al., 2008). Its usage involves to define layers which attenuates incoming velocities and stresses, with null boundary conditions at all the borders. This method has been proved to reduce significantly the numerical, non physical, wave reflections at the system boundaries, and it is currently being used for several studies on wave propagation(Bean et al., 2014).

3.2.5 CPML in non-zero initial and boundary conditions

Due to the construction of the CPML layers, null boundary conditions have to be imposed, and initial stress profiles are also zero. This is an issue when the scope of the research goes beyond wave propagation, as the case we are treating here, when the stress profiles are of vital importance to the fluid motion, and different from zero. If the CPML method is applied directly in the system, a boundary wave is generated, which alters the final results. To handle this difficulty, we represent the dynamical behavior of the system as composed in two parts: base section, when wave motion is not considered with physical, non-zero stress profiles, plus a dynamic part, which considers only the wave motion, with null initial stresses and where the CPML method is used. This means that a stress σ_{ik} and a velocity v_i fulfill the following equations:

$$\sigma_{ik} = \sigma_{ik}^{(\mathrm{b})} + \sigma_{ik}^{(\mathrm{d})}\,, \tag{3.22}$$

$$v_i = v_i^{(\mathrm{b})} + v_i^{(\mathrm{d})}\,, \tag{3.23}$$

where the (b) and (d) labels stand for the base and dynamic parts, respectively. Using Eq. (3.22) in Eq. (3.11), effective stresses can be written as:

$$\sigma_{ik}^{\text{eff}} = \sigma_{ik}^{\text{eff (b)}} + \sigma_{ik}^{(\text{d})} \,, \tag{3.24}$$

where

$$\sigma_{ik}^{\text{eff (b)}} = \sigma_{ik}^{(\text{b})} - \delta_{ik} P \,,$$

is the effective stress in the base phase. Using Eq. (3.24) in Eqs. (3.1) and (3.2), it follows:

$$\frac{dv_x}{dt} = \frac{1}{\rho}\left(\frac{\partial \sigma_{xx}^{\text{eff}(b)}}{\partial x} + \frac{\partial \sigma_{xz}^{\text{eff (b)}}}{\partial z}\right) + \frac{1}{\rho}\left(\frac{\partial \sigma_{xx}^{(\text{d})}}{\partial x} + \frac{\partial \sigma_{xz}^{(\text{d})}}{\partial z}\right) , \tag{3.25}$$

$$\frac{dv_z}{dt} = \frac{1}{\rho}\left(\frac{\partial \sigma_{xz}^{\text{eff (b)}}}{\partial x} + \frac{\partial \sigma_{zz}^{\text{eff (b)}}}{\partial z}\right) + g + \frac{1}{\rho}\left(\frac{\partial \sigma_{xz}^{(\text{d})}}{\partial x} + \frac{\partial \sigma_{zz}^{(\text{d})}}{\partial z}\right) , \tag{3.26}$$

which can be arranged as

$$\frac{dv_x}{dt} = \frac{dv_x^{(\text{b})}}{dt} + \frac{dv_x^{(\text{d})}}{dt} \,, \tag{3.27}$$

$$\frac{dv_z}{dt} = \frac{dv_z^{(\text{b})}}{dt} + \frac{dv_z^{(\text{d})}}{dt} \,, \tag{3.28}$$

where $dv_z^{(\text{b})}/dt$ takes gravity into account.

Likewise, using Eq. (3.23) in Eqs. (3.3), (3.4), and (3.5), it follows:

$$\frac{d\sigma_{xx}}{dt} = (\lambda + 2\mu)\frac{\partial v_x^{(\text{b})}}{\partial x} + \lambda \frac{\partial v_z^{(\text{b})}}{\partial z} + (\lambda + 2\mu)\frac{\partial v_x^{(\text{d})}}{\partial x} + \lambda \frac{\partial v_z^{(\text{d})}}{\partial z} \,, \tag{3.29}$$

$$\frac{d\sigma_{zz}}{dt} = (\lambda + 2\mu)\frac{\partial v_z^{(\text{b})}}{\partial z} + \lambda \frac{\partial v_x^{(\text{b})}}{\partial x} + (\lambda + 2\mu)\frac{\partial v_z^{(\text{d})}}{\partial z} + \lambda \frac{\partial v_x^{(\text{d})}}{\partial x} \,, \tag{3.30}$$

$$\frac{d\sigma_{xz}}{dt} = \mu\left[\frac{\partial v_z^{(\text{b})}}{\partial x} + \frac{\partial v_x^{(\text{b})}}{\partial z}\right] + \mu\left[\frac{\partial v_z^{(\text{d})}}{\partial x} + \frac{\partial v_x^{(\text{d})}}{\partial z}\right] , \tag{3.31}$$

which can be written as

$$\frac{d\sigma_{xx}}{dt} = \frac{d\sigma_{xx}^{(\text{b})}}{dt} + \frac{d\sigma_{xx}^{(\text{d})}}{dt} \,, \tag{3.32}$$

$$\frac{d\sigma_{zz}}{dt} = \frac{d\sigma_{zz}^{(\text{b})}}{dt} + \frac{d\sigma_{zz}^{(\text{d})}}{dt} \,, \tag{3.33}$$

$$\frac{d\sigma_{xz}}{dt} = \frac{d\sigma_{xz}^{(\text{b})}}{dt} + \frac{d\sigma_{xz}^{(\text{d})}}{dt} \,. \tag{3.34}$$

Eqs. (3.27),(3.28),(3.32),(3.33), and (3.34) are the derivatives of Eqs. (3.22) and (3.23). Thus, $\sigma_{ik}^{(\text{b})}$ and $v_i^{(\text{b})}$ evolve satisfying the system of differential equations of a

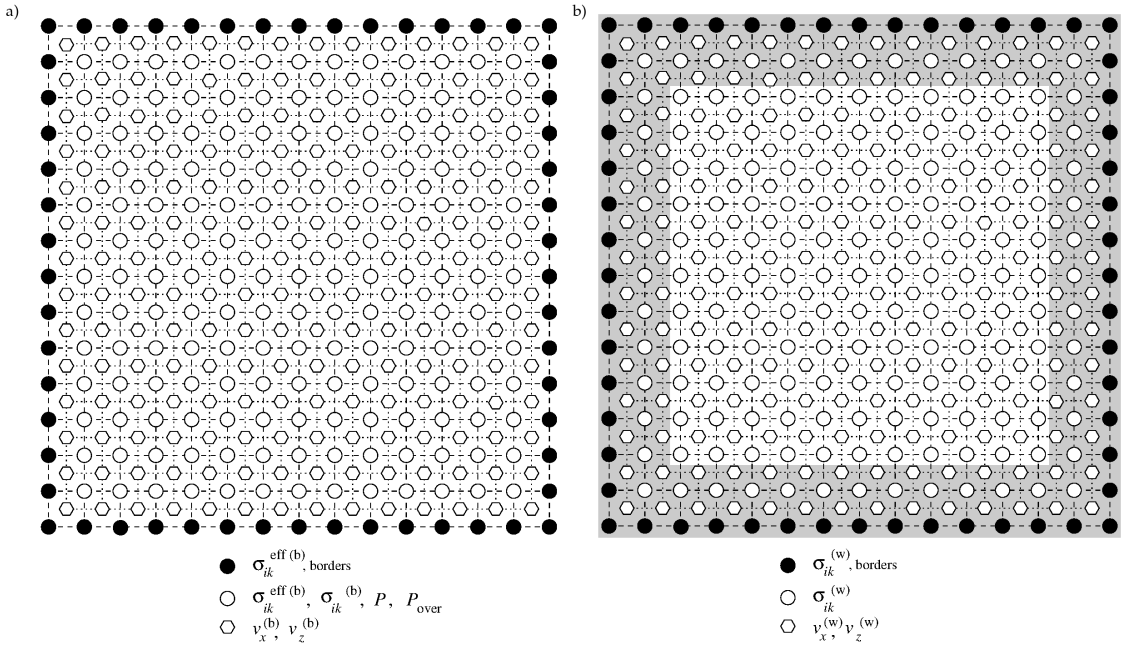

Figure 3.6: a) Grid used to compute the quantities in the base part, with physical boundary conditions applied into the stresses. b) Grid used to compute the quantities in the dynamic part, with the location of the Convolutive Perfect Matched Layers, on gray. Null boundary conditions are applied to the stresses.

fluid-saturated poroelastic medium with gravity, with non-zero boundary conditions, whereas $\sigma_{ik}^{(\mathrm{d})}$ and $v_i^{(\mathrm{d})}$ satisfy the system of differential equations of a elastic medium without gravity, with null initial stress profiles. The CPML method can be therefore used on $\sigma_{ik}^{(\mathrm{d})}$ and $v_i^{(\mathrm{d})}$. The perturbation which generates waves in the system is also applied to these w-variables.
Here we presented the derivation corresponding to the vertical experiments. For NS experiments, following the same procedure, we can reach the same result.

3.2.6 Grids

The system separation in two parts creates three different grids: One for the variables in the base part, another for the variables in the dynamic part, and finally, a composite grid, with the sum of both types of variables. Fig. 3.6 shows a sketch of the first two grids, highlighting the differences between them.

3.2.6.1 Algorithm

Physical variables are evolved in a Finite-Differences scheme, fulfilling a stability condition, with the Courant number equal to one. Fig. 3.7 presents a sketch of the described algorithm. To begin a cycle that goes from a time t to a time $t + dt$, we start with a pressure P^t, an overpressure P^t_{over}, total stresses σ^t_{ik}, effective stresses $\sigma^{\text{eff}\,t}_{ik}$, and velocities v^t_x and v^t_z. As mentioned earlier, stresses and velocities are composed by "base" and "dynamic" contributions, which are calculated separately.

The first quantity that is obtained is the normal stress, needed for the overpressure calculation, which is in turn used to calculate the pressure P^{t+dt}. Later, effective stresses are obtained, following Eq. (3.11). They are responsible for the deformation, and since $\sigma_{ik}^{\text{eff }t+dt}$ is the sum of $\sigma_{ik}^{\text{eff (b) }t+dt}$ with $\sigma_{ik}^{\text{(w) }t+dt}$, $\sigma_{ik}^{\text{eff (b) }t+dt}$ is responsible for the deformation of the "base" part of the system, while $\sigma_{ik}^{\text{(w) }t+dt}$ determines the deformation of the "dynamic" part.
When the system is divided in two parts, two separate evolution lines are created. The first one, related to the base part, evolves $v_i^{(\text{b})}$ and $\sigma_{ik}^{\text{eff (w)}}$, imposing Dirichlet Boundary Conditions on the effective stresses. In the second line, related to the dynamic part, $v_i^{(\text{d})}$ is first evolved, then corrected on the edges by using the CPML method. Afterwards, $\sigma_{ik}^{(\text{d})}$ is changed, and is also corrected on the edges by using the CPML method afterwards. To finish the cycle, the contributions for both parts are taking into account, and thus we obtain v_i^{t+dt}, σ_{ik}^{t+dt}, and $\sigma_{ik}^{\text{eff }t+dt}$.

3.2.7 Earthquake generation

An earthquake is the result of the sudden displacement of one block of the cortex respective to another, creating a rupture plane in the process. The direction of this displacement defines its focal mechanism, and it has components in three dimensions. Our simulation is in only two dimensions, so some restrictions have to be applied to the type of earthquake that can be simulated.
The simplest way to model the rupture zone of an earthquake is to represent it as a rectangle of length L and width W. The relative displacement between two blocks is represented by $\mathbf{u}$. In this first model, where all parts of a block move in the same way, the Seismic Moment is given by

$$M_0 = \mu L W |\mathbf{u}| \,, \tag{3.35}$$

where $|\mathbf{u}| = \sqrt{\mathbf{u} \cdot \mathbf{u}}$.

If all the quantities are given in the MKS system, the Moment Magnitude of the earthquake is

$$M_{\text{w}} = \frac{2}{3} \log_{10}(M_0) - 6 \,. \tag{3.36}$$

Scaling relations between L, W, and $u = |\mathbf{u}|$ are used in the simulation. The first-order approximation to them considers a linear relationship between these quantities, as follows:

$$W = \Gamma_1 L \,, \qquad u = \Gamma_2 L \,, \tag{3.37}$$

where Γ_1 and Γ_2 are parameters obtained empirically after fitting real data, and are given by

$$\Gamma_1 = \frac{1}{3} \,, \qquad \Gamma_2 = 1.5 \times 10^{-5} \,. \tag{3.38}$$

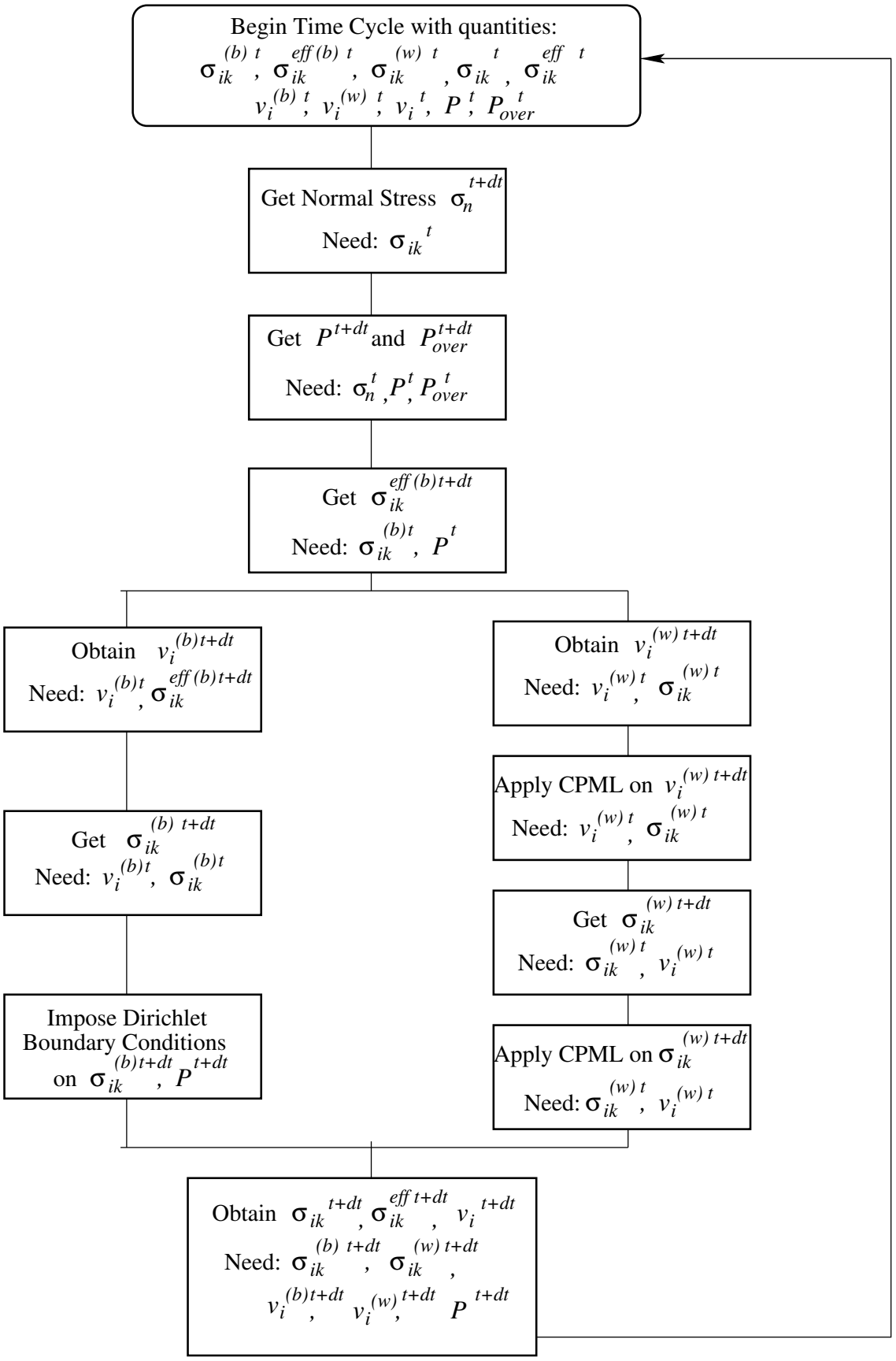

Figure 3.7: Calculation cycle.

In the vertical experiment, where only the $\hat{x}$ and the $\hat{z}$ axis are used, not all the directions of $\mathbf{u}$ can be represented. This dimension restriction allows only to simulate dip-slip motions, with a fault width W and a relative displacement u. In the NS experiment, on the other hand, we generate typical subduction earthquakes. Due to the 2-D constrain of our setting, we consider the projection in the North-East plane as our source. We calculate the earthquake rupture length, width, and slip, by using the relations given by Eqs. (3.37) and (3.38).
To generate the earthquake in the vertical experiments, we build up stress by slowly moving two neighboring rectangles, both with length L and a small width Δ, one next to each other, to generate a relative displacement $|\mathbf{u}|$. Both rectangles have an inclination angle θ, which is the earthquake's dip angle. Then, after the right amount of slip has been reached, we release the blocks, which move generating the seismic waves. In the case of the NS experiments, we follow a similar procedure, but this time we move block of length L_{proj} and width W_{proj}, which are the projections of L and W into our 2-D domain.

3.3 Results

The main goal of this article is to understand the role that different earthquakes have in a system composed by simple systems of fluid reservoirs connected to faults, and what is the role that local structures play in that interaction. We are interested in how the change of earthquakes characteristics such as the dip and strike angles, as well as it hypocentral position and magnitude, do affect the influence that an earthquake has in out studied systems. Here, we present the results from our experiments.

3.3.1 Vertical Experiment

The main goal of this experiment is to quantify the static and dynamic changes induced by several earthquakes in a simple system composed by a fluid reservoir and a single fault. To study this, we followed the co-seismic effect of several earthquakes at the whole system, with emphasis on the 9 stations displayed in Fig. 3.1. We will refer to the earthquake locations as type 1, type 2 and type 3 events, following the description given in section 3.2.

3.3.1.1 Overpressure evolution without external perturbations

Overpressure evolution, without the influence of external earthquakes, is important to understand the natural behavior of the system. Fig. 3.8 shows five snapshots of the overpressure in the system, highlighting the preferred diffusion direction, which is upwards along the fault. Of the nine stations sketched in Fig. 3.1, the first one to record a change in the overpressure value is Fault-Res, thus making it a important station for the recording of Physical properties.

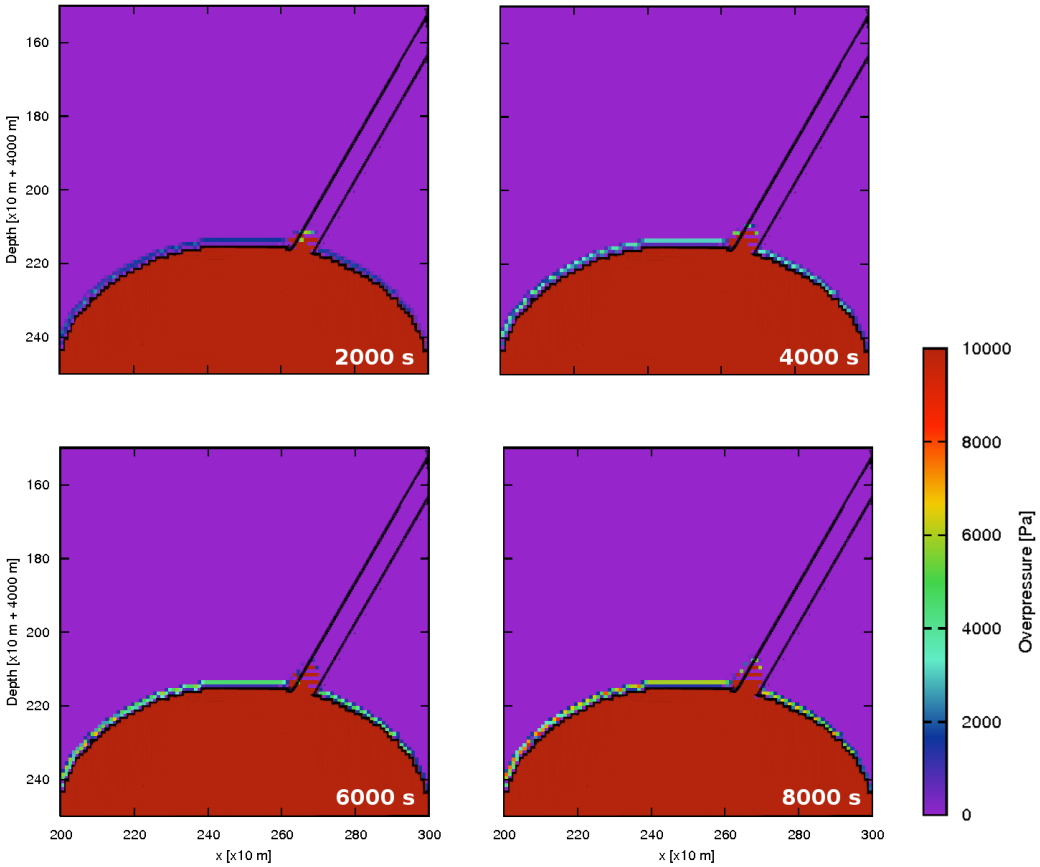

Figure 3.8: Overpressure evolution in 8000 seconds, without the influence of an external earthquake. We also sketch the local structures (fluid reservoir and main fault). The main fluid direction is up along the system main fault, which is the structure with lower permeability.

3.3.1.2 Static overpressure change, in two different settings

We first analyzed the total overpressure change due to the effect of the external earthquakes, for each one of the types of earthquakes. We varied the dip angle in the [50°:75°] range, and we simulate the system dynamics for each one of them in two settings: fault-present, and fault-free.

3.3.1.2.1 Type 1 earthquakes Static overpressure transfer is important since it alters the stress state of a region permanently. Fig. 3.9 shows several maps of overpressure change for type 1 earthquakes, in a fault-present environment, for different dip angle values. All dip angles are measured respective to the horizontal. Compression/extension areas are dominated by the radiation pattern of each event, with the fluid reservoir being compressed and the fault being mostly extended. An anomalous compressive region is found beneath the reservoir, with a similar shape for all the earthquakes, that does not relate with what should be expected in a typical double couple radiation pattern. This effect is particularly noticeable for dip angle values larger than 60°, and is related to the deformations created by the presence of the reservoir when it is under the influence of an external earthquake.
An important feature is the discontinuity in the overpressure induced by the earthquake, at the system fault. Mainly, static overpressure change is reduced inside the structure, and also there is a "transferring" effect, in which part of the induced compression/extension pattern is moved downwards the fault. The effect of the fault seems to be more pronounced for dip angle values between 50° and 65°, when the larger extensions are induced in the structure.
Static overpressure changes in a fault-free setting are presented in Fig. 3.10. The clearest difference with the results presented in Fig. 3.9 is the absence of the discontinuity at the fault, due to the lack of it. The compression/extension patterns are otherwise very similar.
In order to have a better insight on the differences generated by the system fault, we analyze the static overpressure change at each one of the nine system stations. Fig. 3.11 presents a station by station comparison of the static overpressure change, measured in both fault-present and fault-free settings, as a function of the dip angle values. While there is some perturbations in our results, due to reflections at the reservoir level that are not completely absorbed by the cpml layers, there are clear trends, which are dominated by the radiation pattern of each earthquake. Larger volumetric extensions are found at the system fault, with the maximum values at a 50° dip angle value. Results at FO and FM stations, located right outside the structure and at the middle of it respectively, present overpressure variations up to 23 kPa between the different events. Similar variations are featured in reservoir stations (RL, RM, RR, and RD), but with compressive values.
Timeseries analysis featured in Fig. 3.11 show how the overpressure changes differ mostly inside the fault region, with the absolute value of the total changes being lower when the fault is present than when it is not. This affects not only the fault itself, but also its vicinity, as the the results of FO station show. Differences between settings are more noticeable when the volumetric change is more pronounced, and

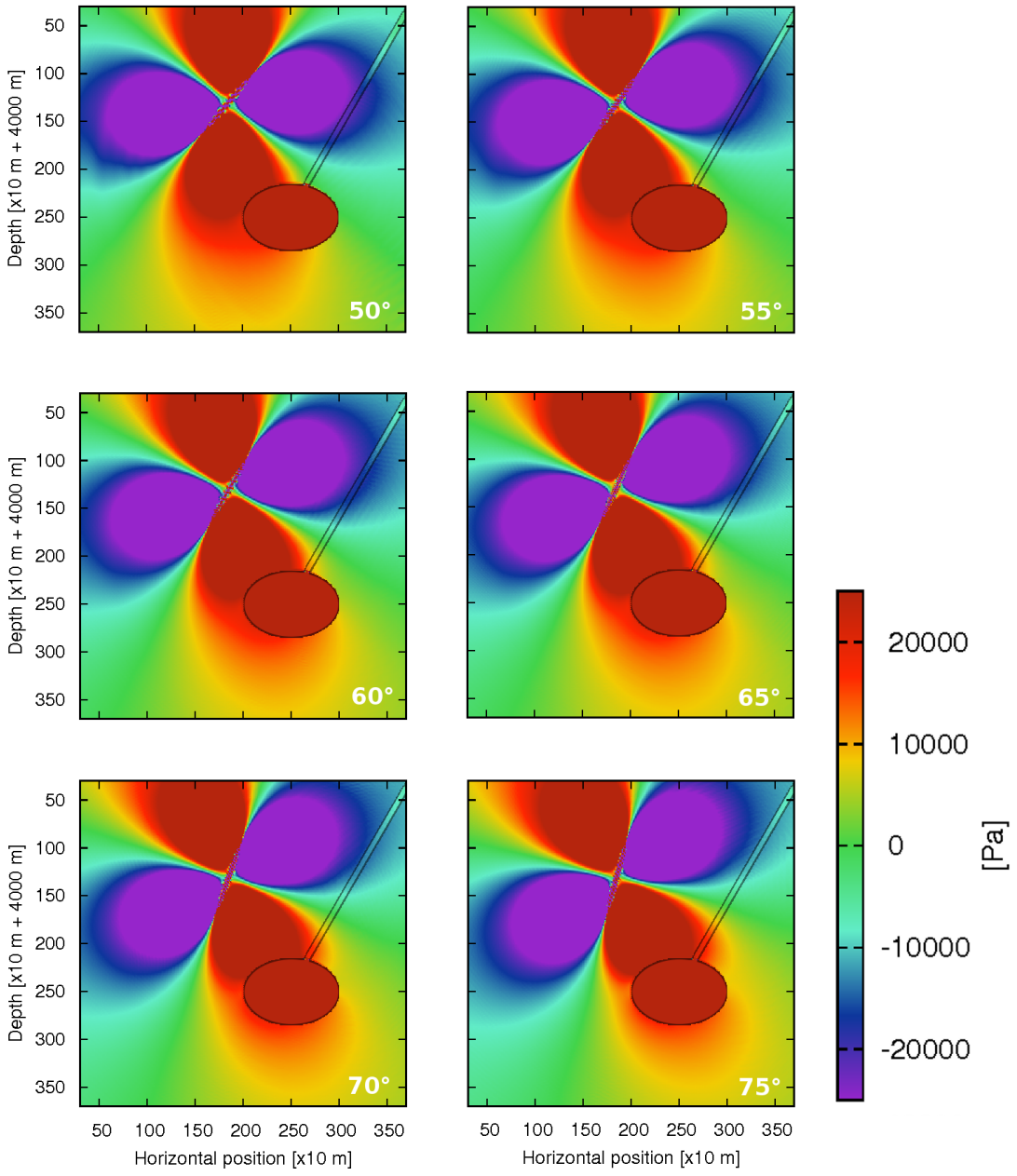

Figure 3.9: Overpressure change maps for several type 1 earthquakes, with different dip angles, in a fault-present setting. Overpressure is plotted in the $[-25\text{ kPa} : 25\text{ kPa}]$ range. Maps were obtained at the end of each simulations, and hence some small vibrations remained, which explains the small perturbations in out results. Main system structures are also sketched.

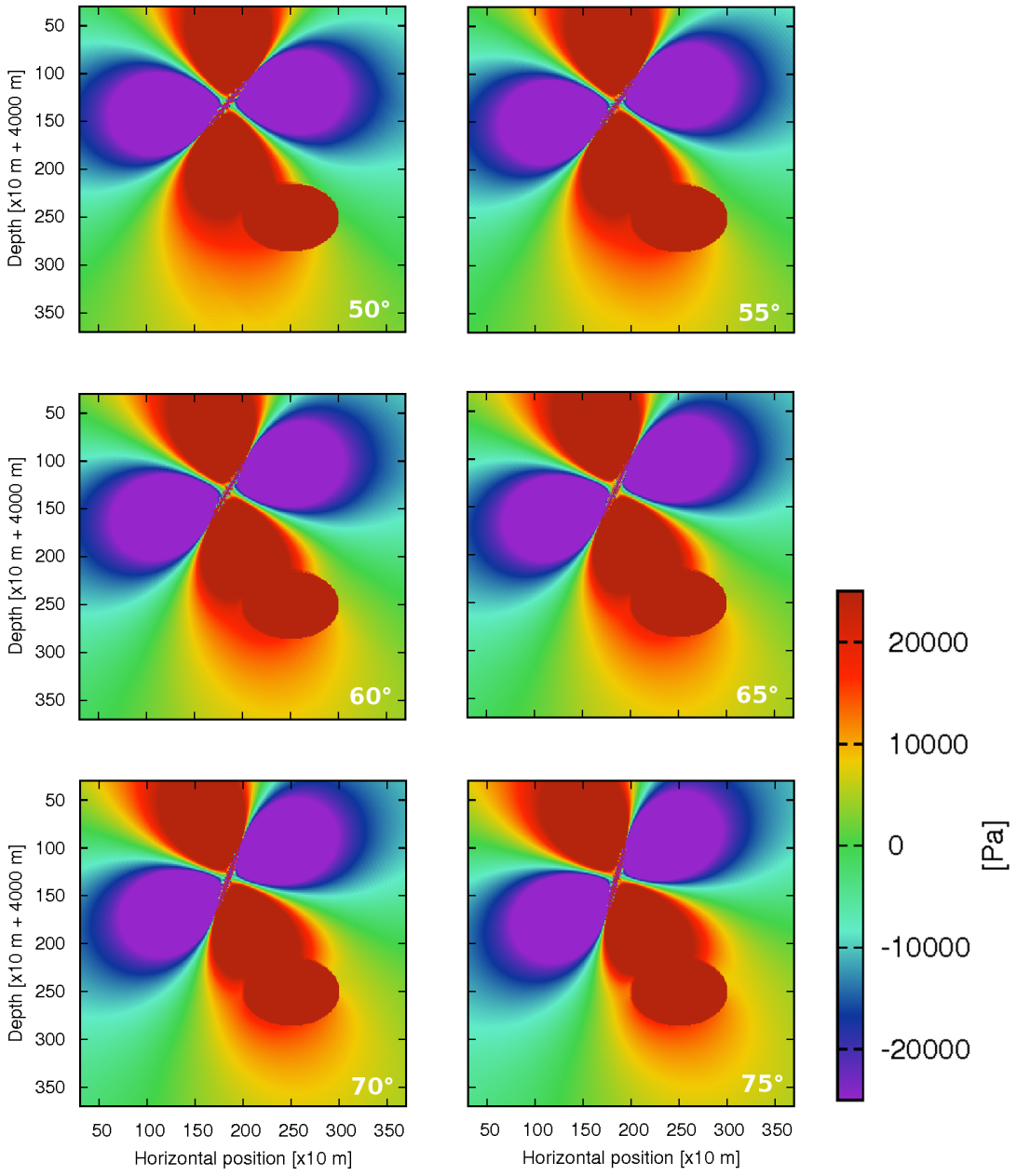

Figure 3.10: Overpressure change induced by a type 1 earthquake, for several dip angles values, in a fault-free setting. Dip angle values and overpressure range are the same ones as in Fig. 3.9. Notice how an anomalous compressive region is generated beneath the fluid reservoir.

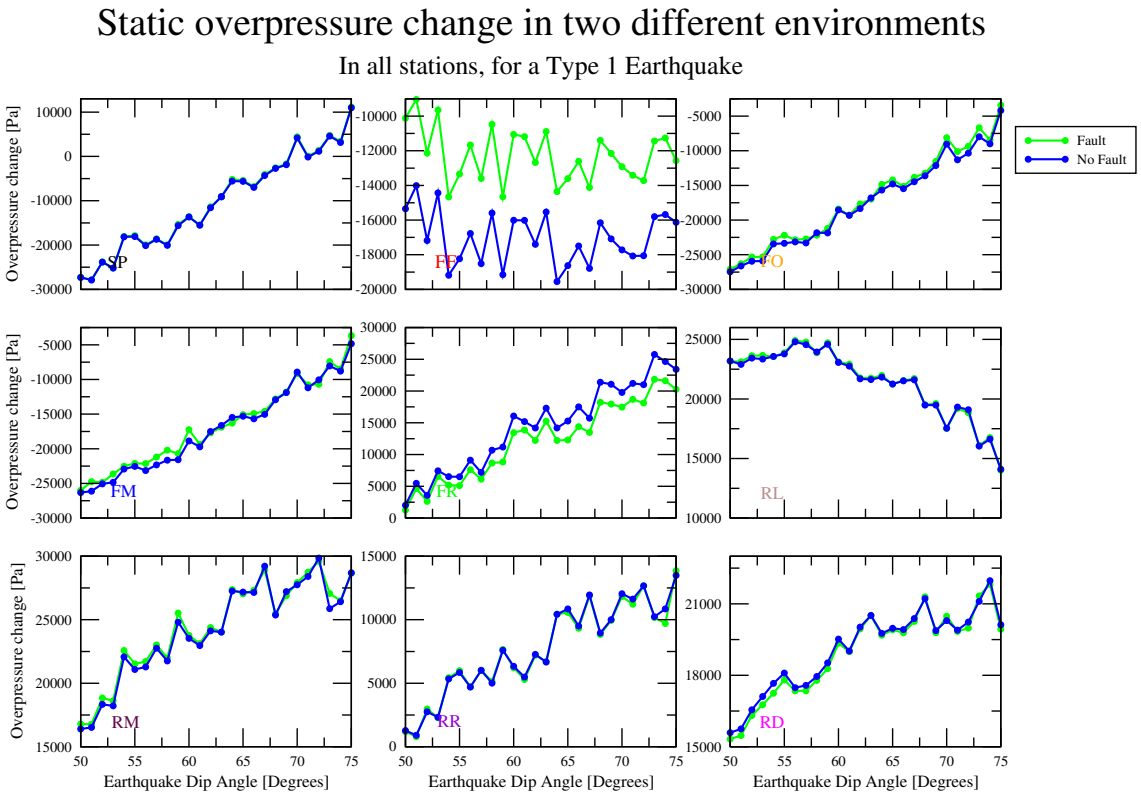

Figure 3.11: Station-by-station comparison of the overpressure change induced by a type 1 earthquake, for several dip angle values, in two environments: with and without a system fault. Clear trends are found in all stations, with the fault zone stations (FF, FO, FM, and FR) recording most important differences in the results between settings.

also at the most distant places of the fault, like FF station and FR station, with the former suffering volumetric extensions whilst the latter recording volumetric compression.

3.3.1.2.2 Type 2 earthquakes Type 2 earthquakes are generated with their hypocenter at the system fault. Fig. 3.12 shows the static overpressure change for the same magnitude earthquakes, for several values of the dip angle, in a fault-present setting. Outside the system structures, the volumetric change is dominated by the earthquake radiation pattern. Fluid reservoir undergoes volumetric extension on its left region, and compression on its right border. It also distorts the compression pattern on its right edge, being this effect most noticeable for larger input compressions, which in our case are found for dip angles lower than 65º.
The system main fault also plays a role in altering the static overpressure pattern. This is more noticeable at its edges, when larger extensions are induced on the structure. The input compression/extension pattern depends strongly on the earthquake dip angle value, inducing mostly volumetric compression at the fault for dip values smaller than 60º, and volumetric extension for dip angle values higher than 60º. The value of the induced volumetric change is decreased inside the fault, as can be specially noticed when comparing the results to the ones obtained in a fault-free setting, presented in Fig. 3.13.
Given that the earthquake is generated at the system fault, the effect on the structure is more complex than the for type 1 events. Fig. 3.14 shows a station-by-station comparison of the results between the fault-free and fault-present settings. Important overpressure changes are found at FO and FM stations due to their location, which for some dip angles is right on top of the earthquake rupture zone. In general, for all the stations located in the fault region, the volumetric change is smaller than it would be expected in a fault-free setting. Due to the transition from a compressive to a extensive state at a 60º, the overpressure change at the fault goes from less compressive to less extensive when compared with the results from a fault-free system. In the rest of the stations, the contrast between settings is not so straightforward, showing that the fault does have a large influence on the static overpressure change. In terms of values, the larger overpressure contrasts between settings are found in the fault, specially in the edges of the structure, as it can be appreciated on FF and FR stations, with maximum differences of $\sim$ 23 kPa in FF station for a 75º dip angle value, and $\sim$ 15 kPa for a 73º dip angle. Differences between settings differ from the case of type 1 earthquakes, where stations outside the fault show similar results.

3.3.1.2.3 Type 3 earthquakes From the three different earthquake families considered in this study, type 3 earthquakes are the most distant to the main structures of the system, and therefore the volumetric changes at the system structures are smaller than in the previous two cases. Fig. 3.15 shows the overpressure change for this type of earthquakes, in a fault-present setting. The volumetric changes are dominated by the radiation pattern of the events, but there is a distortion at the right hand side of the reservoir, with the creation of an extensive region that is not

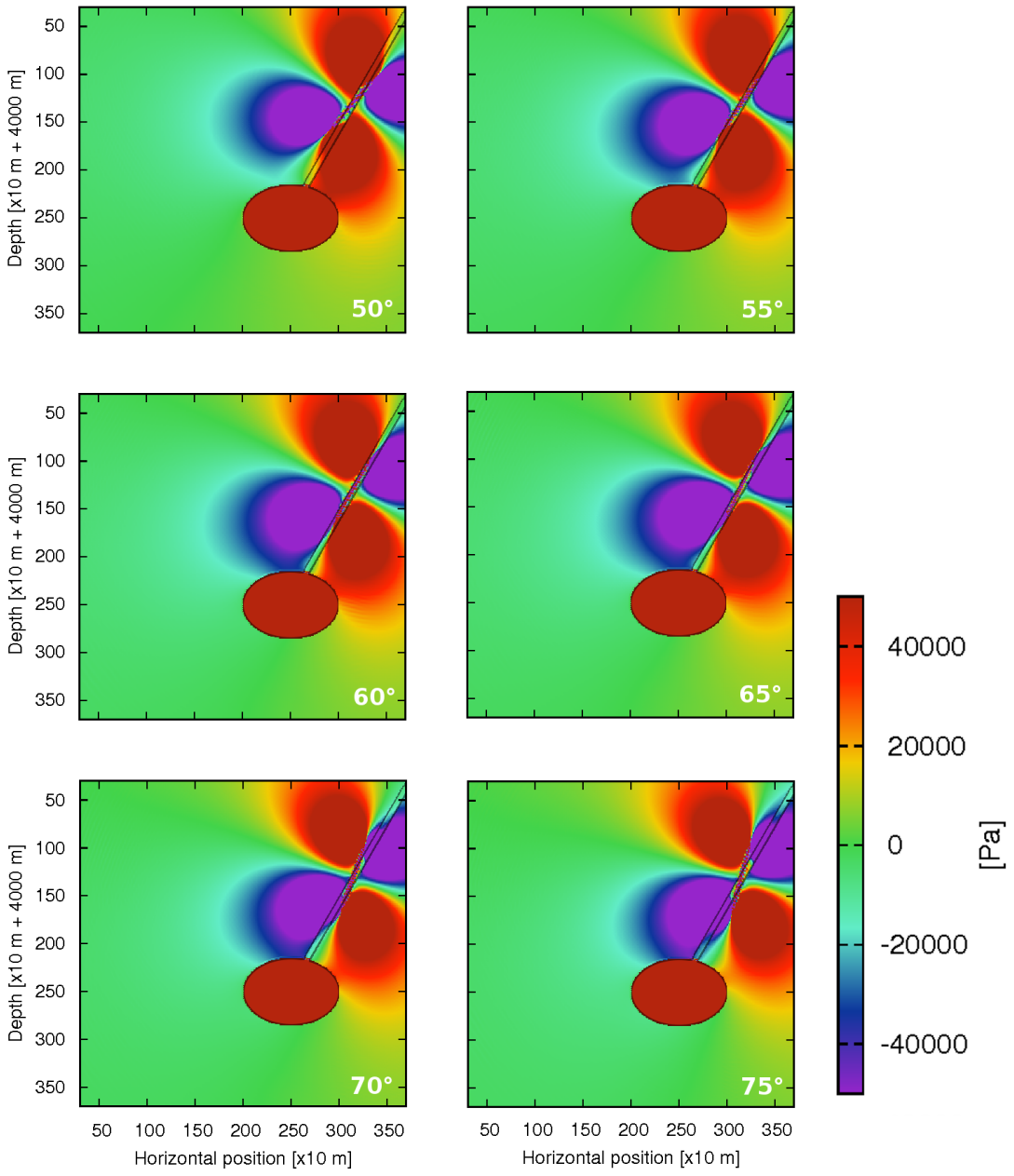

Figure 3.12: Static overpressure change in the simulation domain for type 2 earthquakes, obtained for several dip angle values, marked at each picture. Overpressure is plotted in the $[-45\ \text{kPa} : 45\ \text{kPa}]$ range. We also sketch the local structures of the system. Distortions produced by the fault are found inside the structure, and are more noticeable for larger dip angle values.

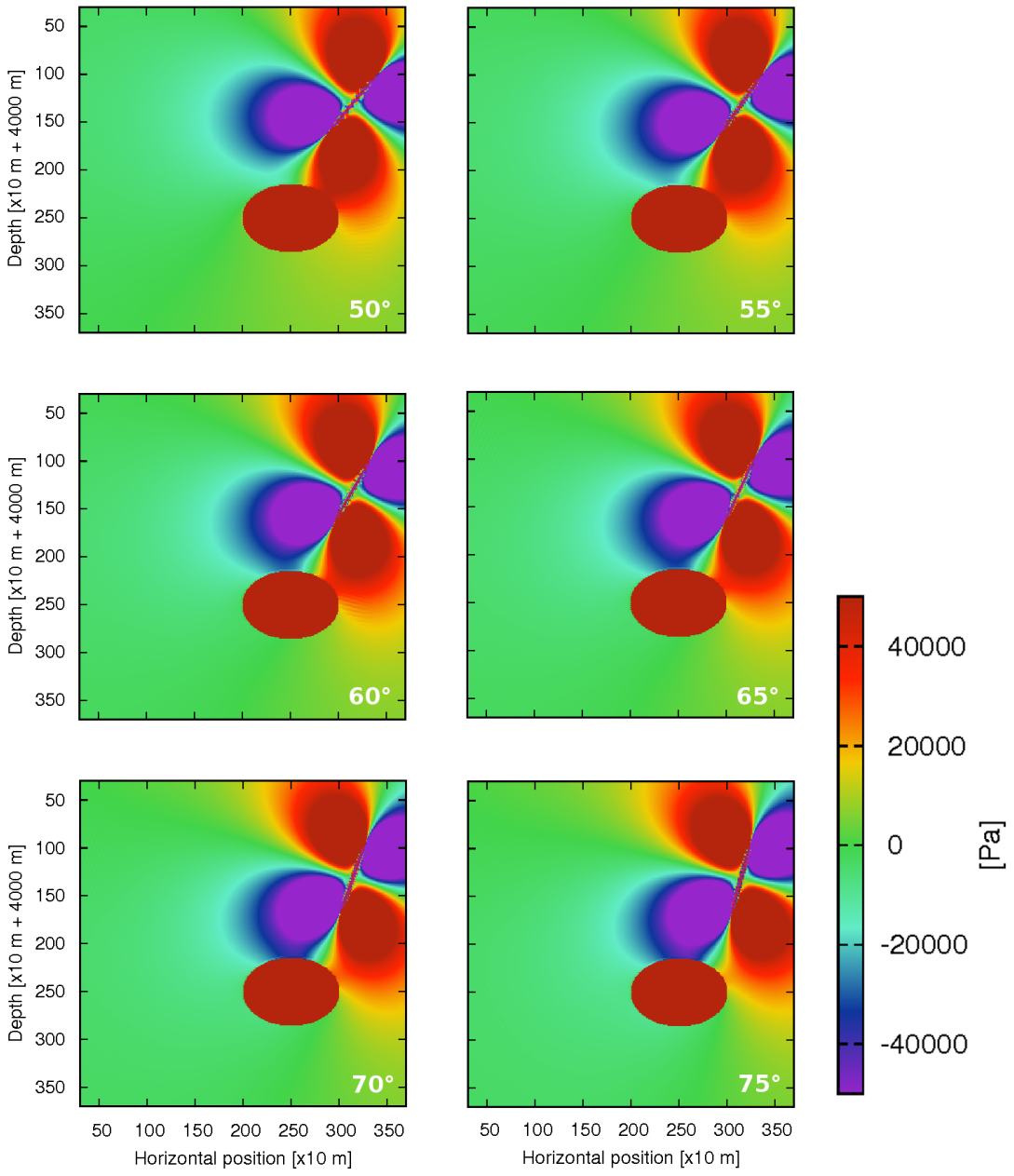

Figure 3.13: Overpressure change maps for several type 2 earthquakes, with different dip angles, in a fault-free setting. Dip values are marked at each picture. Overpressure is plotted in the $[-45\ \text{kPa} : 45\ \text{kPa}]$ range. The fluid reservoir generates a distortion in the earthquake-induced overpressure pattern, particularly at its borders.

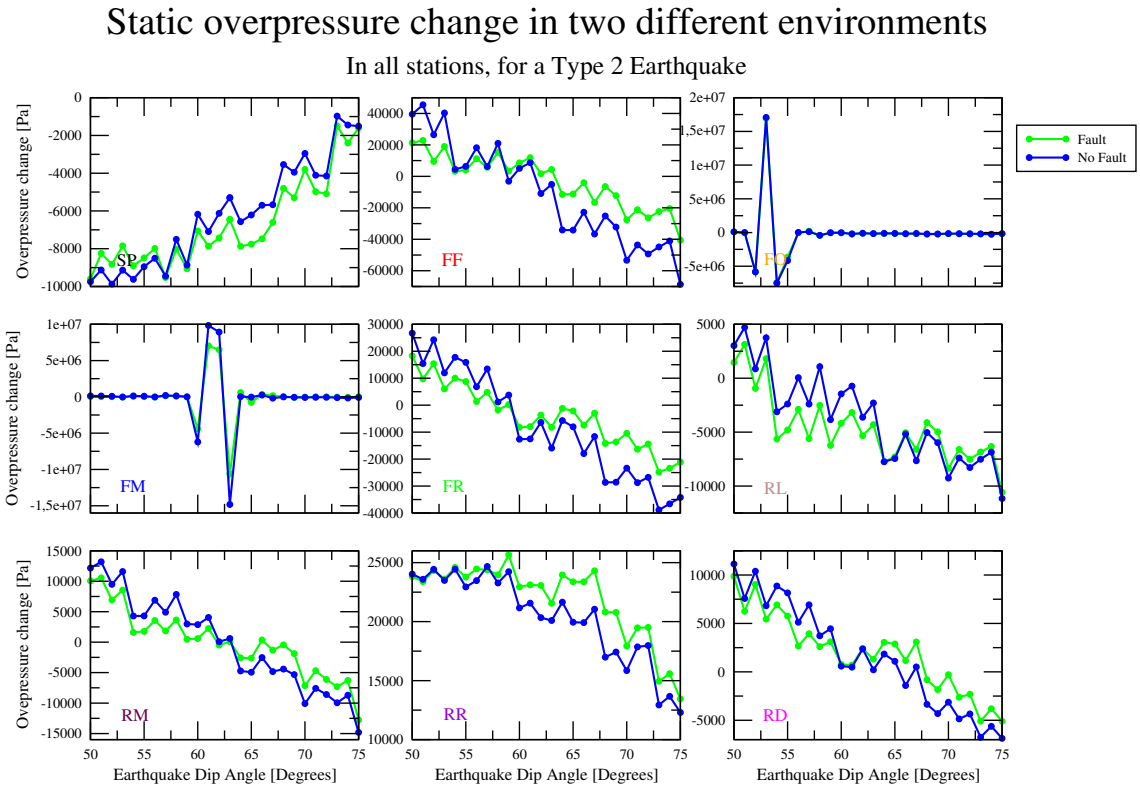

Figure 3.14: Station by station comparison of the overpressure change induced by type 2 earthquakes, between a fault-free and a fault-present setting. Static overpressure changes are plotted as a function of the dip angle value of the seismic event.

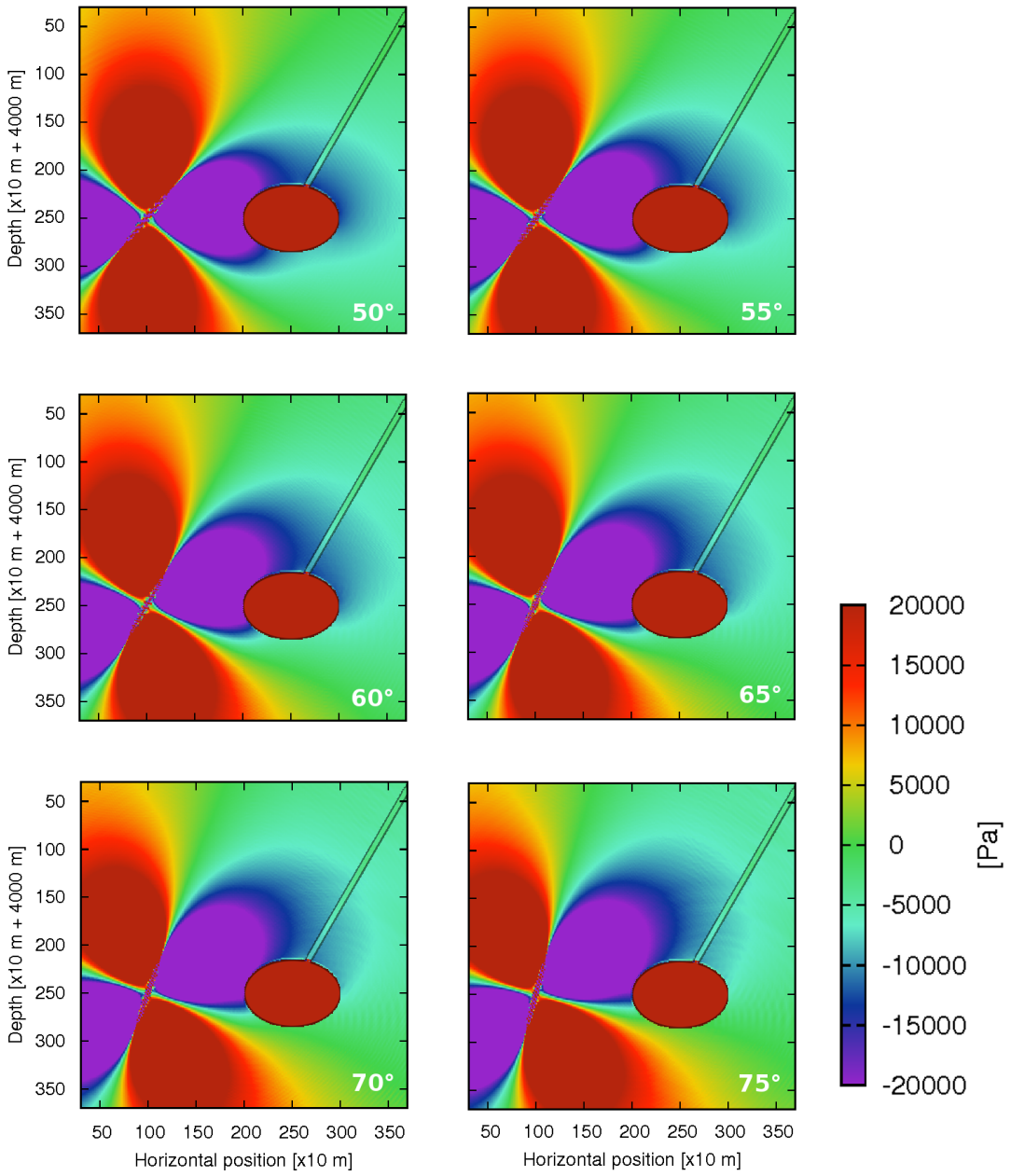

Figure 3.15: Earthquake-induced static overpressure change for type 3 earthquakes, obtained for several dip angle values, in a fault-present setting. For better visualization, the main structures of the system are drawn in each map. Overpressure is plotted in the $[-20\ \text{kPa} : 20\ \text{kPa}]$ range, and it can be noticed how it is slightly reduced inside the main system fault.

expected in a regular double-couple earthquake radiation pattern. The role of the system fault is not so prominent for this type of earthquake, but it does reduce the amount of volumetric extension inside itself, being particularly noticeable at dip angle values between 50° and 65°.
Fig. 3.16 presents the static overpressure change for several type 3 earthquakes, in a fault-free environment. When contrasting with the results presented in Fig. 3.15, the role of the system fault becomes evident, and it is more prominent at the boundary between the fault and the fluid reservoir, which undergoes an important volumetric extension, due to the existence of the reservoir.
Fig. 3.17 presents the station-by-station comparison between settings. Space and reservoir stations show clear trends, which depend mostly on the earthquake radiation pattern. The influence of the reservoir is seen in the distortion recorded at the fault stations (FF, FO, FM, and FR), where the overpressure patterns have important variations between dip angle values. Nevertheless, the role of the fault is still unveiled, as less extensive patterns are recorded at the fault-present setting, which is consistent with what was found in type 1 and type 2 earthquakes. These differences can be as high as $\sim$ 4 kPa in FM station, and are correlated with the absolute value of the mean stress change induced by the earthquake, with the larger contrasts being found at the larger volumetric changes. The role of the fault in the static overpressure change is also noticeable in its vicinity, as it can be seen in the results from FO station, located right outside the fault. A slight difference between settings was recorded at that station, with larger extensions being found at the fault-present system.

3.3.1.3 Dynamic Maximum Overpressure Amplitude

Dynamic changes are more predominant at larger distances from the earthquake rupture zone(Hill, 2008). While these variations are transient, their magnitude can be important for the dynamics of the system, as they can be used to identify sudden pressure increases, and they can also induce faulting, which in turn can explain sudden increases in seismicity in several regions around the world, right after (and even during) the passage of the earthquake waves(Manga and Brodsky, 2006). In this subsection, we present the results for the dynamic stress transfer, for the three earthquake families.

3.3.1.3.1 Type 1 earthquakes Fig. 3.18 presents the overpressure peak changes in all stations as functions of the earthquake dip angle, for type 1 events, with a comparison between the fault-present and fault-free settings. Peak overpressure patterns are complex in all stations, with some particular dip angles for which maximum compression is achieved. For this earthquake family, the vast majority of the peak overpressure values are compressive. The complexity of the maximum overpressure change patterns does not correlate with the ones of the static overpressure change. Such a difference might be related to the effect of multiple reflections at the system structures: main fault and fluid reservoir.
Differences between settings are found mostly in fault and RR stations. In the

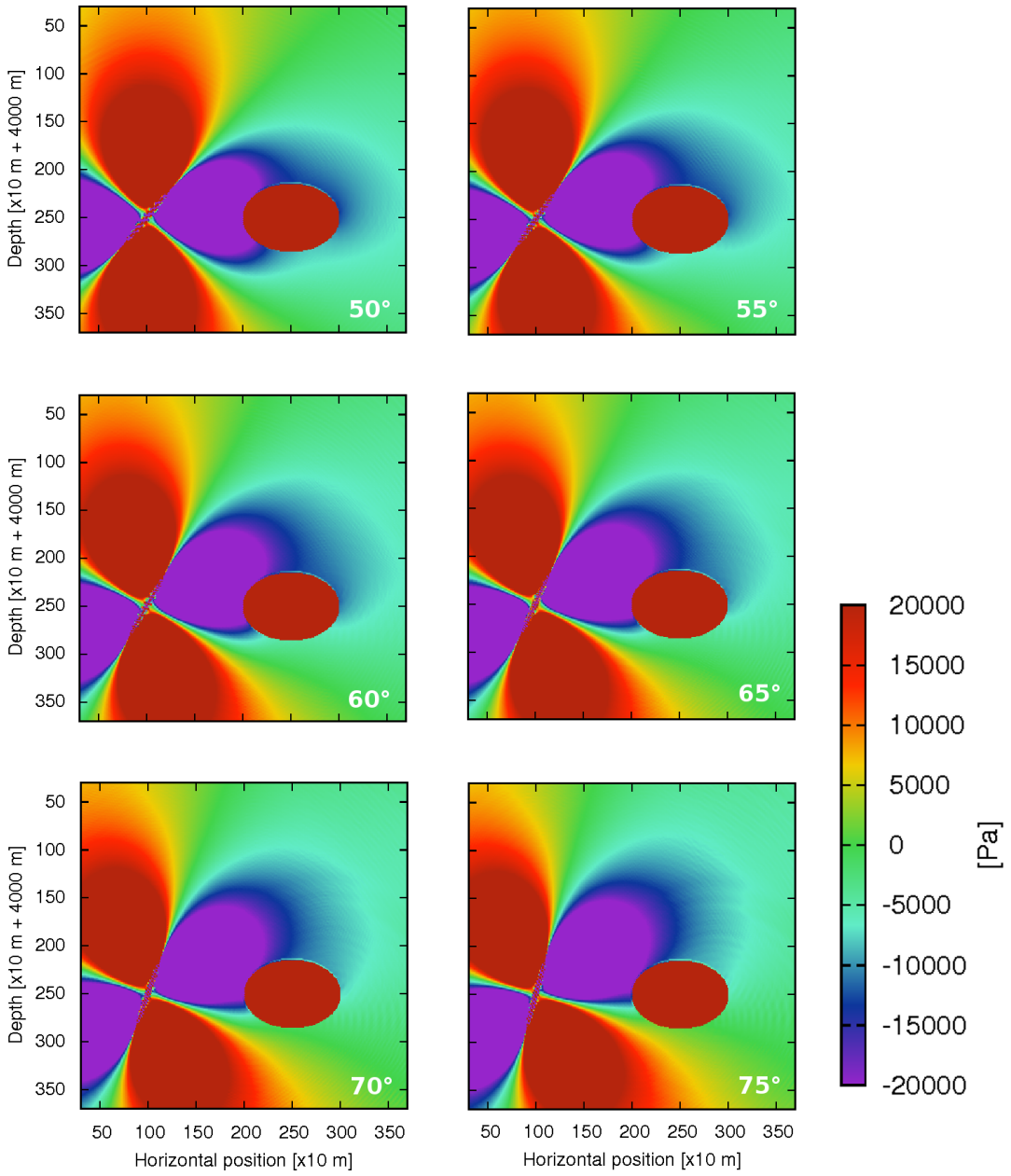

Figure 3.16: Static overpressure change, for type 3 earthquakes, measured at several dip angles, in a fault-free environment. Overpressure is plotted in the $[-20$ kPa : 20 kPa$]$. Results highlight the presence of an extensive region to the right hand side of the fluid reservoir, whose size depends on the volumetric extension induced by the incoming earthquake.

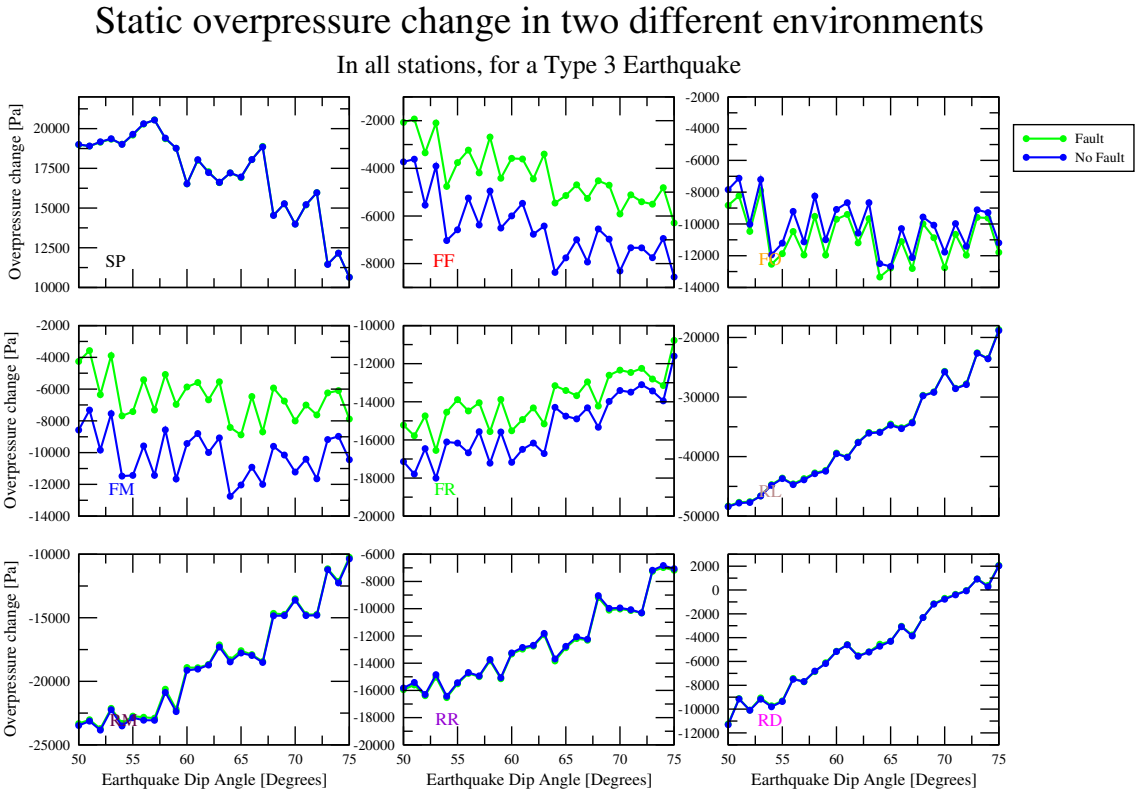

Figure 3.17: Comparison of the overpressure change induced by type 3 earthquakes between a fault-free and fault-present setting, as a function of the earthquake dip angle. Larger differences are found at the fault zone stations (FF, FO, FM, and FR).

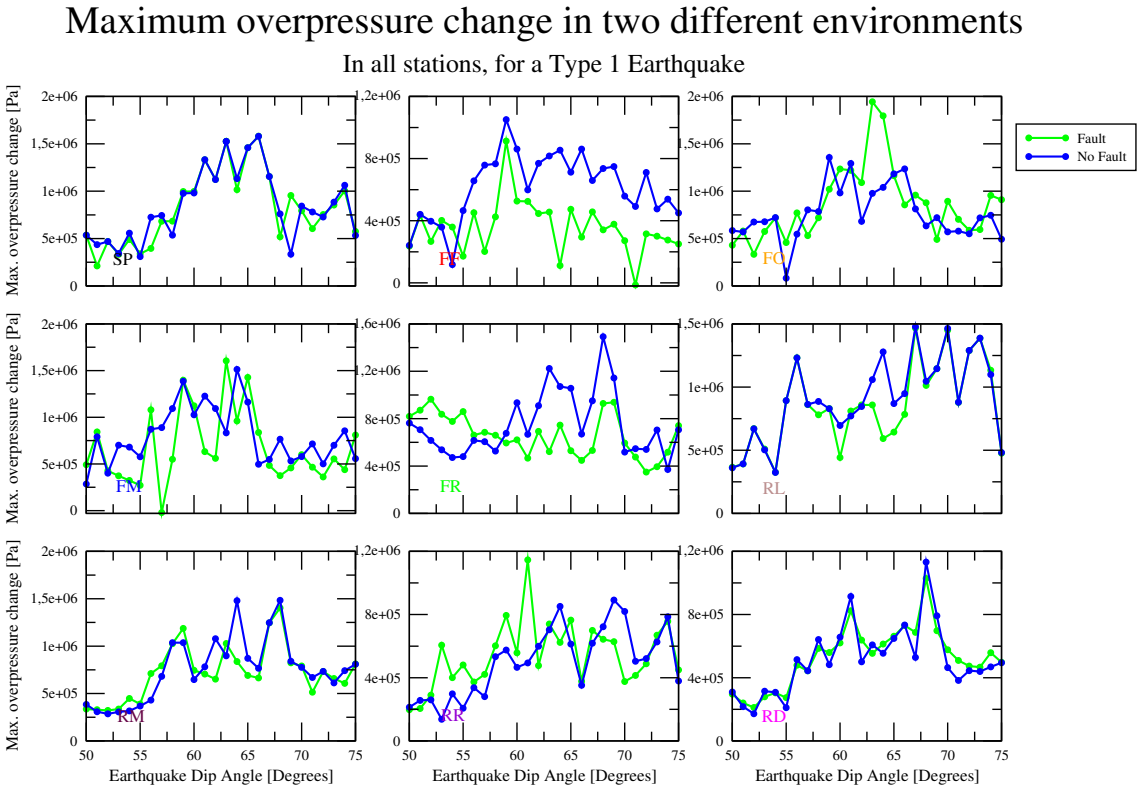

Figure 3.18: Maximum dynamic overpressure change recorded at each station during the passage of the waves generated by a type 1 earthquake, as a function of the dip angle. Main differences between settings are found inside the main system fault, with mostly lower overpressure peaks inside the structure.

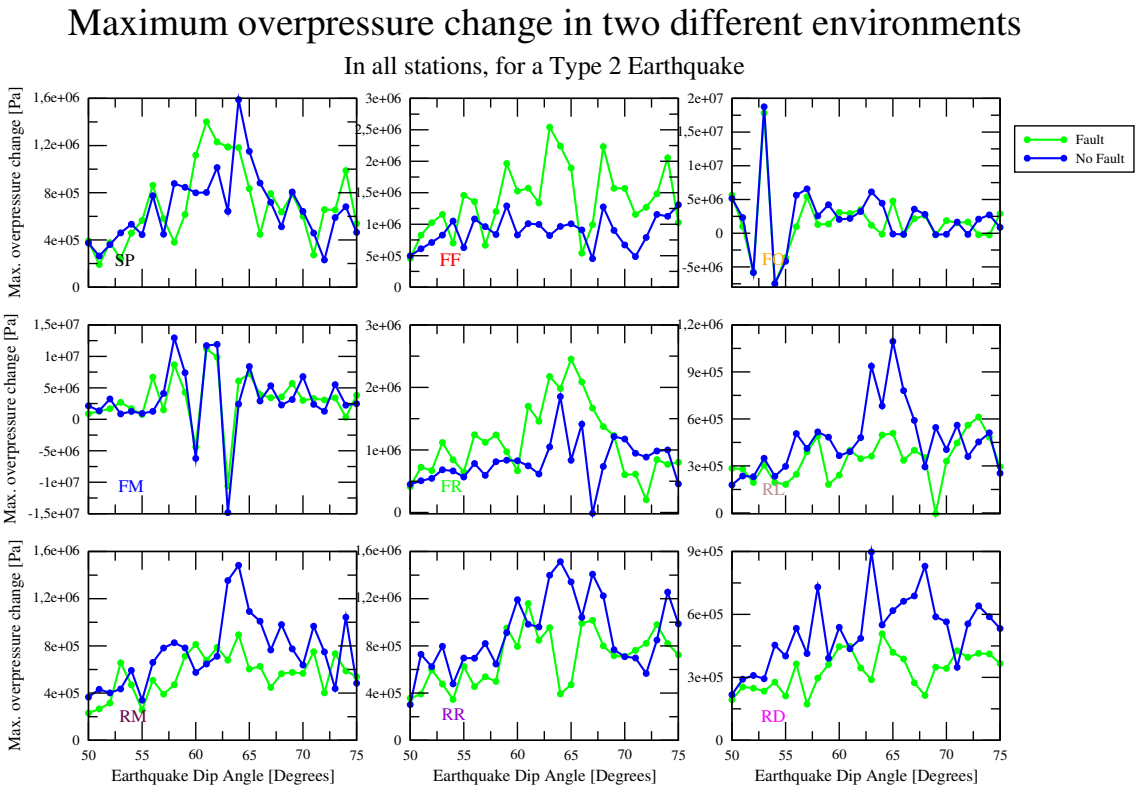

Figure 3.19: Maximum overpressure amplitude recorded at each station, as functions of the earthquake dip angle, for a type 2 events. Blue lines show the results obtained in a fault-free system, whilst green lines present the results measured in a fault-present system.

stations located in the fault zone, maximum overpressure changes are usually smaller in the fault-present setting than at the fault-free environment. An exception to this is found at FO station, which presents larger maximum overpressure amplitudes at the fault-present setting for dip angle values between 62° and 65°. This contrast between ambiances also highlights the difference in amplitudes between FO and FM stations when the fault is present. In that case, average peak overpressure inside the fault are smaller than outside the structure.

3.3.1.3.2 Type 2 earthquakes Type 2 earthquakes are generated very close to the main system fault, thus generating more complex patterns in peak overpressure, specially in the stations located at the structure. It also generates larger differences between settings. Fig. 3.19 shows how the larger peak overpressure amplitudes are registered at FO and FM stations, with the former registering the largest peak. For both stations, the largest overpressure amplitude is found for the same dip angle values at which the overpressure change was the largest, as can be seen in Fig. 3.14. Due to the several wave reflections, important differences in maximum overpressure are found between settings. Taking the results from the fault-free setting as a reference, we can see how the maximum overpressure changes are larger at the fault stations, and smaller at the reservoir ones. This suggest that most of the volumetric change induced by the earthquake is concentrated inside the system main fault,

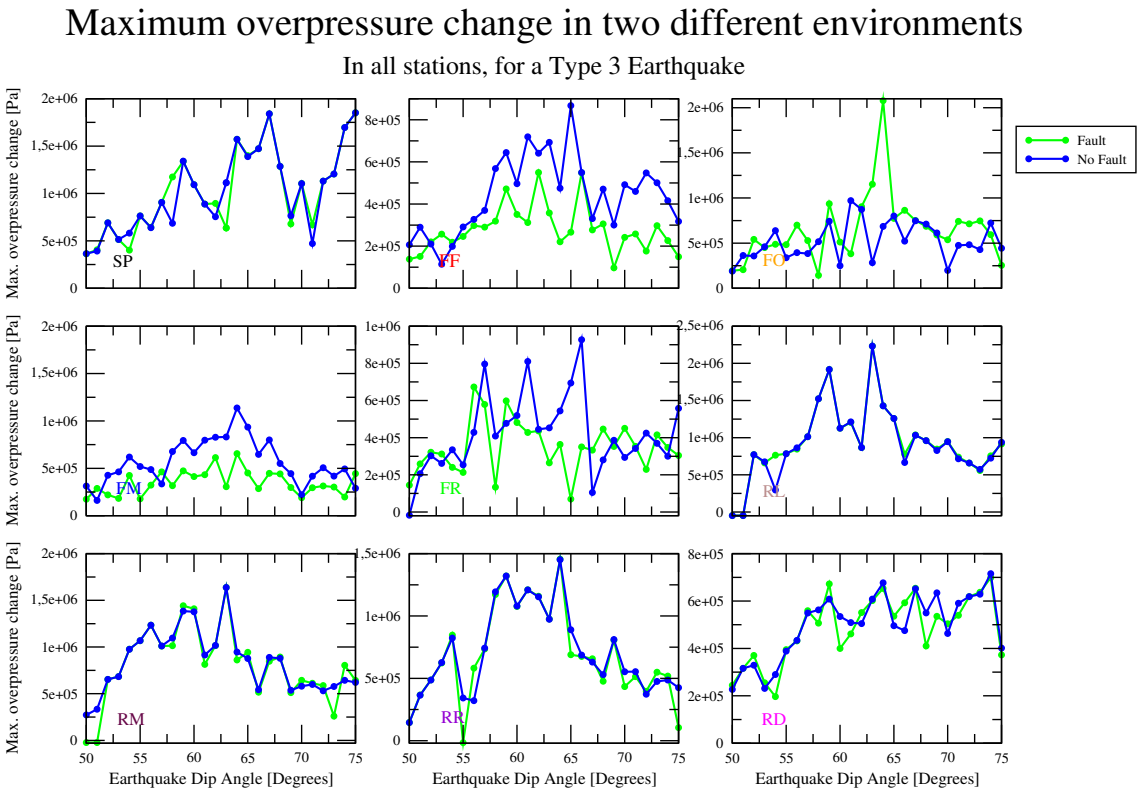

Figure 3.20: Maximum overpressure amplitude for a type 3 earthquake, measured in all stations, as a function of the earthquake dip angle values. We also show a comparison of the results obtained in two settings: the first one does not contain a main fault, and the second does involve this structure. Blue lines show the results in the fault-free environment, and green lines present the results obtained in a fault-present setting.

reducing the influence of the seismic event outside the structure. In terms of values, the larger differences between settings are found in FF and FR stations, which are located at the two edges of the system fault.

3.3.1.3.3 Type 3 earthquakes Type 3 earthquakes are generated close to the bottom-left corner of the space, thus converting them in the most distant events from the system main fault. Fig. 3.20 shows how the maximum induced overpressure values are smaller at the fault stations for this family of earthquakes than for the other two we have introduced. One more time, and due to reflections at the fluid reservoir, patterns are complex. Nevertheless, the larger peaks are found mostly in the $55^o - 65^o$ dip angle band for all stations but SP and RD, which is located at the right hand side of the fluid reservoir.
Differences between settings are most noticeable at the fault stations, where the common trend is to have larger overpressure peaks in a fault-free setting. However, this is not true for FO station, located right outside the fault. The maximum overpressure values at that station are consistently higher in the fault-present environment than in the fault-free setting, specially after a 62^o dip angle value.
In the fault-present setting, the difference in the results recorded at FO and FM

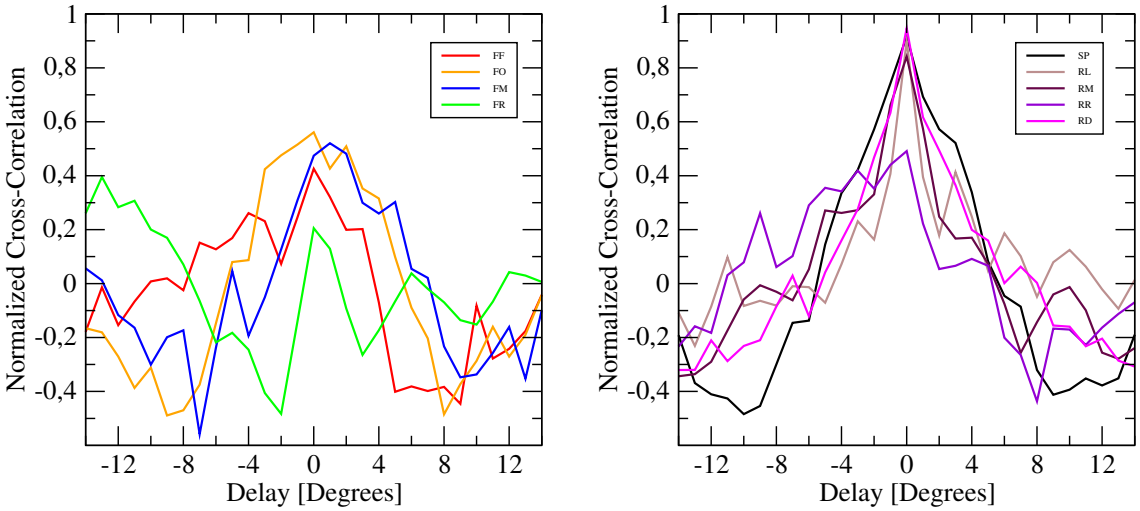

Figure 3.21: Normalized cross correlation between the maximum overpressure amplitude vs dip angle series obtained in two different settings, for type 1 earthquakes.

stations also highlights a strong difference in two neighboring recording points, which is due to the existence of the system main fault. This steep contrast between them, which can be as high as a more than 4 times larger at FO station when compared with the FM observations, highlights a "breakwater" effect on wave motion, which is reflected in this abrupt overpressure change.

3.3.1.4 Cross correlation in maximum overpressure amplitudes

Cross correlation analysis between Amplitude/Dip angle series for both settings is a good technique to compare how similar they are. Due to the intricacy of the patterns obtained in our study, this technique is particularly useful to determine the degree of complexity in wave propagation, as well as it is helpful to isolate the role of local structures, such as the fluid reservoir and the system main fault. Figs. 3.21, 3.22, and 3.23 show the normalized cross correlation for the three earthquake types, as a function of a delay D, defined by

$$r(D) = \frac{1}{N} \frac{\sum_t [(f(t) - \bar{f})(g(t - D) - \bar{g})]}{\sigma_f \sigma_g}, \tag{3.39}$$

where $f(t)$ and $g(t)$ are the series. The series averages are given by $\bar{f}$ and $\bar{g}$. N is the total number of data points, and σ_f with σ_g are the standard variations of each function.

For type 1 earthquakes, all space and reservoir stations show a maximum cross-correlation near to 1 at zero delay, meaning that the maximum amplitude vs dip angle timeseries are very similar between the studied settings. Results in fault region stations shows otherwise, with lower correlations being the norm, and even finding anti-correlations almost as high, in absolute value, to the highest cross correlation values. FR station is the one that presents the largest differences between maximum overpressure amplitude/dip angle timeseries.

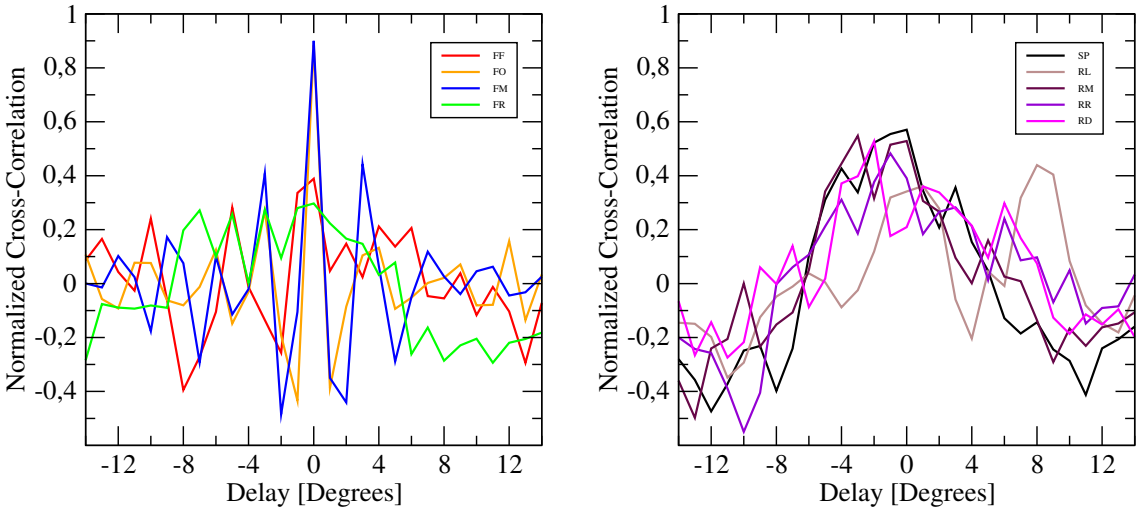

Figure 3.22: Normalized cross correlation coefficient between the maximum overpressure amplitude vs dip angle timeseries induced by type 2 earthquakes, in two settings: fault-present, and fault-free.

Higher similarities between settings, for type 2 earthquakes, are found at zero delay, as can be appreciated in Fig. 3.22. Our results also highlight low correlation values for all stations but Fault Out and Fault Mid stations. These stations get this high similarity between settings because of their relative position respective to the system fault. Interestingly, the rest of the stations located at the fault area recorded much lower correlation values than reservoir stations, meaning that the larges discrepancies between settings are found in the near field of the earthquakes.
The cross correlation for type 3 earthquakes highlights a maximum value close to 1 for all space and reservoir stations. Our results show that the larger difference between settings is found at the fault stations, with FM and FF stations being the ones with less differences between environments.

3.3.1.5 Maximum cross correlation in overpressure timeseries

Our results show that the local structures do play a role in both static and dynamic overpressure changes at the system. Comparisons between a fault-present and a fault-free setting unveil a more complex role of these structures, mostly due to alterations in wave motion due to wave reflections and refractions on them. While we already studied the peak overpressure values during the passing of the seismic waves, we do not know for sure if the influence of the local structures affects only at the maximum amplitudes or to the whole waveform. Cross correlation analysis of the overpressure timeseries at each one of the stations can shed some light on the dynamic role of fluid reservoir and the main fault of the system.
To be able to perform a proper cross-correlation analysis for all our earthquakes, we use Eq. 3.39 to calculate the cross correlation between two overpressure timeseries, for the same earthquake and station but in two different settings, as a function of a delay D. We then obtain the maximum correlation value, which depends on the

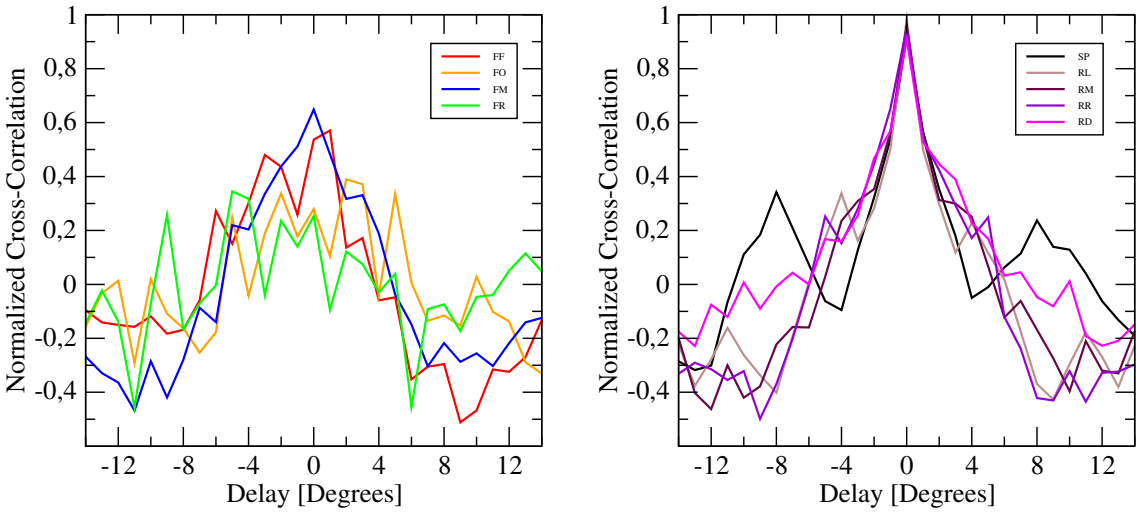

Figure 3.23: Normalized cross correlation coefficient between maximum overpressure amplitude vs dip angle timeseries, measured at both fault-free and fault-present settings, for type 3 earthquakes.

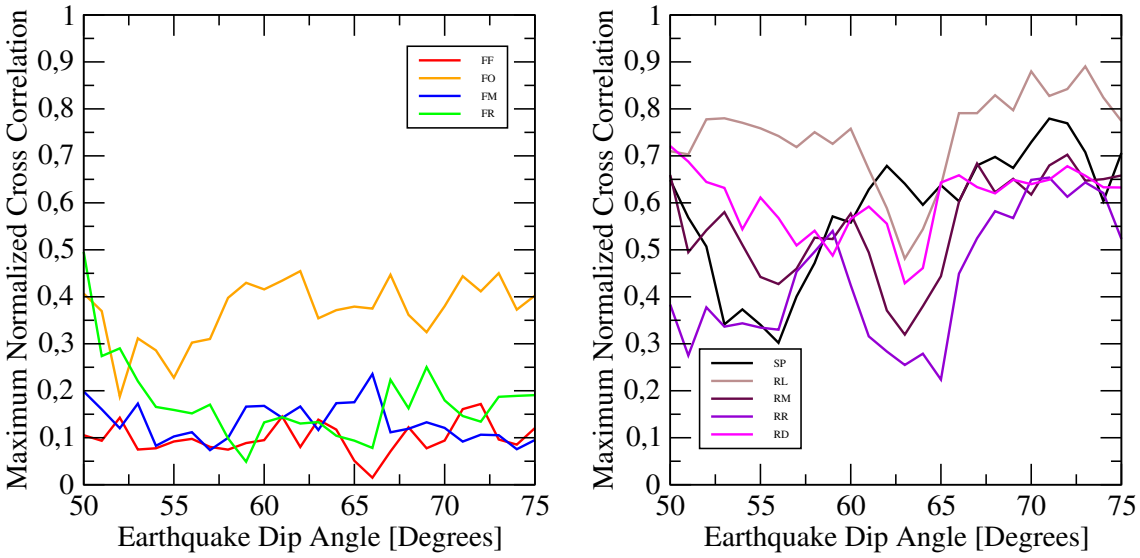

Figure 3.24: Maximum cross correlation value obtained between overpressure waveforms generated by type 1 earthquakes, in two different settings: fault-present and fault-free. The maximum coefficient value is presented in all the stations, as a function of the earthquake dip angle. The plot located to the left presents the results recorded at the fault stations, while the right-hand side plot shows the values obtained in the remaining stations.

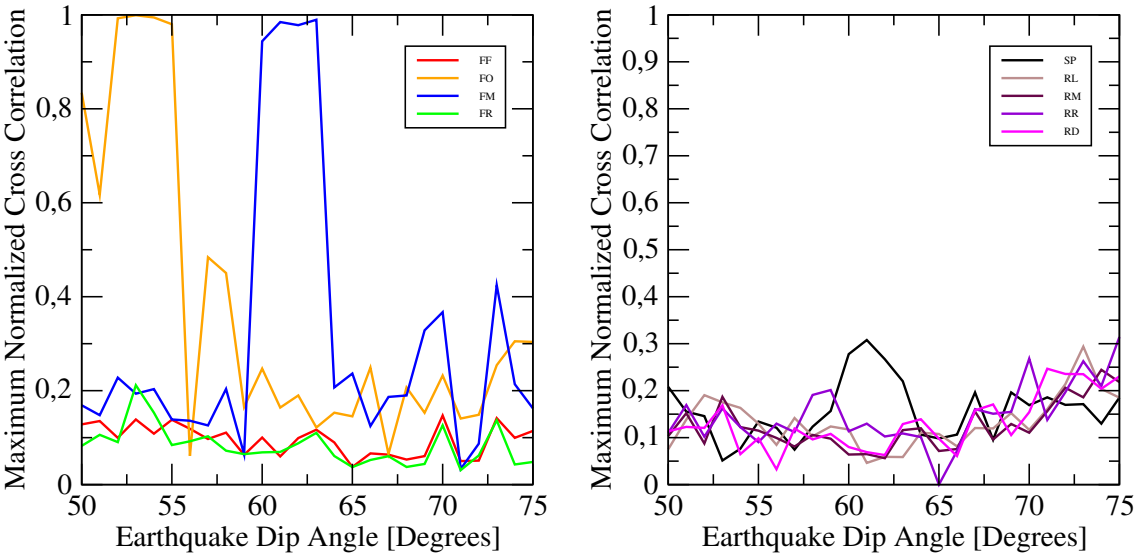

Figure 3.25: Maximum cross correlation value for the dynamic overpressure timeseries measured at a fault-free and a fault-present setting, for type 2 earthquakes. Maximum correlation value is presented in all stations, as a function of dip angle value of the seismic event. Left hand side plot shows the results recorded in fault zone stations, while right-hand side plot shows the values obtained in the remaining recording spots.

earthquake dip angle.

Fig. 3.24 shows the maximum cross correlation value for type 1 earthquakes, as a function of the dip angle. The first important feature is that the lower correlation values are recorded in fault stations. Out of those, Fault Out station, which is located just outside the local structure, records the highest values, with a relatively flat dependence on the dip angle value. On the other hand, larger similarities between settings are obtained in space and reservoir stations. Res Right station has correlation values comparable to the ones of the fault stations, though. This might be due to reflections with the system fault, and with a "barrier" effect the fault might have on wave propagation, due to the relative position of the station and the earthquake rupture. It is also very interesting how the largest differences between settings recorded at the reservoir stations are found between 60º and 65º, in particular when it is considered the inclination angle of the fault, that is 60º.

The same analysis for type 2 earthquakes is presented in Fig. 3.25. Cross correlation patterns are radically different to the ones of type 1 events. Low correlations are the norm here, most likely due to wave reflections in the main fault, which is the place in which the earthquake epicenter is located. The exception comes from Fault Mid and Fault Out stations, which are closer to the earthquake rupture. The highest correlation values for these stations are closer to 1, and are present in the same dip angle range as the higher overpressure changes presented in Fig. 3.14. This is due to the closeness of the stations to the earthquake rupture zone.

The effect of wave reflections and how they affect dynamic stress transfer is also noticeable in space station, which is located away from the local structures of the system and should, therefore, present higher correlation values. This is not true for

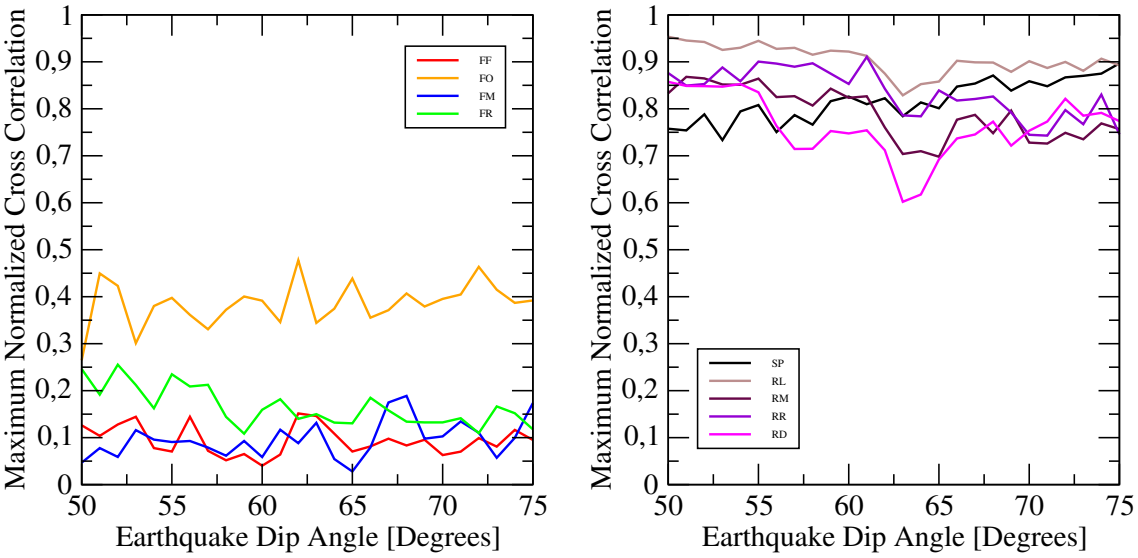

Figure 3.26: Maximum cross correlation value obtained between dynamic overpressure timeseries, measured in all the stations, for a type 3 earthquake, in a fault-free and a fault-present setting. Results are plotted as functions of the dip angle value. Left hand plot shows the results recorded in fault zone stations, whilst the right-hand side plot presents the values obtained in the remaining recording locations.

type 2 earthquakes, possibly due to the location of the rupture zone, which promotes inner reflections in the fault, and affects the wave motion.
Fig. 3.26 shows the maximum cross correlation value for overpressure timeseries at the same station, but for different settings, as a function of the earthquake dip angle, for type 3 events. Just as with type 1 earthquakes, lower correlation values are present in the stations located in the main fault zone, with FO station featuring the larger similarities between settings. Reservoir and space stations, on the other hand, present high maximum cross correlation values, with a small dependence on the earthquake dip angle. These observations are indicative of the role the system main fault has on wave propagation, altering not only the maximum overpressure amplitude, but also the whole waveform. This effect does not seem to depend strongly on the value of the earthquake dip angle.

3.3.1.6 Dynamic Energy Transfer

We also studied the kinetic energy density at the system, which gives us an idea of what parts of the system are more affected by the incoming waves of an earthquake. Energy density here is defined as

$$\varepsilon = \frac{1}{2}\rho(v_x^2 + v_z^2) \ , \tag{3.40}$$

with ρ the density of the elastic space.
Fig. 3.27 presents the results for type 1 earthquakes. The effect of the main structures of the system is clearly noticeable here. Reflections and refractions at the fluid reservoir are visible for all the dip angle values of the incoming earthquakes, with

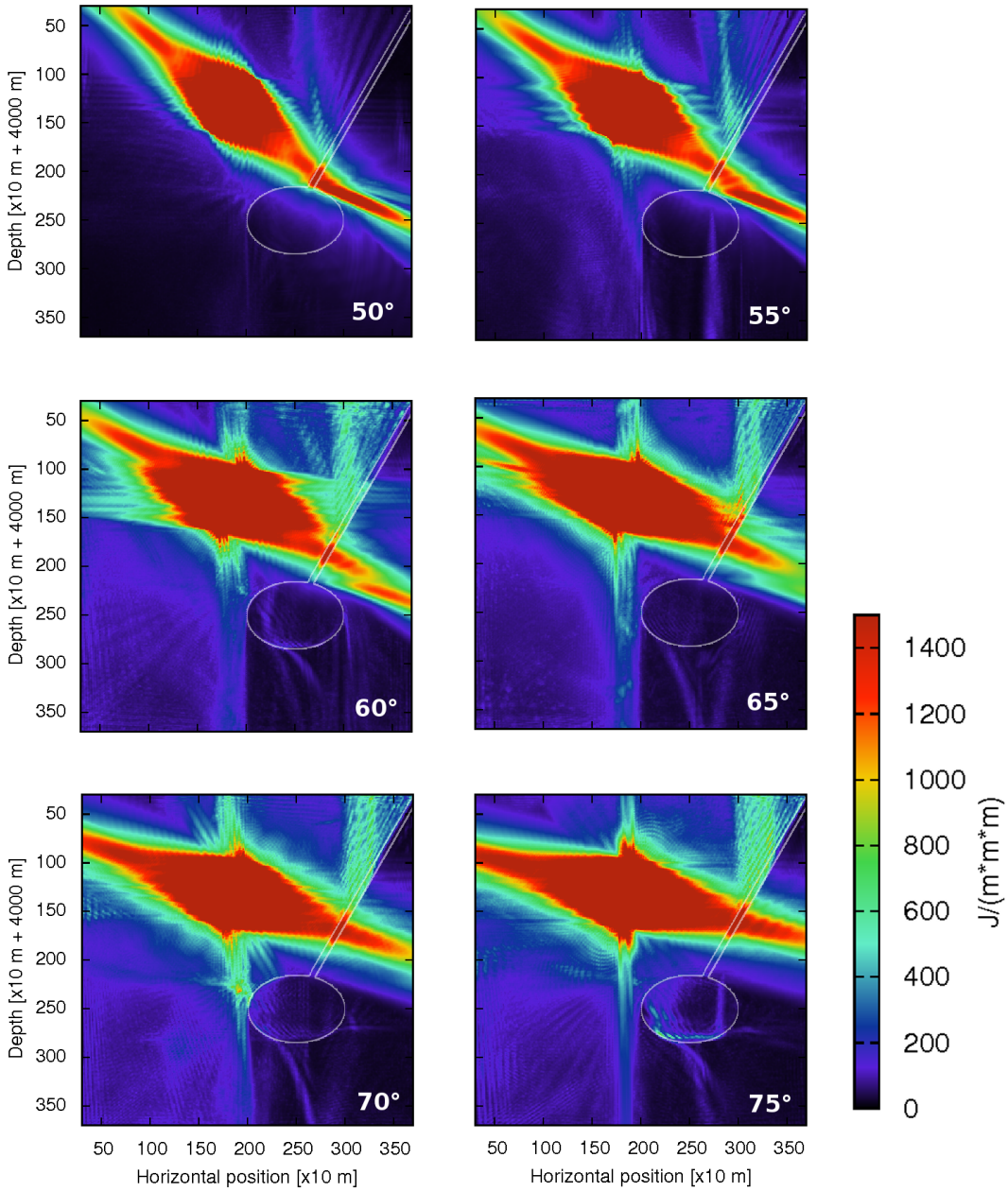

Figure 3.27: Maximum energy density for type 1 earthquakes, plotted for several dip angle values, in a fault-present environment. Both fluid reservoir and system main fault are sketched, and are also visible in the maps, which emphasizes their role in wave motion.

most of the wave energy being reflected at low dip angle values, such as 50º. When kinetic energy is transferred into the reservoir, internal reflections at this structure are also a predominant feature, as it does create some energy concentration zones at its borders. This effect allows us to discern the shape of the reservoir in these energy density maps, and it is particularly noticeable for a dip angle value of 75º.

The system main fault also plays an important role in energy distribution. When comparing the maximum energy density maps in a fault-present setting, just presented in Fig. 3.27, with the maps of the same physical quantity in a fault-free environment, which are presented in Fig. 3.28, the role of this structure is unveiled. Reflections of the incoming waves on its left border creates an energy concentration region between the earthquake rupture zone and the structure, but it also prevents the right hand side of the fault to receive part of the kinetic energy from the seismic event. This is most noticeable when the earthquake dip angle is equal or close to the inclination angle of the main fault, which is 60º. This "breakwater effect" of the system fault is not visible in the results from a fault-free environment, due to the absence of the structure. Energy density is also concentrated inside the main fault, with the size of this region being correlated with the size of the higher energy zones from the earthquake.

Fig. 3.29 presents the respective results for type 2 earthquakes. While the "breakwater" effect of the system main fault is noticeable with the creation of high energy zones between the earthquake rupture and the system structure, the most remarkable feature is the energy concentration inside it. This effect is particularly noticeable for dip angles between 60º and 65º, and the energy is mostly captured inside the structure, as it is evidenced by the low energy areas outside it. For larger dip angle values, the fault keeps concentrating the energy, but more complex patterns are found outside it, possibly related to reflections at the fault.

The role of the main system fault can be more clearly appreciated after comparing the results on a fault-present system with the results on a fault-free setting, which are presented in Fig. 3.30. here, distortions in spatial energy density patterns are due to the presence of the fluid reservoir, whose boundaries are visible due to the reflections at it. Some energy is also concentrated in the right-hand boundary of the reservoir. The strong difference between settings unveil a waveguide behavior from the system main fault, as energy is concentrated inside it but, due to internal reflections, only a little fraction of this energy is released outside the structure.

Energy transfer for type 3 earthquakes is somewhat similar to the one registered for type 1 perturbations. Fig. 3.31 shows high energy regions at the left reservoir boundary, and at the left hand side of the system main fault. The breakwater-like features of the fault are also noticeable, with lower energy regions at the right hand side of the structure.

The comparison with a fault-free setting is found when studying the results of Fig. 3.32. There, wave motion is distorted by the presence of the fluid reservoir, an effect that is more noticeable for higher dip angle values. We do not see anomalies in energy transfer on top of this structure, in the way we appreciate them in the fault-present system.

Figs. 3.33, 3.34 and 3.35 present the maximum energy density as function of the

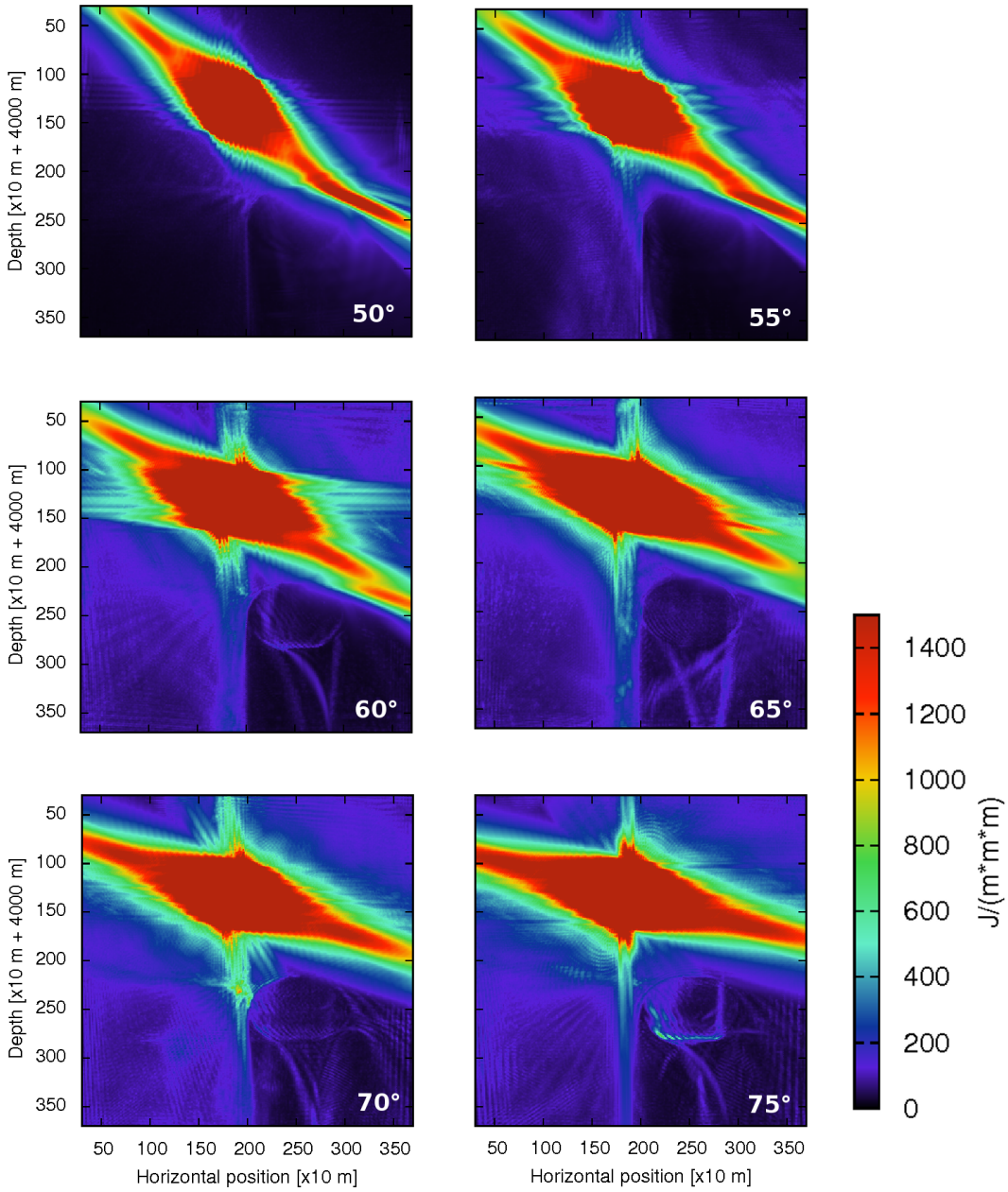

Figure 3.28: Maximum energy density for type 1 earthquakes, plotted for several dip angle values, in a fault-free environment. The absence of the system fault is clearly marked as the only visible structure is the fluid reservoir.

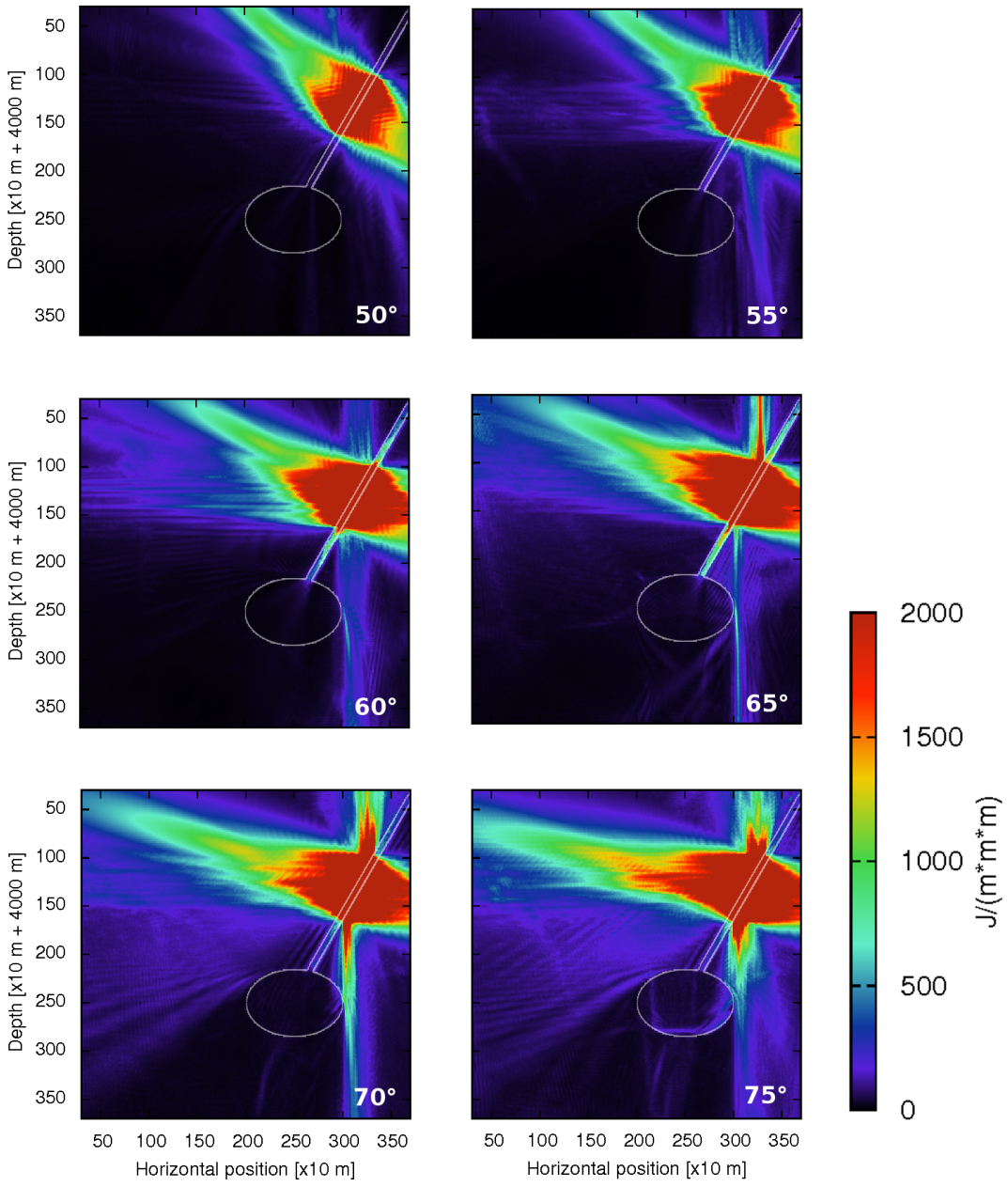

Figure 3.29: Maximum energy density for type 2 earthquakes, measured for several dip angle values. Both fluid reservoir and system main fault are sketched. Note how energy is concentrated inside the fault for dip angle values close to the main fault inclination angle, which is 60°, without too much energy concentration outside the structure, resembling the behavior of a fiber optic light cable.

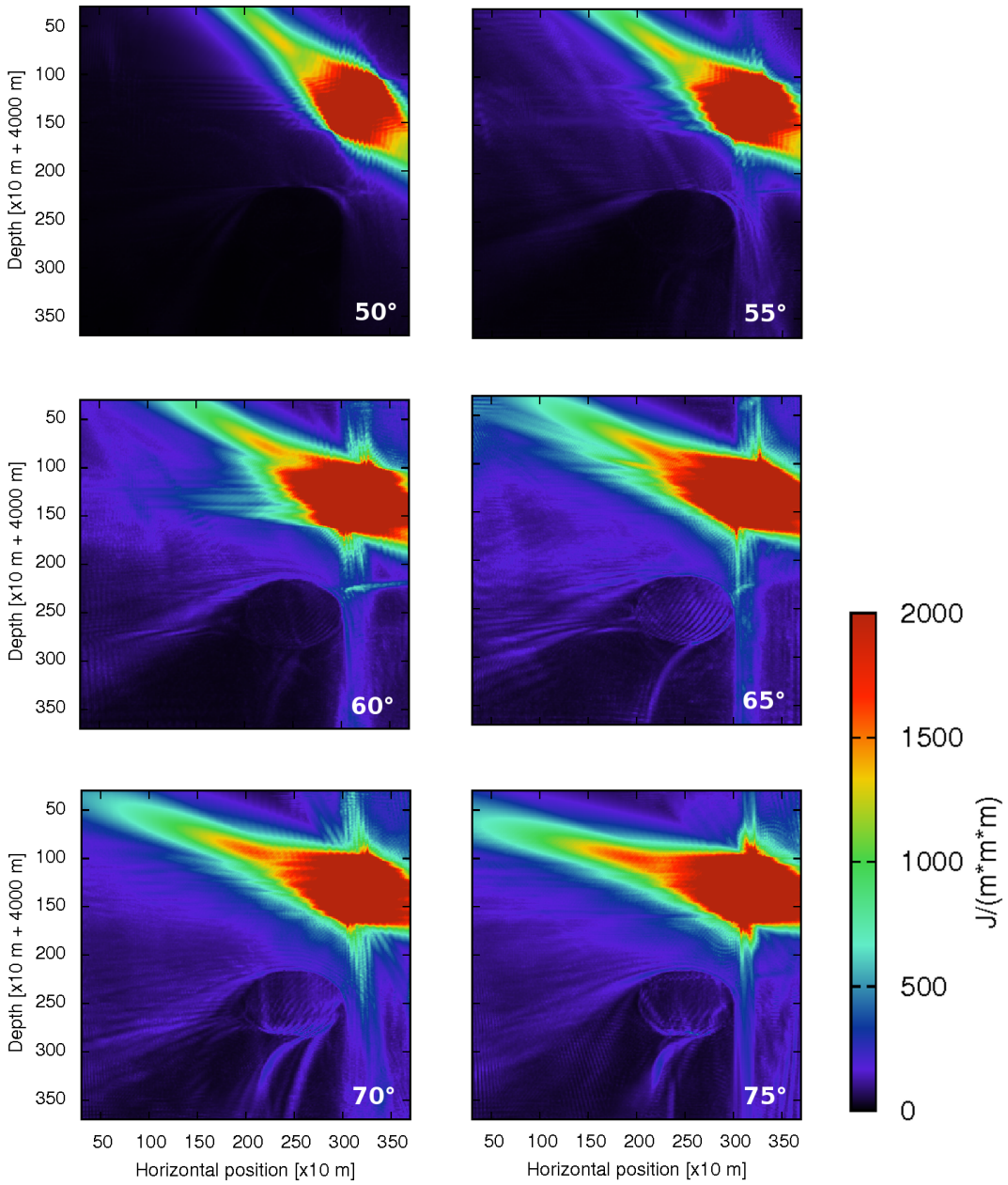

Figure 3.30: Maximum energy density for type 2 earthquakes, measured for several dip angle values, in a fault-free setting. Reflections at the fluid reservoir are noticeable, as they alter the energy density spatial patterns.

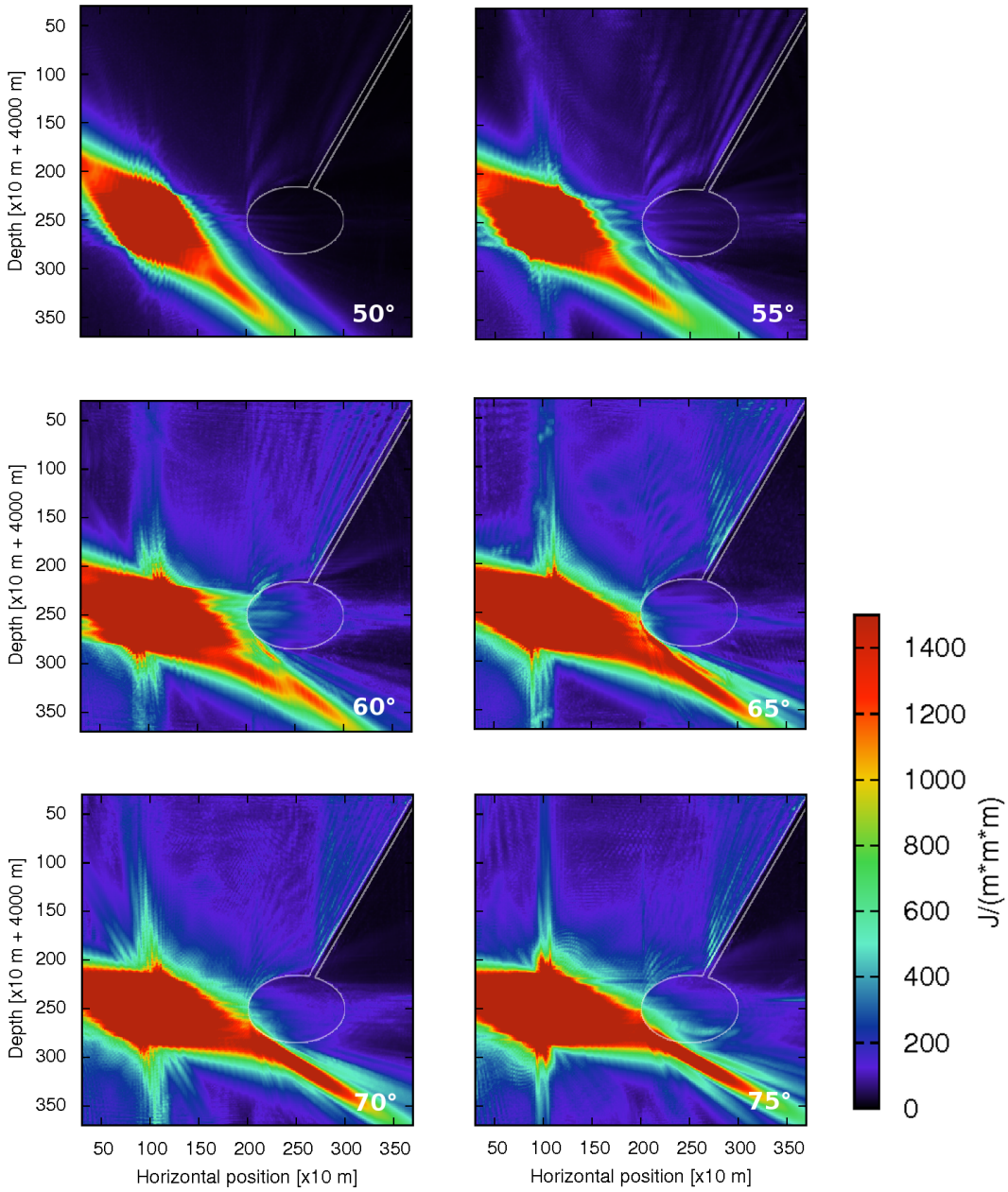

Figure 3.31: Maximum energy density for type 3 earthquakes, measured at several dip angle values, in a fault-present setting. Both reservoir and main fault are visible here, due to wave reflections in these structures.

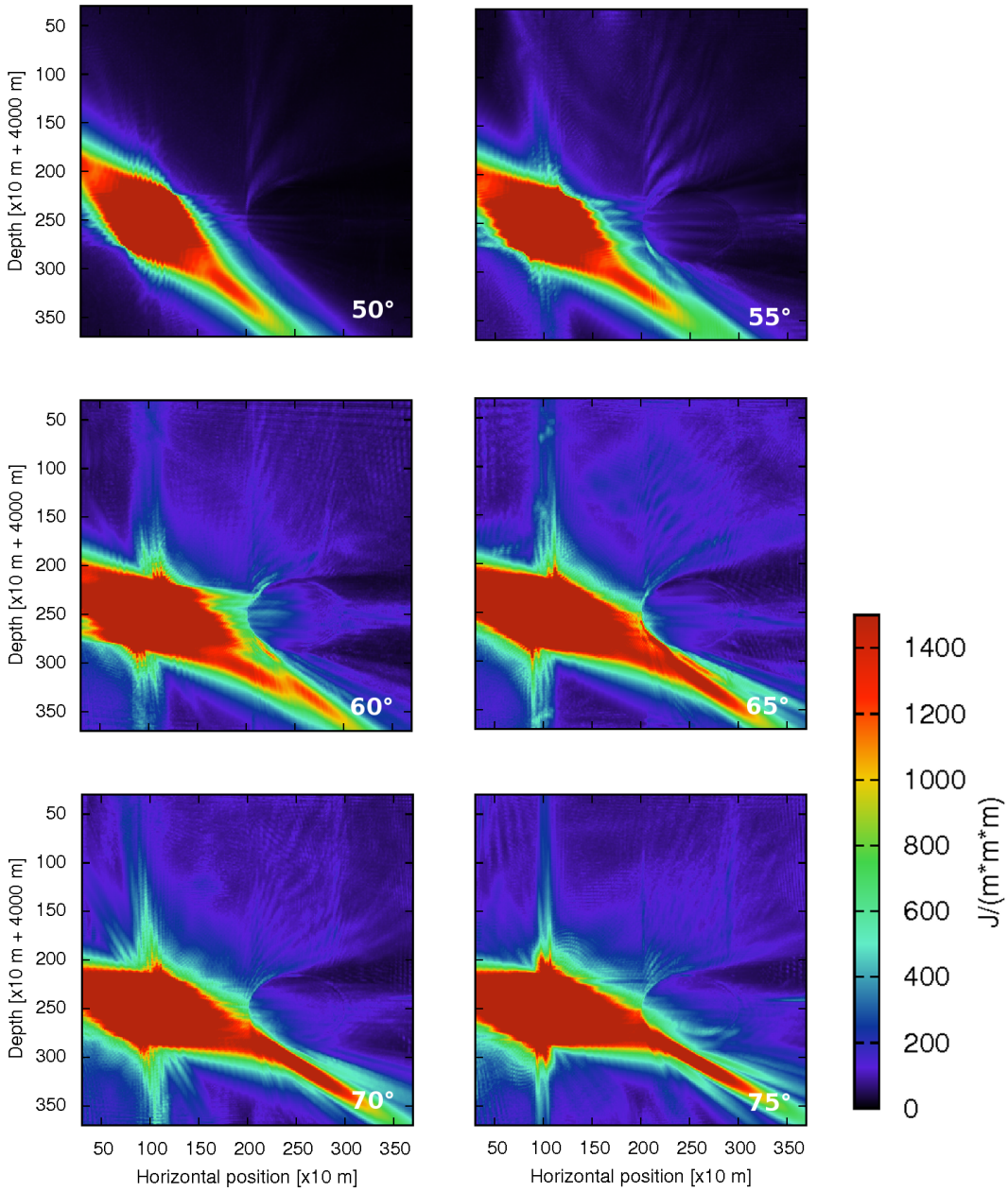

Figure 3.32: Maximum energy density for type 3 earthquakes, measured at several dip angle values, in a fault-free setting. Reflections at the fluid reservoir alter the wave motion, creating high energy regions at its boundaries.

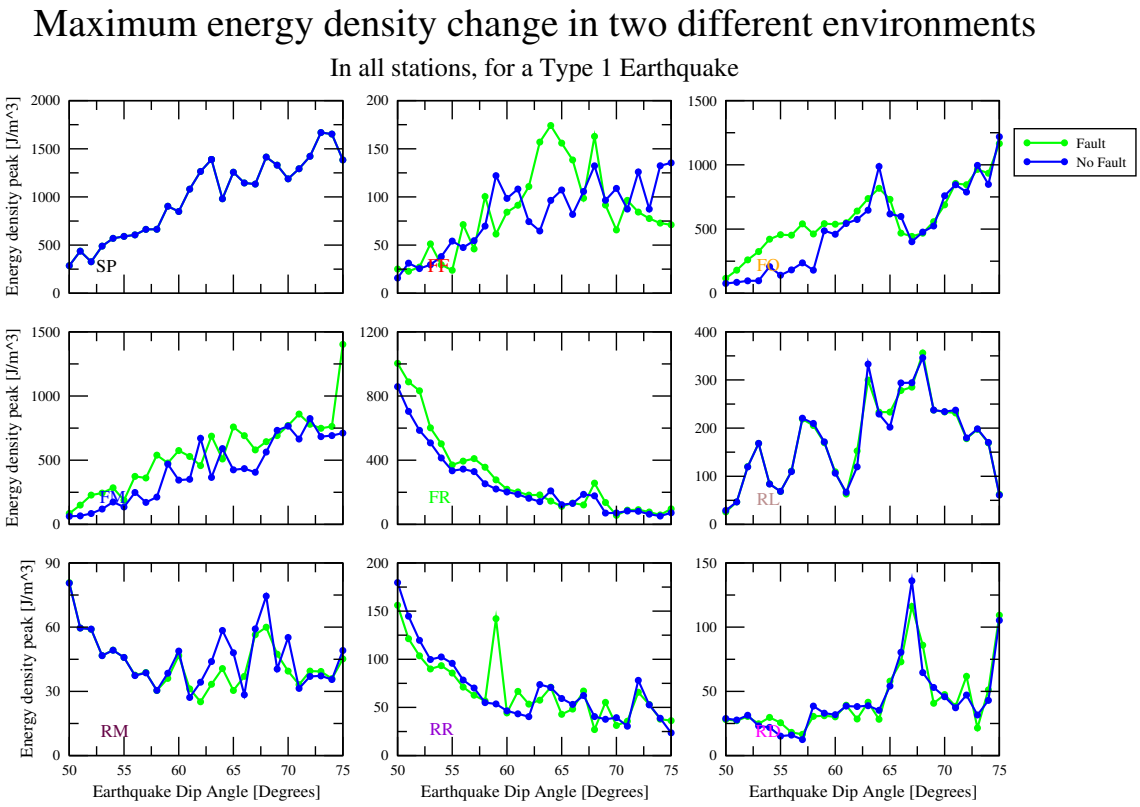

Figure 3.33: Maximum energy density as a function of the earthquake dip angle, for type 1 earthquakes, in all stations. Two lines are plotted in each station, corresponding to the results obtained at two different settings: fault-present and fault-free.

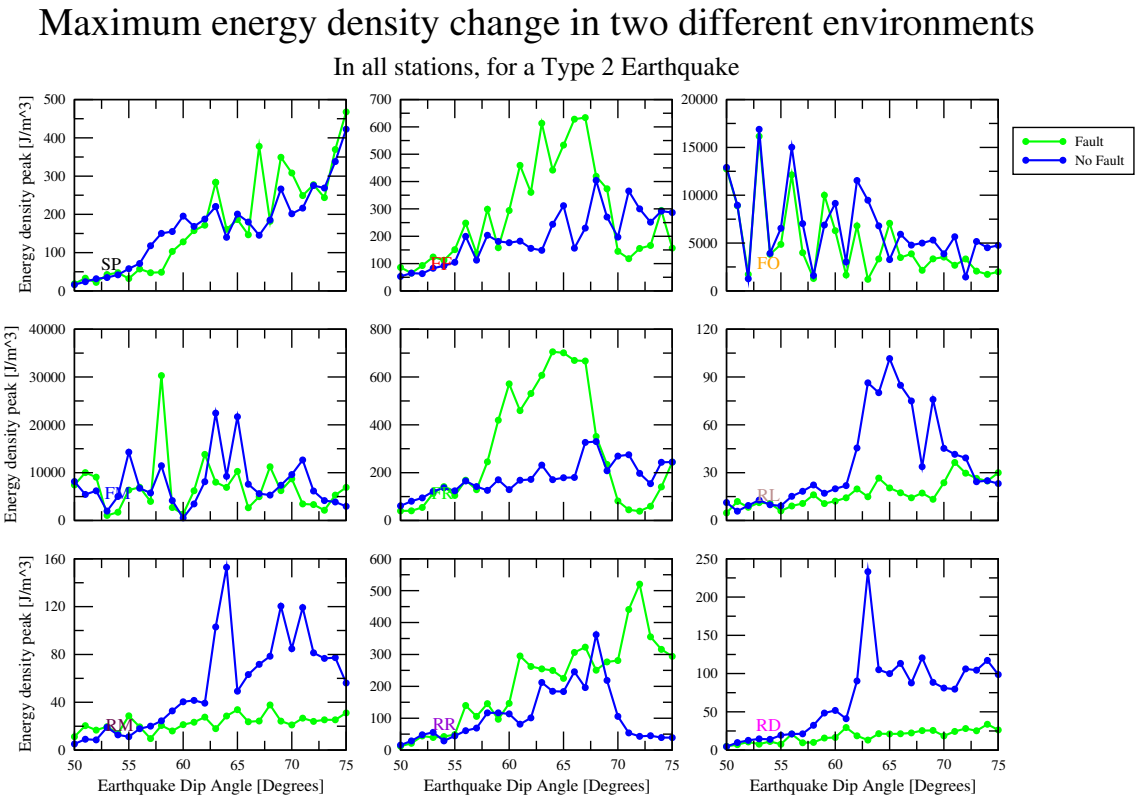

Figure 3.34: Maximum energy density as a function of the earthquake dip angle, for type 2 earthquakes, in all stations. Two lines are plotted in each station, corresponding to the results obtained at two different settings: fault-present and fault-free. Important differences between environments are found at FF and FR stations, located at the edges of the system fault.

dip angle at each station, for two settings: fault-present and fault-free. Type 1 earthquakes present the larger energy density values at SP, FR, FO, and FM stations, mainly due to the radiation pattern of the earthquake and the reflections on top of the fluid reservoir. Difference between settings for this earthquake family are found in the fault zone stations, with larger energy values in the fault-present environment, with the exception of FF station, which has similar values except for dip angles between 66° and 69°. There, energy density peaks are larger in the fault-present system. The breakwater effect of the fault is appreciated in the FO station, in particular for lower dip angle values.

Type 2 earthquakes show important differences between settings, being more important at FF and FR stations, where the maximum energy density is considerably larger when the system main fault is present. This effect is particularly important for dip angle values between 55° and 75°, and it is an evidence of an energy concentration at this structure, which is in agreement with what was presented in Fig. 3.29. Results of the stations located outside the main system fault show how energy concentration is usually lower in the fault-present setting than in the fault-free environment, which reinforces the energy concentration effect inside the fault, preventing the rest of the space to move as strongly as when the main fault is not present.

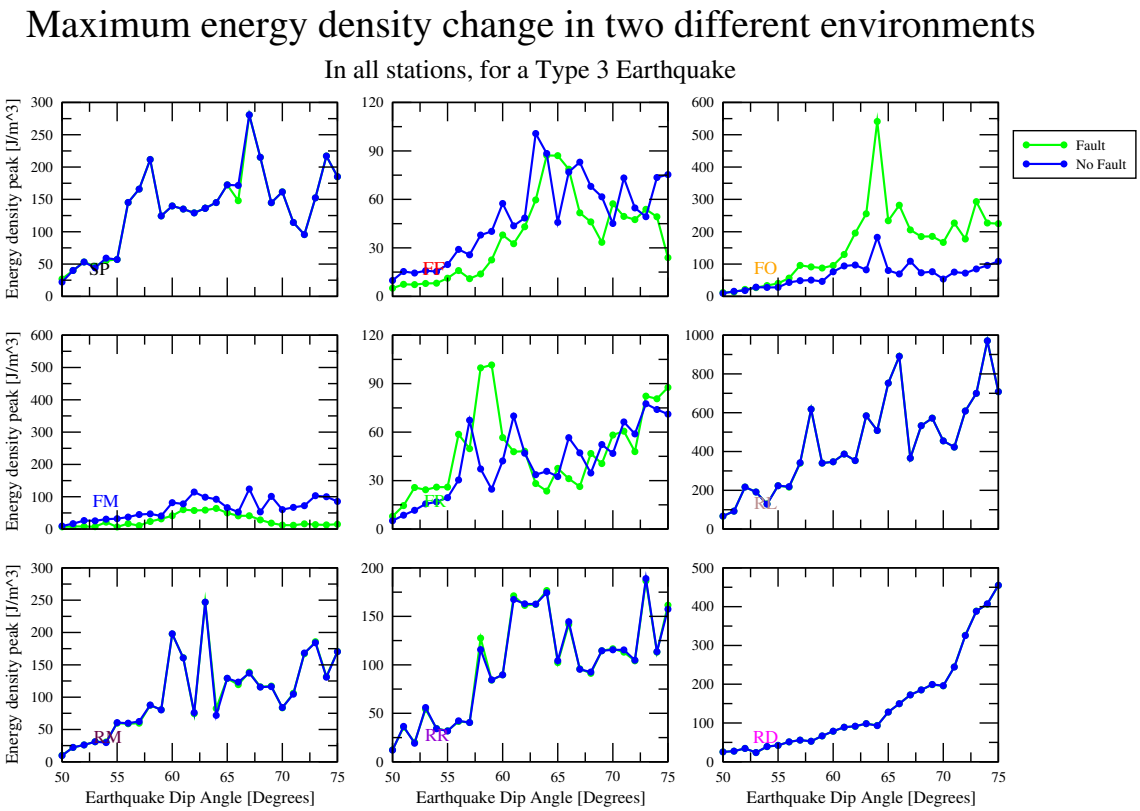

Figure 3.35: Maximum energy density as a function of the earthquake dip angle, for type 3 earthquakes, in all stations. Results obtained at the fault-present setting are plotted with a green line, whilst the blue line presents the results measures in a fault-free system. Larger energy density amplitudes are found at reservoir and space stations, but the differences between settings are present at the fault zone stations.

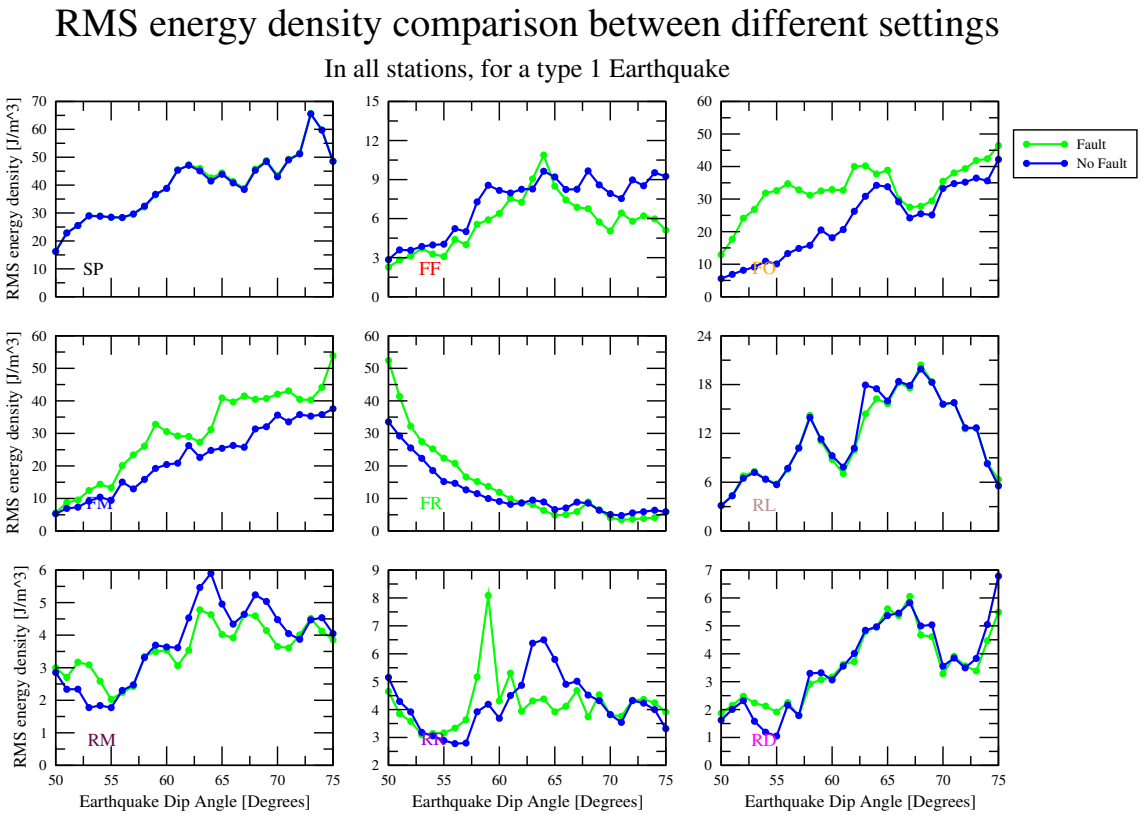

Figure 3.36: Root mean square energy density for type 1 earthquakes as a function of earthquake dip angle, recorded at the all the stations, in two different settings. Smoother patterns are found here, but they are closely correlated with the maximum energy density results. Larger differences between settings are present at the fault stations.

Differences between settings for type 3 earthquakes are mostly noticeable at the stations located at the fault zone region. The breakwater effect of the main fault is evidenced when looking at the contrast between FO and FM stations, with FO recording the larger energy peaks, in particular for larger dip angle values. A more complex comparison is found at FR station, where for some earthquake dip angles the energy concentration is larger when the fault is present, with the opposite occurring at other values of the dip.
While the maximum energy density value gives information about the amplitude of the motion, root mean square energy density value gives an idea of how much kinetic energy is transferred in the system. It is defined as

$$\varepsilon_{\mathrm{RMS}} = \sqrt{\frac{1}{T}\int \varepsilon^2(t)dt}\,, \tag{3.41}$$

with T the total time of the waveform, and $\epsilon(t)$ the kinetic energy density, given by Eq. 3.40.
Figs. 3.36, 3.37, and 3.38 present $\varepsilon_{\mathrm{RMS}}$ in all stations, contrasting the results in out two studied settings, for all types of earthquakes. For type 1 earthquakes, $\varepsilon_{\mathrm{RMS}}$ vs dip angle patterns have a certain level of correlation to the ones obtained for the

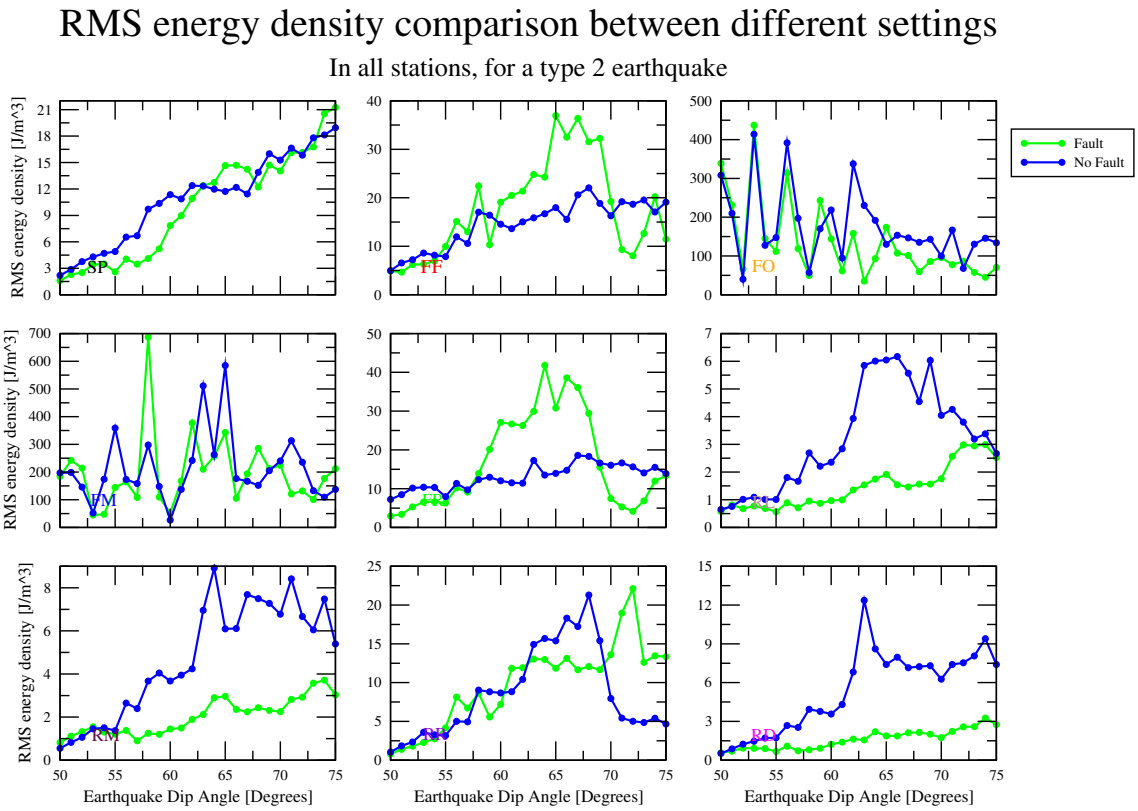

Figure 3.37: Root mean square energy density for type 2 earthquakes as a function of earthquake dip angle. in two different settings. We present our results at each recording point, highlighting an energy concentration at the stations located to the borders of the system main fault that is only found for certain dip angle values in a fault-present system.

maximum energy density vs dip angle value, presented in Fig. 3.33, with similar differences found between settings. This reinforces the idea of the system fault having breakwater like features, which are not only related to the maximum energy amplitudes, but to the whole wave motion, that is sustained with time. We can also see the energy concentration inside the main fault, particularly in FR and FM stations.

Type 2 earthquake results for $\varepsilon_{\mathrm{RMS}}$ at the fault stations are also correlated with the maximum energy density, but in this case differences between settings are more pronounced, which shows that there is significant differences in the recorded waveforms at the same station between two different environments. Major differences between settings are recorded at FF and FR stations, which are the ones located at the edges of the main system fault, and they reinforce the idea of a energy concentration in the structure, which is sustained on time.

The $\varepsilon_{\mathrm{RMS}}$ vs dip angle patterns for type 3 earthquakes are correlated with the patterns for maximum energy density vs dip angle presented in Fig. 3.38, but once again the differences between settings are more pronounced in this case. This is particularly noticeable at the stations located inside the fault (FF, FM, and FR), which have a $\varepsilon_{\mathrm{RMS}}$ value that can be as a low as only half of the value obtained in a

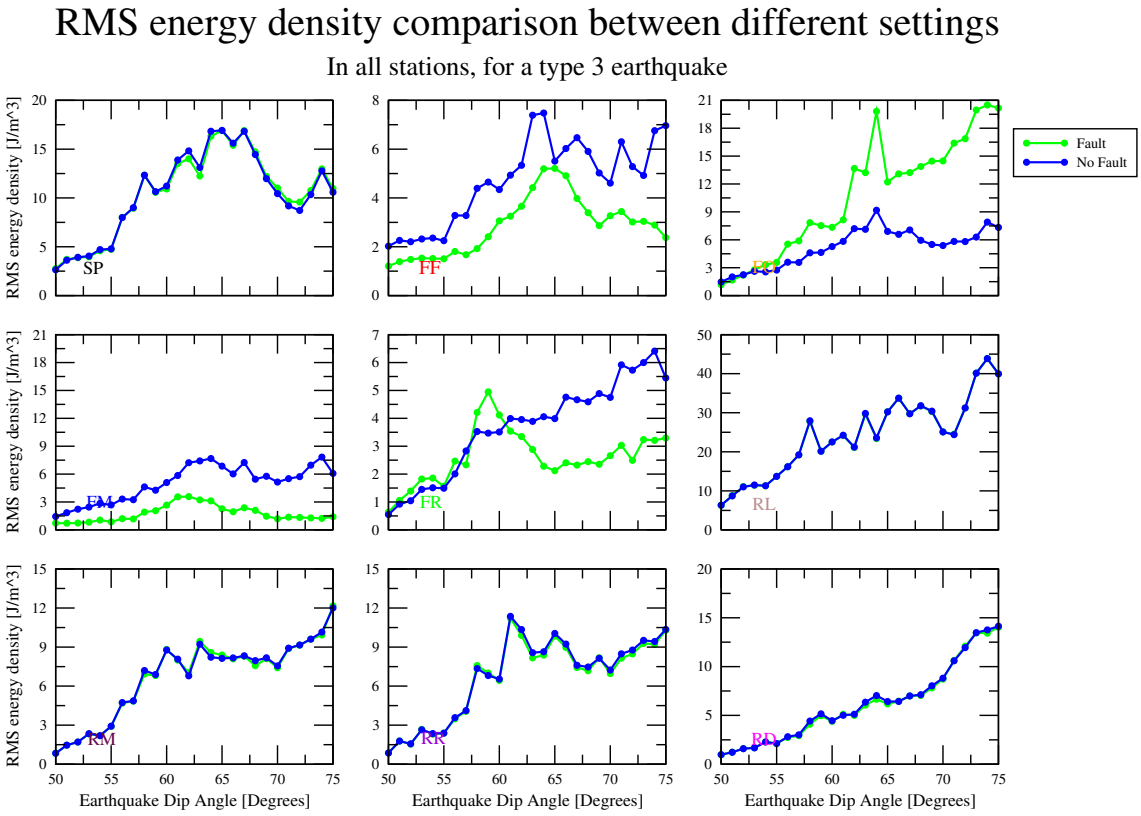

Figure 3.38: Root mean square energy density for type 3 earthquakes as a function of earthquake dip angle, recorded at the all the stations, in two different settings. Results highlight a larger energy concentration right outside the main system alignment at the fault-present system, as can be noticed when comparing the curves plotted at the fault region stations.

fault-free setting. The breakwater effect of the fault is also more pronounced, with an important difference between the results in FO and FM stations.

3.3.1.7 Yield function change

During the passage of the seismic waves, the local value of the Coulomb yield function changes in the whole space, and under certain conditions it can be greater than zero, which is a condition for failure at that point. Therefore, the study of the dynamic change of the yield function provides us with a tool to understand which are the regions of our system that are most likely to break due to the effect of the incoming earthquake waves.
We consider the Coulomb yield function as the sum of two contributions: the one of the base part of the system, corresponding to the long term initial stresses and their interaction with the local structures, and a wave-related contribution, which is due the interaction between the seismic waves with the system. Therefore, we write the Coulomb yield function as

$$f_{\text{yield}}(t) = f_{\text{yield}}^{(\text{base})}(t) + f_{\text{yield}}^{(\text{wave})}(t)\,, \tag{3.42}$$

with the condition that yield occurs when $f_{\text{yield}}(t) \geq 0$. For our dynamic study, we want to look at the largest possible changes of the $f_{\text{yield}}^{(\text{wave})}(t)$ term, as it gives us the information on what regions of space are more likely to fault during the earthquake. Figs. 3.39, 3.40, and 3.41 show several maps of the maximum value of $f_{\text{yield}}^{(\text{wave})}$, obtained for the three earthquake families under study. Maps are made for six different dip angle values, and they were all calculated in a fault-present setting. A common feature for all the experiments is the existence of an interaction between the seismic waves and the system structures which generate higher values for the dynamic part of the yield function at them, as well as in their vicinity.
Due to the relative position of the earthquake rupture zones, type 1 earthquakes induce important changes in the yield function at lower section of the system main fault, with particularly high values near its border with the fluid reservoir, thus converting this region in space the most likely to break because of the influence of the incoming earthquake. This feature is particularly present for lower dip angle values. The breakwater-like characteristics of the fault are also present, as higher yield function values are found on its left border, due to wave reflections at the structure. This contrasts with the low yield value region located at the right hand side of the fault, which emphasizes the shield features it does have. Another interesting feature is the reduction of the maximum change in the yield function inside the fault, which is not correlated with what was found in the energy density transfer, presented in Fig. 3.27.
The largest earthquake-structure interaction for type 2 events is found at the system main fault which, depending on the dip angle value of the incoming earthquake, concentrate the higher yield function values. The interaction is very interesting: while at a 50° angle both reservoir and fault are regions of low values for $f_{\text{yield}}^{(\text{wave})}$, this does change when the dip angle increases, reaching a point in which high and almost uniform values for $f_{\text{yield}}^{(\text{wave})}$ are found inside the main fault. This last effect, which

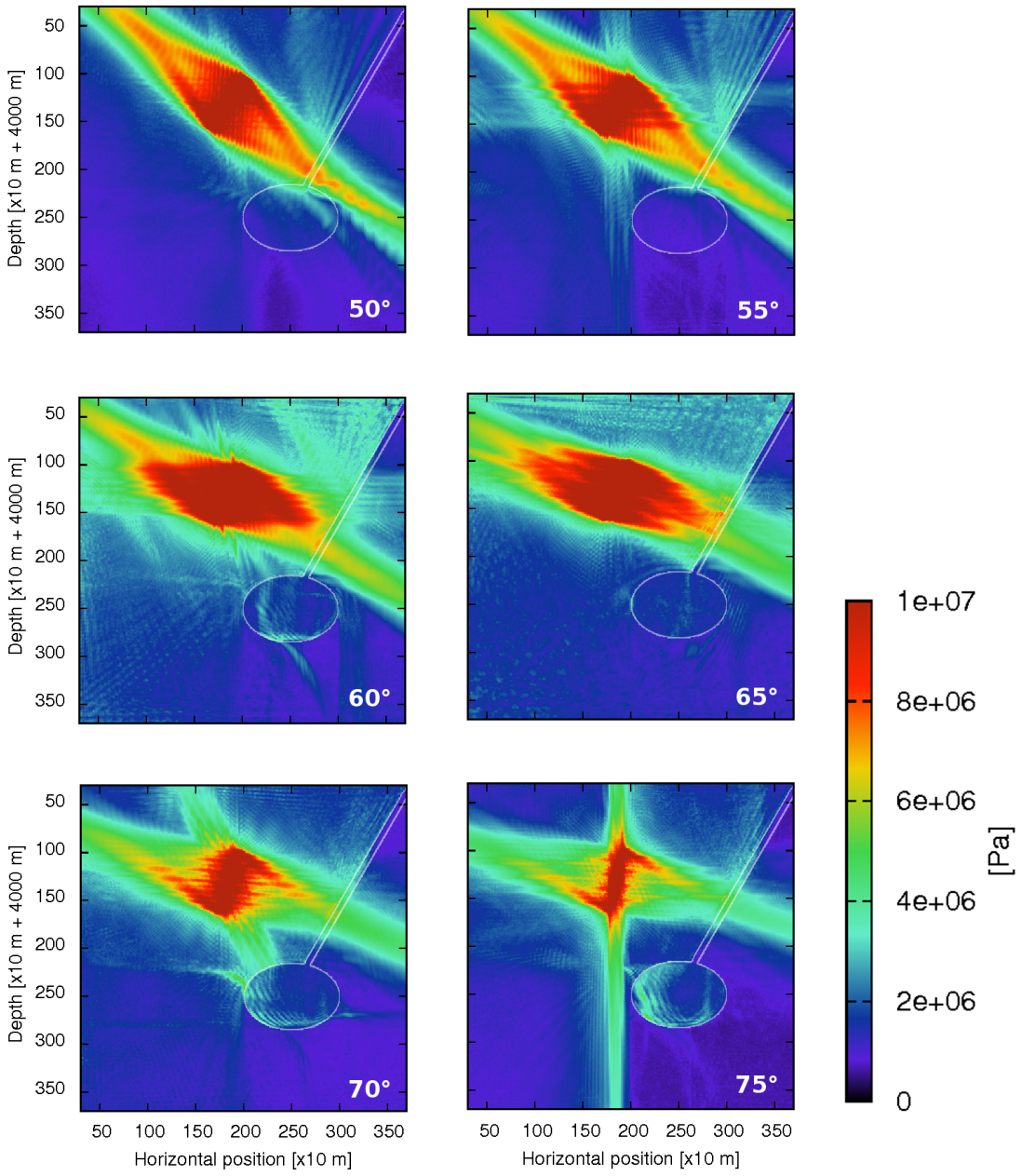

Figure 3.39: Maximum increment in the dynamic part of the Coulomb yield function, $f_{\text{yield}}^{(\text{wave})}$, as defined in Eq. (3.42), for several type 1 earthquakes, with different dip angle values. The most affected regions are strongly defined by the presence of the local structures of the system.

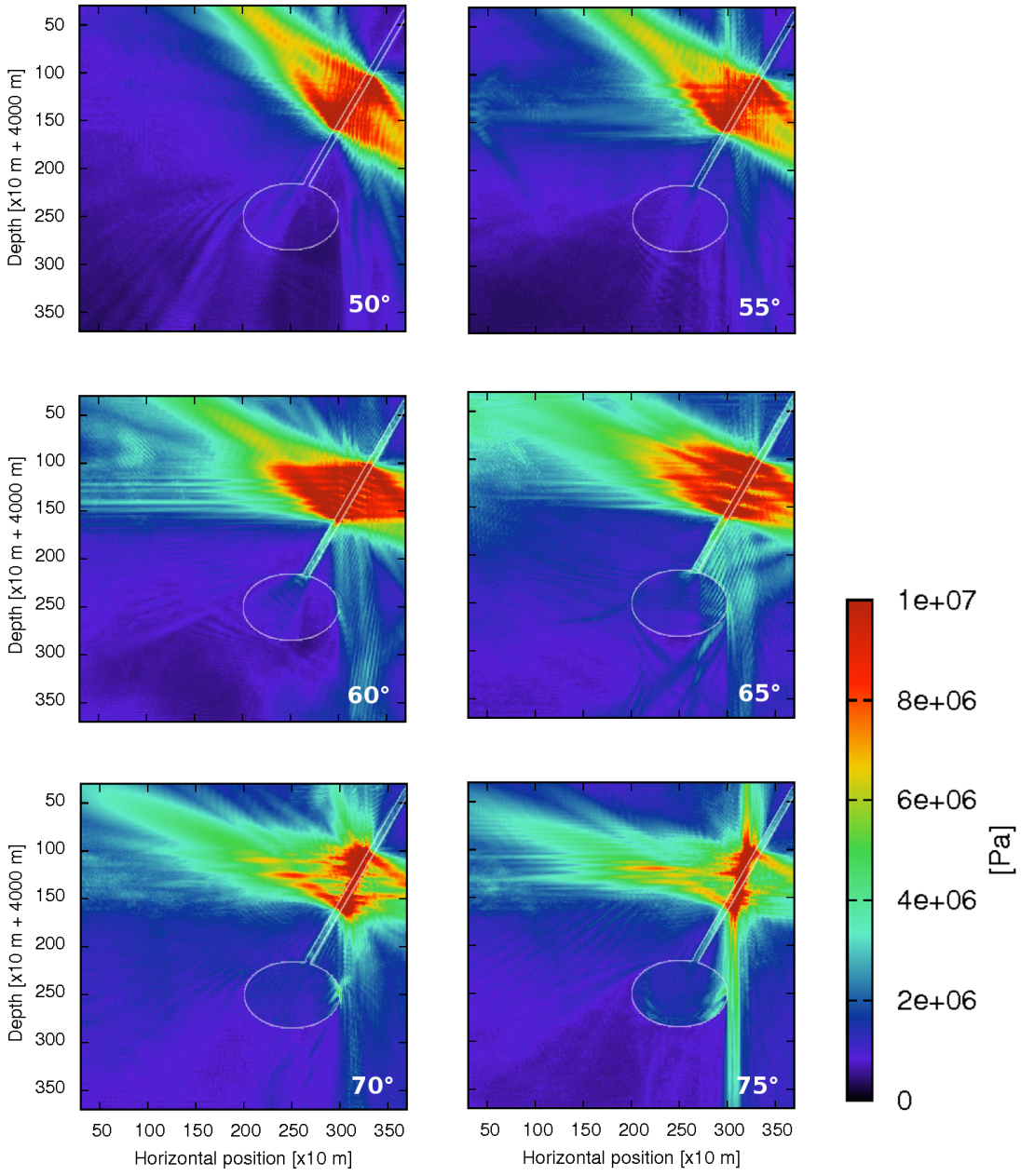

Figure 3.40: Maximum change in $f_{\text{yield}}^{(\text{wave})}$, defined in Eq. 3.42, for several type 2 earthquakes, with different dip angle values. Notice how the main system fault is the most affected structure, with the fluid reservoir being only slightly affected by the earthquakes.

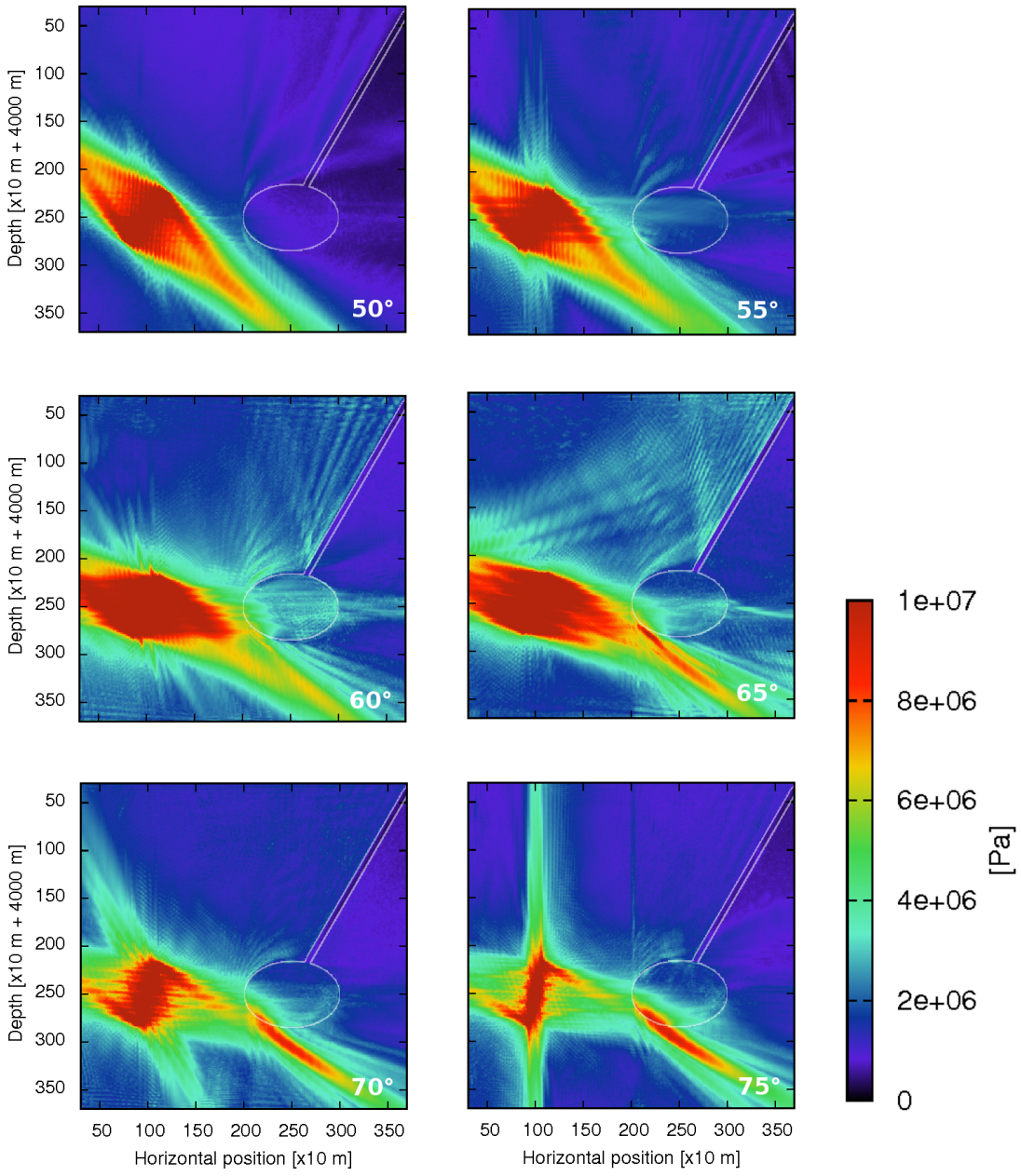

Figure 3.41: Maximum increment in Coulomb yield function for several type 3 earthquakes, with different dip angle values. While the barrier characteristics of the system main fault are noticeable, the larger changes of the yield function are found at the left boundary of the fluid reservoir.

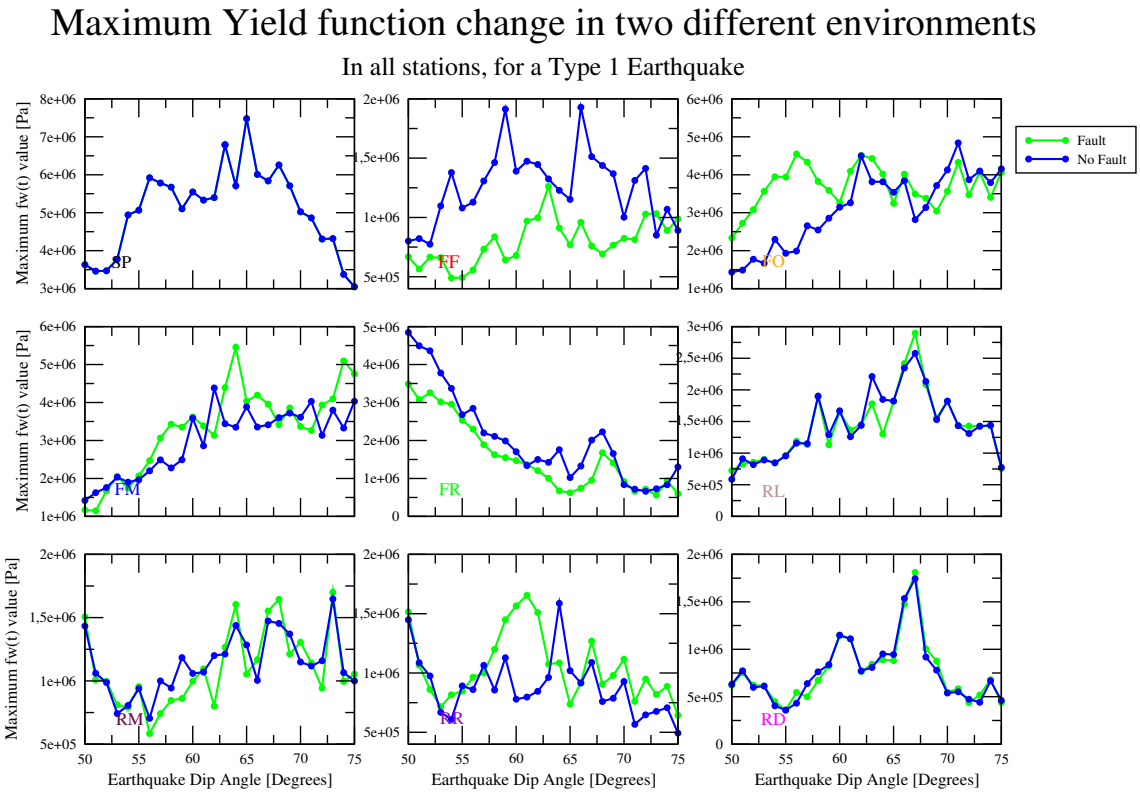

Figure 3.42: Maximum yield function change, for several dip angles, for type 1 earthquakes. Values are plotted at each station, with results from a fault-present and a fault-free setting.

was also found in the analysis of the energy density transfer, is more noticeable for dip angle values between 60° and 65°. It is also very interesting to see that the larger yield function changes are not concentrated in the reservoir, most likely to a composite effect of both the earthquake radiation pattern, and reflections at the reservoir, which present the inner section of the structure to be importantly affected by the incoming earthquake.

The effect of the fluid reservoir in wave propagation is very much noticeable in type 3 earthquakes. Seismic wave reflections are very important here, as high yield values are found on the boundaries of the reservoir that face the earthquake rupture zone, and also in their vicinity. This effect is particularly visible for dip angle values larger than 60°. The role of the system fault is also noticeable, with the regions with the higher yield function values being located at the left hand side of the structure, with much lower values to its right.

Differences between settings, for each earthquake families, are sketched in Figs. 3.42, 3.43 and 3.44, where we show the values of the maximum yield function change at each system station in both environments.

When the system is disturbed by type 1 earthquakes, it behaves differently when the is a fault present than when there is none. Results show how the maximum changes in the yield function are consistently lower in the fault region in the fault present setting, compared to the fault-free one. Exceptions are found at FM station,

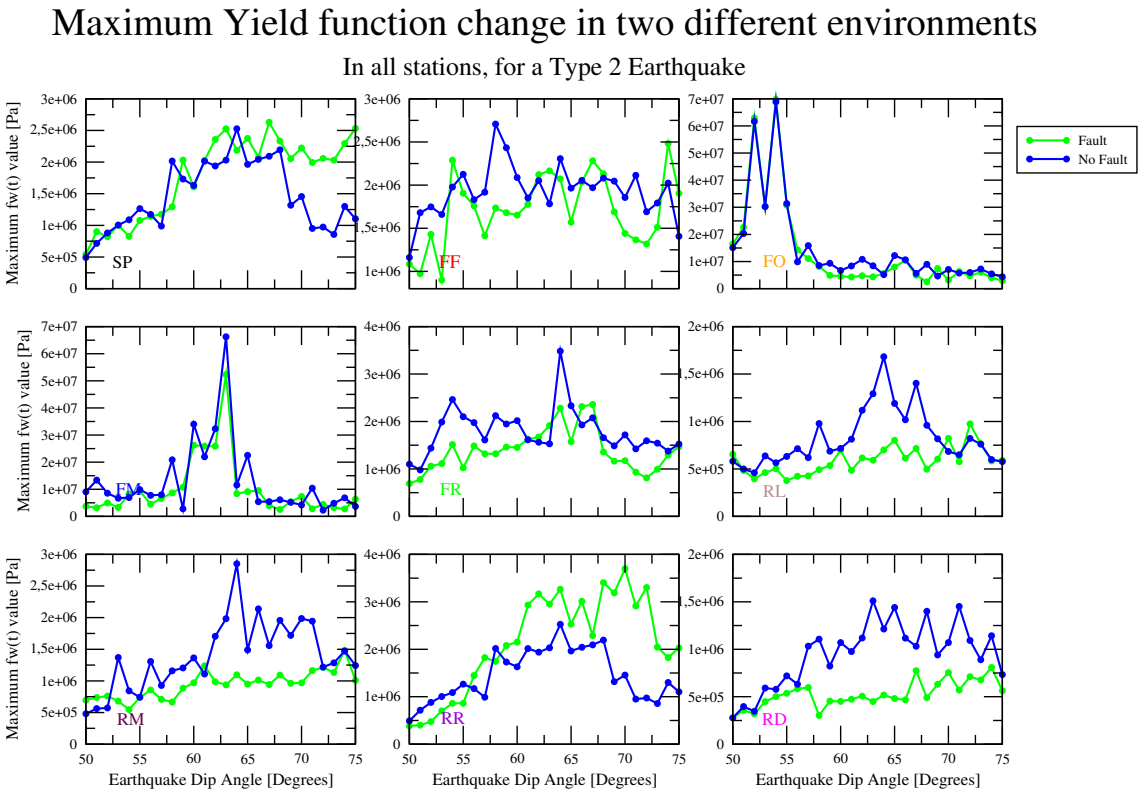

Figure 3.43: Maximum yield function change induced by the seismic waves, for several dip angle values, measures at the nine system stations. Results are shown for type 2 earthquakes, comparing behaviors between a fault-present and a fault-free environment.

for some specific dip angle values, and in FO station, which is located right outside the structure, where the maximum changes in yield function are obtained when the fault is present, therefore reflecting the breakwater-like characteristics of the system main fault.

Type 2 earthquakes induce very different behaviors in the whole system at the different settings, so the difference in the dynamics is not only present at the main fault. This is evident when analyzing the results of Fig. 3.43, where important differences between environments are found at all the stations. Interestingly, the larger contrasts are present at the reservoir stations, where the maximum yield function change is consistently lower at the fault-present setting than at the fault-free one, except at RR station for dip angle values larger than 55°, when the opposite happens. Dampening effects inside the upper and lower ends of the main fault are also found, as results from FF and FR stations show.

Differences between settings for the type 3 earthquakes are found mostly at the fault region. There, our results show yield function values that are consistently low at the fault-present environment. FO station, on the other hand, records mostly higher yield function values at this setting, in particular in the $61° - 65°$ dip angle range. This effect is consistent with the breakwater-like characteristics we found at the fault in the energy density analysis.

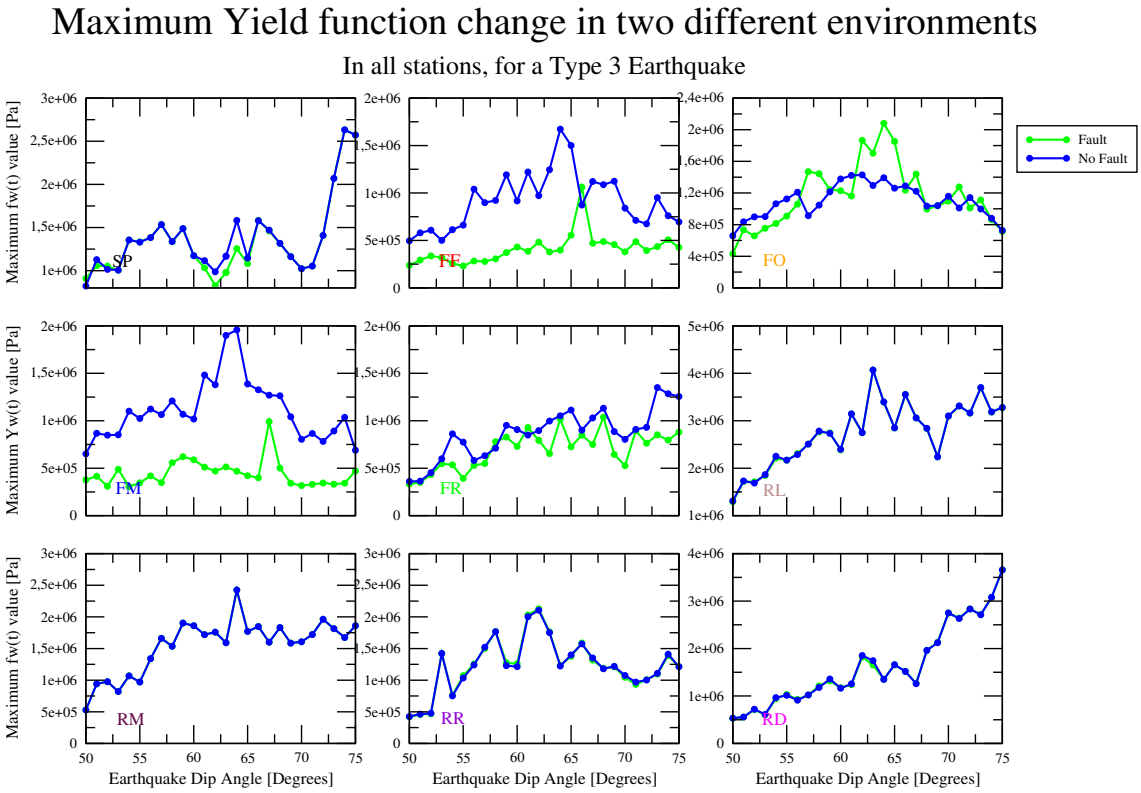

Figure 3.44: Maximum dynamic yield function change, for type 3 earthquakes. Results are plotted in all stations, with a comparison between what was obtained in both a fault-free and a fault-present setting.

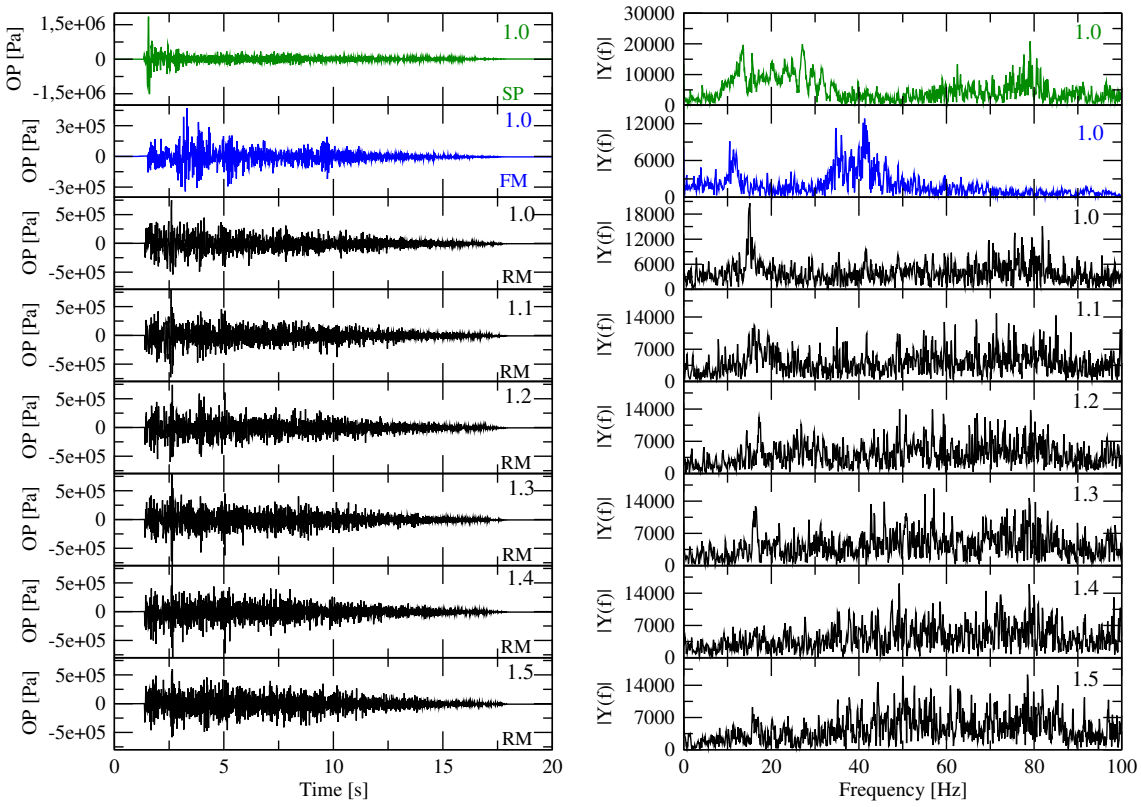

Figure 3.45: Overpressure waveforms and power spectrum, measured at three stations: SP, located at the upper left corner of the space, FM, located at the middle of the main system fault, and RM, located at the mid point of the fluid reservoir. Green lines show the waveform and power spectrum measured at the SP station, and blue lines show the corresponding results for FM station. Black lines present the results obtained at RM station, for several Poisson ratios, defined by the value of the factor b, which ranges from 1.0 to 1.5. Young modulus is kept fixed, with an increasing factor $a = 1.00$. Factors a and b are defined in Eq. (3.43).

3.3.1.8 Energy density and waveform changes at the fluid reservoir

The system main fault and the fluid reservoir are the two local structures of our physical system, with each one of them defined by different elastic properties than the ones from the rest of the medium. While the results we have presented so far put a large emphasis in the system fault, the fluid reservoir also plays a role in stress and energy transfer. This role depends strongly in the elastic parameters of the reservoir, and we study it by simulating the effect of a type 3 earthquake, with a 75° dip angle, on the same system defined sketched in Fig. 3.1, but changing the Young modulus and the Poisson ratio at the fluid reservoir. This alteration is made by using $Y_{\rm res}$ and $\nu_{\rm res}$, defined by

$$Y_{\rm res} = aY_{\rm space}\ , \qquad \nu_{\rm res} = b\nu_{\rm space}\ . \tag{3.43}$$

For increasing factor a, we took the values $a = 1.00, 1.25, 1.50$, and 1.75, whilst for b the chosen values were $b = 1.0, 1.1, 1.2, 1.3, 1.4$, and 1.5. To have a contrast with

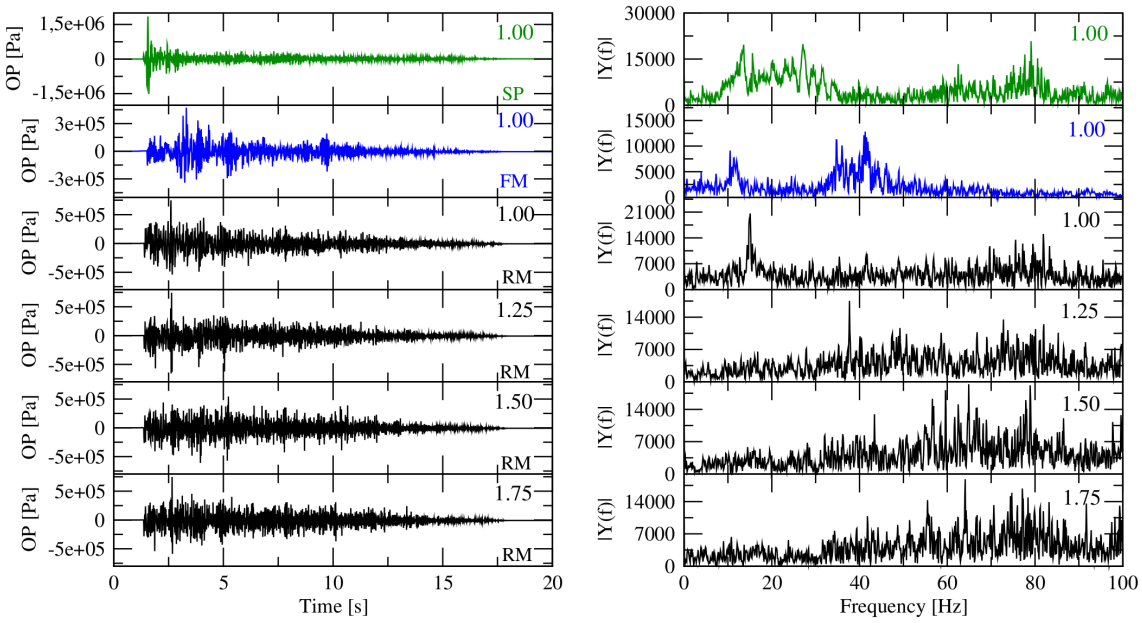

Figure 3.46: Overpressure waveforms and power spectrum obtained at SP, FM, and RM stations, for a fixed Poisson ratio, defined by an increasing factor $b = 1.0$. Green lines show the waveform and power spectrum measured at the SP station, and blue lines show the corresponding results for FM station. Black lines present the results obtained at RM station, for several Poisson ratios, defined by the value of the a increasing factor, which ranges from 1.00 to 1.75.

other earthquake location, we also studied the change in elastic parameters at the reservoir in a type 1 earthquake, with a 60° dip angle value.

Waveform frequency content change locally at the structures. Fig. 3.45 shows the overpressure timeseries, along with its respective power spectrum, measured at three stations: SP, FM, and RM, with the latter located in the middle of the fluid reservoir. Results at SP and FM stations were obtained when $a = b = 1$, while the measurements recorded at RM station were obtained with a fixed value of $a = 1$, with b changing from 1.0 to 1.5. Taking the results of SP station as a reference, the shift to higher frequencies is clear inside the main fault of the system, but a low frequency component is kept, around 12 Hz. At the fluid reservoir, as b increases, the lower frequency content of the waveform tends to disappear, and an increase of the higher frequencies is also observed. With this effect, the frequency content is more uniform, with a slight dominance of the high frequency oscillations.

When the stiffness of the fluid reservoir increases, the low frequency nodes inside the structure get gradually less present. This contrast is presented in Fig. 3.46, where we can see how the most prominent vibration band gets wider and more noisy, with a size that depends on the stiffness of the structure. This effect is also noticeable in an earthquake coming from a different source, such as a type 1 event, with a 60° dip angle value. The results for this earthquake, presented in Fig. 3.47, show also a shift towards high frequencies as the reservoir gets stiffer. The frequency content is different between earthquakes, which talks about changes in the wave motion due to

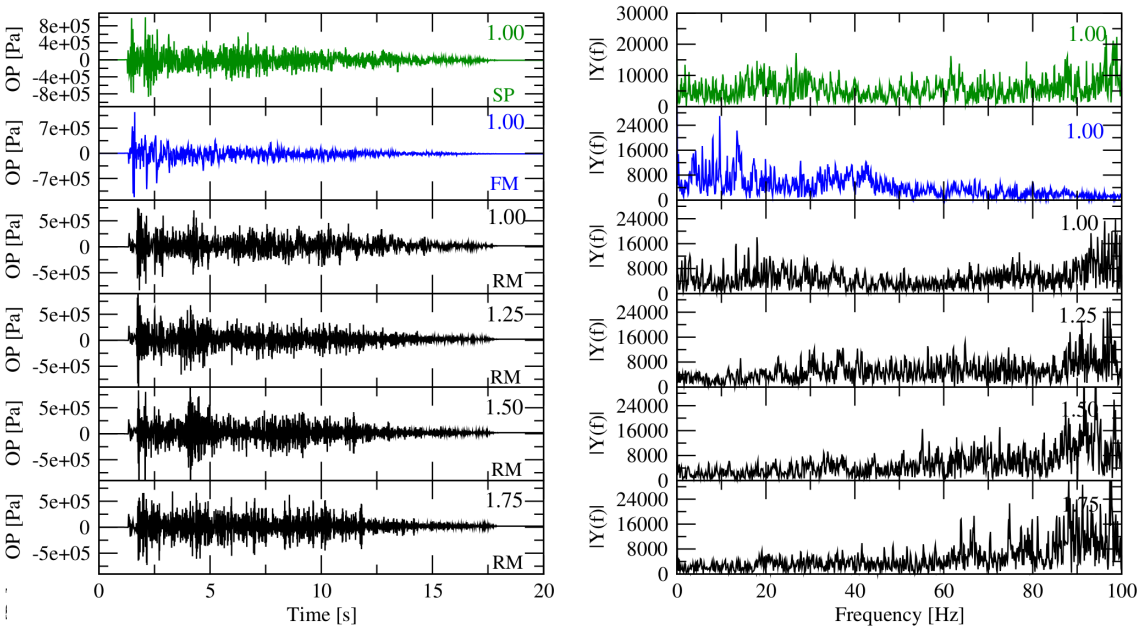

Figure 3.47: Overpressure waveforms and power spectrum obtained at SP, FM, and RM stations for a type 1 earthquake with a 60° dip angle value. Poisson ratio is fixed, defined by an increasing factor $b = 1.0$. Green lines show the waveform and power spectrum measured at the SP station, and blue lines show the corresponding results for FM station. Black lines present the results obtained at RM station, for several Poisson ratios, defined by the value of the a increasing factor, which ranges from 1.00 to 1.75.

the presence of the structures, which also affects the frequency content of the waves that arrive into the inner section of the fluid reservoir.

The effect of an increased reservoir stiffness is also evident when the energy density transfer is studied. Fig. 3.48 presents the maximum energy density maps, obtained for a fixed Poisson ratio, which is unchanged from the base ν_{space} value. Young modulus is increased in a factor a. For $a = 1$ the reservoir is not noticeable in these maps, meaning that there is no influence of the structure in wave motion. When the stiffness increases, the boundaries of the reservoir are visible. Due to reflections at the structure, energy gets concentrated at these edges. Energy transfer inside the reservoir is also discouraged for a larger Young modulus, with important reflections at the lower boundary of the reservoir, which affect the dynamics of the system. This decrease in energy transfer is also noticeable in the overpressure waveforms at RM station, which have a smaller maximum amplitude when the material gets stiffer, as it is evidenced in Fig. 3.46.

The effect of an increasing Poisson ratio in wave-structure interaction is not very noticeable, as it can be seen in Fig. 3.49. There is a distortion on the maximum energy density region for higher Poisson ratios, moving this section upwards. Energy gets also more concentrated at the left hand side of the fault for higher values of the Poisson ratio. Nevertheless, these changes are not as important as the changes observed with an increase of the Young modulus, meaning that the role of the Poisson ratio is not as important as the role of the Young modulus in the influence of the

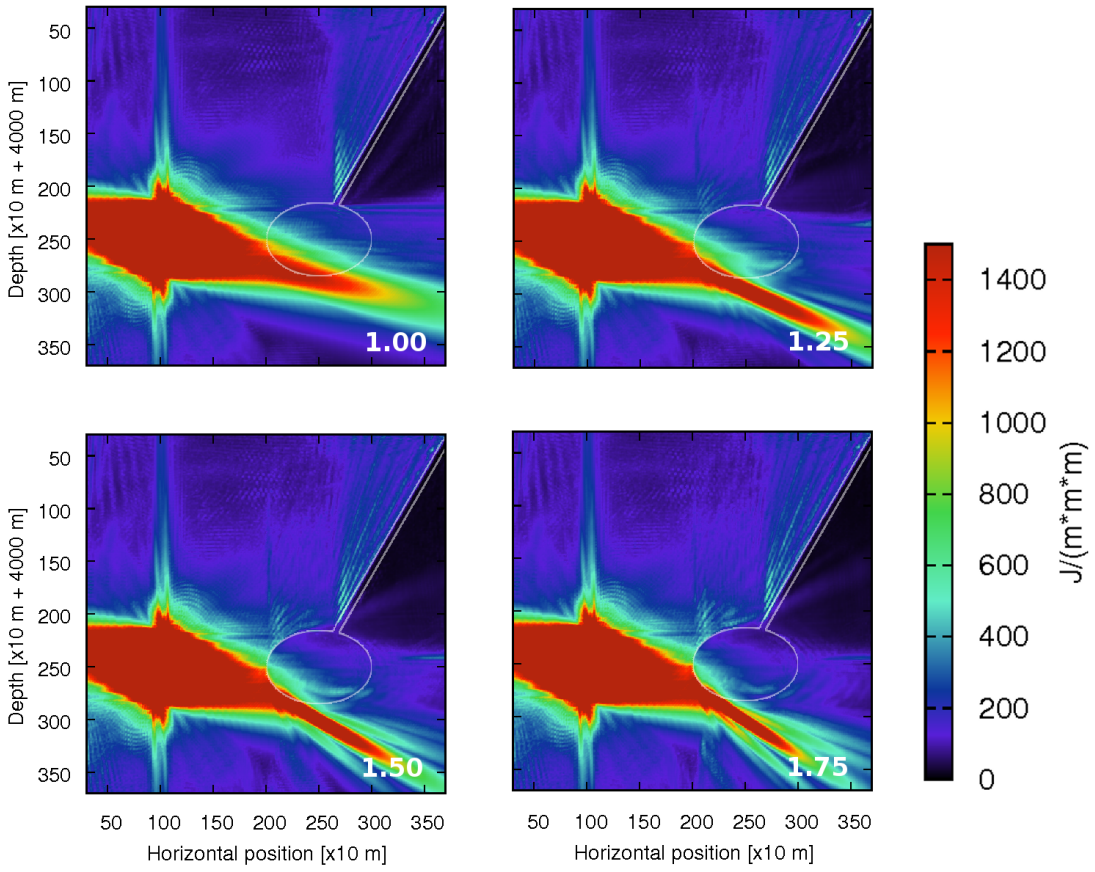

Figure 3.48: Maximum energy density maps, obtained for a fixed Poisson ratio defined by $b = 1$, for an increasing Young modulus at the fluid reservoir, defined by the a values sketched at the bottom right corner of each plot. Notice how a larger reservoir stiffness generates more reflections at its borders and allow less energy to enter into the inner section of the structure.

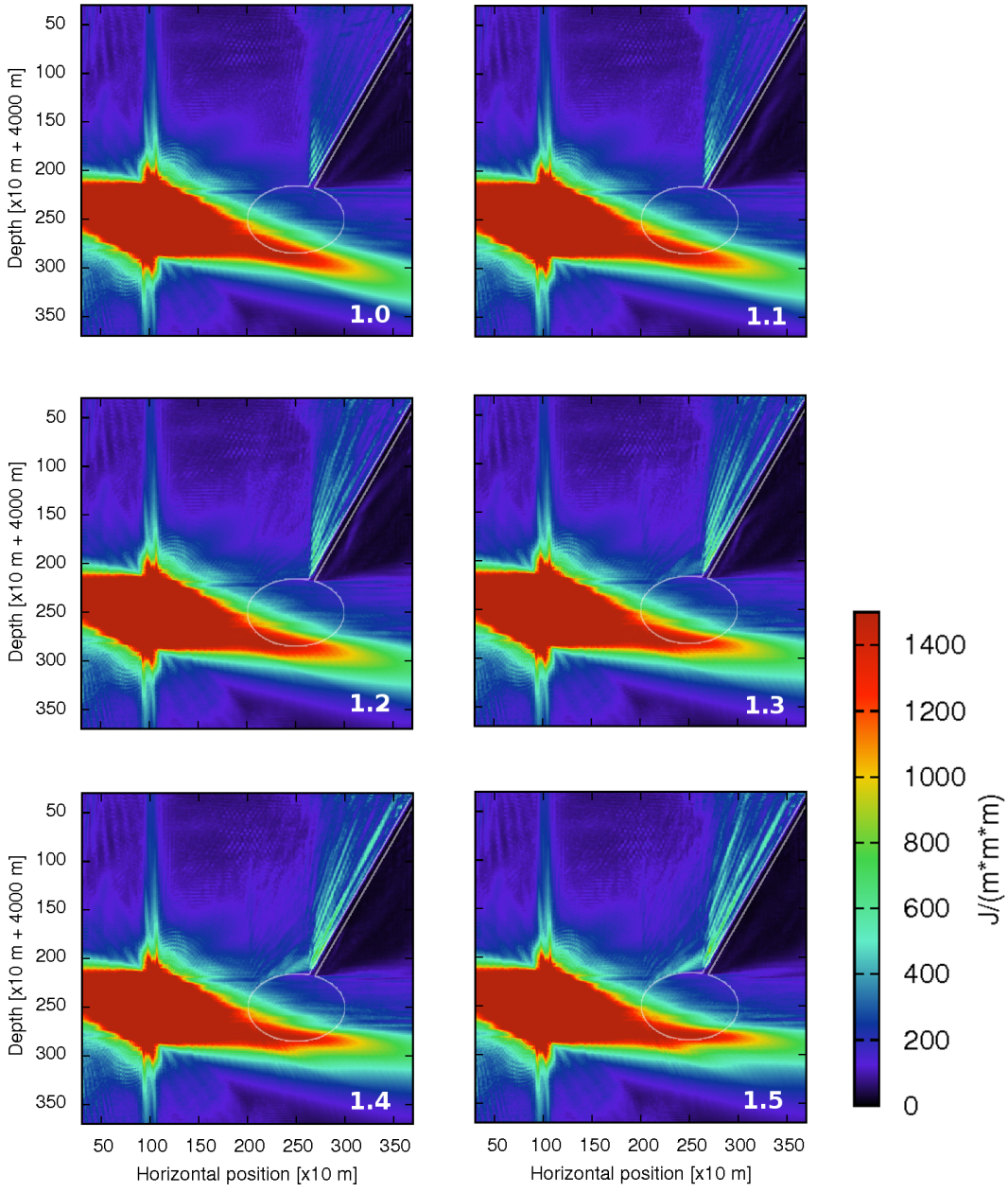

Figure 3.49: Maximum energy density maps, obtained for a fixed Young modulus defined by $a = 1$, for an increasing Poisson ratio at the fluid reservoir, defined by the b values sketched at the bottom right corner of each plot. Differences in the results are not as large as the variations on the Young modulus, meaning that small variations on the Poisson ratio do not play a relevant role in kinetic energy transfer.

local structures in dynamic stress and energy transfer.

3.3.2 NS experiment

At distances longer than 2-3 fault lengths, static stress changes generated by earthquakes are small, and therefore it is not likely they can produce changes in the activity of a hydrothermal/volcanic system(Manga and Brodsky, 2006). Dynamic stress changes are larger at those distances, but their effect is transitory. Nevertheless, they can produce important effects in system that are close to a critical state. According to Hill(Hill, 2008), models of dynamic stress triggering usually fall in two categories: the ones which consider the potential seismic waves have to generate ruptures in a system, and the ones who consider the effect of seismic waves in high-pressurized fluids(Brodsky et al., 1998). The earthquakes we study in this experiment have a 22 km rupture length, and their hypocenters are located 100 km from the westernmost fluid reservoir of the system. Such a distance is longer than 4 rupture lengths, meaning that static stresses are negligible at reservoir level. To study the dynamic changes of the system, we studied the maximum changes of overpressure, energy density, and normal stresses along the structures.

Fig. 3.50 shows maps of the maximum overpressure change induced by the seismic waves in the space, for the three earthquake locations considered in our experiment. As expected, the radiation pattern of each earthquake dominates the spatial distribution of the maximum overpressure induced during the passing of the seismic waves, but the structures of the system do produce alterations to the expected pattern. Fluid reservoirs distort it at their vicinity, sometimes increasing the maximum overpressure, and other times reducing it. This is related with both the earthquake location, and the value of the strike. We can see this in the variation of a higher peak overpressure zone left to the leftmost reservoir when under the influence of the "north" events. For negative values of the strike, this region is more noticeable, and it gets less important as the strike gets more positive. Other examples are the shadow of higher peak overpressure values that is generated to the right hand side of the rightmost reservoir when under the influence of the earthquakes located at the north, particularly for positive strike angle values. Other interesting shadows are generated at both fluid reservoirs, when under the action of a "middle" event. In this case the effect is that the maximum volumetric variation is an extension, not a compression. This is due to alterations in wave motion at reservoir level, most likely because of reflections with the borders of the structure. A third shadow is seen at the up and right to the leftmost reservoir, when it is under the influence of a "south" earthquake. This effect is most visible for negative strike angle values, and it is composed by the creation of a more compressive peak overpressure zone, which does not correspond with what should be expected in a pure elastic space, without structures.
The two faults also play an important role on the dynamic response of the system to external perturbations. The most common feature of these structures is the reduction of the maximum overpressure inside them. This is noticeable for the three

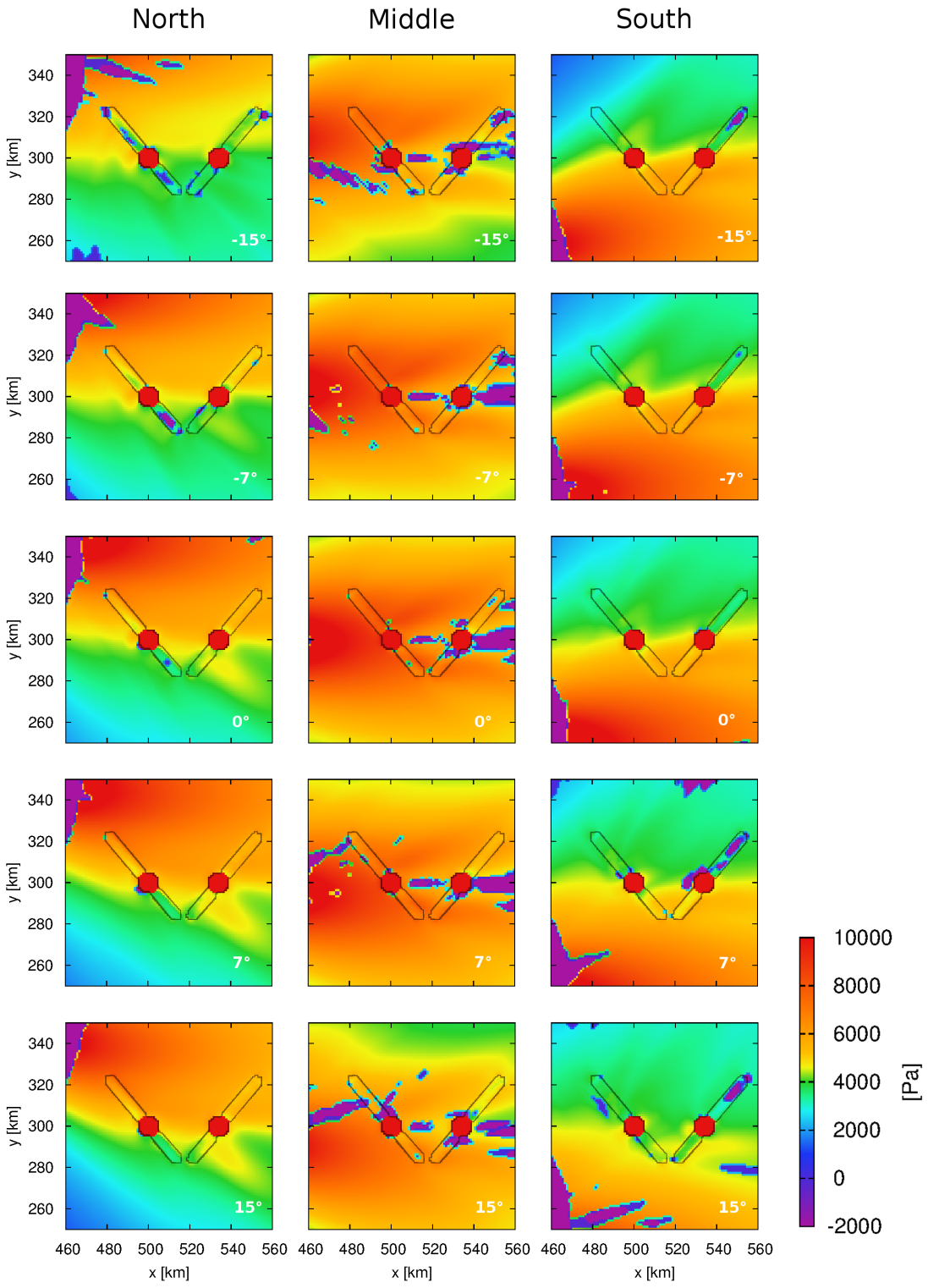

Figure 3.50: Maximum earthquake-induced overpressure maps at the two-fault system, for the three earthquake locations, and several values of the strike. The first column presents the results from the "north" events, whilst the second and the third columns show the results from the "middle" and "south" earthquakes. The values of the strike are also marked, and they are, from top to bottom, $-15^o, -7^o, 0^o, 7^o$, and 15^o. The shape of the two-fault system is marked in the maps for better data visualization.

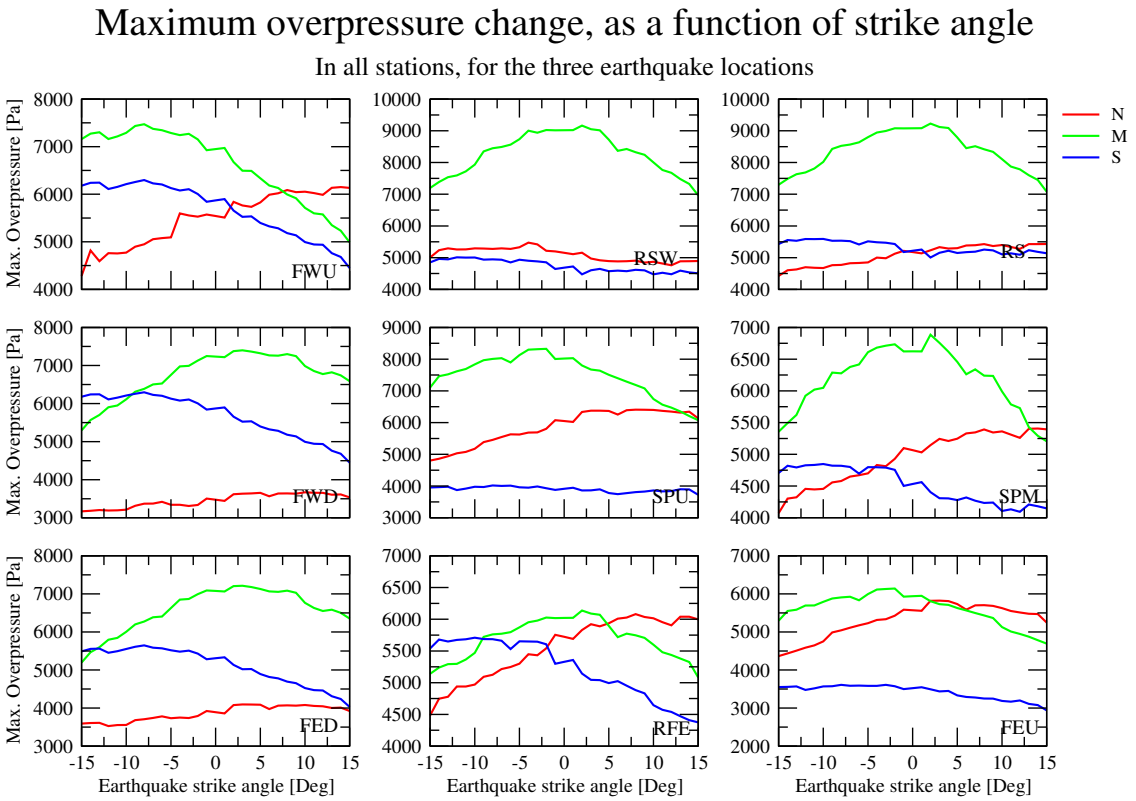

Figure 3.51: Absolute value of peak overpressure, as a function of strike angle, measured in all the system stations, for each earthquake location. Red lines show the results of the northern events, green lines for the middle earthquakes, and blue lines for events located at the south.

earthquake locations, for all the values of the strike angles, and depends strongly on the incoming wave signal, and in the relative position of the faults with respect to the earthquake epicenter. For "north" earthquakes, the fault that changes the system dynamics the most varies with the strike angle. For more negative values, it is the left fault, but for more positive values, it is the right fault. A similar trend is found for the "south" earthquakes, but with the lower section of both faults, which becomes more relevant as the strike angle increases. For "middle" earthquakes, some negative peak overpressure regions are created inside the faults, presumably due to reflections at the reservoirs and the fault boundaries.

Closer details on the dependence of peak overpressure change as a function of strike angle are showed in Fig. 3.51. At each one the stations we calculated the absolute value of the peak overpressure change during the passing of the waves, for each earthquake epicentral position and strike angle. Due to the relative position of the stations respective to the earthquake epicenters, induced overpressure by the "middle" earthquake dominates the records, specially at the stations located along the line connecting the earthquake epicenter and the fluid reservoirs (RSW, RS, SPM). The exception comes from the rightmost reservoir, which is located in the line of these stations. There, the effect of the three earthquakes is comparable and depends strongly on the strike angle. An interesting case occurs in the neighboring stations

RSW and RS, where the maximum overpressure pattern for "mid" earthquakes is almost the same, but we find important differences for the "north" and "south" events, with the latter event going from being the least important event at RSW station, to the second most important at the RS station, for negative values of the strike. The results for the "north" earthquake also show how the peak overpressure/strike angle pattern goes from being almost flat at RSW station, to having a variation of about 1 kPa between angles at RS station.

Watching along the fault lines we can notice how, for the left fault, it is the "middle" earthquake the one that induces the larger overpressure peaks inside the structure for most of the strike angle values. At the north edge of this structure, the influence of the "south" and "north" events changes with the strike angle, with the former events being more important for negative strike values, and with the latter being more relevant for positive strike values. At the southern edge of the left fault, the "south" events induce a larger peak overpressure than the "north" ones. In the case of the right fault, the influence of the "north" earthquake is increasingly higher as we move towards the northern edge of the structure, with the opposite occurring for the "south" events. Interestingly, the peak volumetric changes generated by the "middle" earthquakes are lower at the fluid reservoir, which is located in front of the rupture zone, than at the borders of the fault.

Geometrically, there are four stations that represent symmetrical points for the northern and southern earthquakes. They are RSW, RS, SPM, and RFE. Therefore, we should get very similar values at these stations when strike angle is zero, and opposite values outside. The fact that this does not happen suggests that there may be an effect of both reservoirs and faults in the wave motion, thus altering the patterns.

A very important dynamic quantity is the energy density. It has been studied by several authors(Manga and Brodsky, 2006)(Lupi et al., 2013), and it is particularly interesting because it can be obtained in the field using a empirical relation that depends on earthquake magnitude and the distance between the hypocenter to the observation point(Manga and Brodsky, 2006). In our case, our method allow us to follow this quantity in the whole space of interest. Fig. 3.52 shows the maps of the maximum energy density for the three earthquake locations, plotted for five values of the strike. Both fluid reservoirs appear as regions where the peak energy density is smaller than it would be expected in a pure elastic space, and this effect depends on the value of the incoming energy density of the seismic waves.

The role of the faults is more noticeable for the "middle" earthquakes, where the energy is focused inside the structures, correlating with the incoming amount of energy density from the seismic waves. The northern event induces a noticeable concentration at the right fault, being this feature more prominent for strike values between 0^o and 7^o. The southern events generate an energy concentration at the left fault, and also at the lower section of both structures. This effect is again related

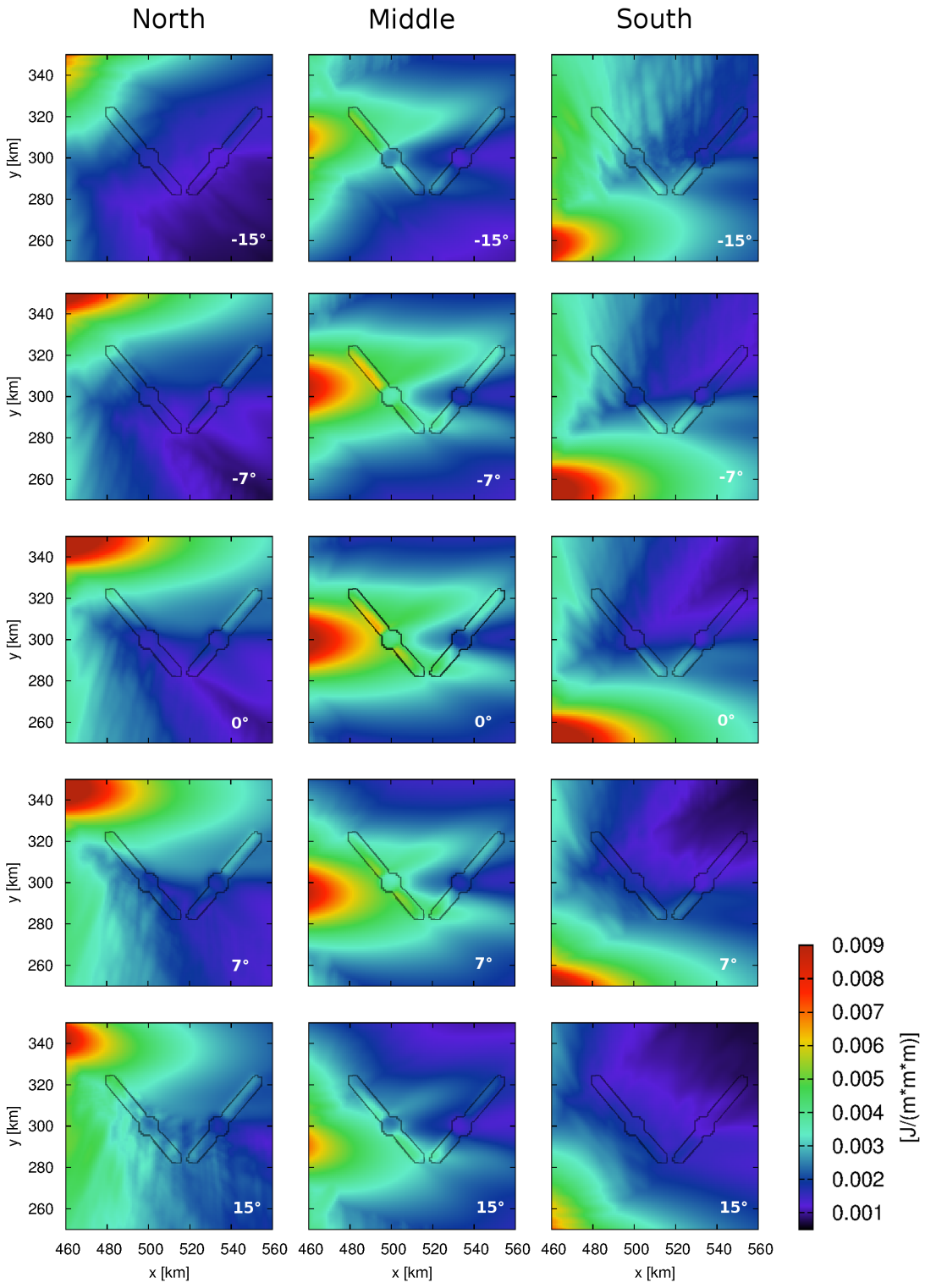

Figure 3.52: Maps of the maximum kinetic energy density generated by the passage of the earthquake waves, obtained at five strike values for each earthquake type. First column presents the values obtained from the influence of "north" events, while the second and third columns show results from the "middle" and "south" earthquakes. Strike values are annotated and they are, from top to bottom: -15^o, -7^o, 0^o, 7^o, and 15^o.

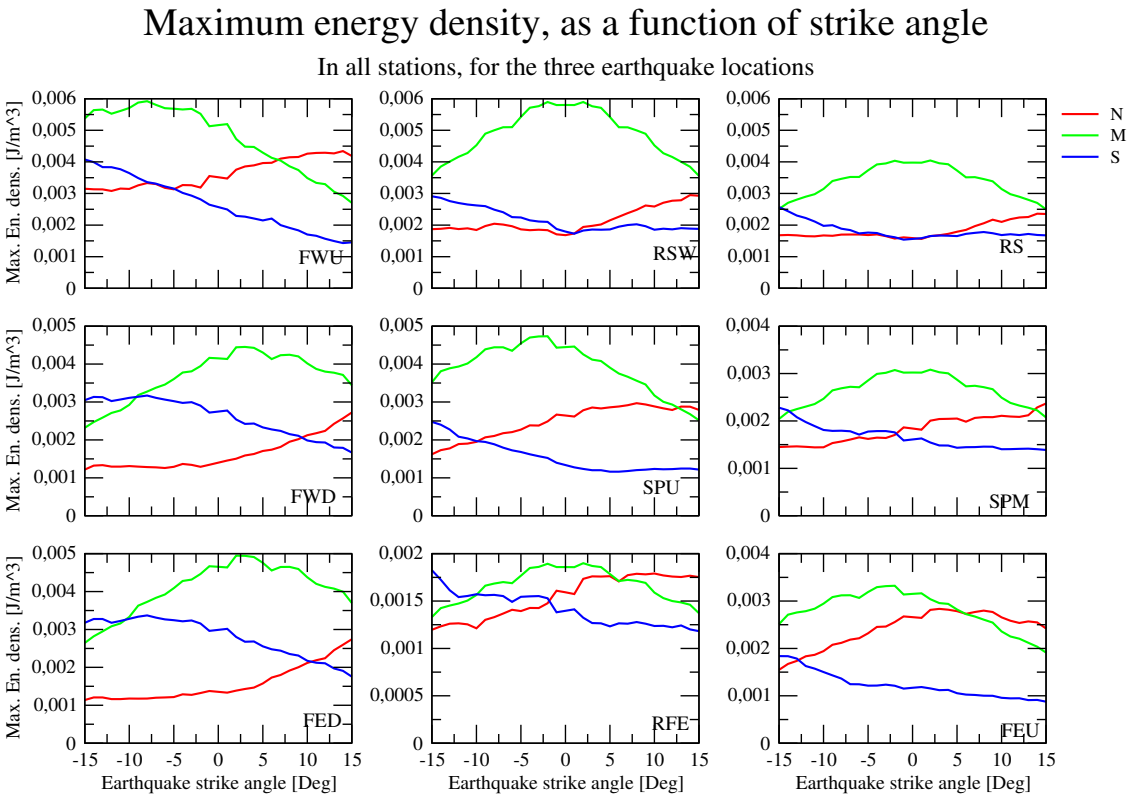

Figure 3.53: Maximum energy density change as a function of strike angle, measured in all the system stations, for each earthquake type. Red lines show the results for for the northern events, green lines the middle earthquakes, and blue lines show the results for southern events. Fig. 3.2 and Table 3.2 give the detail on the location and name of each one of the stations.

to the incoming energy density, and it is more prominent for negative strike values.

Fig. 3.53 presents the peaks on energy density, recorded at each system station, as a function of earthquake strike. In contraposition to the maximum overpressure results, the records show more symmetrical patterns for northern and southern earthquakes at RSW, RS, and RFE stations, where these earthquakes induce the same energy density value around a 0° strike angle. The same feature is not found in SPM station, where the intersection between these curves is located at a strike value around $-2.5°$.

The dampening effect of the reservoirs in kinetic energy transfer is highlighted when comparing the results of RSW and RS stations, where the peaks in energy are lower inside the reservoir, for all perturbations. The most important occurs for "middle" earthquakes, and consists the reduction in about a 30% of the peak energy value for "middle" earthquakes at RS station, compared with the value at RSW station. It is important to remember that RS station is located at the fluid reservoir, and therefore has a larger Young modulus than RSW station. This feature is not replicated in the peak overpressure results.

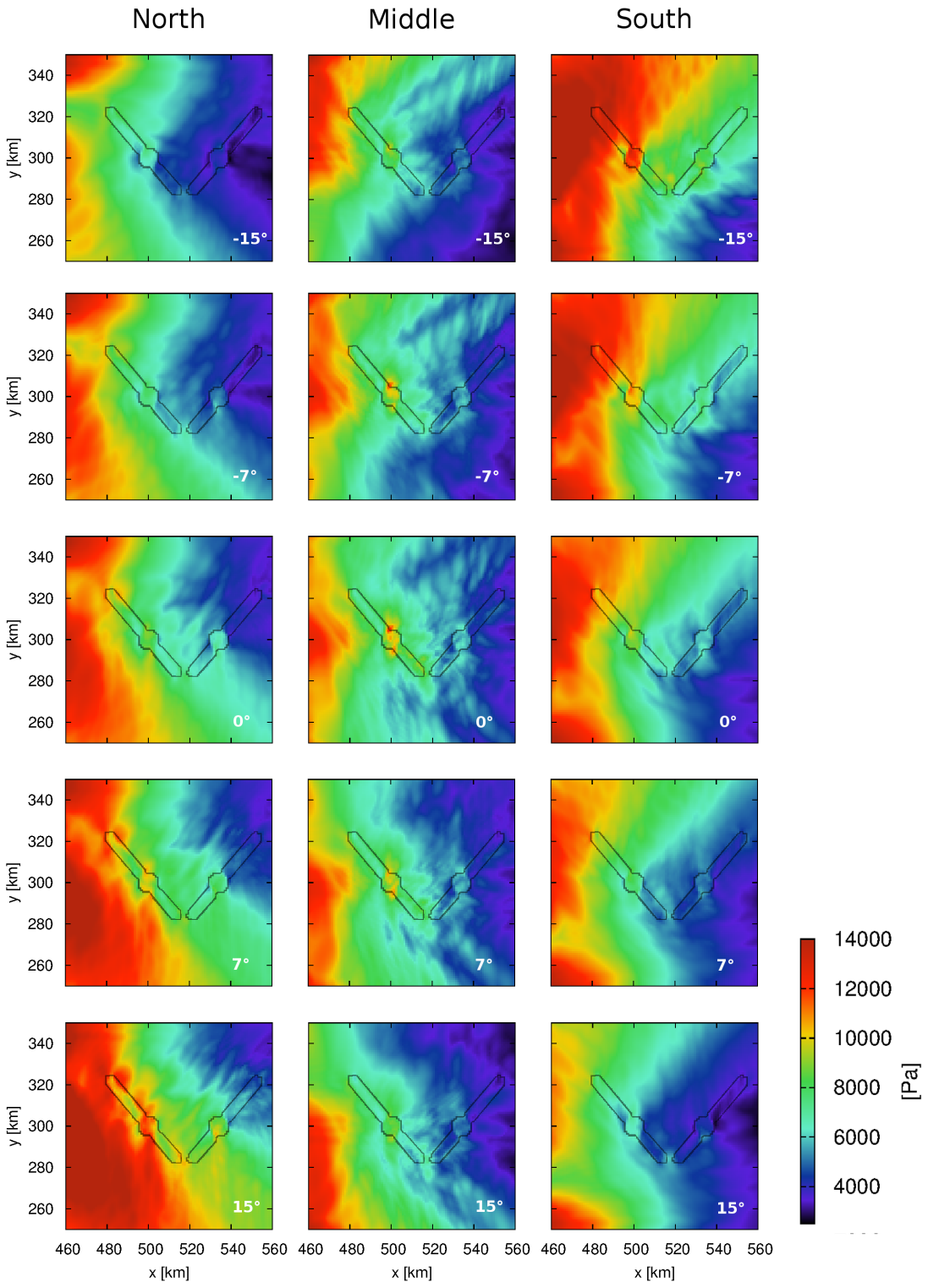

Figure 3.54: Maximum increment in Coulomb yield function during the passage of the seismic waves in the system, for each one of the three earthquake locations. We present results for several seismic events, each one characterized by its strike angle value. First column presents the results for the northern events, second column shows the results for the "middle" earthquakes, and the third column presents the results for the southern perturbations. Strike angles are annotated, and they are, from top to bottom: -15^o, -7^o, 0^o, 7^o, and 15^o.

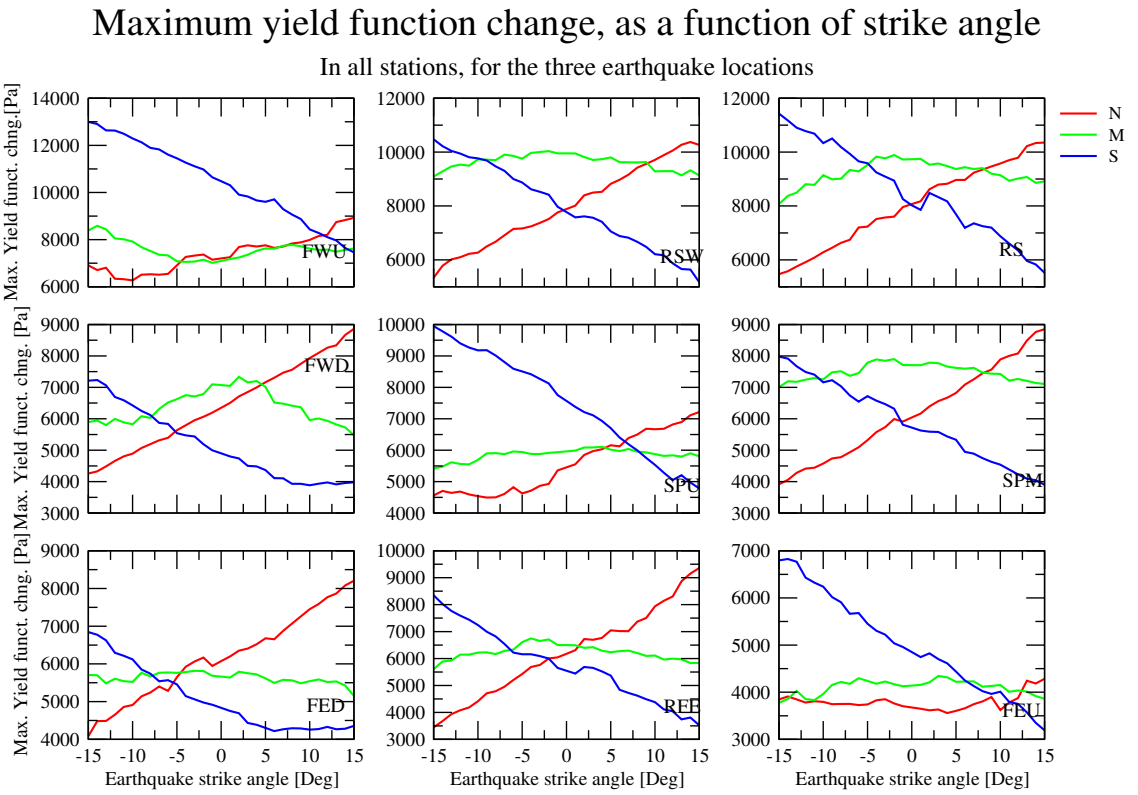

Figure 3.55: Maximum increment in yield function as a function of strike angle, measured in all the system stations, for all the earthquakes. The influence of the northern events is presented in the red lines, whilst green and blue lines present the results for "middle" and "south" earthquakes, respectively.

Dynamic changes on the Coulomb yield function are particularly important, as they allow us to get a better insight on where are the spots with a higher faulting potential due to the shaking induced by the different earthquakes. Fig. 3.54 shows the maximum changes in this function for the three earthquake locations, obtained at several strike angle values. Changes in space for Coulomb yield function are dominated by the earthquake radiation pattern, but the structures of the system do play a local role. The peak increments in the yield function are larger inside the fluid reservoirs than outside them, thus converting them in two of the most affected regions of the system in terms of faulting potential due to the earthquakes.

System faults, on the other hand, do not play a very important role here, but we can see a slight reduction in the peak increment in the yield function inside them, with the larger values being recorded at their boundaries. In particular, the reservoir-fault interface does present a significant increase in the Coulomb yield function.

Fig. 3.55 shows the maximum changes in the yield function in all the stations of the system, for all the values of the strike angle. We can see how the dependence of this quantity on the strike angle is significantly stronger for "north" and "south"

events than for the "middle" earthquakes. At the northern sections of both system faults it is the southern earthquake the one that has the greater influence on the system, while at the southern sections of the faults, it is the northern event the one the more dominant.

There are three main lineaments in the stations from left to right. On the northern one, composed by FWU, SPU, and FEU stations, it is the southern earthquakes the ones that induce the larger changes in the yield function. At the middle line, composed by RSW, RS, SPM, and REF stations, the largest disturbances on the yield function are not particularly associated with one earthquake type, since the three of them alternate their dominance in the system. The results from the southern lineament, composed by FWD and FED stations, show how the northern earthquakes are more influential than the other two event types for larger strike angles, although this is not true for lower angles.

At the four stations that present a geometrical symmetry respective to north and south earthquakes, we do not find the expected symmetry in the change of the yield function, as we did find it for the energy density results. This might be due to the action of the shear stress transferred from the seismic events.

3.4 Discussion

We investigated the effect of an earthquake in the dynamics of a hydrothermal/volcanic system. We studied this from the perspective of two type of experiments: one composed by several $M_W = 4.0$ earthquakes arriving at a single fault system, connected to a fluid reservoir, at a close range, and a second experiment defined by several $M_W = 6.1$ seismic events affecting a two fault system, each one of them connected to a fluid reservoir, at a larger distance. Both faults and fluid reservoirs possess different elastic parameters than the rest of the space. Faults have a lower Young modulus, while fluid reservoirs have a larger Young modulus, and a slightly larger Poisson ratio. Both type of experiments were performed in two dimensions, with the first one in an horizontal and a vertical axis, thus considering gravity to play an important role, and the second one considering only the horizontal axes.

3.4.1 Vertical experiment

Earthquake-induced static and dynamic changes at one particular point in space depend mainly of four source parameters: magnitude, relative earthquake source position respective to the measuring point, focal mechanism, and in our experiment, dip angle value. The first two dominate mainly the magnitude of the perturbation, while the latter ones are more important to determine the directivity of the induced change. While in the literature there is extensive analysis of the static extension/compression patterns generated by earthquakes, and in the dynamic triggering potential of a particular event, a complete dynamic and static analysis of the influence of several earthquake parameters on a system composed by several structures

has not been fully completed. Our study, one of the firsts in its area, has attempted to get a better understanding of the role of these parameters en in earthquake/fluid motion interactions. Our approach based on numerical simulations found that the influence of the dip angle is important in both in dynamic and static changes, although is more dominant for the static overpressure changes. This is mostly due to the radiation pattern of the earthquake. This is in agreement with the extensive literature in this subject. Nevertheless, our results also show that there are important differences in the behavior of the setting depending on the local structures, since they introduce a level of complexity in the system that is not always easy to foresee.

The fluid reservoir is represented by a stiffer region in the elastic space compared to the surroundings, and also by a marked overpressure value, which in our experiment was of 10 MPa. The increased Young modulus creates wave reflections at the reservoir boundaries, which in turn distorts patterns for kinetic energy transfer when compared with what should be expected from a simple elastic experiment, when local structures are not present. This effect is particularly noticeable when the stiffness is increased, and also for certain incoming earthquake, and it is present, in different ways, for dynamic and static changes.

Distortions in the static stress patterns due to the presence of the reservoir are more evident for type 1 and 3 earthquakes. For the former, a compressive region is formed down the reservoir, behind its bottom wall, which is the back wall from the earthquake's perspective. While the radiation patterns of the type 1 earthquakes indicate that this should be a compressive region, the shape of it does not correspond to what should be expected for a normal double-couple solution, and thus create a "compressive shadow" behind the structure. In the case of type 3 earthquakes, an extensive region is generated behind the back wall of the reservoir, which in this case is its right hand side border. Just in the case of type 1 events, this region does not correspond to what should be expected for a double-couple solution, but the main difference is that the earthquake induces volumetric extension in this region, and thus a "extensive shadow" is generated. This particular effect is an important feature, as it affects significantly the post-seismic stress state in the region, as well as the local permeability. According to our results, the compressive/extensive characteristic of this shadow depends strongly in the radiation pattern of the earthquake, both in sign as in absolute value.

The interaction of the fluid reservoir with the incoming seismic waves is also important, and strongly depends on both relative hypocentral location and dip angle value of the earthquake. As results from dynamic energy transfer show, wave reflections from type 1 events at the front wall of the reservoir increase with the earthquake dip angle value, while the energy transfer inside the structure decreases. This reflection and refraction of seismic waves, as well as internal reflections at the inner section of the structure, generate energy concentration at the boundaries, which is also evidenced in an important change in the yield function at them. The same feature appears in type 2 and 3 earthquakes, which evidences a local effect of the structure.

Reservoir dynamics also depend on its elastic properties, in particular with stiffness changes. A stiffer reservoir not only increases wave reflections at the reservoir borders, but it also focuses energy at them, and decreases the amount of energy

that is transferred into its inner section. A larger amount of reflections introduce complexity into the system, and also concentrates more energy at the fault region. Waveform frequency content also changes inside the reservoir, with a shift to higher frequencies that is more noticeable for larger Young moduli. A similar shift is also found at the system main fault. High frequency vibrations have been found to increase the amount of interaction between gas and liquid in narrow capillaries(Vandu et al., 2004), meaning that the elastic properties of the local structures can help to increase the interaction between fluid and gas.

The system main fault,represented as a portion of the space with larger permeability and lower Young modulus than the ones proper of the surroundings, also plays an important role in the static and dynamic changes induced by the external earthquakes, as well as in the fluid dynamics of the system. Due to its lower permeability, it defines the preferred fluid motion direction. It also changes slightly the pre-seismic stress regime on its vicinity, which is important to determine the rupture potential external earthquake waves have when they strike the system.

This structure generates a discontinuity in the overpressure change induced by the earthquake along itself, and in its immediate vicinity. This discontinuity is seen as an overpressure reduction inside the structure, accompanied by a small transfer of the compression/extension pattern, moving it downwards the fault. This effect generates pressure gradients that are not expected in a common Coulomb stress analysis. In particular, it creates noticeable differences between two neighboring points, one of which is located at the fault and the other right outside it. There is a correspondence between how large is the volumetric extension/compression endured by the system, and how important the role of the fault is, as can be seen in Figs. 3.11 and 3.17.

Type 2 earthquakes, which are generated with the epicenter in a point at the fault, affect the fluid dynamics in a more complex manner. In particular, FM and FO stations do register an important overpressure change for certain dip angles, as Fig. 3.14 shows. Such a change is due to the closeness these stations have to the earthquake rupture zone, and highlight how large overpressure changes can be obtained along the structure from relatively small earthquakes. Moreover, this type of earthquakes, depending on the relative angle between the system main fault and the earthquake rupture zone, generates important pressure gradients along the structure, which is critical for the ascension of the fluid.

A closer look at results obtained in two different settings, with and without the system main fault, reveals how the change in overpressure in both regimes is expressed mainly in the fault stations, with important changes specially in FR and FF stations, which are the ones located at the edges of the structure. This is particularly true for type 1 and 3 earthquakes. Type 2 events show an important departure at FF and FR stations between the results from the fault-present setting when compared to the ones of the fault-free system. We also found an interesting shift in the derivative of the static overpressure change respective to the dip angle values when comparing the data from the two settings. These changes account for a very relevant role of the local structures, which should be taking into account when dealing with earthquake/fluid interactions.

The influence of the system fault in dynamic changes is also important, with some common trends. Maximum induced overpressure changes show how the results in the fault-present setting are clearly different than the ones obtained in a fault-free environment at the system fault and its vicinity. Such a difference is particularly noticeable for type 1 and 3 earthquakes, where the maximum earthquake-induced overpressure change is smaller inside the fault in a fault-present system, but larger than in a fault-free setting right outside the structure. This highlights breakwater-like characteristics of the system main fault, where larger overpressure amplitudes are found at the boundary that faces the earthquake, due to reflections at the structure. At the same time, smaller overpressure amplitudes are found at the backwall of the fault, as the structure acts like a shield, diminishing the earthquake influence on it.

Peak overpressure amplitudes for type 2 earthquakes show more complex contrasts between settings. The most noticeable differences are present at the boundaries of the main fault, in FF and FR stations, where we can find larger overpressure changes in the fault-present setting. We also found differences in the reservoir stations, usually with lower overpressure amplitudes in the fault-present setting, with some exceptions at specific dip angle values, often in the $60^o - 65^o$ range. Considering that the dip angle of the main fault of the system is 60^o, we suggest that earthquakes with a dip angle slightly larger than the one of the structure create the most important changes in the system, at the reservoir level. This might be due to the effect of the reflections of the seismic waves at the fault, which creates an extra wave train that travels to the reservoir, thus enhancing the influence an earthquake has in that region.

The dynamic role of the system main fault is not only restricted to a change on the maximum earthquake-induced overpressure amplitude, but on its whole waveform. This is confirmed by a cross correlation analysis, which clearly shows how the larger contrasts between overpressure waveforms is found at the fault region stations, and some others at the reservoir, which depend on the particular earthquake location. This is evidence of the strong impact that wave reflections and refractions at the fault have in the whole system.

Maximum energy density maps also highlight the breakwater-like effect of the system fault, which is consistent with the overpressure results. This effect is dominant for earthquakes located outside the structure, such as type 1 and 3 events. In the case of type 2 earthquakes, we found an energy concentration inside the fault, which is more noticeable for earthquake dip angle values close to the inclination angle of the structure. This might be related to inner reflections inside the structure, like a waveguide. Some energy concentration in the fault is also found in type 1 earthquakes, but only at certain points, which are related with the radiation pattern of the original event. The more detailed waveform analysis presented in Figs. 3.33, 3.34 and 3.35 show the two fault characteristics we have mentioned here, as type 1 and 3 earthquakes present larger energy amplitudes at the the fault stations, but particularly in the one located right outside the structure, FO station. Results for type 2 earthquakes show an important difference between settings at the edges of the fault, where the earthquake-induced maximum energy density amplitude is

significantly larger at the fault-present setting, thus revealing an important energy concentration inside the structure. This effect also creates a reduction in the amount of energy received by the rest of the stations.
The maximum energy density vs dip angle patterns are very similar to RMS energy density vs dip angle trends, for the three types of earthquakes. This observation supports the idea of a different oscillation pattern inside the system fault, which scales with its maximum amplitude. These results also support the idea that inner reflections at local structures help to concentrate energy, thus being another argument to assign waveguide-like characteristics to the system fault.
The maximum change in Coulomb yield function gives us an idea of which are the regions that are most affected by an external earthquake. Our show a concordance between these measurements with the ones obtained for the maximum energy density, reinforcing the breakwater and fiber optic light cable behaviors of the system main fault. This concordance allow us to suggest that the effect of the earthquake in a hydrothermal/volcanic region is profoundly affected by the local structures, converting them in key players in earthquake-volcano interactions.

3.4.2 NS experiment

We carried out an analysis of the dynamic influence that a $M_W = 6.1$ earthquake, whose hypocenter is located 100 km from a system composed by two mirroring faults, each one connected to a fluid reservoir. Peak overpressure changes on the system depend mostly on the earthquake radiation pattern, but local structures do produce an alteration on the spatial distribution of these peak values. Fluid reservoirs distort the wave motion and generate distortions at their vicinity, which depend on the input value of peak overpressure induced by the earthquake. For north and south earthquakes, the larger values on dynamic overpressure are found on the borders of the reservoirs, while for middle events, shadows where the maximum overpressure is negative are found behind each one of the reservoirs.
Maximum overpressure change is dampened inside the faults. Our results show that the most affected fault of the two that compose the system depends on the earthquake location, and the strike angle value. Thus, for north events and negative strike angle values, it is the right fault the one that reduces the peak overpressure the most, while for positive values of the strike angle it is the left fault the one that plays a larger role on the system dynamics. The opposite occurs with the southern earthquakes.
The structures do affect the wave motion, breaking the symmetry on the dynamic changes that should be expected if we would have not considered their role. And while their features do depend on the stresses transferred by the earthquake, they do play an important role.
Our analysis on the kinetic energy density transferred by the incoming earthquake show how the energy gets concentrated at the faults, and it is decreased inside the fluid reservoirs. The first feature shows a concentration that depends strongly in the incoming amount of kinetic energy of the earthquake, and that is more focused in the fault boundary that faces the earthquake. Depending of the earthquake, it is

possible to concentrate an important amount of energy density inside the faults and still keeping the space between them at a lower energy state. Another region where energy density is focused is at the border between a fault and its correspondent fluid reservoir, and also at the edges of the fault, as can be appreciated for the "north" earthquakes, where energy is more concentrated at the northern tip of the left fault. This effect is consistent with the "breakwater" characteristics we found for the fault in the vertical experiment.

A close station-by-station analysis shows that the energy density can be reduced up to a 30% of what is expected inside the reservoir. This highlights the role that reflections at the border of the structures do have. Our results show that the role of the local structures is of special importance in energy density transfer, and needs to be taken into account when studying earthquake-volcano interactions. A simple empirical estimation of this physical quantity, based only in the distance of the system to the earthquake hypocenter does not take into account this complexity. Based on the importance that the energy density analysis has on the study of the influence of earthquakes in a particular volcanic/hydrothermal system(Manga and Brodsky, 2006), our results are a relevant addition to the state of the art of the earthquake/volcano interactions.

The maximum increment in the Coulomb yield function is very relevant to study the faulting potential that a seismic wave train has on a particular system. Our results on the dynamic analysis of this physical quantity show that the earthquake characteristics play the most important role in the maximum yield function dynamic increment, thus highlighting the role of the earthquake focal mechanism, and its relative location of the respective to the volcanic/hydrothermal system. Nevertheless, the local structures still play a role in focusing the maximum change in the yield function. In particular, fluid reservoirs do concentrate the larger increments, as well as the fault boundaries, and the fault-reservoir interface. Under the influence of an earthquake, these are the regions that are the most affected and thus the ones that are most likely to break, if the increment is large enough.

Another interesting observation is that, for oblique seismic wave arrival, the shear stress transfer becomes very important for the yield function. This allows us to explain why the change on the yield function induced by the southern earthquakes at the northern regions of the system is larger than the one induced by the northern events, even with them being closer to the that region of the system. Given that the larger local increments on the yield function are found at the borders of the faults and at the reservoirs, and that this change scales with the original perturbation of the wave, we consider that the role of the structures on focusing shear stress can be critical to establish the faulting potential of an earthquake on a volcanic/hydrothermal region. This observation also extends the region of maximum influence of an earthquake to more than just the area where the larger compressions/extensions can be found.

3.5 Conclusion

Using numerical simulations, we studied the effect of earthquakes in the dynamics of a simple system of reservoirs connected to faults, which resemble the characteristics of volcanic/hydrothermal fields. We did this by studying two types of experiments: the first one involved several $M_W = 4.0$ affecting, in a close range, a simple system composed by a fluid reservoir connected to a single fault, whilst the second experiment considered the influence of many $M_W = 6.1$ earthquakes on a system compounded by two reservoirs, each one linked to one fault, located 100 km away from the earthquake epicenter. Our results show that the influence of earthquakes in regions where fluid is trapped at high pressures is not straightforward, and it can not be completely understood only by studying static stress changes in a fully elastic space. The role of local structures is very important to the dynamics of the system.

While most static and dynamic changes induced by an earthquake depend strongly on its focal mechanism, magnitude, and relative location respect to the studied system, local structures are important players regionally. Static stress transfer is affected by the presence of them with the creation of unexpected compression/extension regions. Dynamically, faults do concentrate kinetic energy inside them and have breakwater like characteristics, preventing certain regions of the space to receive the full impact of an earthquake. This is more appreciated in the study of the Coulomb yield function and dynamic stress change. The fluid reservoir also plays an important role, affecting the fluid motion and recording larger energy density concentrations as well as larger increments in the Coulomb yield function on its borders. The geometry of the system is also very relevant, and adds a level of complexity in the study of the influence of earthquakes in a volcanic/hydrothermal region. This complexity in system dynamics supports the idea of continuing studying the earthquake-fluid motion connection in more detail, with the extensive use of numerical simulations. Such an approach has been barely used in the literature, mainly because of its many complications in the implementation, and the long calculation times needed. Nevertheless, with increasing computing power, new and better results might arise, thus allowing us to have a better understanding of this complex phenomenon. Due to the characteristics of our simulations, our results can be applied to many different settings, such as hydrothermal and volcanic fields, and also to gas and oil risk assessment.

Finally, we want to focus ourselves in the local role of the structures in the earthquake-volcano interactions. Both fluid reservoirs and fault systems behave differently for the same earthquake, and they have an important role on system dynamics. Advances in the research of the role of local structures, while adding complexity to the problem, can certainly help to improve the understanding of the physics that control the influence of earthquakes in volcanic regions.

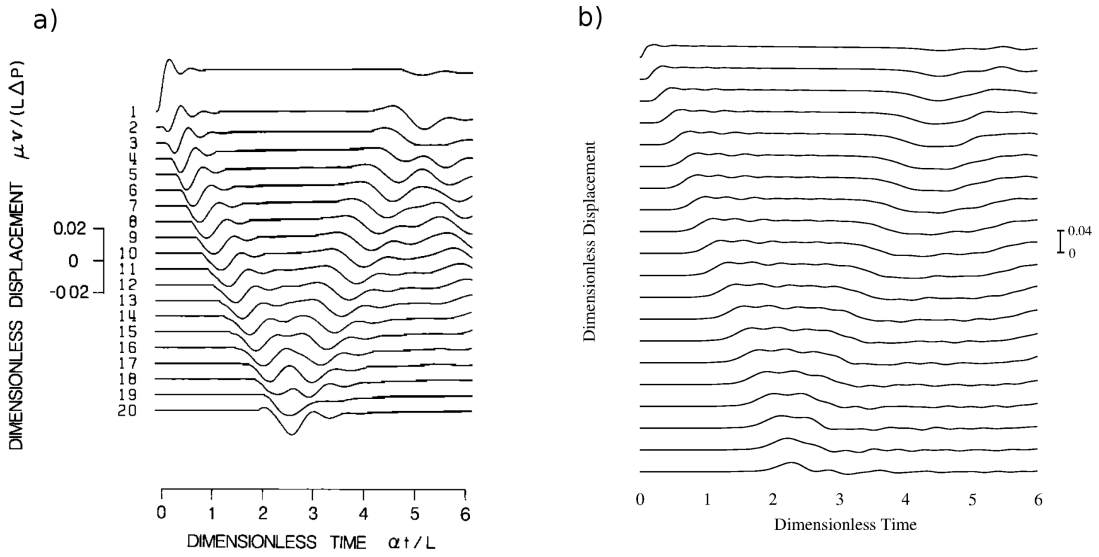

Figure 3.56: Normalized transverse displacement along the crack. We present the results from the original article(Chouet and Julian, 1985) in plot a) and the results obtained with our method in plot b).

3.6 Appendix

3.6.1 Validation

To test the validity of our results, we used our method to reproduce the numerical experiment performed by Chouet *et al*(Chouet and Julian, 1985), which consists in the simulation of the dynamics of an expending fluid-filled crack. The crack has lenght L and a thickness d. To obtain the system dynamics, the authors solve the equations of motion of a 2-D elastic space without gravity, coupled with the conservation of momentum and the continuity equation for the fluid. The equations are coupled by assuming a Poiseuille flow, which relates the shear stress at the crack wall to the fluid velocity.

In our methor we do not explicitly solve the equation of conservation of momentum and the equation of continuity. Instead, we get the dynamics of a system by solving the equations of motion of a 2-D fluid saturated space, coupled with a nonlinear diffusion equation, with a stress dependent permeability for the media. In our approach, the presence of the fluid is taken into account in the usage of effective stresses instead of total stresses as responsible of the deformations. We also assume that the fluid flow velocity is small compared to the wave velocity, thus we can compare our results to the case of a wet crack, when the grid spacing in both fluid and solid phases is the same. Nevertheless, we have to keep in mind that, due to the differences in the methods, some small differences migh be found between them.

Fig. 3.56 shows the evolution of transverse displacement in time at the crack, mea-

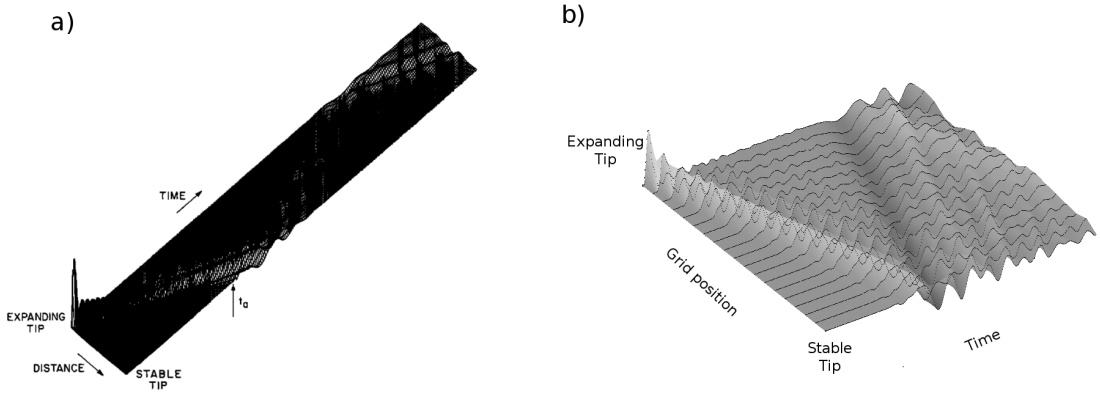

Figure 3.57: Normal velocity evolution during the crack propagation. Plot a) shows the results from the original article(Chouet and Julian, 1985), and b) presents the results obtained with our method. The total calculation time was similar for each experiment.

sured at several grid points along the fault. Plotted quantities were normalized following the indications of the original article. Also in the same figure the results from the original article by Chouet are plotted. While there is some differences between the results, both the scale and the most robust behaviors are reproduced with our method. We see the arrival of a first perturbation, with the consequent reflection, with an inverse dominant motion. This means that, if the first perturbation is an extension, the second major motion is a closure of the spaces.

Normal component of the velocity in time is presented in Fig. 3.57, with a comparison to the result from the original article. The same features discussed before are present in this plot, with the reflection at the fixed tip of the crack clearly marked. A second reflection at the expanding tip of the crack is also recorded, being consistent with the results from the original article. The similarity between the results is evident here.

Chapter 4

Numerical study of the unusual response of Nevados de Chillán volcano to two aftershocks of the 2010 $M_W = 8.8$ Maule earthquake

Abstract

Between January and March, 2012, two important aftershocks of the $M_W = 8.8$ Maule earthquake were recorded near the central chilean shore. Both events, with magnitudes $M_W = 6.1$ and $M_W = 7.1$, were located about 200 km from the Nevados de Chillán volcanic complex. The volcanic/hydrothermal system presented a strange response, with an increase in seismicity for the smaller event, and a reduction of the local activity for the second, larger earthquake. In this article, we show the results of numerical simulations of the dynamic interaction of each earthquake with the system, finding that the reaction to the smaller event was most likely to occur due to important earthquake-induced dynamic volumetric changes in the system, while the influence of the second earthquake was reduced by a combination of the relative position of the earthquake plus the role of the main system fault, which dampened the volumetric changes induced by the earthquake. Our results suggest that the role of local structures in earthquake-volcano interactions can be important under certain conditions, and should therefore not be disregarded.

This chapter will be submitted as an article to *Journal of Volcanology and Geothermal Research*, under the title "Numerical study of the unusual response of Nevados de Chillán volcano to two aftershocks of the 2010 $M_W = 8.8$ Maule earthquake", by C. Farías, B. Galván, and SA. Miller.

4.1 Introduction

Earthquakes can trigger several types of responses around the globe, in wide time and space windows(Bebbington and Marzocchi, 2011b)(Fuchs et al., 2014)(Hardebeck et al., 1998)(Pollitz et al., 2012)(Manga and Brodsky, 2006). While aftershock sequences in the rupture region are the most known phenomena(Harris, 1998), increases in seismic activity immediately after the passage of the waves have also been observed both at the earthquake near and far fields(Wang et al., 2015)(Johnson et al., 2015). Responses are usually recorded in fault zones(Wei et al., 2015)(Hill et al., 1995) and in regions where high-pressurized fluids are present, like geothermal fields, and volcanic zones(Wang et al., 2011)(Lupi et al., 2014)(Brodsky and Prejean, 2005). Long-term reactions have also been observed at several volcanic systems(Bonali et al., 2013)(Hill et al., 2002), with delays that can go as far as several years, and even decades, for some megathrust earthquakes(Marzocchi et al., 2002)(Bonali, 2013)(Bonali et al., 2013). Earthquake-induced static and dynamic stress changes have often been used to explain these connections, and they both operate at different time and distance scales and distances.

Static stress changes promoted by earthquakes decay rapidly outside the rupture zone, as $1/R^3$, with R the distance from the earthquake fault to a particular measuring point. They are permanent and can create important volumetric changes at reservoir level, which in turn may affect the physical properties of the high-pressurized fluids that are trapped in that region. The long-term effect of many large magnitude earthquakes is often studied by analyzing the permanent change in the normal and volumetric stresses at one region, with emphasis on some existing structure, and focusing on induced clamping/unclamping patterns, and total pressure changes where the fluids are believed to be present(Walter and Amelung, 2007) (Sánchez and SR., 2004)(Fujita et al., 2014). Another way to analyze these variations consist in the study of the structural change of both magnitude and orientation of the principal stresses at some volcanic/hydrothermal regions, which may help explain the change in the post-earthquake seismic regime at these regions. This last effect has been observed after megathrust earthquakes in Sumatra, Chile, and Japan (Lupi and Miller, 2014). For smaller earthquakes, the area of influence on the static stress tensor decays dramatically with its magnitude, and their importance is often disregarded at long distance triggering(Manga and Brodsky, 2006)(Freed, 2005).

Dynamic stress changes are transient, but they decay slowly from the rupture zone compared to the static stress changes(Manga and Brodsky, 2006)(Hill, 2008). They are related to the changes in the local stress tensor at a particular point during the passage of the seismic waves, and their magnitude is more important than the static stress changes at long distances. They are often used to explain earthquake responses at several hundreds or even thousands of kilometers from its hypocenter(Husen et al., 2004)(Mazzini et al., 2007)(Lupi et al., 2014). Two main types of physical mechanisms are often used to explain how dynamic stress changes may trig-

ger volcanic/hydrothermal responses to an earthquake: the first one being that the changes on the local stress tensor might lead to an immediate rupture in a distant fault zone(Hill, 2008)(wave potential for triggering tectonic (nonvolcanic) tremor, 2010)(Hill and Prejean, 2007), and the second being related to changes at the physical properties of high-pressurized fluids that are close to a critical state, which in turn can promote ruptures, tremor, and in most extreme cases, eruptions(Brodsky et al., 1998)(Sparks et al., 1977).

The directivity of the earthquake interaction with a volcanic/hydrothermal system is a topic that has not been widely covered, but it is also important. Observations of dynamic triggering show that not all the fault zones and geothermal regions located at the same distance from an earthquake react in the same way. While this might be explained due to the closeness to a critical state of a particular system, data shows that there are some particular directions in which most of the responses have been observed(Convertito et al., 2013). A well known case of this is the seismic response of several fault zones and geothermal fields to the 2002 $M_W = 7.9$ Denali earthquake, in which most of the responses where located in a region that followed the direction of the earthquake rupture(Gomberg et al., 2004). While this might be related to the earthquake radiation pattern, it might also be related to the relative directivity of the receiving fault, which may have an important role in the complete influence of an earthquake in a specific zone (Farías et al., 2016).

To advance in the understanding of the underlying physical mechanisms that control such responses to distant earthquakes, both larger datasets and more detailed theoretical improvements are necessary. Central-south Chile is an ideal setting to study volcanic and hydrothermal responses to distant earthquakes, specially after the occurrence of the $M_W = 8.8$ Maule earthquake, with more than 35 $M_W > 6.0$ events recorded near the chilean shore since. The original earthquake generated significant stress changes at the volcanic arc(Lupi and Miller, 2014), with the Planchón-Peteroa, Copahue, and Laguna del Maule volcanic systems, presenting the most important signs of unrest since the earthquake(Bonali, 2013)(Bonali et al., 2013)(Le Mével et al., 2015)(Venzke, 2013).

One volcanic system that has shown interesting responses to external earthquakes in this region is the Nevados de Chillán complex, located in 36°51′48″ S 71°22′36″ W. This volcanic chain is composed by 24 cones, located along a main lineament heading N 30°W with the most active being Volcán Viejo, Volcán Nuevo, and Volcán Nevados. Several hydrothermal fields are found at the complex, with the Aguas Calientes valley being one of the most prominent(Dixon et al., 1999). Most of the activity of the last 110 years has been recorded at Volcán Nuevo(Venzke, 2013), which was created in an eruption that did begin right after the 1906 $M_W = 8.2$ Valparaíso earthquake(Gonzalez-Ferrán, 1995). From 1900 to 1940, Nevados de Chillán entered in an eruptive phase almost immediately after three large earthquakes located in central Chile, in 1906, 1914, and 1928(Farías et al., 2014)(Gonzalez-Ferrán, 1995).

An interesting response was recorded at Nevados de Chillán volcanic system during the first quarter of 2012. Almost two years after the $M_W = 8.8$ 2010 Maule earthquake, two important aftershocks were registered near the chilean shore. The first one, a $M_W = 6.1$ dip-slip event, was recorded on January 23$^{\text{rd}}$, with its hypocenter located to the west of the volcanic complex, roughly 200 km away from its main structures. Right after the passing of the waves, tremor activity at Nevados de Chillán suddenly increased, and when it subsided, VT event rate increased about 3 times to what the background was before the earthquake. Seismicity was mostly located at a hydrothermal field, called Aguas Calientes valley. On March 5$^{\text{th}}$, the second event was recorded. The aftershock was a $M_W = 7.1$ earthquake, with a similar fault mechanism as the $M_W = 6.1$ event. Its hypocenter was also located around 200 km from the main structures of the volcanic complex, but it was positioned to north-west of the system. Unfortunately, the record during the weeks around the occurrence of the earthquake is not complete, due to a 12-hour data loss time window. Nevertheless, a decrease in volcano tectonic seismicity was observed(Farías et al., 2014). While such a difference in the response might be attributed to the volcano being in a more critical state before the first, smaller, earthquake than before the second, larger event, the rate of VT seismicity shows that the background activity was significantly higher before the second aftershock than before the first. Based on a particle motion analysis, the authors proposed that the difference in the response can be explained by a different induced normal stress change at the main local fault for both earthquakes, with the $M_W = 6.1$ event inducing unclamping, which in turn promoted faulting, and hence the increase in VT activity.

Numerical simulations can result very useful for the interpretation of observations for which direct measurements of physical quantities such as internal fluid pressure and local stresses are not possible to obtain. In this article, we aim to simulate the effect of synthetic earthquakes, similar to the two described before, and to study their effect in a simplification of the Nevados de Chillán volcanic complex, which is composed by a main fault, and a fluid reservoir. We use the method introduced by Farías *et al*(Farías et al., 2016) in a 2-D space, following the dynamic effect of the seismic waves in a situation when static stresses generated by the seismic events are negligible.

4.2 Theory and Methodology

We are interested in the influence that distant earthquakes have in volcanic zones, where fault systems are present. To account for the long distances and the geometry of the setting we are studying, we set up numerical experiments in a 2-D space, looking at the North-East plane. By doing this, we do not take into account the dynamic role of gravity in the system, as it has little impact on wave motion.

To simulate, we begin considering the equations of a 2-D poroelastic space:

$$\frac{\partial \sigma_{xx}}{\partial t} = (\lambda + 2\mu)\frac{\partial v_x}{\partial x} + \lambda \frac{\partial v_y}{\partial y}\,, \tag{4.1}$$

$$\frac{\partial \sigma_{yy}}{\partial t} = (\lambda + 2\mu)\frac{\partial v_y}{\partial y} + \lambda \frac{\partial v_x}{\partial x}\,, \tag{4.2}$$

$$\frac{\partial \sigma_{xy}}{\partial t} = \mu \left[\frac{\partial v_x}{\partial y} + \frac{\partial v_y}{\partial x}\right]\,, \tag{4.3}$$

$$\frac{\partial v_x}{\partial t} = \frac{1}{\rho}\left[\frac{\partial \sigma^{\text{eff}}_{xx}}{\partial x} + \frac{\partial \sigma_{xy}}{dy}\right]\,, \tag{4.4}$$

$$\frac{\partial v_y}{\partial t} = \frac{1}{\rho}\left[\frac{\partial \sigma_{xy}}{\partial x} + \frac{\partial \sigma^{\text{eff}}_{yy}}{dy}\right]\,, \tag{4.5}$$

where σ_{ij} are the total stresses, while $\sigma^{\text{eff}}_{ij} = \sigma_{ij} - \delta_{ij}P$ are the the effective stresses, with P the total pressure at a point in space and δ_{ij} the Kronecker delta. Lamé coefficients are given by λ and μ, while ρ represents the density of the rock. Velocities are represented by v_x and v_y.

The interaction between fluid dynamics and stresses is given by

$$\frac{dP_{\text{over}}}{dt} = \frac{1}{\phi(\beta_{\text{f}} + \beta_\phi)}\left[\nabla \frac{\kappa}{\eta}\nabla P_{\text{over}}\right] + B\frac{d}{dt}\left[\frac{\sigma^{\text{eff}}_{xx} + \sigma^{\text{eff}}_{zz}}{2}\right]\,, \tag{4.6}$$

where β_{f} and β_ϕ are fluid and pore compressibility, κ is the permeability, and η is fluid viscosity. Permeability κ is a function of normal stress, and is given by

$$\kappa = \kappa_0 \exp\left(-\frac{\sigma_n}{\bar{\sigma}}\right)\,, \tag{4.7}$$

where κ_0 is the permeability at zero effective stress, $\bar{\sigma}$ is a constant, and σ_n is the normal stress, defined by

$$\sigma_n = \frac{\sigma^{\text{eff}}_{xx} + \sigma^{\text{eff}}_{zz}}{2} + \frac{\sigma^{\text{eff}}_{xx} - \sigma^{\text{eff}}_{zz}}{2}\cos 2\theta + \sigma^{\text{eff}}_{xz}\sin 2\theta\,, \tag{4.8}$$

where θ is the dip angle of the particular plane in which normal stress is measured.

The last term of Eq. 4.6 is considered as a source term, and it links the pressure evolution with the stresses transferred by the earthquake into the system. There, B is the Skempton coefficient, which typically is considered to be between 0.5-1.0(Jaeger et al., 2007).

To account for the wave motion without the problem of numerical wave reflections at the boundaries, we use Convolutive Perfect Matched Layers (CPML), which are absorbing regions in the space next to the boundaries, in which stresses and velocities are attenuated. The application of this method to poroelastic spaces was developed by Martin and colleagues (Martin et al., 2008), but requires null boundary and initial conditions for velocities and stresses. To adapt this method to our simulations,

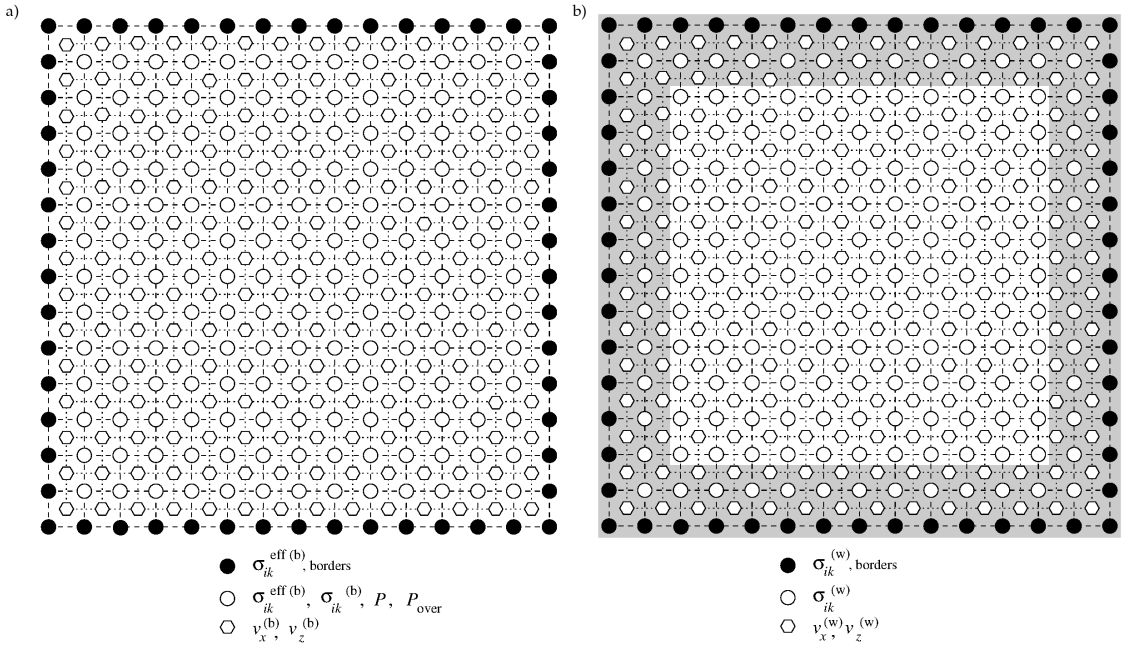

Figure 4.1: Grid for the base (left) and wave (right) phases of our simulations, with indications of what quantities are measured in certain points. Black points indicate the cells which are used to set the boundary conditions on the stresses. Grey areas represent the location of the absorbing boundary layers.

we divided the system in two: a base part, which is related with the initial stress conditions, and a wave part, that accounts for all the dynamic changes induced by the passage of the seismic waves. Details of the superposition method can be found in (Farías et al., 2016).

We use a staggered grid for each phase in our calculations, following the method of Saenger (Saenger et al., 2000). Fig. 4.1 presents sketches of them, with the second one including the absorbing layers. We apply Dirichlet boundary conditions on velocities and stresses in the base grid, and null boundary conditions at the wave grid.

Our system of interest consist on a 2-D poroelastic space, with a NW oriented fault, and a fluid reservoir of the structure. We then generate earthquakes far from the fault region, and follow both the dynamic and static changes induced by them. The scope of the experiment is to simulate the interaction of two earthquakes of magnitudes $M_W = 6.1$ and $M_W = 7.1$ respectively, with our system. The epicenters of both events are located at a distance of about 200 km from the fluid reservoir. This setting is a simplification of central Chile, where Nevados de Chillán volcanic system recorded a intriguing response to two important aftershocks of the 2010 Maule earthquake(Farías et al., 2014).

Fig. 4.2 shows the setting of the experiment. We have 2-D poroelastic space in the North-East plane, at a depth h_0, with a fault defined by a region of lower Young's

Symbol	Parameter Name	Parameter value
B	Skempton coefficient	$B = 0.5$
ρ	Rock density	$\rho = 3000$ kg/m^3
ρ_f	Fluid density	$\rho_f = 1000$ kg/m^3
κ_0	Permeability in the space, at zero stresses	$\kappa_0 = 1 \times 10^{-15}$ m^2
κ_f	Permability at the main fault	$\kappa_f = 1 \times 10^{-13}$ m^2
E_0	Young's modulus outside local structures	$E_0 = 5.93 \times 10^{10}$ Pa
E_f	Young's modulus at the main fault	$E_f = 0.7E_0$
E_r	Young's modulus at the reservoir	$E_r = 1.5E_0$
ν_0	Poisson ratio outside local structures	$\nu_0 = 0.3$
ν_f	Poisson ratio inside the main fault	$\nu_f = \nu_0$
ν_r	Poisson ratio inside the fluid reservoir	$\nu_r = 1.1\nu_0$
φ	Angle of internal friction	$\varphi = 32.6^o$
S_0	Cohesion	$S_0 = 3.1 \times 10^7$ Pa
ΔP_0	Initial overpressure at the reservoir	$\Delta P_0 = 10$ MPa
h	Depth at which the N-S plane is located	$h = 1000$ m
α	Strike angle of the main fault	$\alpha = -40^o$

Table 4.1: List of parameters used for the simulations, with emphasis on fluid and elastic properties of the structures.

modulus, and a larger permeability. The strike angle of the fault is α. Elastic parameters at the fluid reservoir are also different than the ones from the rest of the space, following the observations of Heap *et al*(Heap et al., 2014), with Young's modulus and Poisson's ratio at the reservoir being slightly larger. Reservoir overpressure is ΔP. Values for the most important simulation parameters are presented in Table 4.1.

In our experiment, we generate typical subduction earthquakes. Due to the 2-D constrain of our setting, we consider the projection in the North-East plane as our source. We calculate the earthquake rupture length, width, and slip, by using the following relations:

$$L = \left[\frac{1}{\mu\Gamma_1\Gamma_2} 10^{\frac{3}{2}(M_W+6)}\right]^{\frac{1}{3}}, \qquad W = \Gamma_1 L\,, \qquad \Delta U = \Gamma_2 L\,, \tag{4.9}$$

where μ is the second Lamé coefficient and M_W the earthquake magnitude. Γ_1 and Γ_2 are scaling parameters, given by

$$\Gamma_1 = \frac{1}{3}\,, \qquad \Gamma_2 = \frac{3}{2} \times 10^{-5}\,.$$

To follow the dynamic behavior of the relevant physical quantities, we placed 11 stations at different points of both the fault region and outside it. Their location was designed with the purpose of obtain information on the dynamics of the system at the different structures of the system. Table 4.2 present the location and names of each station.

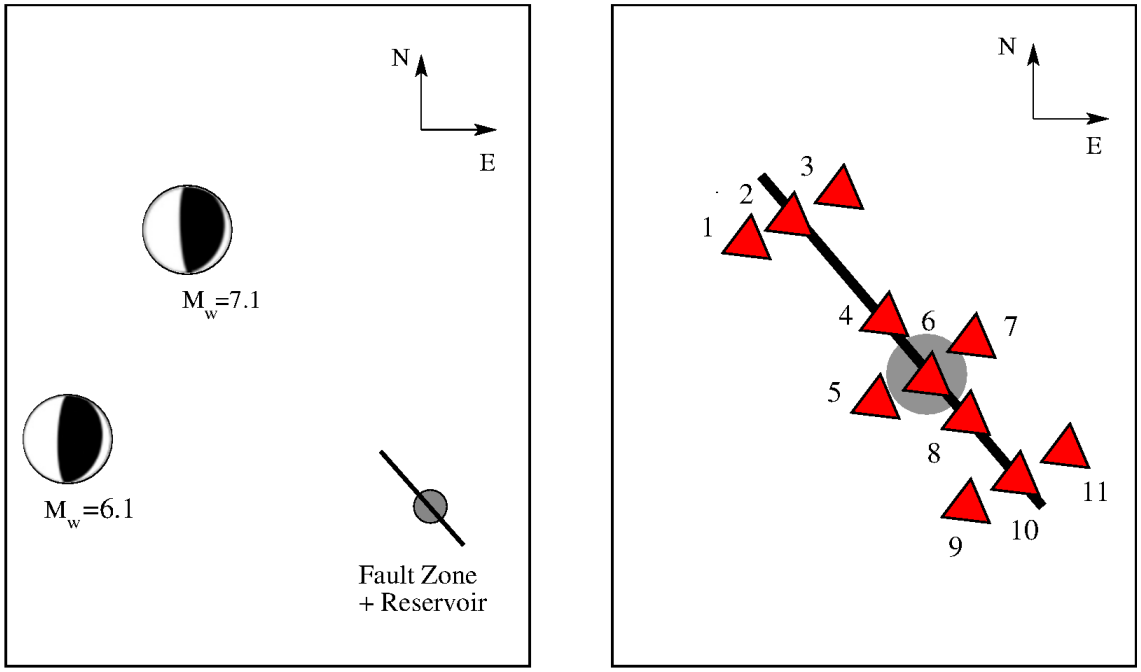

Figure 4.2: Left: Experiment Setting. Two earthquakes are generated about 200 km from the system under study. The volcanic/hydrothermal system is considered to be a NW fault connected to a fluid reservoir. Right: Close-up to the fault zone, showing the placement of the 11 stations we use to records timeseries. This station array allow us to capture more details of the dynamic of each structure of the system. More details on the location of the stations are presented in Table 4.2.

Number	Name	Code	Relative Location
1	Fault Up West	FUW	Space
2	Fault Up	FU	Fault
3	Fault Up East	FUE	Space
4	Reservoir Up	RSU	Fault
5	Reservoir West	RSW	Space
6	Reservoir	RS	Reservoir
7	Reservoir East	RSE	Space
8	Reservoir Down	RSD	Fault
9	Fault Down West	FDW	Space
10	Fault Down	FD	Fault
11	Fault Down East	FDE	Space

Table 4.2: Detail of the used stations, including name, abbreviations, and relative location in the system. Here, space stands for any point which is not inside the main system fault or in the fluid reservoir.

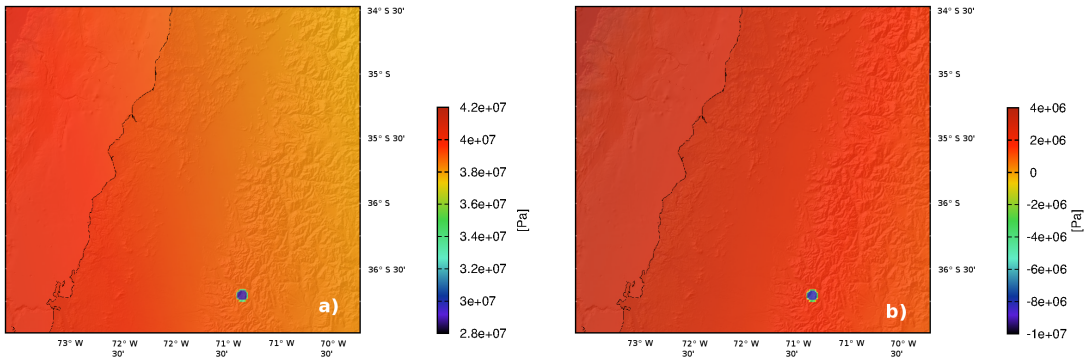

Figure 4.3: Initial principal stresses in our 2-D simulation, being a) $\sigma_1 = \sigma_{xx}$ and b) $\sigma_2 = \sigma_{yy}$. Both stresses were calculated a depth $h = 1$ km. Quantities are plotted in the central-south Chile map.

Since we are focusing on the co-seismic behavior of the system to the two external earthquakes, we assumed a semi-static base behavior, with initial effective stresses as presented in Fig. 4.3, featuring a gradient in σ_1, according with what is expected in a subduction zone. Initial fluid pressure was assumed to be the hydrostatic pressure at a depth $h_0 = 4000$ m.

4.3 Results

Our scope is to study the dynamic changes in the important physical quantities induced by the two $M_W = 6.1$ and $M_W = 7.1$ Maule earthquake aftershocks. Being the latter event about 32 times larger than the former, the magnitude of the perturbations in the space should be significantly different. Fig. 4.4 and 4.5 show the overpressure evolution of the earthquakes, defined by

$$\theta = (B/2)(\sigma_{xx}^{\text{eff}} + \sigma_{zz}^{\text{eff}}) \ , \tag{4.10}$$

with B the Skempton coefficient. The difference in the magnitude of θ is clearly noticeable between the earthquakes, but the differences between them are reduced at the system, which is represented by a red dot, indicating the overpressure of the fluid reservoir. In fact, and due to its radiation pattern, the $M_W = 6.1$ event generates larger volumetric changes at the reservoir level than the $M_W = 7.1$ earthquake. Moreover, the main fault of the volcanic/hydrothermal system is appreciated in the wave motion of this last event, with a reduction of the overpressure change along it. The effect of this main structure is not clearly noticeable in the the volumetric changes induced by the $M_W = 6.1$ earthquake, but it does generate reflections at the fault and reservoir level, as it can be appreciated with some interference patterns after the first main wave train arrives. The effect of the shear wave at the volcanic/hydrothermal system is very different between events, as is presented in Figs. 4.6 and 4.7. The influence of the $M_W = 7.1$ earthquake gets dampened at the

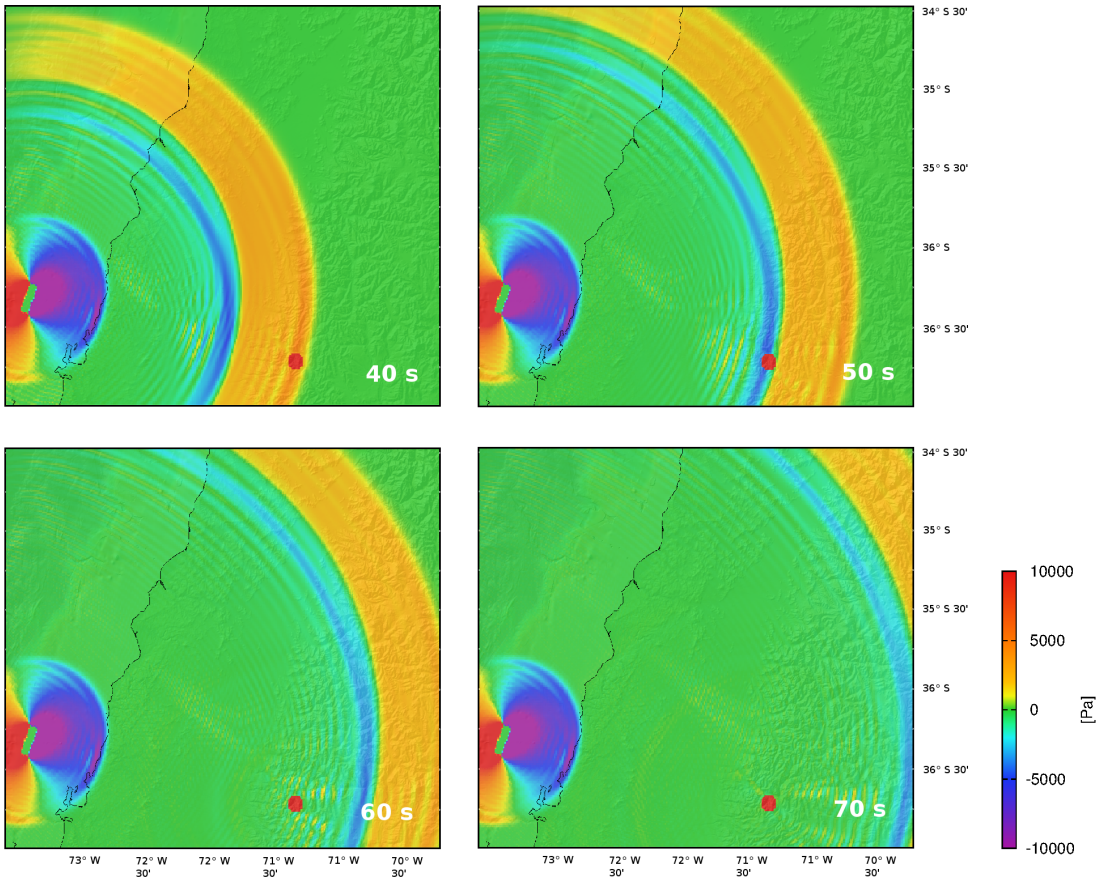

Figure 4.4: Dynamic evolution of the dynamic overpressure θ array during the $M_W = 6.1$ earthquake, where θ is defined in Eq. 4.10. Measurement times are $t = 30, 40, 50$, and 60 s.

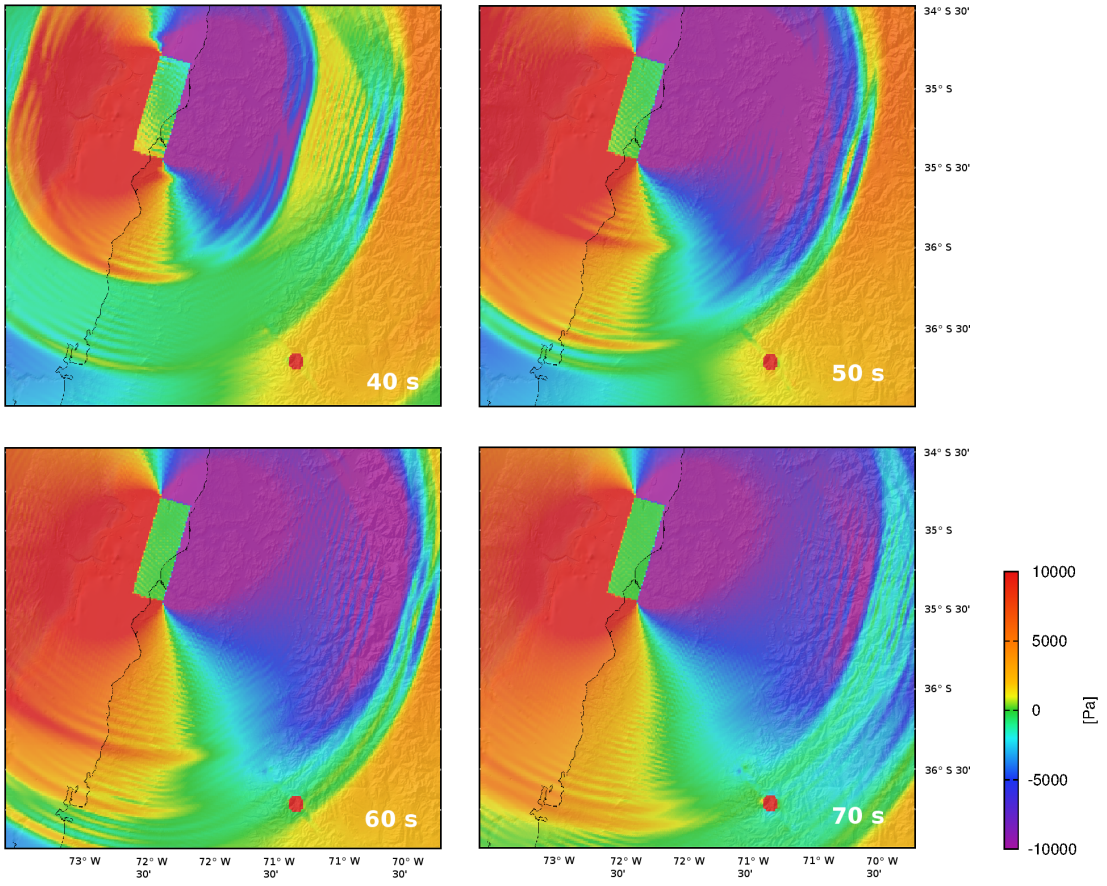

Figure 4.5: Time evolution of θ, defined in Eq. 4.10, for the $M_W = 7.1$ event. We present the results at $t = 30, 40, 50$, and 60 s, with t the time after the wave release at the earthquake rupture zone.

fault, but it is still significantly larger than the $M_W = 6.1$ event.

Overpressure waveforms, recorded at the 11 stations, gives us a closer insight on the dynamic volumetric changes induced by the earthquake. To improve our understanding of the system, and to isolate the role of local structures in the earthquake influence, we performed two experiments for each earthquake: one when the system did include the main lineament, and other one when this fault was not present. Fig. 4.8 shows the overpressure waveforms at all the stations, comparing the results obtained in the two systems. They show little difference between the settings, meaning that the fault does not play a significant role in the system dynamics. The maximum overpressure value, at all stations, is between 4 and 5 kPa, meaning that, during the earthquake, the maximum overpressure change that affects the system is about 10 kPa, which is considered to be high enough to enhance the fluid activity in a reservoir close to a critical state(Fujita et al., 2014). Interestingly, peak overpressure value is slightly larger at the reservoir than at the station located to its west, RSW, which might be due to the reflections at the reservoir level that we can see in the overpressure wave propagation maps presented in Fig. 4.4.

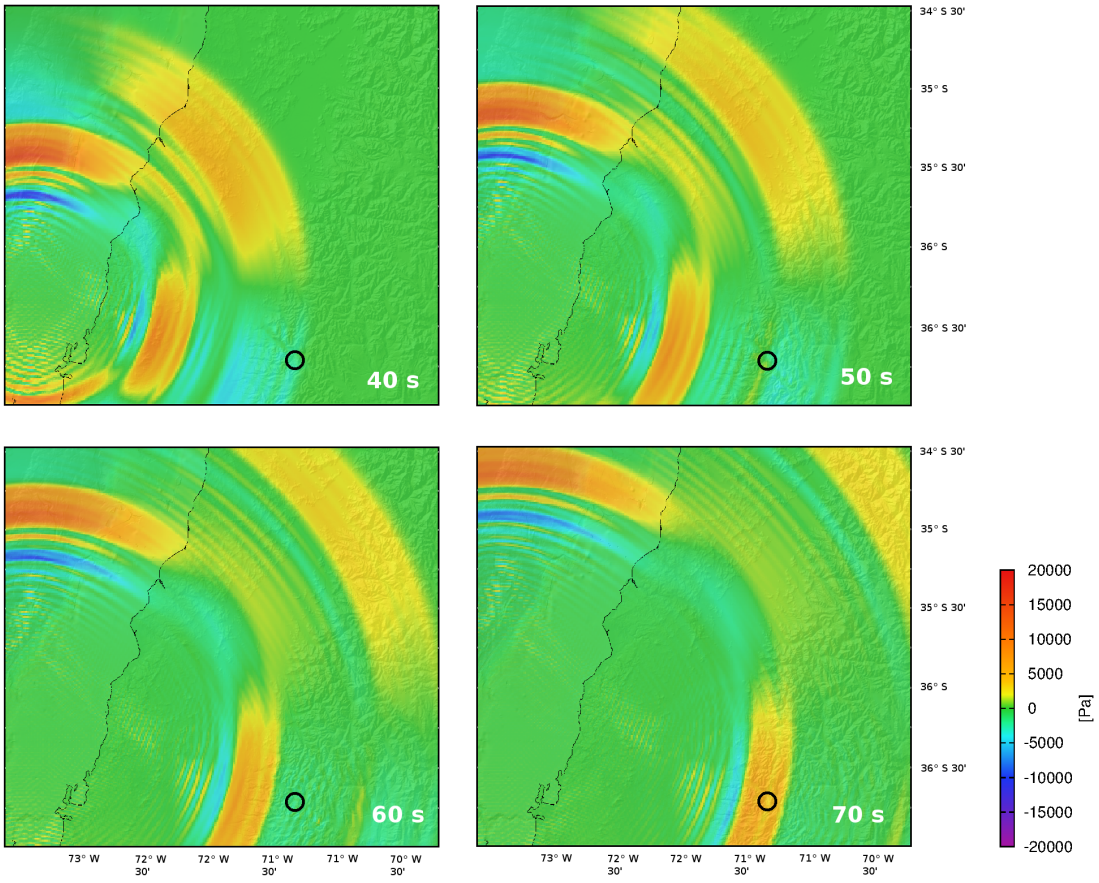

Figure 4.6: Shear stress $\sigma_{xz}^{(w)}$, induced by the $M_W = 6.1$ event, measured at $t = 30, 40, 50,$ and 60 s. Fluid reservoir is marked with a black circle.

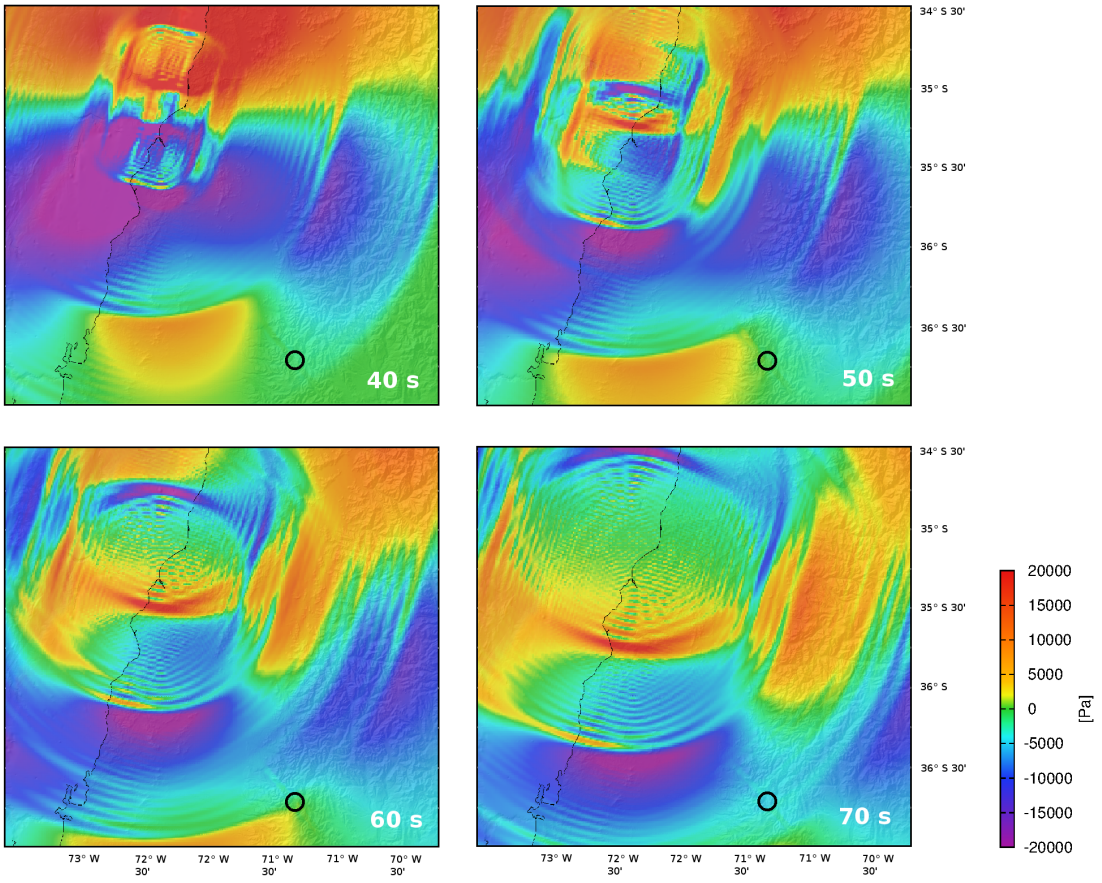

Figure 4.7: Evolution of the shear stress $\sigma_{xz}^{(\mathrm{w})}$, induced by the $M_W = 7.1$ event. We present the measurements obtained at $t = 30, 40, 50$, and 60 s, with t the time after the beginning of the earthquake. The fluid reservoir zone is indicated with a black circle.

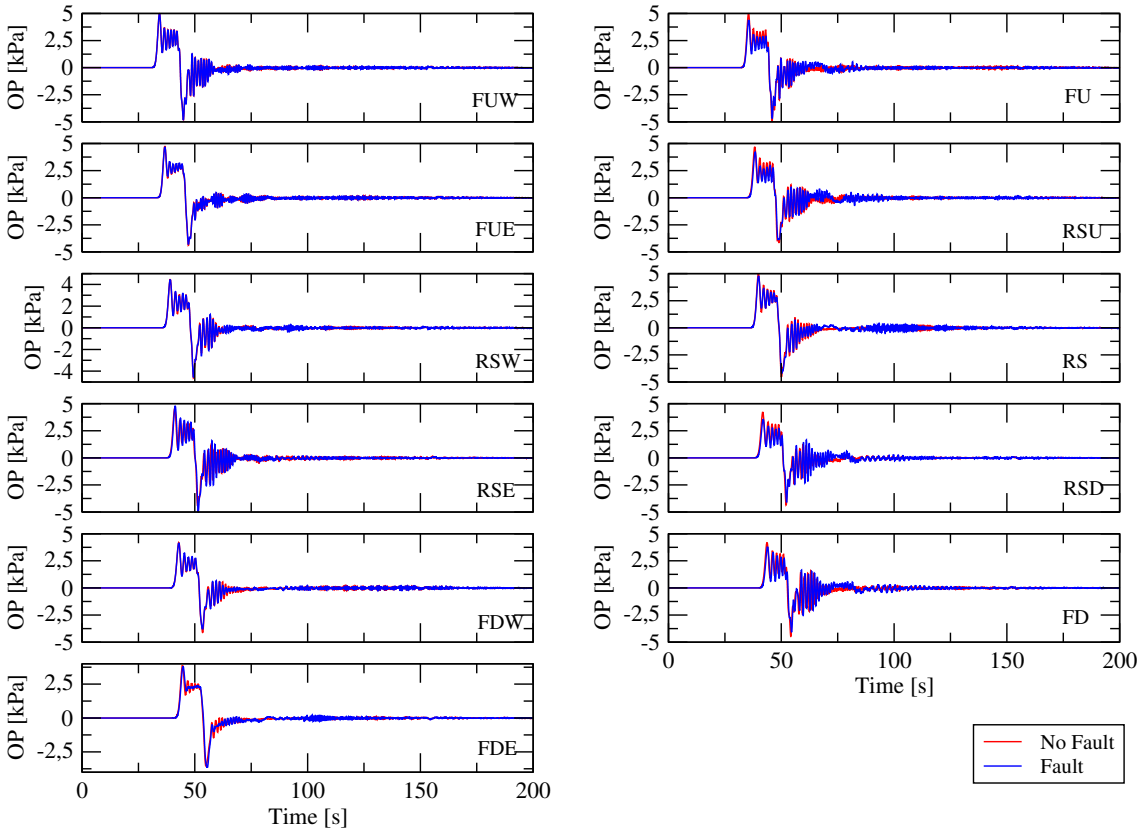

Figure 4.8: Overpressure traces, measured at all the stations, for the $M_W = 6.1$ earthquake. A comparison between a fault-present and a fault-free setting is presented at each recording point. Red lines show the waveforms obtained in a elastic simulation, without a main fault, and blue lines present the timeseries obtained in the fault-present setting introduced in Fig. 4.2. Note how overpresure values are slightly larger in the fault-free setting, specially at FU, RSU, RS, RSD, and FD stations.

The comparison between the overpressure waveforms obtained in a fault-free and a fault-present setting for the $M_W = 7.1$ earthquake is presented in Fig. 4.9. The waveforms show lower overpressure amplitudes than the ones recorded for the $M_W = 6.1$ experiment, which we can see in Fig. 4.8, meaning that the volumetric changes induced by the larger earthquake at the system were not as important as the ones induced by the smaller event. The larger contrasts between settings are found in the stations located at the main lineament (FU, RSU, RS, RSD, FD), where the main differences are found when the structure undergoes volumetric compression, and at the coda of the signal, with the fault-free setting presenting the larger values. This difference can be as high as $\sim 25\%$ of the maximum overpressure value, which talks about a dampening effect of the fault that reduced the volumetric change induced by the earthquake inside itself. Interestingly, the stations located at the north part of the system do record a noticeably post-seismic stress change of about 1 kPa, but it is present only in them, not in the other stations. This post-seismic extension is also dampened inside the fault.

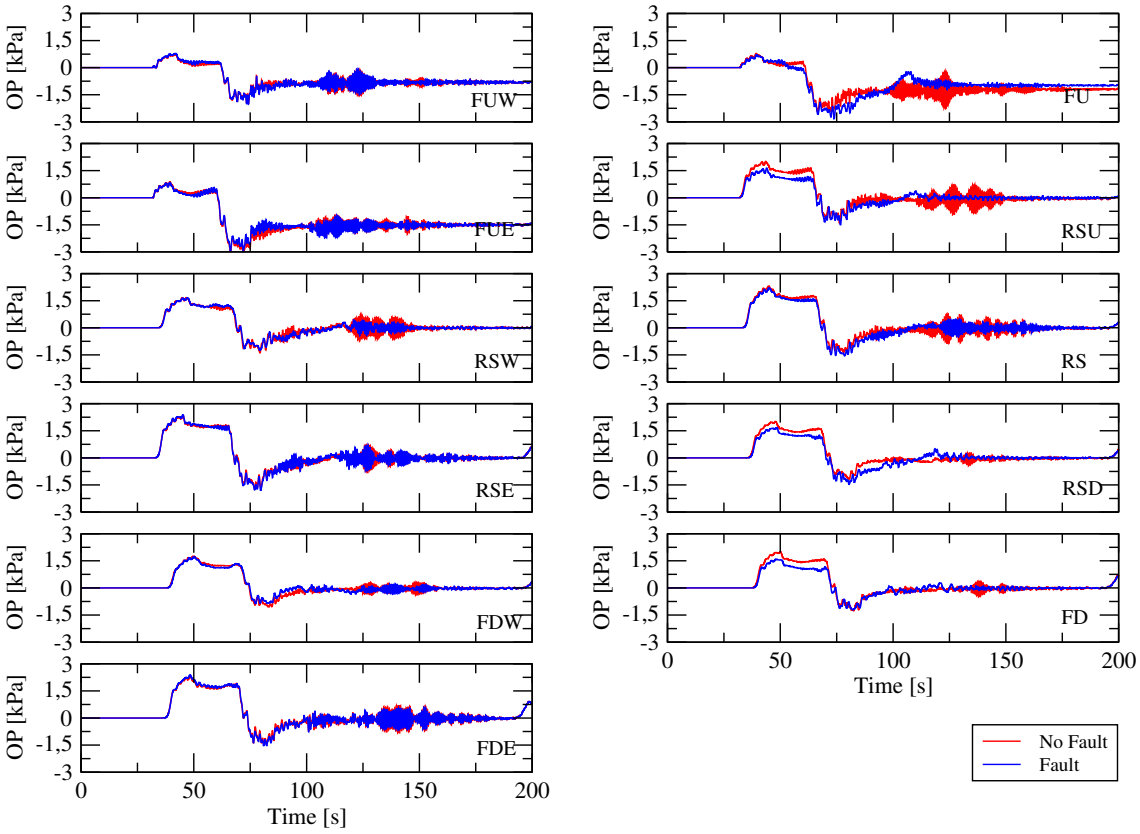

Figure 4.9: Overpressure traces, measured at all the stations, for the $M_W = 7.1$ earthquake. We also present a comparison between a fault-present and a fault-free setting, to isolate the role of the system main fault. Res lines present the results in the fault-free environment, while blue lines show the waveforms obtained in the fault-present setting. Note how the differences in dynamic behaviors between settings are particularly important at FU, RSU, RS, RSD, and FD stations, which are located inside the fault zone.

We also calculated the kinetic energy density, defined as

$$\varepsilon = \frac{1}{2}\rho\left(v_x^2 + v_y^2\right) . \tag{4.11}$$

Fig. 4.10 and 4.11 show the timeseries obtained for ε, for both the $M_W = 6.1$ and the $M_W = 7.1$ events, with their respective comparison between settings. It is evident that the larger earthquake induced larger energy density values, about four times larger than the ones induced by the smaller event. This is consistent with the observation ground motion velocity measured in the field, where the velocities obtained for the $M_W = 7.1$ aftershock were about twice as large as the ones measured by the $M_W = 6.1$ event (Farías et al., 2014).

Little difference is found between settings for energy density in the case of the larger event, with the results obtained at the fault-free setting being slightly larger than the results recorded in the fault-present system. This means that the role of the

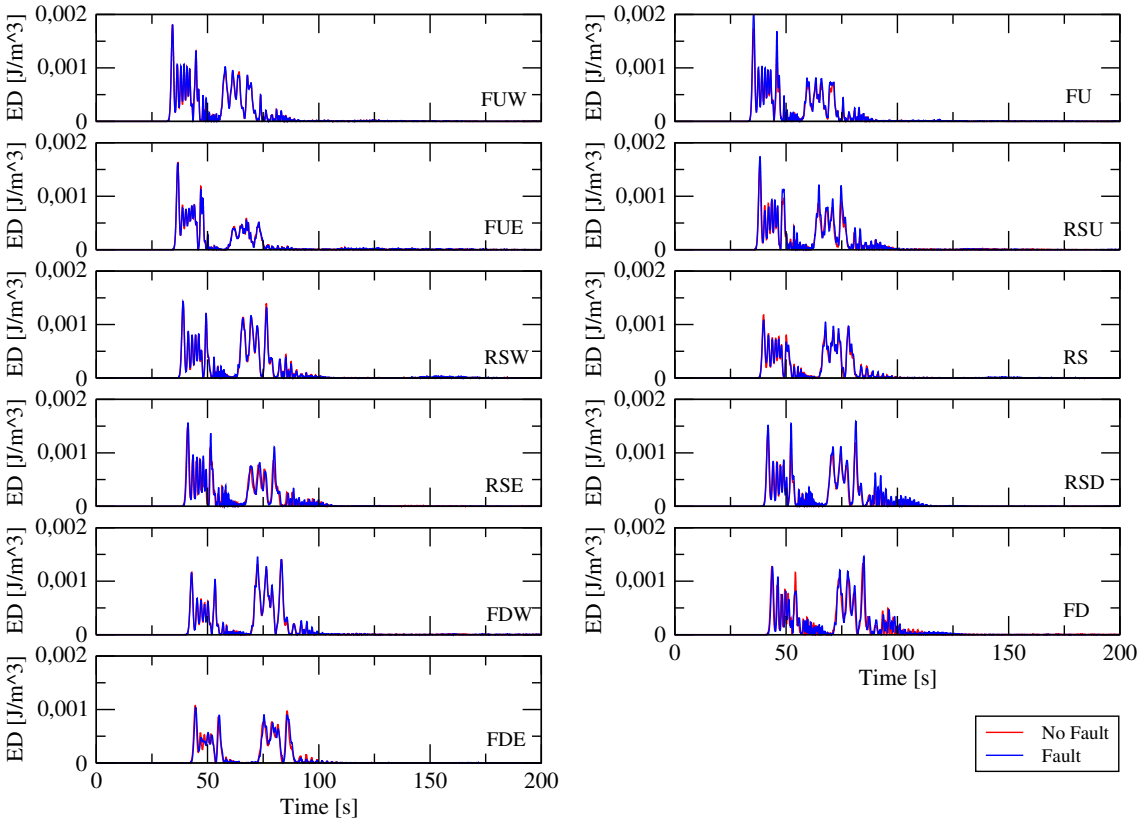

Figure 4.10: Energy density timeseries for the $M_W = 6.1$ event, measured at all the stations. Red lines show the behavior of the system when it is composed only by a fluid reservoir, whilst blue lines show the results obtained in a fault-present setting. The peak values of energy density are larger in the fault-present setting, at the system main alignment, as the results from FU, RSU, RSD, and FD stations show.

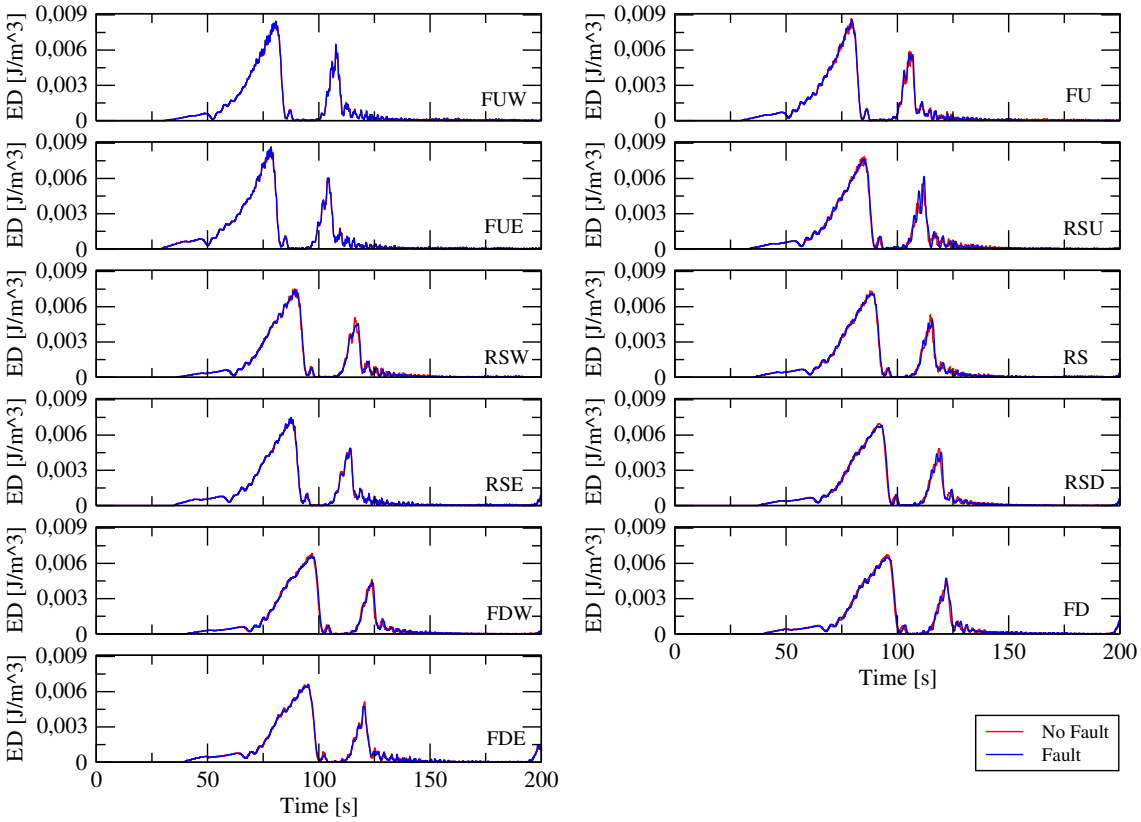

Figure 4.11: Energy density timeseries for the $M_W = 7.1$ event, measured at all the stations. Red lines show the timeseries when the system is composed only by a fluid reservoir, whilst blue lines show the results obtained in a fault-present setting. Differences between settings are small, meaning that the main alignment of the system has little influence in kinetic energy transfer.

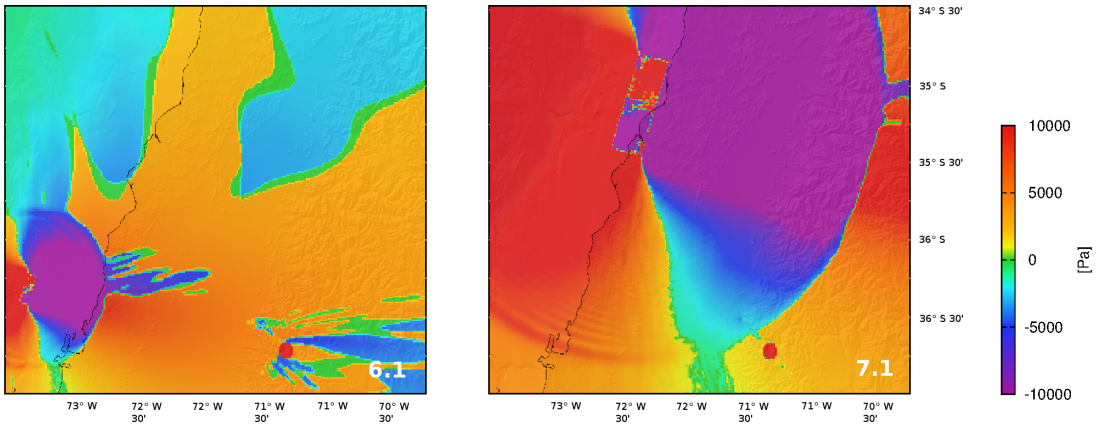

Figure 4.12: Maximum overpressure change, for $M_W = 6.1$ event (left) and the $M_W = 7.1$ earthquake (right), overlapped on the central Chile map. Plotting range is the same for both events, which highlights the difference in sizes of both earthquakes, and allow us to visually compare their influence in the system.

main lineament in energy transfer is negligible for this earthquake. This is not true for the smaller event, where important differences in the energy density amplitudes are found at the stations located inside the main fault. Energy density peaks are considerably larger inside this structure, with increases that can go as high as $\sim 58\%$ of the value obtained in a pure elastic, fault-free, setting. The role of the fault is particularly noticeable in the northern sections of the fault, although at the reservoir itself this difference is almost zero.

Peak values for certain physical quantities allow us to assess the largest influence an earthquake can have in a hydrothermal/volcanic system. We define them as the largest deviation of the studied variable respective to an initial state, which in our case is usually zero. Fig. 4.12 presents the maximum overpressure maps for both $M_W = 6.1$ and $M_W = 7.1$ events, in the whole space, featuring a clear dominance of the earthquake radiation pattern. The local effect of the fault and the fluid reservoir is clearly noticeable, with local variations at our hydrothermal/volcanic system. Fig. 4.13 presents both the maximum energy density and overpressure values at the local system scale. Maximum overpressure changes at the reservoir and fault level show that the $M_W = 6.1$ induced larger overpressure changes than the $M_W = 7.1$ event. Reflections at the fault and the reservoir generate areas where the maximum overpressure is extensive, as opposed to what is expected from a pure elastic case. This is due to reflections at the fault and reservoir, which alter the wave motion. Particularly, we found some portions of the fault where the maximum overpressure is negative, particularly at its north and south edges. The main lineament of the system plays an important role for the $M_W = 7.1$, dampening the maximum overpressure change, and in fact creating changes on the peak volumetric pattern inside the fault, with extensions being recorded mostly at its northern section, and compressions from the vicinity of the reservoir onwards.

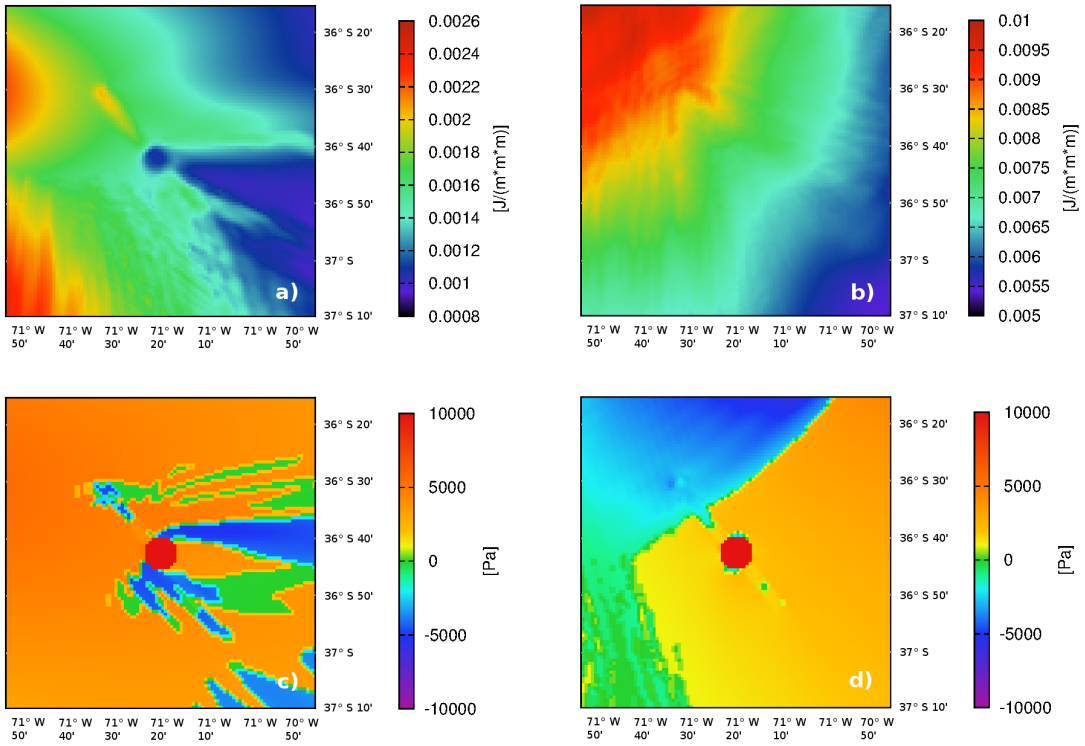

Figure 4.13: Maximum values for several quantities, all measured at the fault level, for both $M_W = 6.1$ and $M_W = 7.1$ events. a) Maximum energy density for $M_W = 6.1$. b) Maximum energy density for $M_W = 7.1$ event. c) Maximum overpressure for $M_W = 6.1$ earthquake. d) Maximum overpressure for the $M_W = 7.1$ event. Note how the role of the system main fault in kinetic energy transfer is more important for the $M_W = 6.1$ earthquake than for the $M_W = 7.1$, whilst it seems to play a more important role in overpressure peak values for the larger event than for the smaller one, which presents the compound effect of the fluid reservoir and the main lineament.

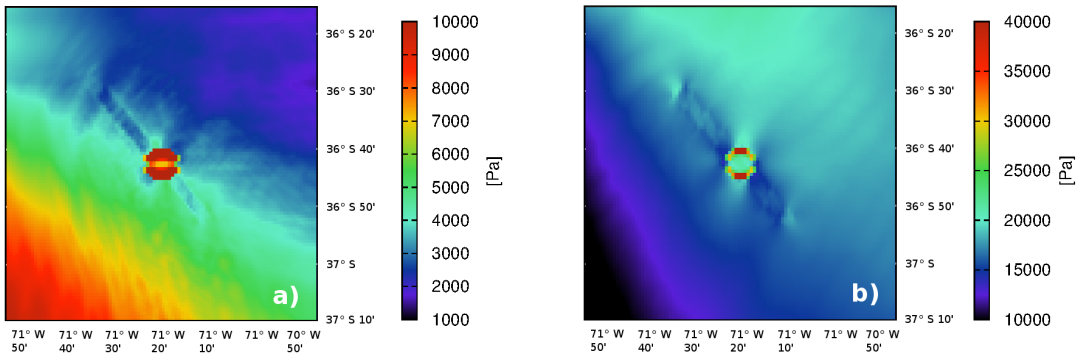

Figure 4.14: Maximum change in the Coulomb yield function at the system level, for both a) $M_W = 6.1$ and b) $M_W = 7.1$ events. Notice how the $M_W = 7.1$ event induced larger changes in the yield function than the $M_W = 6.1$ earthquake, but the patterns are significantly different, specially at the fault level.

Maximum energy density transfer, presented at the fault and reservoir level in Fig. 4.13, shows an important difference between earthquakes, with the larger event transferring more kinetic energy into the system than the smaller one, being 4 to 5 times larger than the largest amount induced by the $M_W = 6.1$ event. The effect of the fault is not easily noticeable for the $M_W = 7.1$ event, as it does not play an important role. The reservoir also does not affect the kinetic energy transfer for this event. A different behavior is found with the $M_W = 6.1$ event. There, the fluid reservoir is the least affected region of the system, with the lowest kinetic energy peaks inside it. The main lineament, nevertheless, presents an energy concentration at both sides of the reservoir, being more dominant at the northern section of the fault. For this earthquake, the main lineament enhances the kinetic energy transfer into the system.

The Coulomb yield function gives us information on how close is a particular point in space to break, and it is specially important when analyzing the faulting potential of an earthquake in a particular region. To study the effect of the earthquake in this function, we consider it to be composed by two main contributions: the base part, which depends on the quasi-static initial state of the system, and the wave part, which consists in the dynamic change of the function due to the influence of a seismic wave. This separation allow us to study the wave contribution separately. Fig. 4.14 presents the maximum value of the dynamic yield function for the two events under study in this article. The effect of the $M_W = 7.1$ in the system is noticeably larger than the one of the $M_W = 6.1$ event, which is due to the effect of an important shear stress contribution for the former earthquake. The spatial patterns at the local structures for this function are different between earthquakes. While the largest changes in the yield function are present at the reservoir level, the patterns at the fault present some important differences. For the smaller earthquake, the maximum changes in the yield function are dampened inside the main lineament of the system, which reduces the influence of the earthquake at that level. In the case of the larger seismic event, maximum dynamic changes on the yield function are slightly smaller inside the system main fault than outside the structure, but the larger changes in the function are present at the edges of the structure, thus making them the places that are more likely to break in the fault zone.

4.4 Discussion

We have simulated the situation presented in Farías *et al*(Farías et al., 2014), where a strange response of the Nevados de Chillán to two distant aftershocks of the 2010 $M_W = 8.8$ Maule earthquake was described. Both aftershocks, with magnitudes $M_W = 6.1$ and $M_W = 7.1$ respectively, had their hypocenters located about 200 km away from the volcanic complex. The system reacted to the smaller earthquake, generated in January 23rd, 2012, with a sudden increase in the number of tremor events, followed by an increase in volcano-tectonic (VT) activity nine hours later.

The response of the system to the second aftershock, that struck on March 25st, 2012, was completely different, with a decrease of the VT activity some hours after the earthquake.

In the original article, most of the seismicity in the Nevados de Chillán volcanic system was found to be related to the presence of a hydrothermal field, called Aguas Calientes valley, which is a very active hotspring spot, with a high rate of small VT events. The responses of the system were concluded to be located at the hydrothermal field and its vicinity, since those were the regions in a critical state, and thus the most likely to be affected by external perturbations.

Due to the large distance that separated the earthquakes from the volcanic zone, the static stress changes were negligible at the reservoir level. Dynamic changes at the fault level where then proposed to be the most plausible explanation for such strange response.

For our simulations we used a 2-D finite difference method to solve the equations of motion of a fluid-saturated poroelastic space, coupled with a non-linear diffusion equation. We found that, due to the relative position of each earthquake, the $M_W = 6.1$ event induced larger volumetric changes at the system, both at reservoir and fault level, than the $M_W = 7.1$ earthquake, up to twice as large. The fault does play an important role in the dynamic changes induced by the larger event on the system, dampening the maximum overpressure change inside the fault, and thus limiting the influence of the earthquake, but it does not play a significant role in the interaction between the smaller earthquake with the system. This means that the role of the larger earthquake at the system, which without a fault was already less important than the one recorded by the smaller earthquake, was significantly reduced by the main lineament of the system, and thus it did not have an important influence at the high-pressurized fluids.

Static stress changes at the reservoir level are negligible for both earthquakes. Nevertheless, the larger event does have a permanent influence on the northern section of the main fault, with a slight volumetric extension. Since we are assuming that the fluid reservoir is connected into the fault, this permanent change has the potential to induce a slight fluid migration from the reservoir level into the northern section of the main lineament. This would be reflected in a discouragement of the local seismicity at the reservoir vicinity. The real-life observation was, indeed, a decrease in VT activity, which in the Nevados de Chillán volcanic complex is linked to fluid mobilization.

Kinetic energy density transfer is larger for the $M_W = 7.1$ event than for the $M_W = 6.1$ earthquake, by a factor of about 4. This leads to a difference in the magnitude of velocity oscillation of 2, which is consistent with the observations of the original article. The role of the fault is not noticeable for the larger event, but it is for the smaller one, presenting energy concentration zones at the edges of the

fault, particularly on its northern section. This observation is not correlated with the maximum overpressure change, meaning that the shear motion for the larger earthquake is very important at the reservoir and the fault.

The differences in the shear motion due to each earthquake are reflected in the dynamic changes of the Coulomb yield function. Of the two earthquakes, it is the $M_W = 7.1$ event the one that induced significantly larger changes in the yield function than the $M_W = 6.1$ aftershock, and thus it was the one that brought the system closer to faulting. Field observations, nonetheless, show that there was not an increase in seismicity after the $M_W = 7.1$ event, which means that the changes in the yield function induced by this earthquake were not high enough to enhance the creation of new fractures in the system. The structure of the maximum change on the yield function is of interest as well, since the larger changes were recorded at the boundaries of the fault zone, and not inside it. This is an indication that, had the system be more close to a tectonic critical state, faulting could have been promoted at the boundaries of the main lineament, and at the reservoir.

The most important influence of the $M_W = 6.1$ was the change in ovepressure, particularly at reservoir level. The real life system can be considered close to a critical state, with a high rate of seismicity associated to its hydrothermal activity. Thus, the earthquake influence was present at fluid level, increasing their pressure, which favored the mobilization of them. This was seen at the Nevados de Chillán complex with an immediate increase in tremor activity, which is linked to fluid motion. Then, after tremor activity subsided, the fluid generated ruptures, which was reflected in a higher VT event rate.

The effect of the $M_W = 7.1$ earthquake consisted mostly in changes in shear stress, which were simply not strong enough to generate faulting neither at the fault nor at the reservoir. The presence of a long-term extension zone at the northern end of the fault might help explain the decline in VT activity at reservoir level, as the post-seismic state of the fault encourages fluid motion to its northern section. Such a decrease in fluid-driven seismicity ratio after an important earthquake has also been observed in other parts of the world(Sánchez and SR., 2004)

4.5 Conclusion

We studied a counter-intuitive response of the Nevados de Chillán volcanic system to two aftershocks of the Maule earthquake, with magnitudes $M_W = 6.1$ and $M_W = 7.1$, both of them located about 200 km from the complex. We did this by simulating the effect of the two earthquakes in a simplification of the system, given by a main lineament, with a fluid reservoir connected to it. The response from the volcanic/hydrothermal system was mostly recorded at the level of the hydrothermal field, and it involved highly pressurized fluids very close to a critical state. Due to the distance of the earthquake hypocenters, static stress changes at the reservoir

were not important, and thus the response was most likely to occur due to the dynamic changes induced by the passage of the seismic waves.

Our results show that both earthquakes affected the system in very different ways. Due to the relative location of the earthquakes respective to the system, the radiation pattern of each event plays an important role, leveling the influence of each earthquake in the volcanic/hydrothermal complex, to a point where we can compare them. The influence of the smaller event, of magnitude $M_W = 6.1$, was found to be mainly focused at the fluid level, with larger changes in overpressure than the ones obtained with the $M_W = 7.1$ earthquake. The effect of the local structures is not significant on the interaction between this event and the system dynamics. The higher dynamic volumetric changes are significant, since they can propitiate fluid motion, which is later reflected in tremor activity. Given that the faulting potential from the earthquake waves is not of large importance, our results support the idea of an earthquake/volcano connection at the fluid reservoir level.

A different conclusion arises from the results of the simulations of the $M_W = 7.1$ earthquake. Due to its magnitude, we should expect it to be more influential in the system than the smaller event, but a combination of the relative position of its hypocenter with respect to the location of the volcanic/hydrothermal field with the dynamic effect of the main fault of the system, prevent this to happen. The volumetric changes induced by this earthquake are lower than the ones generated by the smaller event, but the shear stress transfer is substantially larger, a result that is reflected in a higher dynamic change in the Coulomb yield function. While this tells that the $M_W = 7.1$ event has a larger faulting potential at the system than the $M_W = 6.1$ earthquake, the field observations suggest that they were not high enough to trigger seismic activity, quite possibly due to the fault not being close to a critical state. And while the static stress changes are negligible at the reservoir level, we found a small long term volumetric extension at the northern section of the fault, which may in turn promote fluid mobilization to the northern sections of the structure, thus decreasing the seismicity at the reservoir level. This is consistent with the observations from the field.

We want to emphasize that the local structures do play a role in the interaction between an earthquake and a volcanic/hydrothermal zone, which can be more or less important depending on the incoming earthquake. In our case, the $M_W = 7.1$ earthquake, despite being about 32 times larger than the $M_W = 6.1$ event, did not trigger an increase in seismicity, and the main system fault did play a role by dampening the volumetric changes inside the structure, which is connected to the high-pressurized fluids of the system. Observations like this one add an extra degree of complexity in the study of earthquake/volcano interactions, but they also allow us to have a better understanding of the underlying physical mechanisms that control such connection.

Acknowledgments

Cristian Farías thanks the Becas Chile scholarship program and to the FAZIT foundation for supporting his work.

Chapter 5

General conclusions and future work

Earthquakes can trigger different types of responses in volcanic and hydrothermal systems, ranging from increases in local seismicity to eruptions, with most of the responses being recorded at the hydrothermal level, due to their susceptibility to external perturnations. In this thesis I have presented results from field observations and numerical simulations of the influence of several earthquakes in volcanic and hydrothermal regions.

Field data was adquired during a field campaign at the Nevados de Chillán volcano in central south Chile, from December, 2011, to April, 2012. This is a particularly active volcanic/hydrothermal system that has shown interesting responses to external earthquakes in the past, and that suffered major volumetric extension after the $M_W = 8.8$ 2010 Maule earthquake. Data shows how most of the activity at this volcanic complex is located at the hydrothermal level, not at the magma chamber. During the observation time, two major aftershocks of the Maule earthquake were recorded, both located around 200 km away from the system, but with different magnitudes: the first one was a $M_W = 6.1$ event, whilst the magnitude of the second earthquake was $M_W = 7.1$. The composite volcanic/hydrothermal system showed a response in the form of an increase of the fluid-driven seismicity immediately after the first event, and a slight decrease in seismicityt after the second, and larger, earthquake. This observation highlights a complex earthquake-volcano interaction, with a response that is not intuitive. An interesting fact here is that the static stress changes due to the incoming earthquakes are negligible at the reservoir level, and thus the interaction is related to dynamic stress changes. Particle motion analysis shows how the $M_W = 6.1$ earthquake induced a wave motion in a particular E-W direction at the system, whilst the larger earthquake did not have a preferred direction of motion. This suggest that there is a stress concentration in one particular direction for the smaller earthquake, which might have promoted fluid motion, and therefore, an increase on seismicity. This feature is not present for the second, larger event, even though the ground motion velocity recorded for this event is larger.

The observation on Nevados de Chillán volcanic complex also suggest that there is an effect of the directivity of the earthquake respective to the local structures of the system. To study the influence of seismic events in hydrothermal regions that do account for the presence of local structures such as geological faults, we created a new set of poroelastic codes that allow us to simulate the effect of seismic waves in regions where highly-pressurized fluids are trapped beneath the crust. We studied the effect of the dip angle and relative location of several $M_W = 4.0$ earthquakes, located close to a system composed by a fluid reservoir connected to a main fault, and the effect of the strike angle and relative location of several $M_W = 6.1$ events located 100 km away from a volcanic/hydrothermal system composed by two fluid reservoir, each one connected to a fault. In the first case, both static and dynamic changes in the stress tensor are relevant, whilst only the dynamic part is important for the second experiment. We found out that, while the relative location of the earthquake and its characteristics play a very important role in the changes of the regional stress tensor, the role of the local structures is very important. Static volumetric patterns are distorted in the vicinity and the interior of the structures, particularly in the system fault, where it gets reduced. This result adds a level of complexity that is can not be found in a normal Coulomb stress analysis, where the fault zone is not completely considered. Dynamic changes show how the local structures affect the wave motion. The fluid reservoir concentrates the incoming kinetic energy from the earthquake at its borders, and do not allow too much energy to be concentrated inside itself. The maximum dynamic changes of the overpressure and Coulomb yield function are also found at its borders. The wave frequency inside the reservoir is higher than outside it, and thus are more likely to encourage gas-fluid interaction(Vandu et al., 2004). The system fault concentrates kinetic energy inside it, and shows breakwater-like characteristics for the dynamic changes in the overpressure and Coulomb yield function, concentrating the larger changes at one face of the structure, and reducing the earthquake influence at the other side. For earthquakes located far from the volcanic/hydrothermal system, the role of the local structures is particularly noticeable for the dynamic stress changes, which are more prominent. The geometry of the fault system is also very important, with one earthquake being capable to affect only one fault, depending on its directivity and focal mechanism.

The numerical simulation approach is very useful when dealing with simplifications of real life systems. In particular, we used our numerical tools to simulatte the situation we observed in our field campaign, with the response of the Nevados de Chillán volcanic system to two aftershocks of the Maule earthquake. For both earthquakes, the static stress changes at reservoir level are negligible, with the volumetric stress changes in the order of some tens of kPa, which is enough to trigger small increases in hydrothermal activity(Hill and Prejean, 2007). Due to the relative location of the earthquakes respective to the volcanic/hydrothermal system, the smaller $M_W = 6.1$ event induced larger overpressure change at the hydrothermal reservoir level than the larger earthquake, thus having a more important effect at the fluid level. This is consistent with the observed increase on hydrothermal tremor activity, which was

followed by fluid-driven VT events after the fluids were mobilized. The overpressure change from the $M_W = 7.1$ event was not as strong due to the relative location of the earthquake respect to the system, and it was also dampened inside the fault, thus having an even lower influence on the fluid. Moreover, the $M_W = 7.1$ earthquake induced a small long-term decrease in pressure at the northern edge of the main fault, thus creating a small pressure gradient that may have mobilized the high-pressurized fluid of the hydrothermal system. This type of motion is consistent with a reduction on the seismicity captured at the hydrothermal field that was observed. The largest changes on the stress tensor due to the $M_W = 7.1$ earthquake were at the shear components. This generated larger changes in the yield function due to this event, but they were not strong enough to create new fractures.

The results presented in this thesis show that the interaction between earthquakes and volcanic/hydrothermal systems is far more complex than it is understood so far. The role of the local structures is very important in this connection, and it can not be taken away from future studies. And while this adds an extra degree of complexity to the question on how can earthquakes affect volcanic and hydrothermal activity, it does give more light on the important physical mehanisms that control the interaction. For the future, more in-depth observations on the role between tectonics and volcanic activity are needed, as well as better characterizations of the type of response of a volcanic/hydrothermal system to external perturbations. Improvements on numerical simulations are also necessary, with special emphasis in the implementation of the role of waves in the geochemical/physical characteristics of the fluids. An extension to 3-D spaces is also necessary, as it can allow us to experiment with a wider array of earthquake parameters. Advances in the complexity of the fault systems can also give us a clearer idea on what are the most important players that control the earthquake-volcano interactions. The results presented here can also be used as the foundation for developments in risk assessment in volcanic regions, thus contributing to a better integration between society and their surroundings.

Bibliography

Annen, C., Lénat, J., and Provost, A. (2001). The long-term growth of volcanic edifices: numerical modelling of the role of dyke intrusion and lava-flow emplacement. *Journal of Volcanology and Geothermal Research*, 105:263–289.

Barrientos, S. (1994). Large thrust earthquakes and volcanic eruptions. *Pure and Applied Geophysics*, 142:225–237.

BBC (2010). Ash clouds: Airlines face huge task as ban ends.

Bean, C., De Barros, L., Lokmer, I., Metaxian, J., O' Brien, G., and Murphy, S. (2014). Long-period seismicity in the shallow volcanic edifice formed from slow-rupture earthquakes. *Nature Geoscience*, 7:71–75.

Bebbington, M. and Marzocchi, W. (2011a). Stochastic models for earthquake triggering of volcanic eruptions. *J. Geophys. Res. B*, 116.

Bebbington, M. S. and Marzocchi, W. (2011b). Stochastic models for earthquake triggering of volcanic eruptions. *Journal of Geophysical Research*, 116.

Bizzarri, A. (2011). On the deterministic description of earthquakes. *Reviews of Geophysics*, 49:RG3002.

Bizzarri, A. (2012). Rupture speed and slip velocity: What can we learn from simulated earthquakes? *Earth and Planetary Science Letters*, 317–318:196–203.

Board, O. A. R. (2013). Openmp complete specifications.

Bohm, M., Lüth, S., Echtler, H., Asch, G., Bataille, K., Bruhn, C., Rietbrock, A., and Wigger, P. (2002). The southern andes between 36 and 40s latitude: seismicity and averare seismic velocities. *Tectonophysics*, 356:275–289.

Bonali, F. (2013). Earthquake-induced static stress change on magma pathway in promoting the 2012 copahue eruption. *Tectonophysics*, pages 127–137.

Bonali, F., Tibaldi, A., Corazzato, C., Tormey, D., and Lara, L. (2013). Quantifying the effect of large earthquakes in promoting eruptions due to stress changes on magma pathway: The chile case. *Tectonophysics*, 583:54–67.

Brenguier, F., Campillo, M., Takeda, T., Aoki, T., Shapiro, N., Briand, X., Emoto, K., and Miyake, H. (2014). Mapping pressurized volcanic fluids from induced crustal seismic velocity drops. *Science*, 345:80–82.

Brodsky, E. and Prejean, S. (2005). New constrains on mechanism of remotely triggered seismicity at long valley caldera. *J. Geophys. Res. B*, 110.

Brodsky, E., Sturtevant, B., and Kanamori, H. (1998). Earthquakes, volcanoes, and rectified diffusion. *J. Geophys. Res.*, 103:23827–23838.

Brooks, B., Bevis, M., Whipple, K., Arrowsmith, J., Foster, J., Zapata, T., Kendrick, E., Minaya, E., Echalar, A., Blanco, M., Euillades, P., Sandoval, M., and Smalley, R. (2011). Orogenic-wedge deoformation and potential for great earthquakes in the central andean backarc. *Nature Geoscience*, 4:380–383.

Cembrano, J. (1992). The liquiñe-ofqui fault zone (lofz) in the province of palena: Field and microstructural evidence of a ductile-brittle dextral shear zone. *Universidad de Chile, Departamento de Geología, Comunicaciones.*

Cembrano, J., Hervé, F., and Lavenu, A. (1996). The liquiñe ofqui fault zone: a long-lived intra-arc fault system in southern chile. *Tectonophysics*, 259:55–66.

Cembrano, J. and Lara, L. (2009). The link between volcanism and tectonics in the southern volcanic zone of the chilean andes: A review. *Tectonophysics*, 471:96–113.

Cembrano, J., Schermer, E., Lavenu, A., and Sanhueza, A. (2000). Contrasting nature of deformation along an intraarc shear zone, the liquiñe-ofqui fault zone, southern chilean andes. *Tectonophysics*, 319:129–149.

Chouet, B. and Julian, B. (1985). Dynamics of an expanding fluid-filled crack. *Journal of Geophysical Reseach*, 90:11187–11198.

Convertito, V., Catalli, F., and Emolo, A. (2013). Combining stress transfer and source directivity: the case of the 2012 emilia sequence. *Scientific Reports*, 3:3114.

d'Acremont E., Leroy, S., and Burov, E. (2003). Numerical modelling of a mantle plume: the plume head-lithosphere interaction in the formation of an oceanic large igneous province. *Earth and Planetary Science Letters*, 206:376–396.

Darwin, C. (1840). On the connection of certain volcanic phenomena in south america, and on the formation of mountain chains and volcanoes, as the effect of the same power by which continents are elevated. *Trans. Geol. Soc. London.*

Davis, P., Rubinstein, J., Liu, K., Gao, S., and Knopoff, L. (2000). Northridge earthquake damage caused by geologic focusing of seismic waves. *Science*, 289:1746–1750.

Delle Donne, d., Harris, A., Ripepe, M., and Wright, R. (2010). Earthquake-induced thermal anomalies at active volcanoes. *Geology*, 38:771–774.

Dixon, H. J., Murphy, M. D., Sparks, S. J., Chavez, R., Naranjo, J. A., Dunkley, P. N., Young, S. R., Gilbert, J. S., and Pringle, M. R. (1999). The geology of nevados de chillán volcano, chile. *Revista geológica de Chile*, 26(2):227–253.

Drossaert, F. and Giannopoulos, A. (2007). A nonsplit complex frequency-shifted pml based on recursive integration for fdtd modeling of elastic waves. *Geophysics*, 72:T9–T17.

Dzierma, Y. and Wehrmann, H. (2010). Eruption time series statistically examined: Probabilities of future eruptions at villarrica and llaima volcanoes, southern volcanic zone, chile. *J. Volcanol. Geotherm. Res.*, 193:82–92.

Eggert, S. and Walter, T. (2009). Volcanic activity before and after large tectonic earthquakes: Observations and statistical significance. *Tectonophysics*, 471:14–26.

Elkhoury, J. E., Brodsky, E. E., and Agnew, D. C. (2006). Seismic waves increase permeability. *Nature*, 441(7097):1135–1138.

Farías, C., Galván, B., and Miller, S. (2016). Numerical study on the influence of pre-existing local structures and seismic source characteristics in earthquake-volcano interactions. *Journal of Geophysical Research, on preparation.*

Farías, C., Lupi, M., Fuchs, F., and Miller, S. (2014). Seismic activity of the nevados de chillán volcanic complex after the 2010 mw8.8 maule, chile, earthquake. *Journal of Volcanology and Geothermal Research*, 283:116–126.

Freed, A. (2005). Earthquake triggering by static, dynamic, and post-seismic stress transfer. *Annual Review of Earth and Planetary Sciences*, 33:335–367.

Fuchs, F., Lupi, M., and Miller, S. (2014). Remotely triggered nonvolcanic tremor in sumbawa, indonesia. *Geophysical Research Letters*, 41:4185–4193.

Fujita, E., Kozono, T., Ueda, H., Kohno, Y., Yoshioka, S., Toda, N., Kikuchi, A., and Ida, Y. (2014). Mapping pressurized volcanic fluids from induced crustal seismic velocity drops. *Science*, 345:80–82.

Gahalaut, K., Gahalaut, V., and Kayal, J. (2008). Poroelastic relaxation and aftershocks of the 2001 bhuj earthquake, india. *Tectonophysics*, 460:76–82.

Giordano, D., Russell, J., and Dingwell, D. (2008). Viscosity of magmatic liquids: A model. *Earth and Planetary Science Letters*, 271:123–134.

Gomberg, J., Bodin, P., Larson, K., and Dragert, H. (2004). Earthquake nucleation by transient deformations caused by the $m = 7.9$ denali, alaska, earthquake. *Nature*, 427:621–624.

Gonnermann, H. and Manga, M. (2007). The fluid mechanics inside a volcano. *Annual Review of Fluid Mechanics*, 39:321–356.

Gonzalez-Ferrán, O. (1995). *Volcanes de Chile*. Instituto Geográfico Militar, Chile.

Hardebeck, J., Nazareth, J., and Hauksson, E. (1998). The static stress change triggering model: Constraints from two southern california aftershock sequences. *Journal of Geophysical Research*, 103:24427–24437.

Harris, R. (1998). Introduction to special section: Stress triggers, stress shadows, and implications for seismic hazards. *Journal of Geophysical Research*, 103:24347–24358.

Harris, R. N. and McNutt, M. K. (2007). Heat flow on hot spot swells: Evidence for fluid flow. *J. Geophys. Res. B*, 112(B3).

Heap, M., Baud, P., Meredith, P., Vinciguerra, S., and Reuschlé, T. (2014). Physical properties of tuff from campi flegrei. *Solid Earth*, 5:25–44.

Heinze, T., Galván, B., and Miller, S. (2015). Modeling porous rock fracturing induced by fluid injection. *International Journal of Rock Mechanics and Mining Sciences*, 77:133–141.

Hennings, P., Allwardt, P., Paul, P., Zahm, C., Alley, H., Kirschner, R., Lee, B., and Hough, E. (2012). Relationship between fractures, fault zones, stress, and reservoir productivity in the suban gas field, sumatra, indonesia. *The Am. Assoc. Petr. Geo. Bull.*, 96:753–772.

Hill, D. (2008). Dynamic stresses, coulomb failure, and remote triggering. *Bull. Seism. Soc. Am.*, 102:2313–2336.

Hill, D., Johnston, M., Langbein, J., and Bilham, R. (1995). Response of long valley caldera to the m=7.3 landers, california, earthquake. *Geophys. Res. Lett.*, 100:12985–13005.

Hill, D., Pollitz, P., and Newhall, C. (2002). Earthquake-volcano interactions. *Physics Today*, 55:41–47.

Hill, D. and Prejean, S. (2007). *Earthquake Seismology Treatise on Geophysics*, chapter Dynamic Triggering. Elsevier.

Hill, D., Reasenberg, A., Michael, A., Arabaz, W., Beroza, G., Brumbaugh, D., Brune, J., Castro, R., Davis, S., dePolo, D., Ellsworth, W., Gomberg, J., Harmsen, S., House, L., Jackson, S., Johnston, J., Jones, L., Keller, R., Malone, S., Munguia, L., Nava, S., Pechmann, J., Sanford, A., Simpson, R., Smith, R., Stark, M., Stickney, M., Vidal, A., Walter, S., Wong, V., and Zollweg, J. (1993). Seismicity remotely triggered by the magnitude 7.3 landers, california, earthquake. *Science*, 260:1617–1623.

Husen, S., Taylor, R., Smith, R., and Healser, H. (2004). Changes in geyser eruption behavior and remotely triggered seismicity in yellowstone national park produced by the 2002 m7.9 denali fault earthquake, alaska. *Geology*, 32:537–540.

Ichihara, M. and Brodsky, E. (2006). A limit on the effect of rectified diffusion in volcanic systems. *Geophys. Res. Lett.*, 32.

Jaeger, J., Cook, N., and Zimmerman, R. (2007). *Fundamentals of Rock Mechanics*. Blackwell publishing.

Jay, J., Pritchard, M., West, M., Christensen, D., Haney, M., Minaya, E., Sunagua, M., McNutt, S., and Zabala, M. (2011). Shallow seismicity, triggered seismicity, and ambient noise tomography at the long-dormant uturuncu volcano, bolivia. *Bull. Volcanol.*, 74:817–837.

Johnson, C., Bürgmann, R., and Pollitz, F. (2015). Rare dynamic triggering of remote $m \geq 5.5$ earthquakes from global catalog analysis. *Journal of Geophysical Research: Solid Earth*, 120:1748–1761.

Johnston, M., Hill, D., Langbein, J., and Bilham, R. (1995). Transient deformation during triggered seismicity from the 28 june 1992 $m_w = 7.3$ landers earthquake at long valley volcanic caldera, california. *Bull. Seism. Soc. Am.*, 85:787–795.

Karki, B. and Stixrude, L. (2010). Viscosity of mgsio3 liquid at earth's mantle conditions: Implications for an early magma ocean. *Science*, 328:740.

Kereszturi, G., Cappello, A., Ganci, G., Procter, J., Németh, K., Del Negro, C., and Cronin, S. (2014). Numerical simulation of basaltic lava flows in the auckland volcanic field, new zealand–implication for volcanic hazard assessment. *Bulletin of Volcanology*, 76:879.

Khazaradze, G., Wang, K., Klotz, J., Hu, Y., and He, J. (2002). Prolonges postseismic deformation of the 1960 great chile earthquake and implications for mantle rheology. *Geophys. Res. Lett.*, 29:2050.

Kitagawa, Y., Fujimori, K., and Koizumi, N. (2002). Temporal change in permeability of the rock estimated from repeated water injection experiments near the nojima fault in awaji island, japan. *Geophys. Res. Lett.*, 29(10):1483.

Kundu, B., Legrand, D., Gahalaut, K., Gahalaut, V., Mahesh, P., Kamesh, K., Catherine, J., and Chadha, R. (2012). The 2005 volcano-tectonic earthquake swarm in the andaman sea: Triggered by the 2004 great sumatra-andaman earthquake. *Tectonics*, 31.

Kushiro, I., Yoder, H., and Mysen, B. (1976). Viscosities of basalt and andesite melts at high pressures. *Journal of Geophysical Research*, 81:6251–6356.

Lagmay, A., van Wyk de Vries, B., Kerle, N., and Pyle, D. (2000). Volcano instability induced by strike-slip faulting. *Bulletin of Volcanology*, 62:331–346.

Lange, D., Cembrano, J., Rietbrock, A., Haberland, C., Dahm, T., and Bataille, K. (2008). First seismic record for intra-arc strike-slip tectonics along the liquiñe-ofqui fault zone at the obliquely convergent plate margin of the southern andes. *Tectonophysics*, 455:14–24.

Lara, L., Naranjo, J., and Moreno, H. (2004). Rhyodacitic fissure eruption in southern andes (cordón caulle; 40.5°s) after the 1960 (mw: 9.5) chilean earthquake: a structural interpretation. *J. Volcanol. Geotherm. Res.*, 138:127–138.

Lavenu, A. and Cembrano, J. (1999). Compressional and transpressional stress pattern for pliocene and quaternary brittle deformation in forearc and intra-arc zones (andes of central and southern chile). *Journal Struct. Geol.*, 21:1669–1691.

Le Mével, H., Feigl, K., Córdova, L., DeMets, C., and Lundgren, P. (2015). Evolution of unrest at laguna del maule volcanic field (chile) from insar and gps measurements, 2003 to 2014. *Geophysical Research Letters*, 42:6590–6598.

Leet, R. (1991). *Investigation of Hydrothermal Boiling and Steam Quenching as Possible Sources of Volcanic Tremor and Geothermal Noise.* PhD thesis, University of Washington.

Longo, A., Barbato, D., Papale, P., Saccorotti, G., and Barsanti, M. (2008). Numerical simulation of the dynamics of fluids oscillations in a gravitationally unstable, compositionally stratified fissure. *Geological Society, London, Special Publications*, 307:33–44.

Longo, A., Vassalli, M., Papale, P., and Barsanti, M. (2006). Numerical simulation of convection and mixing in magma chambers replenished with co_2-rich magma. *Geophysical Research Letters*, 33:L21305.

Lupi, M., Fuchs, F., and Pacheco, F. (2014). Fault reactivation due to the $m7.6$ nicoya earthquake at the turrialba-irazú volcanic complex, costa rica: Effects of dynamic stress triggering. *Geophysical Research Letters*, 41:4142–4148.

Lupi, M. and Miller, S. (2014). Short-lived tectonic switch mechanism for long-term pulses of volcanic activity after mega-thrust earthquakes. *Solid Earth*, 5:13–24.

Lupi, M., Saenger, H., Fuchs, F., and Miller, S. (2013). Lusi mud eruption triggered by geometric focusing of seismic waves. *Nature Geoscience*, 6:642–646.

Mandeville, C., Carey, S., and Sigurdsson, H. (1996). Magma mixing, fractional crystallization and volatile degassing during the 1883 eruption of krakatau volcano, indonesia. *Journal of Volcanology and Geothermal Research*, 74:243–274.

Manga, M. and Brodsky, E. (2006). Seismic triggering of eruptions in the far field: Volcanoes and geysers. *Annu. Rev. Earth Planet. Sci.*, 34:263–291.

Martin, R., Komatisch, D., and Ezziani, A. (2008). An unsplit convolutional perfectly matched layer improved at grazing incidence for seismic wave propagation in poroelastic media. *Geophysics*, 73:T51–T61.

Marzocchi, W., Casarotti, E., and Piersanti, A. (2002). Modeling the stress variations induced by great earthquakes on the largest volcanic eruptions of the 20th century. *J. Geophys. Res.*, 107.

Mazzini, A., Svensen, H., Akhmanov, G., Aloisi, G., Planke, S., Malthe-Sorenssen, A., and Istadi, B. (2007). Triggering and dynamic evolution of the lusi mud volcano, indonesia. *Earth and Planetary Science Letters*, 261:375–388.

McNutt, S. (2005). Volcanic seismology. *Annu. Rev. Earth Planet. Sci.*, 32:461–491.

Merle, O., Vidal, N., and van Wyk de Vries, B. (2001). Experiments on vertical basement fault reactivation below volcanoes. *Journal of Geophysical Research*, 106:2153–2162.

Miller, S., Colletini, C., Chiaraluce, L., Cocco, M., Barchi, M., and Kaus, B. (2004). Aftershocks driven by high-pressure $c0_2$ source at depth. *Nature*, 427:724–727.

Miyazawa, M. and Mori, J. (2005). Detection of triggered deep low-frequency events from the 2003 tokachi-oki earthquake. *Geophysical Research Letters*, 32.

Miyazawa, M. and Mori, J. (2006). Evidence suggesting fluid flow beneath japan due to periodic seismic triggering from the 2004 sumatra-andaman earthquake. *Geophysical Research Letters*, 33.

Mora-Stock, C., Thorwart, M., Wunderlich, T., Bredemeyer, S., Hansteen, T., and Rabbel, W. (2012). Comparison of seismic activity for llaima and villarrica volcanoes prior to and after the maule 2010 earthquake. *Int. J. Earth Sci.*, pages 1–14.

Moreno, M., Rosenau, M., and Oncken, O. (2010). 2010 maule earthquake slip correlates with pre-seismic locking of andean subduction zone. *Nature*, 467(7312):198–202.

Nakamura, K. (1977). Volcanoes as possible indicators of tectonic stress orientation: principle and proposal. *J. Volcanol. Geotherm. Res.*, 2:1–16.

Neri, A., Di Muro, A., and Rosi, M. (2002). Mass partition during collapsing and transitional columns by using numerical simulations. *Journal of Volcanology and Geothermal Research*, 115:1–18.

Okada, Y. (1985). Surface deformation due to a shear and tensile faults in a half-space. *Bulletin of the Seismological Society of America*, 75:1135–1154.

Ottemöller, Voss, and Havskov (2011). *Seisan Earthquake Analysis Software for Windows, Solaris, Linux, and Macosx*. Ottemöller, Voss, and Havskov.

Papale, P. (1999). Numerical simulations of magma ascent along volcanic conduits. *Physics and Chemistry of the Earth*, 24:957–961.

Pollitz, F., Stein, RS. abd Sevilgen, V., and BÚrgmann, R. (2012). The 11 april 2012 east indian ocean earthquake triggered large aftershocks worldwide. *Nature*, 490:250–253.

Pritchard, M., Jay, J., Aron, F., Henderson, S., and Lara, L. (2013). Subsidence at southern andes volcanoes induced by the 2010 maule, chile earthquake. *Nature Geoscience*, 6:632–636.

Proussevitch, A. and Sahagian, D. (1998). Dynamics and energetics of bubble growth in magmas: Analytical formulation and numerical modeling. *Journal of Geophysical Research*, 103:18223–18251.

Rozhko, A. (2007). *Role of seepage forced on hydraulic fracturing and failure patterns*. PhD thesis, Department of Physics, University of Oslo, Norway.

Ruch, J. and Walter, T. (2010). Relationship between the insar-measured uplift, the structural framework, and the present-day stress field at lazufre volcanic area, central andes. *Tectonophysics*, 492:133–140.

Saenger, E., Gold, N., and Saphiro, S. (2000). Modelling the propagation of elastic waves using a modified finite-difference grid. *Wave Motion*, 31:77–21.

Sahagian, D. and Proussevitch, A. (1992). Bubbles in volcanic systems. *Nature*, 359.

Sánchez, J. and SR., M. (2004). Intermediate-term declines in seismicity at mt. wrangell and mt. veniaminof volcanoes, alaska, following the 3 november 2002 m_w 7.9 denali fault earthquake. *Bulletin of the Seismological Society of America*, 94:S370–S383.

Siebert, L., Simkin, T., and Kimberly, P. (2012). *Volcanoes of the World*. University of California Press, USA.

Sparks, R., Sigurdsson, J., and Wilson, L. (1977). Magma mixing: A mechanism for triggering acid explosive eruptions. *Nature*, 267:315–318.

SSN (2013). http://www.sismologia.cl/links/terremotos/index.html. Technical report, Chilean Seismological Service.

Stein, S. and Wysession, M. (2003). *An introduction to seismology, earthquakes, and Earth structure*. Blackwell publishing.

Takada, Y. and Fukushima, Y. (2013). Volcanic subsidence triggered by the 2011 tohoku earthquake in japan. *Nature Geoscience*, 6:637–641.

Terakawa, T., Yamanaka, Y., Nakamichi, H., Watanabe, T., Yamazaki, F., Horikawa, S., and Okuda, T. (2013). Effect of pore fluid pressure and tectonic stress on diverse seismic activities around the mt. ontake volcano, central japan. *Tectonophysics*, 608:138–148.

Times, L. A. (2011). Japan damage could reach $235 billion, world bank estimates.

Todesco, M., Rutqvist, J., Chiodini, G., Pruess, K., and Oldenburg, C. (2004). Modeling of recent volcanic episodes at phlegrean fields (italy): geochemical variations and ground deformation. *Geothermics*, 33:531–547.

UNEP (2011). Unep year book: emerging issues in our global environment 2011.

Vandu, C., Ellenberg, J., and Krishna, R. (2004). Hydrodynamics and mass transfer in an upflow monolith loop reactor: influence of vibration excitement. *Chemical Engineering Science*, 59:4999–5008.

Venzke, E. e. S. I. (2013). Global volcanism program, 2013. volcanoes of the world, v. 4.4.1.

Walter, T. and Amelung, F. (2006). Volcano-earthquake interaction at mauna loa volcano, hawaii. *Journal of Geophysical Research*, 111:B05204.

Walter, T. and Amelung, F. (2007). Volcanic eruptions following m≥9 megathrust earthquakes: Implications for the sumatra-andaman volcanoes. *Geology*, 35:539–542.

Wang, B., Harrington, R., Liu, Y., Yu, H., Carey, A., and van der Elst, N. (2015). Isolated cases of remote dynamic triggering in canada detected using cataloged earthquakes combined with a matched-filter approach. *Geophysical Research Letters*, 42:5187–5196.

Wang, F., Shen, Z., Wang, Y., and Wang, M. (2011). Influence of the march 11, 2011 m_w 9.0 tohoku-oki earthquake on regional volcanic activities. *Chinese Science Bulletin*, 56:2077–2081.

Wassermann, J. (2012). *Volcano Seismology, IASPEI New Manual of seismological observatory practice 2*. Potsdam: Deutsches GeoForschungsZentrum GFZ.

Watt, S., Pyle, D., and Mather, T. (2009). The influence of great earthquakes on volcanic eruption rate along the chilean subduction zone. *Earth and Planetary Science Letters*, 277:399–407.

wave potential for triggering tectonic (nonvolcanic) tremor, S. (2010). Hill, dp. *Bulletin of the Seismological Society of America*, 100:1859–1878.

Wei, M., Liu, Y., McGuire, J., and Bilham, R. (2015). Dynamic triggering of creep events in the salton trough, southern california by regional $m \geq 5.4$ earthquakes constrained by geodetic observations and numerical simulations. *Earth and Planetary Science Letters*, 427:1–10.

Wicks, C., de la Llera, J., Lara, L., and Lowenstern, J. (2011). The role of dyking and fault control in the rapid onset of eruption at chaitén volcano, chile. *Nature*, 478:374–377.

Withers, M., Aster, R., Young, C., Beiriger, J., Harris, M., Moore, S., and Trujillo, J. (1998). A comparison of select trigger algorithm for automated global seismic phase and event detection. *Bull. Seism. Soc. Am.*, 88:95–106.

Yu, W., Lashgari, H., Wu, K., and Sepehynoori, K. (2015). Co_2 injection for enhanced oil recovery in bakken right oil reservoirs. *Fuel*, 159:354–363.

Acknowledgments

This thesis comes as the conclusion of a very important stage of a journey that began more than 27 years ago when, as little kid, I saw the 1988 eruption of Lonquimay volcano, in south Chile. I do not remember any of it now, but I do recall myself building small volcanic cones out of dirt, putting some tree leaves on top, and asking my parent to light them for me. I was three then. Now, at 30, I'm studying volcanoes, with a new road opening ahead. The days of the student are about to be over and, who knows, maybe one day I will be the one who will lit some tree leaves for my children.

There is a lot of people to be thankful now, and I ask their forgiveness if they do not find themselves in this list. First and foremost, I have to thank the Becas Chile scholarship program and the FAZIT scholarship for giving me the necessary funding that allowed me to pursue my PhD studies in Geophysics. I hope the trust you put in my project is paying off now.

I'm also very thankful to everybody who shared this journey with me at the Steinmann Institute of the University of Bonn, in particular to Prof. Dr. Stephen Miller, Prof. Dr. Andreas Kemna, Dr. Florian Fuchs, Dr. Thomas Heinze, Dr. Boris Galván, Dr. Shiva Pudasaini, Dr. Andreas Dreist, Dr. Matteo Lupi, Sahar Samidi, Johannes Kenkel, Maximilian Weigand, and Lisa Takacs. Thank you for everything, guys. It's been great!

About one year ago I had a lot of work done, but not too many results to show. At that point, I said to my younger brother: "Right now, Borussia Dortmund are struggling, but they will be back on top. And I know my thesis will progress with them". Sure enough, we all are in a very good place right now. Heja BVB!

I also want to thank the friends, who have been there for me at different stages of the PhD: Elisa, Cindy, Philipp, Pablo, Lucho, Nena, Denise, Carolina, Pablo, Víctor, Max, Patricio. Thanks a lot guys! We are in different places of the world, but that will change.

Family has played a very important role during this time abroad. They are many, so I can't cover them all, but I want to say thanks to Filomena, Oscar, Ricardo, Ivo, Guillermo, Toño, Mercedes, Nino, Adelqui, Carolina, Jacqueline, Belén, Jessica, and my grandparents María and Guillermo.

On January 29th, 2012, I began this part of my journey. I said goodbye to my parents, Alexis and Aurora, to my brothers, Camilo and Gonzalo, and to my wife, Ximena, who 4 months later joined me here in Bonn. All this would have been impossible without them. I love you all, and I keep you always very close to my heart. Sadly, one of us is not here anymore, so I hope you can be reading this from the skies, dad. We all love you, and remember, you were the one who pushed me into this! It was because of your job that I got to see the volcanoes, and it was you the one who gave me that book of volcanoes. I love you very much, dad, and I know that we will meet again, some sunny day. And yes, the vinyls are not for sale!

And finally, my closest ones, the loves of my life: Ximena, Julieta, and Oscar. You have given me all the support I have needed during this time. You have made sacrifices for me, and I'm the happiest man on earth just to be able to be next to you. Oscar, thank you for accepting me, and be there with us. We will be together very soon, the four of us. Julieta, your birth has been one of the highlights of my life, and you are a light in the dark for many of us. We love you, all your family. And Ximena, my dearest Xime. It is because of you that I keep pursuing my dreams. It is because of you that I can finish everyday of my life with a smile in my heart. You are the love of my life, and this thesis goes to you. I love you.